Thermal Kinetics Study of Paper and Plastic Waste Gasification

Thesis submitted to Cardiff University in Fulfilment of the Requirements for the degree of Doctor of Philosophy in Chemical Engineering- Renewable Energy

By

Ahmad Mohamed S H Al-Moftah

BEng. Chemical Eng. & M.Sc. Eng. Management

School of Engineering

Cardiff University, Wales, United Kingdom

March 2022

Declaration

This thesis is the result of my own work, I declare that N + P group was not involved in way in the process of developing this work. I have no links to N + P group thus they did not fund or offer other forms of support to this thesis. I studied Subcoal™ because it was selected as a suitable and reliable candidate study material.

Acknowledgments

My experience in the PhD study was a long journey and I was fortunate to have continued support from various people who encouraged me throughout. I would like to begin by expressing my heartfelt gratitude to my academic supervisors, Prof. Richard Marsh and Dr Julian Steer, for their critical roles in allowing me to pursue this PhD at Cardiff University. Also, I would like to acknowledge Qatar National Research Fund (QNRF) and Graduate Sponsor Research Award (GSRA) for funding my doctoral project number GSRA5-1-0404-18034. This financial support is greatly appreciated as it made my dream of completing my PhD study a reality. I also extend my special gratitude to the QNRF staff who coordinated and advised me during my research. My special thanks go to the Qatar embassy in the UK as well. Prof. Richard and Dr Julian, I have learned so much from you, and I would like to express my thanks for your advise, motivation, and support in inspiring me and assisting me in overcoming the challenges that have come my way. I would also especially like to appreciate you for always investing your precious time in guiding me to achieve my goals. Your support during the coronavirus (COVID-19) pandemic is highly appreciated. Despite the challenges that the COVID-19 has brought to our world, you always supported me in the lab, responded to my emails and followed my PhD progress. In addition, I acknowledge your generosity demonstrated by your willingness to provide me with Subcoal™ sample from N+ P Company, catalyst and silica sand to conduct my experiments, without which my PhD research and experimental analysis would not have been possible. I am greatly honoured by the assistance provided by the technical staff at Cardiff University. I am extending my heartfelt thanks to Mr. Malcolm Seaborne for helping me to set up my FBGR experimental rigs and installing a complex control system in the combustion lab. I am also extremely grateful to Mr. Jeff Rowlands for his technical support on XRD, XRF, LECO, Bomb Calorimeter and other equipment at the chemistry lab. I further extend my gratitude to all staff in the postgraduate research office, finance office and IT in school of engineering at Cardiff University for their assistance. Finally, I would like to thank my family members; they have been important to me in pursuing this project more than everyone. I would thus especially like to thank my wonderful mother, whose love and motivation are with me in anything I pursue. I am most essentially grateful to my loving and supportive wife, Mrs. Kholoud Al-Mulla, and my lovely children, Fatima, Alhanouf, Aljohara and Tamim, for their understanding and tolerance of my absence at times devoted to the completion of this thesis.

Abstract

This thesis focuses on studying the thermal kinetics behaviour of Subcoal™ gasification using fixed bed thermogravimetric analysis (TGA) and bubbling fluidised bed gasifier reactor (BFBGR). Applying this fundamental study to a modern scenario, the current situation of Municipal Solid Waste (MSW) management and the environmental impact of utilising Solid Recovered Fuel (SRF) gasification technology to produce more environmentally friendly electricity in Qatar is investigated. Novel kinetic parameters of Subcoal™ pyrolysis, carbon dioxide (CO_2) gasification, and combustion at various heating rates without catalyst were obtained in TGA using a model free method. The TGA curves showed that the thermal degradation of Subcoal™ comprises three main processes: dehydration, devolatilisation, and char and ash formation. Nevertheless, substantial variance in activation energy (E_a) was noted between the four stages of thermal decomposition of Subcoal™ on all experiments. The results showed that Kissinger-Akahira-Sunose (KAS), Tang (TA), and Starink (ST) are more accurate mathematical methods than Ozawa–Flynn–Wall (OFW) method. The effect of olivine and dolomite loadings on kinetic parameters of Subcoal™ pyrolysis, CO_2 gasification and combustion has been investigated using Coats-Redfern (CR) model fitting method. Among the 19 mechanism models, second order chemical reaction model (G15) was the best linearity for pyrolysis, while third order chemical reaction model (G14) was the best linearity for CO_2 gasification and combustion with dolomite 15 wt.%. First life cycle assessment of SRF air gasification was also conducted using the Recipe2016 model considering five environmental impact categories and four scenarios in Qatar. It considered alternative methods to reduce MSW landfills and produce sustainable energy in line with Qatar's national vision for 2030. The introduction of the SRF gasification reduced climate change-causing emissions by 41.3% because of production of renewable electricity. Thermal gasification behaviour of Subcoal™ pellet and pulverised pellet were also investigated in BFBGR. The producer gas parameters were used to investigate the performance of gasification at different conditions. The findings showed that the increase in temperature enhances the performance of gasification of both Subcoal™ types. Moreover, the optimum gasification temperature tested for Subcoal™ was 750 ºC at equivalence ratio (ER)=0.15. In terms of catalyst effects, the addition of dolomite showed better performance in catalysing the gasification reactions compared to olivine under the same conditions. The Pulverised Subcoal™ pellet performed better than Subcoal™ pellet for gasification due to a shorter reaction time. The Subcoal™ pellet size reduction enhances the conversion efficiency and reduces char formation.

Publications

Al-Moftah, A.M.S., Marsh, R. and Steer, J., 2021. Thermal decomposition kinetic study of non-recyclable paper and plastic waste by thermogravimetric analysis. *ChemEngineering*, *5*(3), p.54.

Al-Moftah, A.M.S., Marsh, R. and Steer, J., 2021. Life cycle assessment of solid recovered fuel gasification in the state of Qatar. *ChemEngineering*, *5*(4), p.81.

Al-Moftah, A.M.S., Marsh, R. and Steer, J., 2022. Thermogravimetric Kinetic Analysis of Non-Recyclable Waste CO_2 Gasification with Catalysts Using Coats–Redfern Method. *ChemEngineering*, *6*(2), p.22.

Conference Presentation

Ahmad Mohamed S H Al-Moftah, Richard Marsh, Julian Steer-Gasification of Biomass from the Waste to Produce Biofuel as Renewable Energy. Cardiff School of Engineering PGR Research Conference. 19 – 21 June, 2019. Gregynog, Wales, UK.

Ahmad Mohamed S H Al-Moftah, Richard Marsh, Julian Steer-Thermal Kinetics Techniques of Subcoal™ Gasification to Produce Syngas. Speaking of Science. Cardiff School of Engineering PGR Research Conference. 20 May, 2021., Virtual Conference, Wales, UK.

Ahmad Mohamed S H Al-Moftah, Richard Marsh, Julian Steer-Thermal Kinetics Study of Plastic and Paper Waste Gasification. 1st FERIA Conference. The European Conference on Fuel and Energy Research and its Applications. 06-08 September, 2021., University of Nottingham, UK.

Table of Contents

List of Tables

List of Figures

Nomenclature

E_a	Activation energy	kJ/mol
T	Temperature	°C, K
A	Pre-exponential factor	min^{-1}
R	Universal gas constant	J/mole.K
t	Time	Second
β	Heating rate	°C/min
R^2	Correlation coefficient	
X	Conversion	dimensionless
T_m	Maximum peak temperature at which peak differential thermal analysis deflection occurs	°C
T_i	Initial temperature	°C
T_f	Final temperature	°C
$\overline{T}$	Mean experimental temperature	°C
DTG	Derivative thermogravimetry	Wt.%/min
a	Numerical integration constant	-
m_o	Initial sample mass	gram
m_f	Final sample mass	gram
m	Mass of sample at any time	gram
m_k	slope	-
y-intercept	b_k	-
k	Reaction rate	s^{-1}
f(X)	Reaction function	dimensionless
d_p^*	Dimensionless particle size	dimensionless
u^*	Dimensionless gas velocity	dimensionless
d_p	Mean particle size of sand	μm
u	Superficial velocity	m/sec
g	Acceleration of gravity	m/s^2
μ	Viscosity of air	g/cm.s
ρ_s	Density of sand	g/cm^3
ρ_g	Density of air	g/cm^3
u_{mf}	Minimum fluidization velocity	m/sec
ER	Equivalence ratio	-
$[AFR]_a$	Actual air fuel ratio	-
$[AFR]_s$	Stoichiometry air fuel ratio	-
$\dot{m}_f$	Mass rate of fuel	g/min, kg/hr
$\dot{m}_{air}$	Mass rate of air	g/min
Q_a	Volume flow rate of air	Nm^3/hr
Y	Gas yield	Nm^3/kg
μ_c	Carbon conversion efficiency	%
η	Cold gas efficiency	%
HHV_f	The gross caloric value of the fuel	MJ/kg
LHV	Low heating value	MJ/kg
HHV	High heating value	MJ/kg
ΔHr	Enthalpy change	kJ/mol
M_{ad}	Moisture content	%
V_d	Volatile matter content	%
A_d	Ash content	%
FC	Fixed carbon content	%
D_d	Bulk density of biomass	kg/m^3

List of abbreviations

BTU	British Thermal Unit
CEN	European Committee for Standardisation
CH_4	Methane
CO	Carbon Monoxide
CO_2	Carbon Dioxide
COS	Carbonyl Sulphide
CR	Coats-Redfern method
CS_2	Carbon Disulphide
DSWMC	Domestic Solid Waste Management Centre
DTG	Differential Thermogravimetry
ECN	Energy Centre Netherlands
Eq.	Equation
EU	European Union
FBGR	Fluidised Bed Gasifier Reactor
FIFA	International Federation of Association Football
GCC	Gulf Cooperation Council
GDP	Gross Domestic Product
GHG	Greenhous Gas
GSDP	General Secretariat for Development Planning
H_2	Hydrogen
H_2S	Hydrogen Sulphide
HCl	Hydrochloric Acid
HDPE	High-Density Polyethylene
HSE	Health, Safety and Environment
IEA	International Energy Agency
KAS	Kissinger-Akahira-Sunose method
LCA	Life Cycle Assessment
LN	Licence Number
MRF	Material Recovery Facility
MSW	Municipal Solid Waste
N_2	Nitrogen
NaOH	Sodium Hydroxide
NH_3	Ammonia
NO_x	Nitrogen Oxides
O_2	Oxygen
OFW	Ozawa–Flynn–Wall method.
P&ID	Piping and Instrument Diagram
PET	Polyethylene Terephthalate
PV	Photovoltaic
QEWC	Qatar Electricity and Water Company
QF	Qatar Foundation
QGBC	Qatar Green Building Council
QNDS	Qatar National Development Strategy
QNRF	Qatar National Research Fund
RDF	Refuse Derived Fuel
SiO_2	Silica Sand
SNG	Syngas
SO_x	Sulphur Oxides
SRF	Solid Recovered Fuel
ST	Starink method
TA	Tang method
TGA	Thermogravimetric Analysis
TM	Trademark

UK	United Kingdom
XRD	X-ray Diffraction
XRF	X-ray Fluorescence

Units

°C/s	Degree Celsius Per Second
µm	Micrometre
kg	Kilogram
kJ/mol	KiloJoule Per Mole
kV	Kilovolt
kWh	Kilowatt Hour
m^3	Cubic meter
mA	Milliampere
mg	Miligram
MJ	Megajoule
ml/min	Milliliters Per Minute
mm	Millimetre
MW	Molecular Weight
nm	Nanometers
ppm	Parts Per Million
wt%/min	Weight percent Per Minute

Chapter 1: Introduction

1.1 Background

Global climate change poses a very real risk to human civilisation and the planet's natural biosystem. The use of alternative energy resources has been advocated to curtail the escalating problem of greenhouse gas (GHG) emissions. For instance, the European Union (EU) has set targets to reduce CO_2 emissions systematically to 20% by 2020 and 40% by 2030 compared to that of CO_2 emissions level in 1990. United Kingdom (UK) as a major economy has also set its own target of becoming carbon zero by 2050. Low or zero carbon energy has now become an important part of sustainable economic growth. Exploitation of renewable sources of energy that include biomass, wind, and solar is anticipated to contribute towards the realization of the CO_2 reduction targets [3]. Figure 1-1 displays the CO_2 life cycle of bioenergy.

Figure 1-1 Bioenergy CO_2 cycle [4]

Biomass plays an imperative role as a reliable renewable energy source. It helps to generate energy on demand with relatively low to carbon emissions in comparison to the fossil fuels [5]. It has not been agreed yet in the science community whether biomass-based energy is carbon neutral or not. The carbon-neutral feature depends on the type and geographical location of biomass. The carbon emissions from the thermal conversion of biomass are classified as forestry and agriculture emissions. In other words, the carbon emissions released from biomass combustion are already obtained from atmospheric CO_2. Therefore, no additional carbon is added to the atmosphere that

contributes to more global warming. However, carbon emissions from fossil fuel combustion contribute to trapping heat and temperature rise.

CO_2 released from biofuel combustion and gasification process can be consumed by implanting and growing new crops (biomass) which improves the carbon neutrality of biomass. This process can be done based on a long-term cycle of carbon between the atmosphere and biomass. However, global efforts are aiming to reduce greenhouse gases in the near future.

Besides energy conversion, the carbon cycle of biofuel is affected by fossil fuel according to the following processes:

- Transportation of biomass (raw material) and biofuel (final product) may cause emissions of greenhouse gases including CO_2 and nitrogen oxides.
- The use of chemical fertilisers in the crop growth phase may result in nitrogen oxides (NO, N_2O, NO_2) in addition to emissions from manufacturing fertilisers [6].
- The agriculture of biomass crops is occasionally associated with water and soil pollution due to the spillage of chemicals and fuel.
- The use of various machinery in agriculture may lead to harmful emissions.

The above stages of biomass processing impact the biofuel carbon neutrality and carbon cycle. Fossil fuel combustion is the common factor between all the stages. However, when biomass is utilised to produce energy it releases no new CO_2 emissions in to the atmosphere, rather it recycles the CO_2 in the environment to be taken up by plants during the photosynthesis to form the organic matter for reuse again thus leading to a circular economy [7]. In comparison when fossil fuels are burnt they releases carbon in the form of CO_2 that has been trapped below ground for millennia, adding more CO_2 into the atmosphere leading to climate change [5]. The CO_2 concentration in the atmosphere has increased from 310 parts per million (ppm) in 1960 to more than 400 ppm in 2019 due to anthropogenic activities. Thus, biomass gasification is attractive as it releases no new carbon dioxide that would not have been witnessed as a result of any natural decaying of biological materials. Therefore, it is imperative that energy production from biomass is synchronized with biomass growth and natural biochemical cycles to meet the economic development needs of the human beings [4]. A major controversy in this area is the disagreement on the need to cut tress in order to promote energy sustainability. While one part of the divide views forest biomass to be ecofriendly and sustainable, forest advocates claim that the practice is destructive [4].

1.2 Overview of global energy resources

Global energy demand has been on the rise over the years to support economic growth driven by the consumption of oil, natural gas, renewables and coal, among others. According to Statistical Review

of World Energy 2019 of British Petroleum (BP) [3], there was a 2.9% growth in global energy demand in 2018 compared to the year before. The total primary energy supply on a global scale will bring about an increase in the utilisation of all other fuels while a small decline of nuclear energy and coal has been predicted for Europe, leading to an increase in renewables share in all sectors globally. Although, there will be a decrease in nuclear energy in Europe, it is predicted to grow slightly globally. In Europe, the decrease in nuclear energy is due to the policies encouraging the production of renewable energy.

Biomass has been the most important resource known to mankind for thousands of years. However, coal and fossil fuels have taken over that role since the industrial revolution. The use of coal was on the increase at the end of the 19th century. Inexpensive gasoline became widely available after World War II, resulting in the increase in oil usage for power generation and transportation needs. However, fossil fuels reserves are unlikely for the distant future, owing to the increasing energy requirement. The existence of the energy trilemma has diffused the focus from fossil fuels to the relationship between energy security, social impact, and environmental sensitivity. The scope for renewable energy such as biomass in the current era has emerged to have significant potential owing to the fact that it is more sustainable, especially for agricultural countries. Sources of renewable energy include biomass, geothermal, hydro, wind, and solar among others [8]. There has been a consistent increase in the use of locally available energy resources to support economic development. Figure 1-2 below shows the comparison based on prediction of increase in renewable energy sources over the years compared to the decrease in fossil fuels usage and the current share of primary fuels.

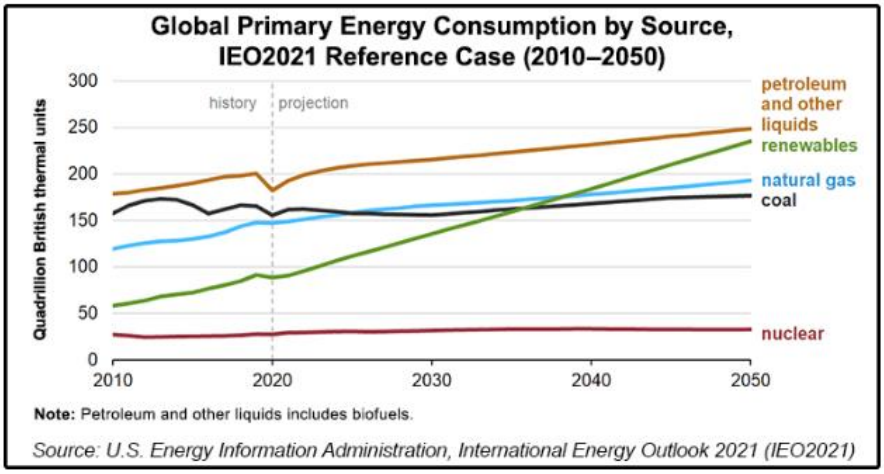

Figure 1-2 A forecasted comparison of global energy consumption for renewables and fossil fuels between 2010 and 2050 [9]

In recent years, the alarming increase in the CO_2 emissions (over 400 ppm in 2019) from the consumption of fossil fuels has significantly shifted attention to low carbon alternative fuels to reduce such emissions. Renewable energy has been preferred to fossil fuels because the energy production by the latter has accelerated the dilemma of GHG emissions (CO_2 being the major contributor to climate change). Population growth increase and the subsequent electricity demand to support economic activities have contributed to the worldwide accelerating the use of fuels [10]. Figure 1-3

shows the International Energy Agency (IEA) CO_2 analysis of future energy and fuel consumption scenarios.

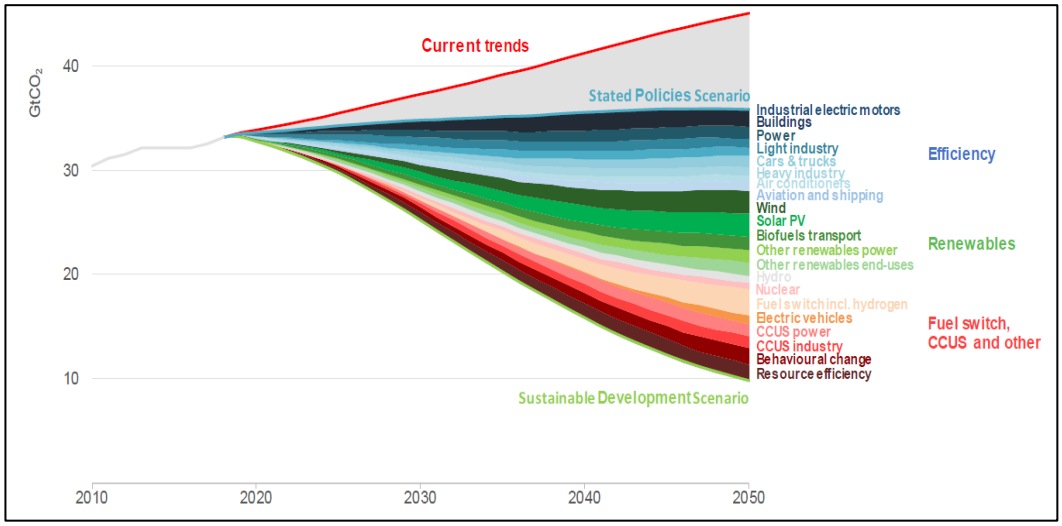

Figure 1-3 The IEA CO_2 analysis of the current and future energy consumption scenarios [11]

CO_2 imposes a significant impact on the global warming as it's more abundant than other greenhouse gases. The industrial, commercial, and domestic sections have been monitored to evaluate carbon emissions. This helps to prepare effective global warming mitigation strategy. The carbon emissions from the renewable energy sources decreases due to placing mitigation measures.

1.3 Qatar energy and national vision 2030

Qatar is one of the leading Gulf Cooperation Council (GCC) countries located in Middle East with total land area 11, 586 km^2, predominantly dependent on its crude oil and natural gas industry [12]. Qatar has a significant role to play in support of the global sustainability development by exporting the cleanest fossil fuels such as natural gas to global markets as the world transitions towards renewable energy [13]. Qatar is ranked 76th on global GHG emissions, and carbon emission is estimated at about 37 tonnes per capita in 2020 [14]. Oil and natural gas fossil fuels are non-renewable with reserves depleting faster than the discovery of new wells. Currently, the focus of the country is to transform its economy from heavily dependent on oil and natural gas exports industry to knowledge based global player. Therefore, Qatar has increasingly focused on the diversification of energy sources by investing in renewable energy and encouraging a culture of research and innovation development. This will result in an increase in the use of renewable energy technologies in future due to the decline in production of fossil fuels owing to depletion of fossil fuel resources [15].

The nation has taken significant endeavors to achieve these objectives that are in alignment with its national vision, geography, culture, political scenario, education, energy, and public health [16]. Thus, keeping in line with those objectives, it is worthwhile to conduct an investigation into Qatar as knowledge based global player in a post-oil era. The nation endeavors to enrich the security of its

citizens and their standards of living through the Qatar National Vision 2030 [17]. Figure 1-4 illustrates a Qatar map with main oil and gas pipeline distribution.

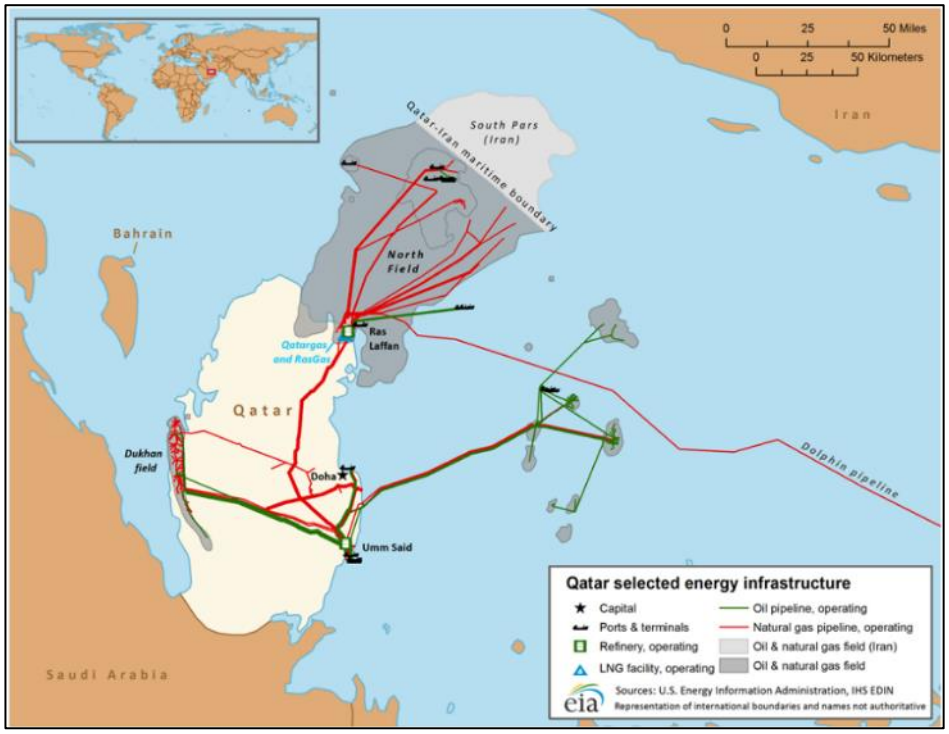

Figure 1-4 Current state of oil and natural gas industry in Qatar [18]

Compared to seven billion people across the world, Qatar comprises of a relatively small population of approximately two and half million people, based on the United Nation estimates for 2021 [12]. Despite this small population, the nation has a considerably large ecological footprint. Waste generation per capita, which is about 2.5 million tons of municipal waste, has resulted from a lack of sustainable waste management. This has been the main contributor to this large ecological footprint. To respond to this dilemma, the nation has made concentrated efforts by exploring waste management plants, waste treatment systems, creation of green spaces and a broad range of energy management incentives. A broad range of studies have been conducted on the waste management practices, with a few key studies indicating municipal solid waste (MSW) generation rate and its composition are two key factors that impact waste management in Qatar, along with the climatic conditions, geographical conditions, Qatar population and the socio-cultural factors [19].

Sustainable development has to be underpinned by transforming the culture and traditions of a nation. Clearly, this demands substantial challenges to be addressed, such as transforming the Qatar nation towards modernisation of culture and traditional value, while at the same time ensuring that the nation preserves the religious sentiments, upholds its core cultural values while at the same time addressing the needs of the future generations of the country [13]. The nation needs to achieve its growth and expansion objectives in context of the national population, such as the demographics, education and quality of labor that needs to be in alignment with the sustainable development plans to safeguard its economic development at a global level [12].

These endeavors of the Qatar nation to transform into a developed country and be a key global player are reflected in national vision 2030 based on the four pillars to achieve the following objectives.

1. Arts, Social Sciences and Humanities Development: One of the key endeavors of nation is to develop the culture, education, population growth, welfare of the people to ensure quality of life, economic development that can sustain a high living standard for the present and future generation [16].

2. Social and Health Development: The nation endeavors to develop a caring and fair society based on a high standard of morals and values that helps the nation to be a significant global player in the international arena. In addition, to focus on health development especially with chronic diseases such as cancer, diabetes and genetic disorders [20].

3. Information and communication technologies (ICT) Development: The nation endeavors towards the development of Qatar ICT plan that involves networking, cybersecurity, smart grids, artificial intelligence and computer science.

4. Energy and Environmental Development: Sustainability is one of the key demands of the contemporary world, the nation endeavors to strike a balance between the national visions of growth, development and sustainability. Therefore, the national vision is planned in coordination with the framework of Qatar National Development Strategy (QNDS) and General Secretariat for Development Planning (GSDP) [16]. However, the success of this framework depends on the efficient coordination between the government, ministries, stakeholders, government agencies and overall support of the nation. The key endeavor is to transform Qatar into a developed advanced nation with the focus on sustainability [8]. The national vision focuses on a sustainable energy future by improving uptake of solar PV technology, employing water desalination and storage, improving urban air quality, cutting emissions from the oil and natural gas industry, using sustainable oil separation and transportation techniques [16]. Currently, the nation endeavors to execute these plans in coordination with the inputs from subsequent institutions, projects and policies that would further support the national vision [13]. Thus, the endeavor is to bring a transformation at a grass root level with the help of education that leads to the building of knowledge based economy through active participation of the Qatari society [16].

These objectives are planned to be achieved with the help of Qatar Foundation (QF) and other organisations to transform Qatar into a knowledge-based economy. Through facilitation of research by Qatar National Research Fund (QNRF) and Qatar Environment and Energy Research Institute, the underpinning of the four pillars of the national vision will be realised [21].

The enriched national values, culture and economic development is heavily reliant on its significant reserves of oil and gas, the nation has realised its resources and capabilities that can help the nation

grow and establish itself further as an international player. Therefore, the nation has decided to execute a plan that will help it diversify its economy beyond its reliance on its oil industry and transition into uptake of renewable energy as a sustainable alternative [16]. This success already becoming evident due to growth and development the country has achieved in the economic, political, and social dimensions with emphasis on the principles of sustainability [15].

Furthermore, hosting FIFA 2022 provides an opportunity to the nation to emerge as global brand and establish itself as a key international player, especially in terms of sustainable development. This is also one of national 2030 vision pillars and an opportunity for the nation to elevate itself as a sustainable nation that have not yet been achieved by many of the developed nations [15].

1.4 Qatar solar energy and gasification

The QatarEnergy and Qatar Foundation (QF) are the largest producer of solar energy in Qatar. QF is equipped with real-time administration of solar energy quality monitoring systems based in a central location that helps the nation with the efficient maintenance and operation of their smart solar system. Also, a new solar test facility situated in the Qatar Science and Technology Park, and a program to develop research institutions and biofuels industries. Moreover, the leadership of QF is completely committed towards a sustainable approach to promote the use of renewable energy [22]. QatarEnergy has set a new sustainability strategy for three core pillars: economic and social development, operational responsibility and mitigation of climate change, which focuses on the establishment of low carbon energy through the growth of the renewable energy capacity where solar projects can generate 2-4 gigawatts (GW) by the end of 2030. As a result, memorandums of understanding (MoU) have been signed between Siraj energy (QatarEnergy 51% and QEWC 49%) with QF to develop PV solar systems that will support national vision 2030 and enhance the distribution of sustainable power to various facilities throughout the country.

Many studies also endeavour to investigate how solar energy can be combined with biomass gasification technology to further bring down costs and the carbon footprint to displace fossil fuel consumption [23]. Traditionally, biomass gasification uses 20-30% of feedstock to produce exothermic heat, necessary for the process of gasification [24]. However, the process can be made far more efficient with the help of solar energy when supplied from a concentrated solar source, as shown in Figure 1-5 [25].

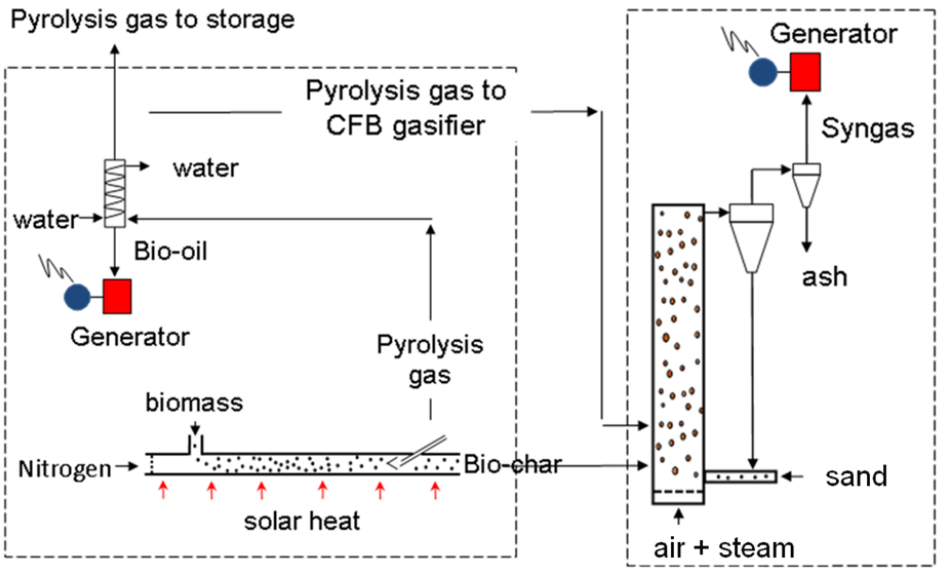

Figure 1-5 Solar thermal Integrated pyrolysis and gasification systems [26]

Research conducted recently at the University of Minnesota Institute indicates that this approach not only reduces cost but will also help to sell the syngas at a profit because of gasification cost savings [27]. The gasification of biomass through utilisation of solar energy ensures that there is elimination of the requirement for equipment that is capital-intensive in the approach of traditional gasification of biomass, and the creation of the combination that contributes in increasing syngas product quantity [28]. For the climate of arid Qatar, there is a significant element of direct solar irradiation and high temperatures that impact solar panels [29]. Along with the solar PV, the nation depicts a significant direct normal irradiance (DNI) and concentrated solar power (CSP) with the approximate value of 2009 kWh per m^2 per year that exceeding the annual supply demand of 1800 kWh per m^2 annually [29].

Biomass sources in Qatar include livestock manure and agricultural residues such as date palm, date stone, rice straw, waste, wheat straw, sugarcane bagasse, and maize stover. Other possible sources include municipal solid wastes, industrial organic wastes, construction and demolition waste wood, and sewage sludge. The recent advancements in waste-to-energy through gasification technology have paved the way for sustainable waste management by converting it into energy and chemicals. Gasification presents a sustainable solution for dealing with MSW that has been a major environmental pollutant in Qatar. Unlike the traditional incineration approach to waste management, gasification imposes insignificant impact on global warming and ozone layer as no new GHG emissions are released to the atmosphere [30]. In addition, the syngas produced from waste gasification can be converted to electrical power or chemicals depending on the end usage needs in Qatar. The clean syngas product can also be used in the petrochemical industry for the production of ammonia and methanol that helps the nation to reduce its dependency on natural gas. [31].

1.5 Waste management practices

Waste refers to a general term that comprises of several unwanted or unusable materials whose source originate from different human activities and development in society. The terminology has a natural heterogeneous state, making it very difficult to segregate it into individual types of waste. Currently, the main practice of the Qatar government towards waste management is landfills and recycling. The waste disposal statistics and locations are reported in Section 8.2. Figure 1-6 illustrates solid and household waste types in Qatar. Considering the increasing Qatar population, and waste generation and carbon footprint per capita, Qatar is planning to diversify its energy mix portfolio and at the same time minimise the environmental impact of waste from its multiple sectors [32]. Currently, due to production and abundance of fossil resources, the nation has depended on fossil fuels to drive its economic growth from an energy sector that releases significant GHGs into the atmosphere.

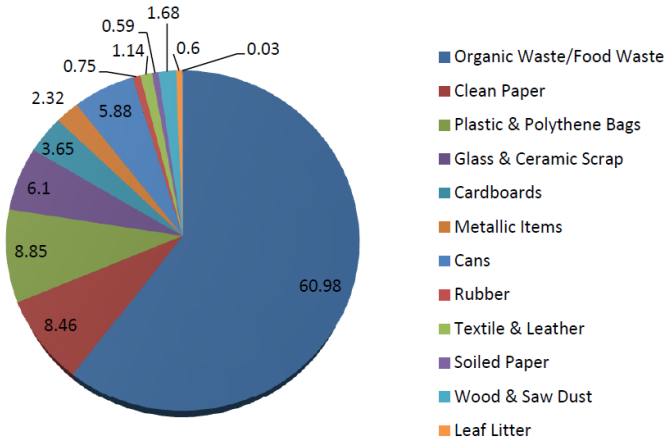

Figure 1-6 Solid and household waste types in Qatar [33,2]

Before proceeding to the benefits of recycling it would be worthwhile to highlight the current approach of Qatar to managing domestic, industrial, and construction waste. In Qatar, the daily waste generation per capita is estimated at 28000 tonnes, of which only 3% is recycled. Only the domestic waste is expected to attain 19,000 tonnes in 2032. [33]. Each individual in the country produces about 1.6 kg/day of solid waste [34]. Table 1-1 below shows the amount of solid waste produced in other countries, measured by the amount each individual produces daily.

Table 1-1 Shows solid waste production produced in different countries [1].

Country	Solid Waste Production per Person (Kg person a day)	Solid Waste Production in Million Metric Tons
United States	1.99	258
United Kingdom	1.34	31.57
Asia	0.56	760
China	0.31	220
Canada	2.13	25.1
India	0.37	168.4

There have been continuous improvement strategies by the government to control and reduce this waste but a more sustainable treatment method is required to achieve Qatar's vision by 2030 [13]. It has been reported that the waste generation per capita figures are significantly high compared to most of the developed and industrialised countries in Europe and Asia. In developing countries these results have been achieved due to the uptake of technologies that help to transform waste into energy. Predominantly, this can be done with a process known as gasification that converts waste materials into valuable fuel gas [27]. The resultant gas mixture is called syngas (synthesis gas) and can be utilised as a renewable fuel for use in various process in Qatar.

Currently, a solid waste incineration plant is utilised in Qatar at the Domestic Solid Waste Management Centre (DSWMC) in Mesaieed as waste-to-energy technology. The process accepts two types of wastes, Grade A organic and Grade B inorganic, that arises from municipal solid waste. [34]. These stations treat approximately 1550 tonnes of waste per day and generate adequate power that can potentially support power for in-house requirements along with a surplus 34.4 MW for the national grid [35]. However, the method of waste landfilling is challenging for a country such as Qatar that has a limited land area.

Industrial waste management is more developed and is progressing positively towards successfully established best practices in Qatar. One of the key reasons for this scenario is robust law and regulations to ensure compliance of the oil and gas sectors in accordance with the national and international market [35]. This makes it mandatory for the nation to ensure compliance with Health, Safety and Environment (HSE) and the Enforcement Directorate (EG) in the process of waste handling, treatment, and disposal [2].

Construction waste consists of 75% of the overall solid waste in Qatar and is mostly destined for landfilling in the specific area [36]. This has resulted in increasing contamination levels in the land, demanding urgent action in the waste management sector. There is a dire need for a collaborative approach between key stakeholders such as research institutions, several governmental departments, and the industry [36]. Currently, there have been attempts to improve construction waste management by developing and implementing codes of practice. One such act is by the Ministry of Municipality and Environment through collaboration with three private companies to recycle construction waste in a significant amount at Rawdat Rashid. This has led to producing primary materials by recycling approximately 41 million tonnes of waste into fillers to lay foundations of roads and buildings, within the timespan of five years to meet the urbanisation requirements in Qatar [37]. This has been one of the significant achievements of the nation to transform waste. However, the upcoming FIFA World Cup 2022 international sporting event is forecast to significantly increase waste generation. This clearly demands a robust waste management strategy to be put in place by 2022 [13].

1.6 Separation of municipal solid waste (MSW)

Qatar is a rapidly progressing economy and one of the key challenges it faces is MSW management. The government faces one of the key challenges of the process of constant change due to the evolving expatriate population that impacts the waste stream composition. Table 1-2 below presents a summary of different categories of MSW.

Table 1-2 Types and compositions of MSW [2].

Waste Source	Type	Composition
MSW	Residential	• Cardboard waste, paper, food, plastic, fabric, cardboard, wood, metal, glass, e-waste, ashes, household hazardous waste, leather, textiles.
	Industrial	• Wood, steel, ashes, bricks, hazardous waste, food waste, housekeeping waste, packaging, concrete.
	Commercial	• Paper, food, packaging, steel, ash, bricks, concrete, hazardous waste, cardboard, plastics, wood, glass, metals, e-waste.
	Construction	• Wood, steel, soil bricks, concrete, tiles, plastics, hazardous waste, glass.
	Municipal services	• Sludge, street sweepings, landscape and tree trimmings.

Qatar needs a comprehensive MSW management strategy that coordinates activities that includes planning and management of waste from industrial, households, construction, and commercial establishments [38]. One such good practice has been the realisation of the Qatar National Development Strategy 2011-2016 with its solid waste management installation at Mesaieed. However, capacity has already been exhausted and there is a need for many such facilities to address sustainable waste management. The separation of MSW can be performed by using a material recovery facility (MRF) to produce solid fuel which can be used in energy sectors. MRF is a central operation whereby recyclable materials are received, sorted, and prepared for selling to buyers or end users with a view to adding value to it by meeting end product specifications and then placing them into an existing market for sale [39]. There are several MRF in Qatar but these facilities need to develop MSW separation processes and produce Refuse derived fuel (RDF)/ Solid recovered fuel (SRF) or Subcoal™ (defined in Section 2.6) which can be used in gasification [40].

RDF refers to a product of mixed solid waste that includes biodegradable material, paper, and non-recyclable plastics that are converted to combustible material to be used as a fuel for energy conversion [41]. The solid waste materials are recovered for recycling before the RDF is prepared. RDF processing typically includes the removal of ferrous material from MSW, shredding, screening, and crushing, although it may also include separation by eddy current or classification of air for the

recovery of aluminium. Approximately 80% of the MSW weight is processed to RDF while at least 85 percent of the BTU remains in the RDF. The heating value for RDF is high and it is approximated to 5,500 Btu/lb, which is almost 50 % of Btu of coal of similar weight [41]. There are a number of advantages for processing MSW to RDF that include lower emissions of the pollutants, high value of heating, reduction of the requirement of excess air for combustion, more homogeneous chemical and physical compositions, and easier handling, storage, and transportation. Moreover, the end product's mass quality and balance is significantly impacted by the number, position, and type of the used equipment [42]. Figure 1-7 below shows a typical line configuration for the production train of RDF. Typically, shredders utilise hammers that run high speeds while shredding and chopping waste. Pelletisers or densifiers are usually added at the end of the process with a view to generate a solid fuel which is easy to store and transport with high energy density [41].

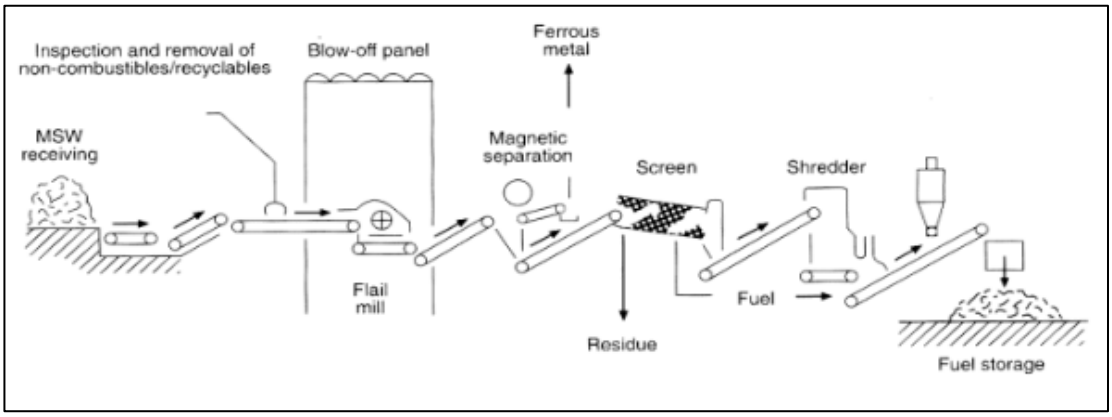

Figure 1-7 Refuse derived fuel (RDF) production process [41]

SRF is typically produced from MSW mainly consisting of wood waste, cardboard, paper, and polyethylene plastic. Although SRF is more refined and more efficient in energy generation process than RDF. In addition, SRF requires a more complex process compared to RDF to make fuel. The MSW used to produce SRF passes through a series of shredders, screens, air classifiers/density separators, and magnets. Inert materials, recyclable plastics, and metals are extracted from the shredded material, leaving a mix of mainly non-recyclable paper, card, wood, textiles, and plastic [30]. SRF's effectiveness in making fuel makes it suitable for the process. In addition, it's higher shredding and segregating grade than RDF makes it a more suitable gasification technology.

The use and marketability of SRF and RDF in gasification is affected by the presence of contaminants and varying fuel quality. A sample analysis to determine a meaningful and reliable fuel characterisation is necessary and this includes the measuring of parameters such as heavy metals, chlorine content, and calorific values that influence the thermochemical conversion conditions. For example, the European Committee for Standardisation (CEN) has developed standards and specifications on SRF classification that have the limit values as the reference point linked to the economic parameter (net calorific value), technical parameter (chlorine content and environmental parameter (mercury content)) [43]. Quality demands for SRF and RDF can be divided into three parameters. Firstly, parameters which describe the economic attributes such as moisture, biomass

content, and calorific value. Secondly, technical attributes which affect the performance of the process such as chlorine content (related to corrosion), ash content (melting and sintering), and bulk density (transport and space). Thirdly, environmental attributes which influence emissions such as presence of sulphur, and heavy metal content (mercury and cadmium) [41].

1.7 Aim and objectives

The present work aims to study the gasification behaviour and kinetics of thermal degradation of non-recyclable paper/plastics mixture waste called Subcoal™ in line with Qatar national vision 2030. It is devoted to achieving a full understanding of the impact of the major conditions and parameters on pyrolysis, gasification and combustion processes.

The objectives of the study are presented as follows:

- To conduct qualitative and quantitative evaluation of Subcoal™ as feedstock for gasification.
- To evaluate the kinetics of pyrolysis, gasification and combustion of Subcoal™ under different operating conditions.
- To assess the gasification behaviour of various types of Subcoal™ pellets.
- To demonstrate the potential benefits of utilising biomass gasification technology to generate renewable electricity in Qatar.
- To investigate the Municipal Solid Waste (MSW) management practices in Qatar by assessing the type and volume of waste resources.
- To carry out a life-cycle assessment of SRF gasification to energy in order to evaluate the main process, environmental impact and support Qatar's national vision 2030.

1.8 Research hypotheses

Based on current waste generation situation in Qatar, it is absolutely essential to manage solid waste appropriately, reduce landfilling, enhance sustainability and at the same time generate electricity. For this reason, it hypothesised that given the complexity and diversity of MSW, a robust technical solution must be implemented in the form of advanced thermochemical conversion by gasification. Due to the sheer magnitude of MSW volumes generated in Qatar, as waste separation and recycling are extremely limited, an appropriate economy of scale processes of megawatt scales must be installed to address waste management in a sustainable manner, reduce landfilling and also to produce renewable energy. The processing of MSW product such as SRF or Subcoal™ also presents challenges as energy containing materials have to be separated first from recyclables and the remaining SRF/Subcoal™ type material to be converted into an ultra-clean syngas which can be utilised for various industrial applications, including power generation. This hypothesis of processing SRF and Subcoal™ for power generation, landfill diversion, and sustainable development will be developed further in this PhD thesis from the perspective of Qatar.

TGA is the most accurate methodology to determine the overall Subcoal™ kinetics data and reaction mechanisms using model-free or model-fitting methods. Therefore, the effect of heating rate on

thermal degradation and kinetic parameters will be investigated in order to identify the best conditions and methods for activation energy (E_a) evaluation. Furthermore, it will be possible to compare the thermal behavior of TGA and FBGR. TGA will be used to investigate the effect of olivine and dolomite loading on Subcoal™ pyrolysis, gasification, combustion to determine which catalyst type and ratio will be best suited for Subcoal™ to justify the process economics and desired syngas quality for end uses.

Air is the most common and least expensive gasification process stream. Using air as a gasifying agent in FBGR will therefore evaluate the oxidation reactions and producer gas.Subcoal™ Pellet and pulverised Subcoal™ pellet gasification at various temperatures in FBGR will assess the effect of temperature on reaction time and gas product, which aids in identifying the best feedstock and isothermal condition for gasification. The tar/char reduction and gas composition will be assessed using Subcoal™ pulverised pellet gasification with varying catalyst loadings, it will also determine which catalyst types are appropriate for suboal gasification in FBGR. This will be influenced by, carbon, water and ash content of the feedstock (which will all be measured by approximate and ultimate analysis).

1.9 Thesis structure

Chapter 1: Introduces Qatar National Vision 2030 and climate change. A discussion on energy resources is provided including the alternative measures to reduce GHG are presented. Research aims, objectives, and hypotheses are also described.

Chapter 2: A brief description of green chemical engineering and biorefinery concepts from literature. An overview of product gas catalytic processing and gasification of biomass. Detailed discussion of the factors that affect the quality of syngas and gasification.

Chapter 3: Describes the materials and methodology of characterisation conducted on the sample and catalysts used in this study.

Chapter 4: Presents chemical kinetic study and TGA. Methods of calculating kinetics of thermal degradation under non-isothermal and isothermal conditions are discussed. Highlights the general overview of gasifier operating conditions and process variables. The method of determining and the factors affecting biomass gasification are presented. Details on the experimental P&ID and a description of the fluidised bed procedures of the Subcoal™ gasification.

Chapter 5: In this chapter, results of Subcoal™ proximate and ultimate analysis include XRD, XRF, LECO, and particle distribution using a Malvern Mastersizer 3000 are presented. Also, the thermal degradation study finding from TGA experiments are discussed and presented.

Chapter 6: In this chapter, TGA kinetics finding are presented and discussed.

Chapter 7: In this chapter, results and discussion of BFBGR experiments are presented. Gasifier performance and product gas composition for hydrodynamic and different operating parameters within various gasification experiments are demonstrated. Moreover, the effect of catalysts on the gasification experiments was also presented and discussed.

Chapter 8: Reviews the current waste situation in Qatar and landfilled environmental impact. Displays SRF waste gasification to energy technology. Demonstrates LCA process and methodology. Demonstrates SRF to energy LCA outcomes from the Qatar perspective.

Chapter 9: Concludes the study and makes recommendations for future work.

Chapter 2: Literature Review

2.1 Introduction

Biomass gasification technology is of great interest in research to produce clean biofuel alternatives to fossil fuels in the past three decades. In this chapter, a literature review of biomass gasification process aspects has been presented and discussed. This includes an overview of biomass processing technologies, biofuel features and production, and Subcoal™ properties as biomass feedstock. Biomass gasification aspects reviewed in this work are the general thermochemical conversion process, the involved chemical reactions, and gasification products. The effect of inorganic matter and catalysts on the gasification process and product quality is also presented. Finally, the design, features, and drawbacks of common types of fluidized bed gasifier reactors are discussed.

2.2 Green chemical engineering and green chemistry

There have been suggestions and recommendations for various principles that can be used to design, develop, and implement chemical processes and products. Green chemical engineering is a science that is applied when measuring the environmental effect of design, development, and operation of different strategies used in chemical engineering. It also assists in the reduction of impact on the environment of the processes and products. Green chemical engineering seeks to attain sustainability by preventing pollution and minimising the use of non-renewable natural resources [44]. The most critical component of a chemical processing industry is a chemical reactor that facilitates key chemical transformations. Chemical reaction engineering (CRE) offers a scientific foundation and approach for quantification of the reactor performance as a function of operational and design variables.

Therefore, CRE is an integral aspect of green chemical engineering. Sustainable development is a continuous course whose descriptions and processes generate constant evolution. Figure 2-1 shows the series of stages required to implement a dependable outline for the attainment of sustainable development [45].

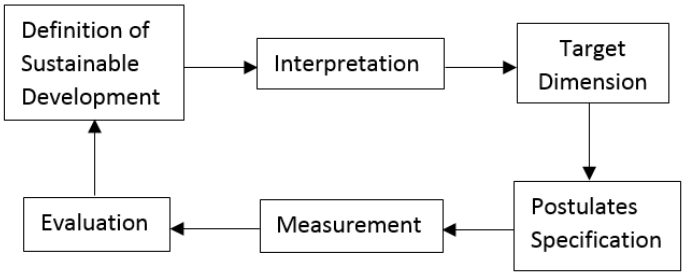

Figure 2-1 Main stages of a sustainability analysis [45]

The principles of green chemistry allow engineers and scientists to safeguard the planet, people, and the economy. It is also beneficial since it identifies innovative and creative ways of reducing waste, conservation of energy, and discovering alternatives for hazardous substances. Green chemistry is part of a more comprehensive drive towards green engineering and the integration of ideologies of sustainability into every tenet of the design process [44]. The philosophies of green engineering seek to utilise renewable feedstocks, avoid or decrease the usage of chemical derivatives, and utilise catalysis as an alternative to reagents [44]. Also, it will aid in the creation of chemicals that degrade after usage, real-time analysis of pollution prevention, and minimisation of possible accidents using safer chemistry. It is projected that by 2025, the capacity of chemical production in Asia alone will increase by between five and six times the capacity recorded in 2000. It should be noted that Asia is the most populous region on the planet. As a consequence of this increase, the consumption of natural resources like fresh water and fossil fuels will rise. A sharper increase in the level of pollution in the environment is also likely to be recorded. Therefore, sustainable development is comprised of complicated interactions between the ecosystem, society, and industry. This implies the chemical engineering community is expected to be more responsible in safeguarding the environment through the development and adaption of production methods and technologies, which are more environmentally friendly [44].

2.3 The biorefinery concept for sustainable conversion

Biorefining has been defined by the International Energy Agency (IEA) as a sustainable process that produces bioproducts such as materials and chemicals, bioenergy in the form of energy, heat, fuel, and food substances. [46].

A biorefinery, which is analogous to refineries that are based on oil is well-established and it uses low-value of biomass waste as the major feedstock before converting them into a range of high value, diverse intermediates that are useful in the industry, well as products that are final in the market [46]. The intermediates and final products can potentially replace their petroleum-derived alternatives [46]. The National Renewable Energy Laboratory described a biorefinery as a facility which combines the equipment and processes for the conversion of biomass for the production of power, biofuels, and chemicals [47]. Clark [46] predicted that sophisticated biorefineries of the future would be capable of generating products of high-volume and low-value that includes fuels comprising of the commodity, biodiesel, and bioethanol, in addition to producing low-volume and high-value chemicals and specialty materials. This will increase the products' value while eliminating or minimising waste streams.

Figure 2-2 shows an example of a biorefinery that has primary and secondary refineries integrated to reduce the amount of waste from biomass input. After the biomass passes through the primary refinery, the primary products are extracted and the rest is considered as waste. The secondary refinery utilises the waste from the initial phase to further produce useful materials and biofuel that

can be used in power generation. The conversion of biomass to energy in a biorefinery is a reliable and appropriate source of renewable energy following the balancing of their growth consistency with consumption. They are regarded as CO_2 neutral fuels owing to their short-term 'carbon cycle' period [47].

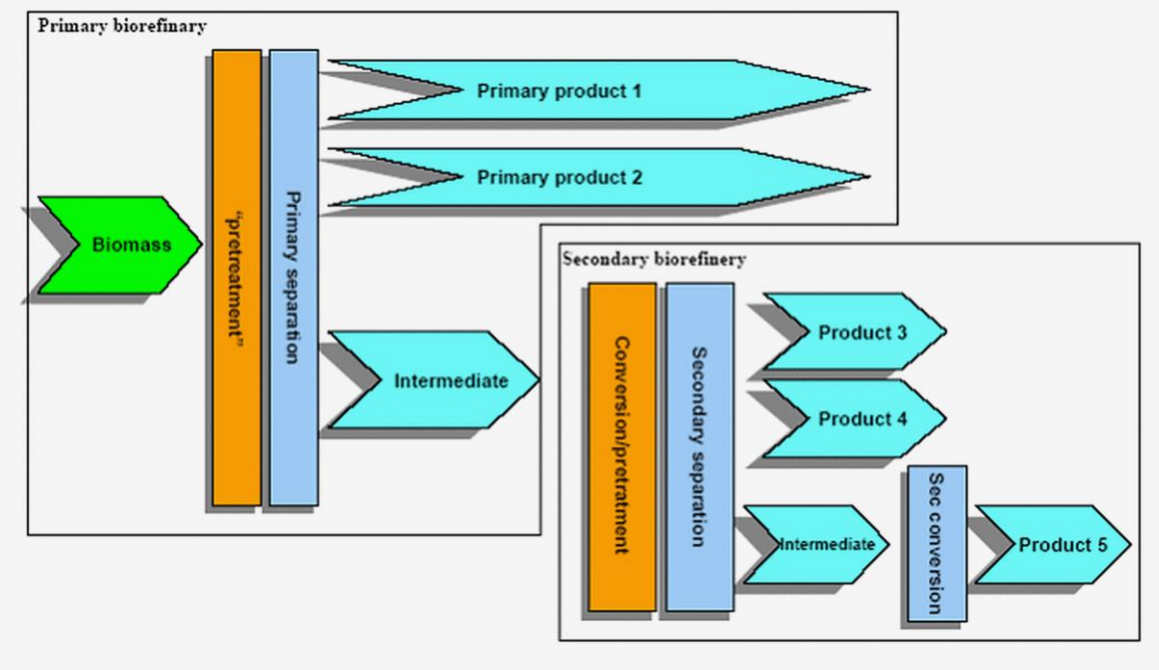

Figure 2-2 Example of the Biorefinery Process [48]

2.4 Biomass energy

The main components of biomass include lignin, cellulose, and hemicelluloses. Biomass is renewable and does not add CO_2 to the environment. Also, biomass can potentially replace conventional fossil fuels and consequently minimise GHG emissions. It is not only cheap but also readily available in a range of forms such as forestry residues, energy crops, organic food waste, animal manure, sewage waste, agricultural residues, and municipal waste [49].

According to Hockenos [50], global annual biomass production by photosynthesis is 220 billion tonnes. It has the potential to provide energy on demand as opposed to solar or wind which always needs storage for continuous utilisation. Biomass is the only alternative to fossil resources to provide both chemicals and biofuels. It is the fifth largest energy source in the United States, after natural gas, petroleum, nuclear energy, and coal [51].

Biofuel is a renewable fuel produced from biomass as a liquid or gas that can be used directly in transportation and power generation. In addition, biofuel helps to create a broad variety of transportation fuels and reduce the demand for traditional petroleum products in addition to limiting the impact of air pollutants from the transportation sector [49].

Figure 2-3 shows that the United States is the largest biofuel producing country, with an output of approximately 38,088,000 metric tonnes in 2019 and the consumption will be increased to

95,000,000 metric tonnes in 2030. However, in the top 10 biofuel producing countries in the world, it is interesting to see that a developing country, Brazil, produced 25,000,000 metric tonnes of biofuel in 2019. Biomass can be used to generate a broad range of biofuels such as cellulosic ethanol, methanol, biobutanes, and diesel [49]. Therefore, biofuel has the potential to provide clean and renewable energy to Qatar.

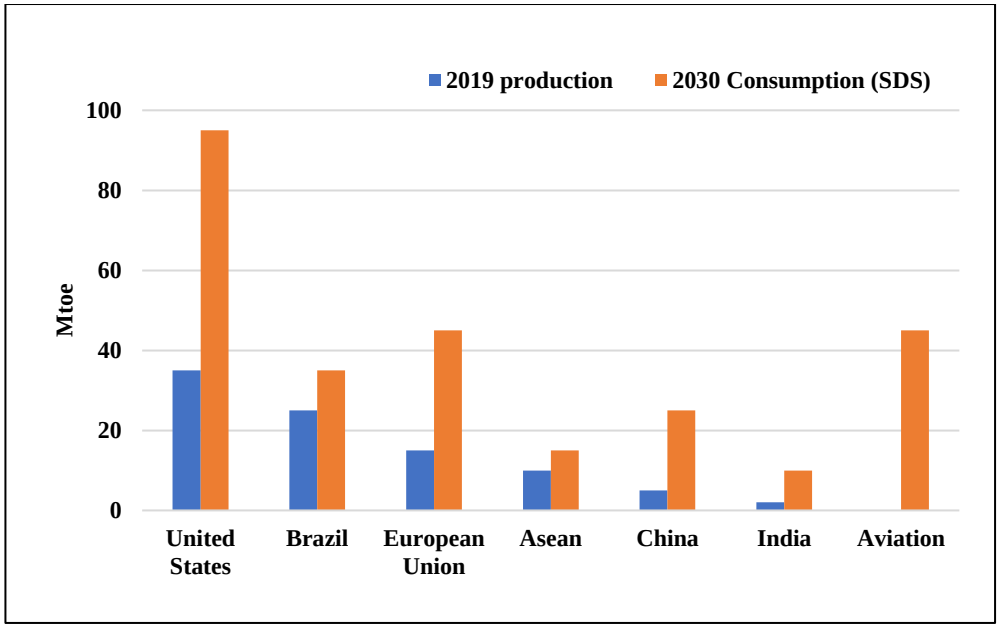

Figure 2-3 Percentage of biofuel production per country and consumption in 2019-2030 [11]

2.5 Biomass conversion technologies

Biomass conversion technologies deal with feedstock that are highly variable in size, energy density and mass, and moisture content, scattered in large areas and with intermittent supply. As such, modern biomass-to-energy conversion technologies are usually a combination of fossil and biomass technologies, which sometimes utilise fossil fuels to dry, preheat, and maintain fuel supply in case of interruption of biomass supply [49]. Thermochemical conversion includes the processes of gasification, carbonisation (torrefaction), pyrolysis, combustion, and catalytic liquefaction. Biochemical conversion includes anaerobic digestion and fermentation. The feedstock molecules are broken down in biochemical processes by bacteria, microorganisms, and enzymes, while in thermochemical processes by temperature and catalysts. These processes help to produce biofuels which can be used as renewable energy carriers [52]. Figure 2-4 shows biomass conversion technologies. The first generation of biofuels includes ethanol and biodiesel produced from edible biomass such as corn, sugarcane, grains, and vegetable oils. However, producing this generation of biofuels leads to competition with food resources (known as the food versus fuel debate). The second generation of biofuels is mostly alcohols derived from lignocellulosic materials such as straw, rice husk, bagasse, and nutshell. This generation was developed to overcome the limitations of the first generation such as food shortages [53]. However, the growth of lignocellulosic crops takes time and needs space. Therefore, the third generation of biofuels is derived from algal biomass which comes

with a distinctive growth yield. The European Union (EU) aims to increase the share of advanced biofuels to 3.5% by 2030. However, an extensive infrastructure is needed to supply biofuels [54].

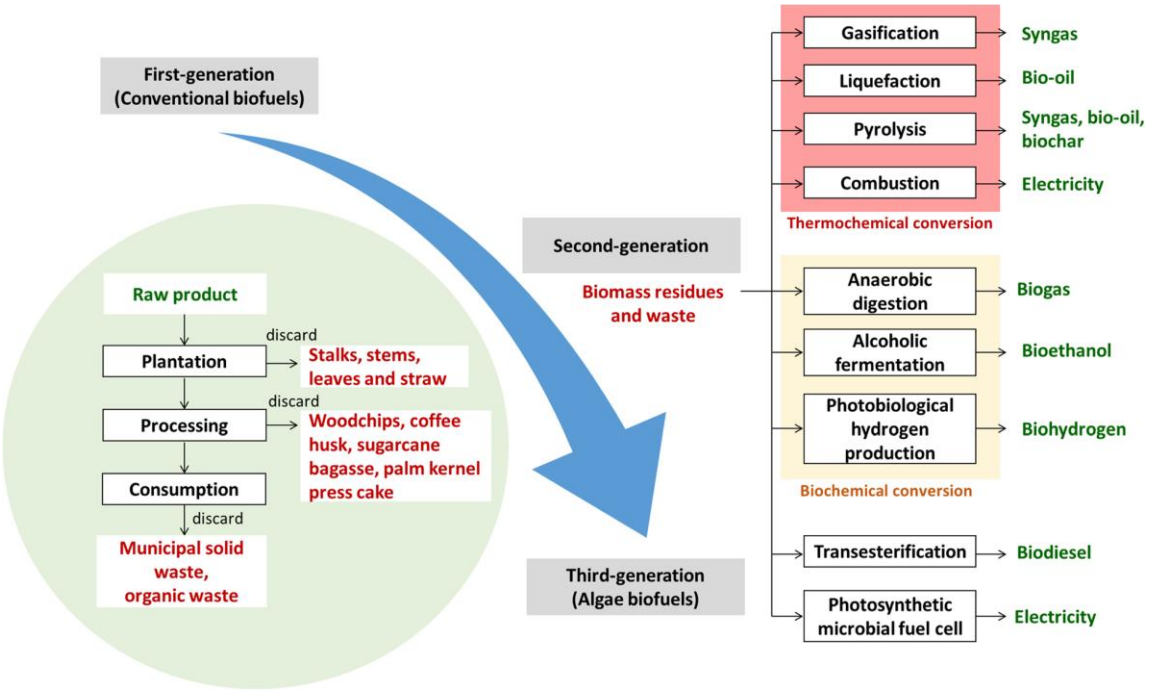

Figure 2-4 Biomass and waste conversion generation pathways to produce bioenergy [52]

The volume of biomass feedstock supplies needed for running a bioenergy plant is dependent on the energy content of the feedstock in the sense that the energy value is inversely proportional to the volume required. Moreover, the growing area that is necessary for the production of biomass that will be supplying a bioenergy plant depends on the feedstock's energy value as well as the power plant capacity, the feedstock yield, and the power plant conversion efficiency [52].

2.6 Subcoal™

Due to the complex nature of MSW and varying material properties, physical properties, and types of contaminants present within the material, it is essential that feedstock is homogenised and prepared to an acceptable quality so that the presence of contaminants, pollutants, ash, and moisture is brought down to a specified level. Various companies around the EU have come up with such solutions, such as standardisation of SRF and RDF in a way that their properties are generally within certain acceptable limits which will not need heavy treatment for flue gases. The production of SRF/RDF from MSW has been described in Section 1.6. However, following the same analogy, N+P Group based in the Netherlands have developed an even more advanced quality feedstock in the form of Subcoal™ pellet (pellet A) and pulverised Subcoal™ pellet (pellet B) as illustrated in Figure 2-5 [55].

(a) (b)

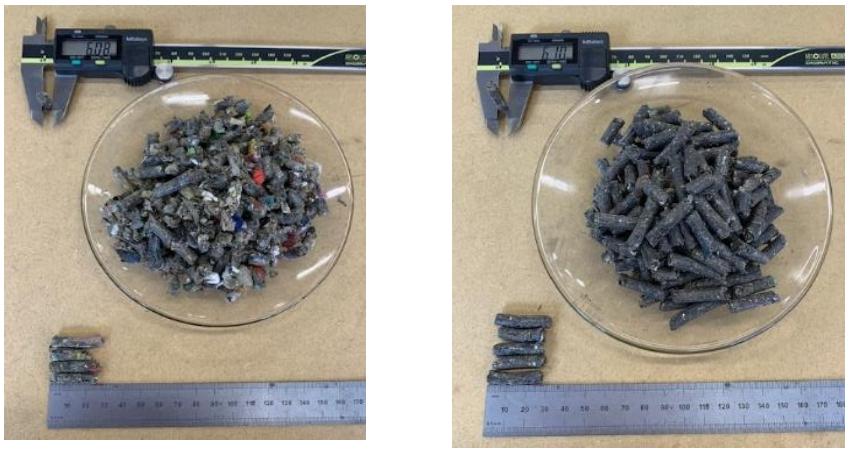

Figure 2-5 Subcoal™ pellet (a) and pulverized pellet (b)

Subcoal™ pellet (pellet A) is the highest quality SRF consist of non-recyclable paper, cardboard, and plastic waste, which are processed into a high quality alternative fuel. However, pulverised Subcoal™ pellet (pellet B) is a highly shredded grade of Subcoal™. The pellet typically has an 8 mm diameter and 27-25 mm length [56]. Subcoal™ is a commercial name that refers to a substitution of coal and was created to bring multiple benefits to power plants as opposed to SRF/RDF, such as the following:

- Fossil fuel substitution: Subcoal™ differs significantly from other waste-derived fuels as it can be used as a direct substitute for coal/coke in industrial processes.

- Co-milling: It can also be co-milled with other biomass or solid fuel such as coal, making the consumption of Subcoal™ a very efficient process for consumers. Milling reduces the size of the biomass particles increasing the surface area to volume ratio; hence it enhances the reactivity and reaction surface of Subcoal™ at lower NOx temperature <(1300°C).

- Hydrophobic: Subcoal™ can be stored outside.

Subcoal™ is now used in cement and lime industries to replace coal, and also used in the steel industry for firing blast furnaces to displace coke and coal, as well as being designed to replace fossil fuels in many other industries where coal is used as the main fuel. In addition, the use of Subcoal™ can reduce end users' ecological footprint due to its 50% biomass content, high energy density, and low moisture content <(5%), which results in flexibility of usage and lower sulphur as well as NOx emissions when compared to SRF or RDF [56].

The possibility of building new MRF facilities in Qatar can potentially lead to preparation of a Subcoal™-like solid fuel for use in gasification systems so that the ecological footprint of Qatar can

be lowered, as well as cost-effective energy being produced with very low CO_2, NOx, SOx, and dioxin emissions. This type of feedstock will also offer huge flexibility for using waste in gasification plants and producing syngas which will be easily usable in either gas engines or gas turbines for energy conversion. Given below in Table 2-1 are some of the distinctive features of Subcoal™ over SRF [56].

Table 2-1 Comparison of SRF and Subcoal™ fuel properties [56].

Parameter	SRF	Subcoal™	Comments
Energy content (MJ/kg)	15-20	>20	Higher energy density allows Subcoal™ to displace fossil fuels in industrial processes such as power generation.
Moisture content (wt.%)	12-20	<5	The lower the moisture content of biomass the easier it combusts. High moisture levels can be very problematic in industries such as cement, and power generation.
Granulate size (mm)	<30	<5	This allows for easier combustion and makes Subcoal™ suitable for co-firing with coal/coke/biomass.
Bulk density (kg/m^3)	150	450	Reduces transport, storage costs significantly and GHG emissions.

In this thesis, Subcoal™ has been selected to be used as feedstock for gasification experiments in line with Qatar national vision 2030 for the following reasons:

- The selection, preparation and use of Subcoal™-like feedstock in Qatar will bring Qatar to the forefront of waste management technology uptake.
- Since some MRF facilities have to be built, it is easy to aim for Subcoal™-like feedstock as design feedstock rather than retrofitting at a later stage.
- The gasification plant utilising this type of feedstock will improve the waste management practices and reduce landfills.
- Lower the ecological footprint of waste management and energy conversion.
- It will potentially have very low CO_2, NOx, SOx, and dioxin emissions compared to SRF and RDF due to the high pellets treatment process. During Subcoal™ drying process, the impurity matters, including ferro and non-ferro materials are removed and then introduced to an optic separator to remove further PVC, which contains high chlorin content.

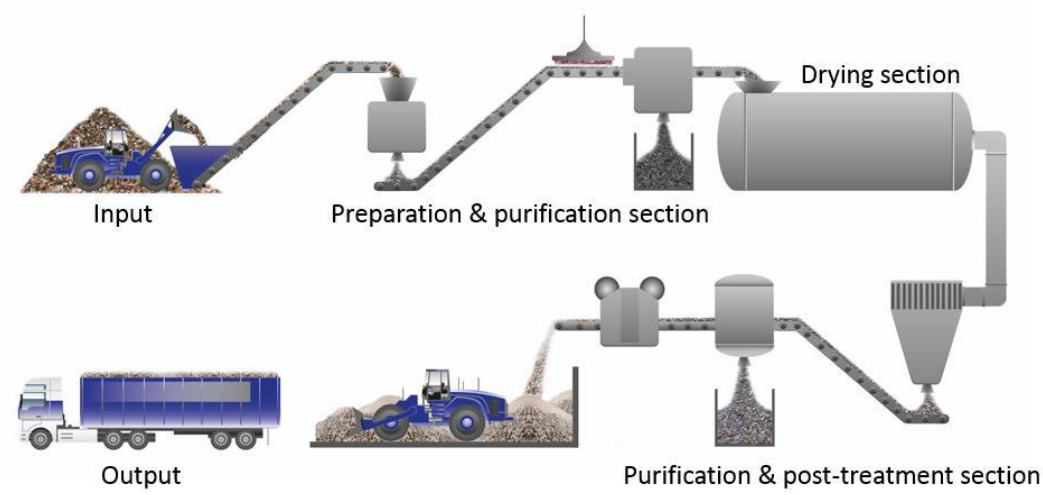

Figure 2-6 Subcoal™ production process [56]

The Subcoal™ production process consists of a number of steps as shown in Figure 2-6. In the first step the raw material is dried then screened, and shredded to a smaller size. The second step is removing impurities such as ferro and non-ferro material. Then raw material is fed to a separator to remove PVC content which contains high chlorine content. The last step is to pelletise the raw material into the required size, and then to store it [56]. It would be crucial to state that the specifications of Subcoal™ from different batches are subject to variation which may affect comparisons and results in the present work. This also applies to the characterisation and analysis of Subcoal™

2.7 Thermochemical conversion

Thermochemical conversion is an effective method to convert biomass into biofuels. Technologies are normally classified based on the principal energy carrier that the conversion process produces. These comprise of various categories: hydrothermal techniques and dry techniques that are nonaqueous. In a dry conversion process, with the temperature increasing, condensable vapours that are degraded, structure destruction for the biomass, and gaseous molecules decomposition [57].

At the medium temperature range (280–370°C) and high pressures (up to 22 MPa), mainly tar (liquid) would be formed in a process termed "torrefaction". Such a process is considered as the main mechanism for the conversion and treatment of biomass to ensure that there is improvement in energy, raw materials grinding, and logistic handling through the removal of moisture and volatilised compounds. The obtained final product is regarded as "torrefied biomass" which contains approximately 60-70% of the total mass while the raw biomass has total energy estimated at 90% [57]. Table 2-2 shows the most common operating conditions for the thermochemical process [58].

Table 2-2 The most common process conditions and reaction products for pyrolysis, gasification, and combustion [58].

	Pyrolysis	Gasification	Combustion
Temperature range (◦C)	250-700	700-1300	>750 - <1500
Pressure (bar)	1	1- 45	1
Atmosphere	Inert, nitrogen	Gasification agent: air, oxygen, steam, CO_2 or mixture thereof	Air
Stoichiometric ratio	0 (no air)	< 1 (partial air)	> 1 (excess air)
Products Gases	H_2, CO, H_2O, N_2 and hydrocarbons	H_2, CO, CO_2, H_2O, N_2, CH_4 and hydrocarbons	CO_2, H_2O, O_2, N_2
Liquids	Pyrolysis oil, water	Tars, water	-
Solids	Ash, char, coke	Ash, char	Ash slag

Thermochemical conversion processes (as shown in Figure 2-7) use heat or thermal energy as the leading mechanism to convert biomass into liquid or gaseous fuel to produce energy.

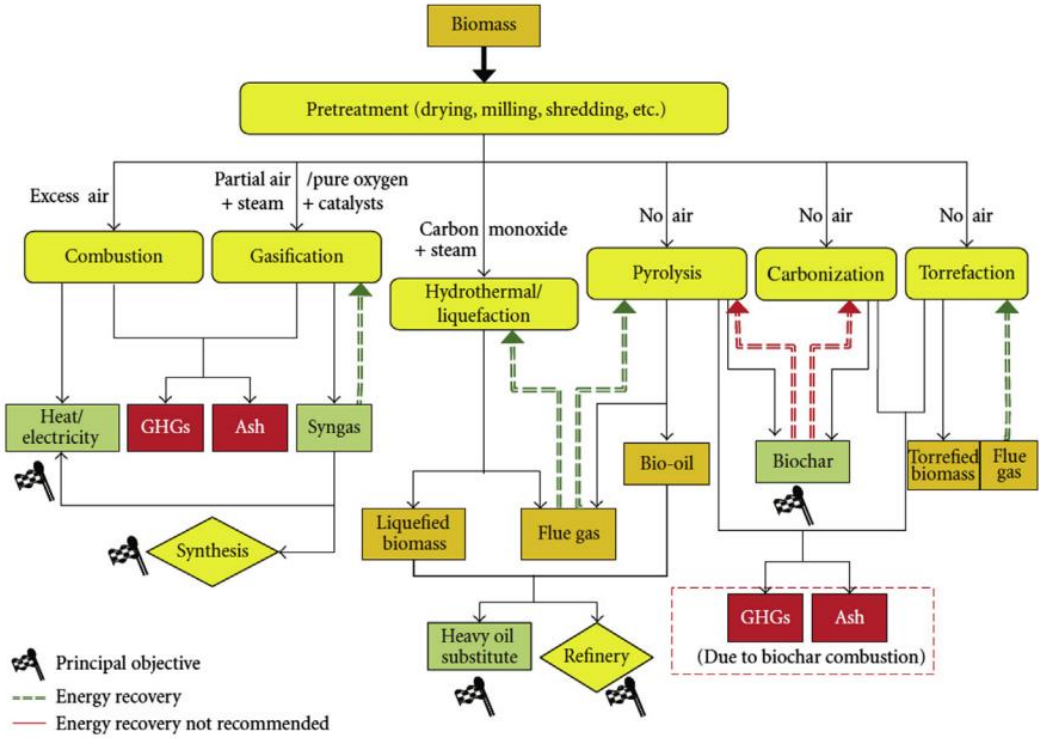

Figure 2-7 Thermochemical conversion pathway [57]

The majority of thermochemical conversions entail second production of the biofuel where lignocellulosic biomass is utilised as the main feedstock. The composition of the lignocellulosic biomass is lignin, hemicellulose, and cellulose. Some of the functions of thermal conversion are the combination of heat, power, and co-firing [59]. By contrast, technologies of thermochemical conversion are considered to be more flexible and efficient.

2.7.1 Pyrolysis

Pyrolysis is defined as the thermal degradation of biomass at a high temperature (200-700ºC) in the absence of oxygen normally at atmospheric pressure [60]. Commonly accepted definitions for slow, flash, and fast pyrolysis are given based on the process parameters of reactor temperature, gas product residence time, temperature, biomass heating rate, reactor pressure, and the rate of thermal quenching of the products. The three primary outputs that are produced are shown in Figure 2-8, all of which have combustible characteristics, include char (solid), pyrolysis oil or tar (liquid), and gas [61].

One of the primary benefits of pyrolysis is the potential recovery of material or biofuel such as methanol from organic matter. According to Halim [62], char is characterised by high carbon content greater than 70%, as well as low content of ash less than 5%. However, pyrolysis oil or tar is a liquid product and has some water content.

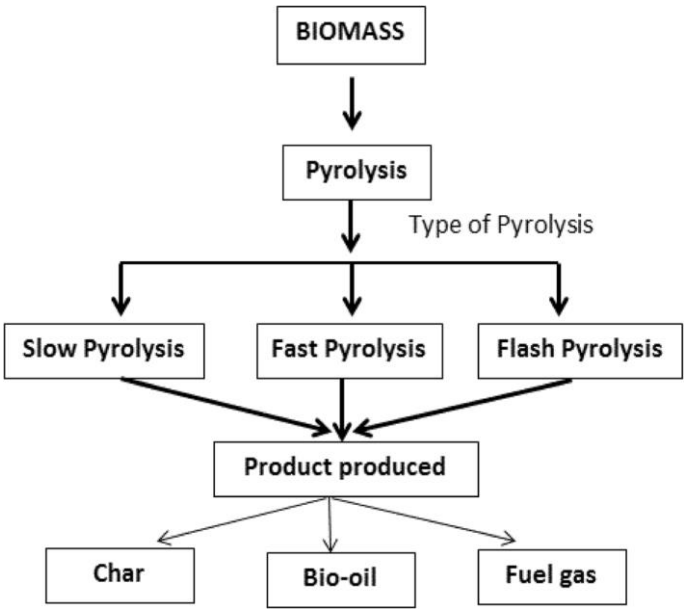

Figure 2-8 An illustration of pyrolysis processes [52]

The relative yields and compositions of pyrolysis products are dependent on the process parameters and biopolymer composition of the feedstock. The main biopolymer components of biomass (cellulose, hemicellulose, and lignin) are decomposed by heat in the absence of oxygen and the volatile compounds are driven off, due to thermal effects from the biomass. At 200 ºC and more, pyrolysis processes slowly begin and the lignin and hemicellulose start to decompose. At about 300 ºC, decomposition of the cellulose begins. The volatile components of the biomass are vapourised below 600 ºC by a complex set of reactions [52]. As a result of the degasification of the biomass during pyrolysis the following gaseous and non-gaseous components are formed:

- A fraction of volatile compounds such as H_2, CO, CH_4, CO_2, N_2, and H_2O
- A carbon rich solid (char)

- Low condensable and high molecular weight compounds (phenols, polyaromatic compounds, polycyclic aromatic hydrocarbons [PAH's]) in trace amounts).

- Liquid products.

Fixed carbon commonly referred to as char, and ash, are the by-products of pyrolysis that are not vapourised. Char conversion involves the gasification and combustion of the carbon remaining after pyrolysis. The proportions of secondary char (soot) and liquid products of degasification decrease with increasing temperature [52]. Table 2-3 shows pyrolysis operating conditions.

Table 2-3 Pyrolysis types and operating conditions [58].

	Mild pyrolysis (or torrefaction)	**Slow pyrolysis (or conventional pyrolysis)**	**Fast pyrolysis**	**Flash pyrolysis**
Temperature range (°C)	200-300	350-800	500-1250	800-1300
Heating rate	Slow (< 10 °C/ min)	Slow (< 10 °C/ min)	Fast (> 100 °C/ min)	Very fast (> 1000 °C/ s)
Residence time	Minutes-hours	Minutes-days (for carbonization)	Seconds (0.5-10 s)	Seconds (< 0.5 s)
Particle size	5-50 mm	5-50 mm	< 1 mm	< 0.2 mm
Primary product	Stabilized friable feedstock	Char	Bio-oil, tar products	Bio-oil, tar products

2.7.1.1 Slow pyrolysis

The volatile products of CO, CO_2, CH_4, and H_2 start to present after 5-30 minutes and during this time the gaseous components react resulting in the formation of char [63]. After the thermal decomposition process is completed, charcoal should be cooled in the absence of air, or combustion will take place. The presence of higher lignin content and diminished levels of hemicellulose content in the biomass has been associated with higher volumes of charcoal production. Thus, slow pyrolysis can be undertaken using large biomass particles unlike fast pyrolysis. Gases, viscous tarry liquid and Char are formed at equal proportions of mass because of the reactions of vapour/gas phase, secondary intra-particle, and biomass that has slow degradation [64].

This process is characterised by a number of disadvantageous factors including long solids and volatile residence times. Also, yields of organic liquid products is typically low, at around 20 wt.% with char yields of typically 20-25 wt.%, 20 wt.% water, and the balance of non-condensable gases comprised mainly of carbon dioxide [63]. A very important phenomenon of this type of pyrolysis is the phase separation of liquid product into an organic phase and aqueous phase. This type of pyrolysis is mainly conducted in an auger-driven system with a heating jacket to provide the heat that supports the process.

2.7.1.2 Fast pyrolysis

For the process of fast pyrolysis, biomass feedstock is exposed to high temperatures (500-1250 ºC), which results in fast mass and heat transfer. The vapour, char, and aerosol (solid particles suspended in a gaseous stream) are formed due to good separation of water soluble and insoluble components. The rapid reaction produces bio-oil upon cooling with a low heating value. The process produces approximately gases of 10-20 wt.% , char of 15-25 wt.%, and 60-75 wt.% of bio-oil [65].

Fast pyrolysis does not produce waste because the char and bio-oil are primary products with fuel potential, while the gas is fed into the process. Fast pyrolysis uses advanced technology such as very small particle size, high heating rates, short vapour residence times (<2s), and higher product yields than slow pyrolysis [66]. The higher heating rates result in higher yield of liquid because there are no secondary reactions that arise from the vapour phase. To achieve the high heating rates, the use of small biomass particles that are less than a millimetre is imperative. The temperature must also be controlled at approximately 500 ºC or higher while the cooling or quenching of vapours should be done rapidly for higher liquid yields [65].

2.7.1.3 Flash pyrolysis

Flash pyrolysis is the use of a rapid fast pyrolysis process where the biomass feed is moved through a hot channel very quickly. The process results in higher heating rates and short residence time compared to fast pyrolysis. Graham et al. [66] reviewed the literature up to 1984 on flash and fast pyrolysis and made a distinction between fast and flash pyrolysis in terms of heating rates, reactor temperatures, and residence time. Flash pyrolysis was characterised by pyrolysis temperatures between 800 and 1300 ºC. Flash pyrolysis was characterised by a number of factors including higher reaction temperatures and heating rate compared to fast pyrolysis, rapid products quenching using thermal approaches, and shorter times for the gas product below 0.5s. Flash pyrolysis results in the generation of higher rates of reaction because of the associated temperatures that are high [65].

2.7.2 Gasification

Gasification is a thermochemical conversion process in which carbonaceous materials dissociate in an oxygen-starved thermal reactor at high temperatures to form producer syngas that mainly consist of CO, CO_2, H_2, CH_4, and N_2 [67]. Gasification is partial oxidation of solid biomass is performed through the use of air, O_2, CO_2, steam, and/or a mixing these depending upon the process requirements. Gasification under air atmosphere produces low calorific value gas (4-7 MJ/Nm^3) that is applicable to run turbine or engine and generate electricity. Gasification under O_2 atmosphere produces a medium calorific value gas (10-18 MJ/Nm^3) suitable for syngas conversion to methanol, and gasoline. A similar medium calorific value gas can also be obtained from steam or O_2 gasification, which is better suited to the synthesis of transport fuels and chemicals because of the absence of N_2 [68].

Air gasification is a common technology that is used since it involves O_2 at low cost and usage and production in multiple reactors. Therefore, the gasification process takes place at a temperature ranging between 500 and 1300 ºC or higher and the resulting syngas can be used for energy purposes such as manufacturing of chemicals and fuels as well as in power generation [69]. Gasification of biomass conversion is a complex set of physical and chemical processes [70]. Figure 2-9 below shows the stages of a gasification process.

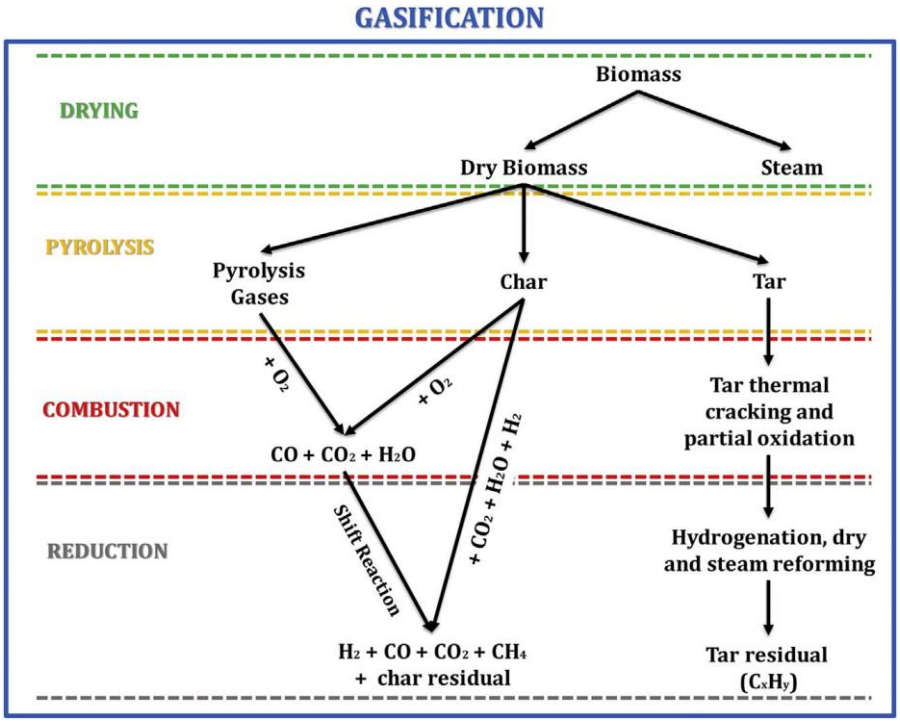

Figure 2-9 The reaction stages for gasification process [69]

There are a number of gasification by-products and these include light hydrocarbons, N_2 and S compounds such as (NO_X, H_2S, NH_3, SO_X, HCl, HCN), inorganic ash and particulates, char and tar (condensable organic compounds). The gasification process has a number of advantages including feedstock flexibility, product flexibility, and high efficiency [69]. The energy density of the syngas is approximately 5.6 MJ/m^3 or below, which is lower when compared to that of the natural gas that is estimated at 38 MJ/m^3 [49].

2.8 Chemical reaction

Biomass gasification in the presence of steam, CO_2, air as a gasifying agent takes place according to different mechanisms and reaction kinetics. A mixture of condensable and non-condensable gaseous products are produced from gasification processes such as H_2, N_2, CO, CO_2, CH_4, C_2H_4, and C_2H_6 [71]. Besides the gaseous products, there are condensable liquid and solid products such as tar and char that contain a high content of carbon. Biomass gasification includes a sophisticated set of chemical reactions that vary based on the gasifying agent [72]. The overall general reaction of biomass gasification is displayed in Equation R2.1 [73].

$$C_nH_mO_k + j\ O_{2\,(g)} + sH_2O \rightarrow \left(\frac{m}{2} + s\right) H_{2\,(g)} + (k + s + 2j)\ CO_{(g)} + (n - k - s - 2j)\ C_{(s)} \quad \text{(R2.1)}$$

Where, $C_nH_mO_k$ is a general formula of a biomass molecule. The first stage of the process is drying in which the volatile impurities and moisture release as a vapour from the biomass at a temperature of 100 – 200 ºC. Char produced from the pyrolysis step undergoes gasification reactions and combustion with a gasifying agent. Then, a series of reactions (R2.2 to R2.6) take place in a homogenous gas phase gas-char in the presence of a gasifying agent [72]. The gas phase reactions involve volatile oxidation, cracking, and steam reforming. The steam produced in the drying stage is employed as a reducing agent in reduction reactions, such as steam reforming and water-gas shifting (WGS) reaction [70].

Oxidation of CO_2

$$CO + 0.5O_2 \rightarrow CO_2 \qquad \Delta H^{\circ} = -283\ kJ/mol \quad \text{(R2.2)}$$

Oxidation of H_2

$$H_2 + 0.5O_2 \rightarrow H_2O \qquad \Delta H^{\circ} = -242\ kJ/mol \quad \text{(R2.3)}$$

Oxidation of CH_4

$$CH_4 + 2O_2 \rightarrow CO_2 + 2H_2O \qquad \Delta H^{\circ} = -802\ kJ/mol \quad \text{(R2.4)}$$

Methanation

$$CO + 3H_2 \leftrightarrow CH_4 + H_2O \qquad \Delta H^{\circ} = -206\ kJ/mol \quad \text{(R2.5)}$$

Dry reforming of CH_4

$$CH_4 + CO_2 \leftrightarrow 2CO + 2H_2 \qquad \Delta H^{\circ} = +247\ kJ/mol \quad \text{(R2.6)}$$

Char burns in the presence of oxygen partially and completely to produce CO and CO_2 in heterogeneous reactions R2.7 and R2.8, respectively. The gasification of char involves reactions with three gasifying agents, namely; CO_2, H_2O, and H_2 in the heterogeneous reactions R2.9, R2.10, R2.11 and R2.12, respectively. Each of R2.7, R2.8, and R2.12 are exothermic reactions which provide the

required energy for gasification endothermic reactions R2.9 and R2.10 [74]. Char reactions produce additional amounts of gaseous products such as syngas. Therefore, char is a necessary by-product of gasification [67]. Using air as an oxidising agent with an air-to-fuel ratio of 0.3 to 0.5 leads to an oxidation layer forming near to the supply point of air due to then high operating temperature.

Partial combustion

$$C + 0.5O_2 \rightarrow CO \qquad \Delta H^{\circ} = -111\ kJ/mol \tag{R2.7}$$

Complete combustion

$$C + O_2 \rightarrow CO_2 \qquad \Delta H^{\circ} = -394\ kJ/mol \tag{R2.8}$$

Boudouard reaction

$$C + CO_2 \leftrightarrow 2CO \qquad \Delta H^{\circ} = +172\ kJ/mol \tag{R2.9}$$

Water gas reaction

$$C + H_2O \leftrightarrow CO + H_2 \quad \Delta H^{\circ} = +131\ kJ/mol \tag{R2.10}$$

Water gas shift reaction

$$CO + H_2O \leftrightarrow CO_2 + H_2 \quad \Delta H^{\circ} = -41\ kJ/mol \tag{R2.11}$$

Hydrogasification reaction

$$C + 2H_2 \leftrightarrow CH_4 \qquad \Delta H^{\circ} = -75\ kJ/mol \tag{R2.12}$$

Hydro-cracking

$$C_6H_6 + 9H_2 \rightarrow 6CH_4 \qquad \Delta H^{\circ} = -529.9\ kJ/mol \tag{R2.13}$$

The reactions of char gasification (R2.7-R2.13) might not occur in one gasifier. A reaction may take place based on the gasifying agent used. For instance, when the biomass gasification uses air as a gasifying agent, both reactions R2.7 and R2.8 are the key reactions that control the gasification performance. In CO_2 gasification, R2.9 is the dominant reaction in the process. If the gasification process is aided by steam (H_2O), then reaction R2.10 is the primary reaction. Moreover, the sequence of reactions may differ from the actual case [75].

Another biomass gasification by-product is tar. Tar is a viscous liquid composing of a mixture of condensable hydrocarbons such as aromatic compounds [76]. The endothermic reactions in R2.14 to R2.17 describe the decomposition conversions of tar. R2.14 represent tar partial oxidation. Reactions R2.15 and R2.16 are dry reforming and thermal cracking reactions of tar, while R2.17 shows the hydrogenation reaction of tar to methane [77]. The formation of tar is undesired for gasification processes. Two main methods have been proposed to remove tar from biomass gasification: catalytic, and thermal cracking [78]. However, the thermal cracking is possible but unfavourable due to high operating temperature and undesired products. As a result, catalytic cracking is adopted instead.

$$\mathrm{C}_n H_m + \left(\frac{\mathrm{n}}{2}\right)\mathrm{O}_2 \rightarrow \mathrm{n}CO + \left(\frac{\mathrm{m}}{2}\right)\mathrm{H}_2 \qquad \Delta H^{\circ} \text{ between } -715 \text{ and } -2538 \text{ kJ/mol} \qquad \text{(R2.14)}$$

$$\mathrm{C}_n H_m + n\mathrm{CO}_2 \rightarrow (2\mathrm{n})CO + \left(\frac{\mathrm{m}}{2}\right)\mathrm{H}_2 \qquad \Delta H^{\circ} \text{ between } +980 \text{ and } +3112 \text{ kJ/mol} \qquad \text{(R2.15)}$$

$$\mathrm{C}_n H_m \rightarrow \left(n - \frac{\mathrm{m}}{4}\right)C + \left(\frac{\mathrm{m}}{4}\right)\mathrm{CH}_4 \qquad \Delta H^{\circ} \text{ between } -161 \text{ and } -505 \text{ kJ/mol} \qquad \text{(R2.16)}$$

$$\mathrm{C}_n H_m + \left(2n - \frac{\mathrm{m}}{2}\right)\mathrm{H}_2 \rightarrow \mathrm{n}C\mathrm{H}_4 \qquad \Delta H^{\circ} \text{ between } -498 \text{ and } -1815 \text{ kJ/mol} \qquad \text{(R2.17)}$$

The presence of a catalyst such as dolomite or olivine enhances tar removal and increases the gas yield. Olivine is a rock-forming mineral, that is naturally available with a general chemical formula of magnesium iron silicate $(Mg_x, Fe_{1-x})_2\ SiO_4$. The presence of iron oxide (Fe_2O_3), magnesite (MgO), and nickel (Ni) in olivine promotes tar cracking reactions [79]. While Dolomite is a widespread inexpensive mineral and a common tar conversion catalyst that is composed of calcium magnesium carbonate CaMg $(CO_3)_2$ [80]. The production of syngas (CO, and H_2) increases as the contact time of the catalyst with fuel increases, as stated by Vassilatos et al. [81]. Chen et al. [82] investigated the effects of dolomite and olivine on the gasification efficiency. The results showed that the combustible gas increased and tar conversion enhanced with catalyst addition. Dolomite presence increased tar removal efficiency from 48.1 to 70.5%.

The reactions R2.5, R2.7, and R2.9 to R2.17 are to some extent desired as it produces combustible gases (syngas). The reactions R2.2-R2.8 are highly exothermic, so it may be able to provide the necessary energy for endothermic gasification reactions [67]. In this case, the reactor is known as an autothermal gasifier. If the energy released from exothermic reactions is insufficient, then external heating is required and the gasifier is known as allothermal.

The reactions that produce non-combustible products are undesired for economic and environmental considerations. The combustible gases (CO, H_2, CH_4) are generally formed from the reduction of CO_2 to CO (according to boudouard reaction), water to H_2 (water-gas shift reaction) and carbon to

methane (water-gas shift reaction) [70,83]. The higher the yield of combustible gas the greater the efficiency of the process.

The side reactions in the gasification occur due to the presence of some impurities such as sulphur. Sulphur in biomass reacts with hydrogen in a series of reactions to form hydrogen sulphide (H_2S), then carbonyl sulphide (COS), and occasionally carbon disulphide (CS_2), as shown in R2.18-R2.20 [38-39].

$$S + H_2 \rightarrow H_2S \quad \text{(R2.18)}$$

$$CO + H_2S \rightarrow COS + H_2 \quad \text{(R2.19)}$$

$$COS + H_2S \rightarrow CS_2 + H_2O \quad \text{(R2.20)}$$

The rate of reaction and the conversion degree of the reactions mentioned above are restricted by achieving thermodynamic equilibrium. Thermodynamic equilibrium theoretically can only be achieved with infinite time of reaction. The reaction kinetics therefore become crucial through influencing the yield and composition of gaseous products [84]. In practice, gasification processes are unable to achieve the thermodynamic equilibrium as a result of short residence time. The conversion rate of solid biomass to gaseous products is limited to mass transfer, heat transfer, and reaction kinetics [85].

The mechanism of gasification char reactions consists of five consecutive steps, as listed below [83]:

- Diffusion of gaseous reactants (CO, CO_2, H_2, H_2O, and O_2) to the surface of solid fuel particle.
- Pore diffusion of gaseous reactants into the particle pores.
- Heterogeneous reaction between the solid reactants (carbon) and gaseous reactants.
- Pore diffusion of gaseous products from fuel pores to the particle surface.
- Diffusion of gaseous products from particle surface to the bulk gas.

The driving force of gas diffusion in all steps is concentration difference. The rate of reaction is dependent of driving force. Other important parameters which influence the diffusion and reaction rates are temperature and the presence of a catalyst. Temperature increases the diffusivity and kinetic energy of gas molecules. Temperature also enhances the reaction constant according to Arrhenius relationship [86]. Therefore, at lower temperatures both mass transfer and reaction are slow. The gasification process under low temperature is surface reaction and diffusion controlled. The presence

of a catalyst is responsible for reducing the temperature of reaction and energy barrier for the reaction to occur. However, the mass transfer of gas is still limited to temperature [87]. When temperature raises, the chemical reaction takes place at the particle surface before gas diffusion to the particle pores. In this case, the gasification rate is mass transfer controlled.

2.9 Presence of inorganics in biomass gasification

Inorganics are typically the ash components of the biomass input during gasification. Also, other inorganics can be present as contaminants, which the biomass may have picked up during harvesting, transportation, and storage. Inorganic components of biomass, both natural materials and contaminants, have a significant influence on the selection of gas cleaning technologies, end uses of the gas, and control of noxious substances. Inorganics in biomass gasification can lead to the formation of volatile by-products, ash sintering and fusion, which results in processing difficulties [59].

Work by Mitsui Babcock [88] recently summarised the effects of inorganics in the production of reactive char and the release of inorganic components at the gas phase. Inorganics in the biomass samples, which were used to produce chars under carefully controlled conditions, were found not to influence the char yield, although they affected the char reactivity [89]. Further research is needed to understand the implications of inorganic components on the gasification process.

The level of inorganics in the feedstock will influence the choice of gas clean up technology and the gasifier configuration. The key compounds that occur naturally in biomass and which are known to be problematic include chlorine, sulphur, and alkali salts such as potassium oxide and sodium oxide. There is a much wider range of possible contaminants in waste materials such as MSW and industrial waste. Implicatively, it is imperative that the feedstock is analysed for contaminants before use of feedstock in gasification, and suitable ways of dealing with such elements determined, especially when it comes to heavy metals and volatile components [89].

Alkali metal salts can vaporise due to the high gasification temperatures in the system. One area of concern is in the formation of eutectics during the combustion phase where lower melting point eutectics can melt and form slag upon cooling down in the system. Chlorine readily vaporises to produce an acid gas (HCl) and can cause downstream corrosion problems in the steel piping and vessels; therefore it needs to be removed from the gas. Different methods for the removal of inorganic elements exist such as the installation of ceramic filters for physical separation, or chemical scrubbers which have been further studied by Kurkela [90]. If the feedstock is contaminated, this will influence the choice of gas cleaning system. This is summarised below in Table 2-4. Further work is required on handling of other problematic inorganics.

Table 2-4 Inorganics in biomass gasification and possible solutions [91-92].

Inorganic Component	Solution
Chlorine	Provision needs to be made for capture of dolomites and calcium oxide in the gas phase or by scrubbing of the gases through the addition of alkali solutions (e.g. NaOH) to the scrubbing medium.
Alkali metals [Na, K]	Cool the gases from the gasifier to less than 600 ºC, preferably 450-550 ºC. Alkali loss in the gases reduced to less than 1 wt.% of the original material in the biomass. Hot ceramic filters are preferable.
Sulphur	Sulphur in biomass turns into a sulphur gas (like H_2S) first, and then the gas is absorbed onto dolomite or calcium oxides as bed materials.
Mercury	Can be adsorbed onto activated carbon prior to use.
Cadmium	May be recovered in the final product and the char from the gasifier.

Different inorganic elements in biomass feedstock have been associated with the deactivation of catalysts in gasification through the introduction of impurities and absorption. Some of the common sources of impurities include chlorine, iron, phosphorous, sodium, silicon, and aluminium, which deter the adsorption of the catalyst, resulting in the formation of unwanted compounds. In addition, the presence of inorganic elements changes the configuration of the catalyst and therefore, lowers the rate of diffusion and prevents the reaction of reagents in the biomass [93].

2.10 Catalyst

Biomass gasification takes place widely in gasifier reactors which bed materials are a mixture of sand and catalyst particles. However, the production of tar during gasification may lead to serious problems in the system such as condensation and clogging, therefore a tar removal procedure is needed [68].

A catalyst is any substance that does not participate in direct reaction and increases the rate of reaction. The presence of a catalyst lowers the activation energy of a chemical reaction thus reaction can proceed with greater speed at much lower temperatures compared to without catalyst application. The catalyst can either be chemical in nature or natural, involving biodegradable materials. One of the significant properties of a catalyst is that it neither wears out nor changes because it only speeds up the rate of a reaction. In cases of municipal solid waste, the amount of material involved is so massive that it would take a very long time for the waste to be gasified [94]. Thus, a catalyst is necessary to speed up the reaction for the production of syngas. Another role of the catalyst in the gasification of biomass is to help lower the cost of cleaning the syngas by resulting in tar cracking and conversion in the gasifier reactor. The metal alloys needed to clean the gas are expensive and require high temperatures. However, when catalysts are used the gas will be cleaned as it is being produced in the reactor itself. Tar, a by-product of the gasification process, is broken down further at around 600-800 ºC with the help of catalysts to produce more syngas [71]. The following process shows how the reaction with or without a catalyst takes place.

Reactant ↔transition state (with or without catalyst) ↔ product

Figure 2-10 represents the effect of a catalyst on the rate of chemical reaction.

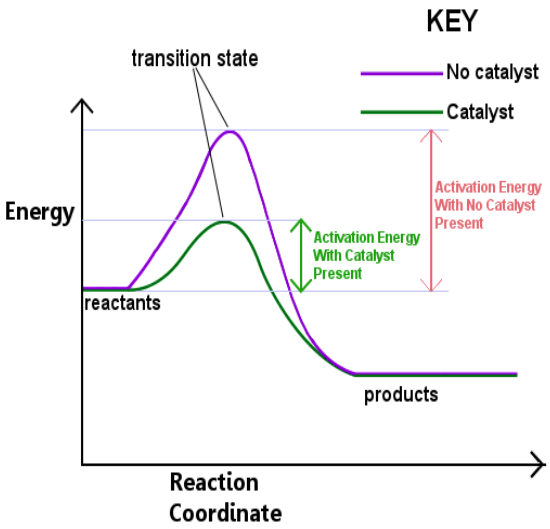

Figure 2-10 Graph showing translation states in the presence and absence of a catalyst [95]

Based on Figure 2-10, it is evident that with a catalyst, activation energy is lowered for the chemical reaction, whereas, without a catalyst, higher activation energy is needed to drive the same chemical reaction. The implication of this effect is that if there are products whose activation energy is lower than that of a reaction without a catalyst, then the chemical reaction cannot take place. In such a reaction, a catalyst is necessary [96]. The process is called catalytic cracking and it includes thermal and hydrocracking. In the gasification of biomass, the main reason why a catalyst is used is to reduce the amount of tar formed in the process, as it lowers the energy content due to the combination of carbon and hydrogen elements [58].

Catalytic cracking can be categorised into two categories. The first category is primary cracking, which can take place in a pyrolysis reactor. A catalyst is either mixed with the biomass or used as bed material. In primary cracking, the hydrocarbons are adsorbed in their dissociative form as well after hydrogen has been removed catalytically [97]. Water or moisture, on the other hand, is broken down and absorbed in the form of OH ions, which are oxidised with the hydrocarbon elements to form CO and H_2. The second category is secondary cracking in which the reaction takes place in a separate reactor [98].

Below are some of the factors that should be considered when determining the right processes and catalysts.

i. The catalyst should eliminate the tar formed and increase the yield of products effectively.
ii. The catalysts should be economical and sustainable.

iii. It should not be easily deactivated.

iv. It should be renewed easily.

Several catalysts that are suitable for biomass conversion can further be subdivided into either synthetic or natural. Natural mineral catalysts found in the earth include dolomite and olivine. They are common used for two main reasons; they are abundantly available in nature, and secondly they are cheap [99]. However, natural catalysts have their drawbacks. For instance, when using olivine, some by-products are formed because of its calcification in the gasifier. Therefore, an alternative to it is dolomite. dolomite is very stable and remains the original state after a reaction. [58]. Hence, it is fair to say that dolomite is more effective for tar conversion than olivine. Furthermore, dolomite is widely available in Qatar at Khor Aludad, so it was chosen for Subcoal™ gasification. [79].

Synthetic-based catalysts are mainly metal-based and alkali-based. Metal-based catalysts include catalysts such as nickel and iron among others. Alkali-based catalysts include potassium, sodium, and lithium among others [100]. Synthetic catalysts are rarely used because they are expensive and not easily available in remote industrial applications. Besides, alkali catalysts have agglomeration problems whereas metal catalysts are easily deactivated due to carbon being deposited on them [99]. The catalysts, in terms of reaction mixture homogeneity, are divided into homogeneous and heterogeneous catalysts. Heterogeneous catalysis is the most common in the industry, which refers to catalyst and reaction species in distinct phases such as a catalysing gas-phase reaction by solid catalyst [101]. The mechanism of catalysis is important for better understanding of catalyst performance in the gasification process

2.10.1 Olivine Mechanism

The catalytic activity of olivine ($(Mg_x, Fe_{1-x})_2\ SiO_4$) for tar reduction can be related to iron oxide (Fe_2O_3), magnesite (MgO), and nickel (Ni) contents. The effectiveness of the iron is evidenced when it becomes present on the catalyst surface. Olivine calcination and oxidation has the impact of ascertaining that iron is brought to the surface. Coke formation has the impact of deactivating olivine, reducing the catalyst surface area, and covering of the sites that are active [79]. The catalytic influence of olivine on biomass gasification was examined in several studies [102]. Some researchers revealed that olivine increases the yield of syngas and tar conversion, and reduces the production of CH_4 and CO_2 [103,79]. These effects were owed to the catalytic activity of olivine towards tar conversion (R2.14-R2.17) and water-gas shift reactions at R2.11. It has been stated that the performance of olivine is dependent on the different oxidation states of the segregated iron at the catalyst particle surface [104].

The activity and performance of olivine can be enhanced by calcination at temperatures between 400 and 1100 °C as expressed by the following reaction [105]:

$$(Mg_xFe_{1-x})_2SiO_4 + \frac{1-x}{2}\ O_2\ \rightarrow xMg_2SiO_4 + (1-x)Fe_2O_3 + (1-x)SiO_2 \qquad \text{(R2.21)}$$

The reaction equation (R2.21) shows that the iron in olivine is removed as Fe_2O_3 during the calcination with oxygen. The Fe_2O_3 is then reduced in two consecutive steps; from Fe_2O_3 into Fe_3O_4, and from Fe_3O_4 to FeO and α−Fe. As can be seen, the oxidation state of iron decreases with each conversion which possesses an increasing impact on tar cracking [106]. The iron has a low oxidation state (α−Fe) therefore is an active phase for C-C and C-H bonds cracking in tar hydrocarbons [107]. The reducing atmosphere promotes the catalytic activity, while the oxidation atmosphere retards the activity [108].

In comparison with the next preferred catalyst, dolomite, olivine produces 4–6 times less fine particles in the product gas, but also 1.4 times less efficiency in tar removal than dolomite in the gasification [102]. The contaminated particles in product gas need to be removed which adds more operating and capital costs. This, therefore, makes olivine the best choice for catalysing the gasification process.

The mechanism of olivine catalysis of biomass gasification may differ with the gasifying agent. The gasification in air atmosphere causes oxidation of olivine in the combustion zone producing binary iron oxide hematite (Fe_2O_3), SiO_2, and iron-depleted olivine. The formed Fe_2O_3 is subsequently reduced by the organic compounds in biomass to FeO, CO, and H_2. In the gasification with diluted air using synthesis olivine $(Mg_{0.5}Fe_{0.5})_2\ SiO_4$, about 10% of iron content in olivine is oxidised at 300 seconds according to thermogravimetric analysis [109]. Moreover, olivine is capable of accommodating excess oxygen from air oxygen as shown in reaction (R2.21):

$$(Mg,Fe)_2\ SiO_4 + \frac{\delta}{2}\ O_2\ \rightarrow\ (Mg,Fe)_2\ SiO_{4+\delta} \qquad \text{(R2.22)}$$

The gained oxygen in olivine is used to partially oxidise methane in the gasification zone when the partial pressure of oxygen is low:

$$(Mg,Fe)_2\ SiO_{4+\delta} +\ \delta\ CH_4\ \rightarrow\ (Mg,Fe)_2\ SiO_4 +\ \delta(CO + 2H_2) \qquad \text{(R2.23)}$$

During air biomass gasification, olivine undergoes a cycle of oxidation and reduction to produce the active iron and then to regenerate the catalyst. The oxidation of iron in olivine takes place during the calcination at a temperature of 400 – 1400 ºC in two steps. The purpose of olivine oxidation is to produce the Fe_2O_3 that promotes the tar removal reactions, as shown in reaction (R2.24). The hematite and magnesioferrite that formed in the oxidation react together according to reduction reaction (R2.25) at 950 ºC in two successive steps. The reduction reaction restores the olivine but

with less iron and magnesium oxide deposition [104]. As a consequence of iron content reduction as well as the formation of oxide deposits, the catalyst needs to be replaced periodically [109].

$$(Mg,Fe)_2SiO_4 \xrightarrow{400-1100\ ^\circ C} \underset{\text{forsterite}}{Mg_2SiO_4} + \underset{\text{amorphous silica}}{SiO_2} + \underset{\text{hematite}}{\alpha\text{-}Fe_2O_3} + \underset{\text{magnesioferrite}}{MgFe_2O_4} \xrightarrow{1100-1400\ ^\circ C} Mg_2SiO_4 + \underset{\text{enstatite}}{MgSiO_3} + \underset{\substack{\text{hematite}\\(\text{traces})}}{\alpha\text{-}Fe_2O_3} + \underset{\text{magnesioferrite}}{MgFe_2O_4} \quad \text{(R2.24)}$$

$$\underset{\text{hematite}}{\alpha\text{-}Fe_2O_3} + \underset{\text{magnesioferrite}}{MgFe_2O_4} \xrightarrow{\text{reduction } 950\ ^\circ C} Fe^0 + Fe^{2+} + MgO \xrightarrow{Mg_2SiO_4} Fe^0 + (Mg,Fe)_2SiO_4 + MgO \quad \text{(R2.25)}$$

Latifi [110] suggested a chemical loop by which the iron oxide (hematite) is reduced to metallic iron (Fe^o) that acts as an active site on the olivine particle surface. The reduction of iron oxide (III) is carried out by hydrogen according to reaction (R2.28) that combines R2.26 and R2.27. The metallic iron could be recovered in calcination to Fe_2O_3.

$$Fe_2O_3 + H_2 \rightarrow 2\,FeO + H_2O \quad \text{(R2.26)}$$

$$FeO + H_2 \rightarrow Fe^o + H_2O \quad \text{(R2.27)}$$

$$Fe_2O_3 + 2H_2 \rightarrow FeO + Fe^o + 2H_2O \quad \text{(R2.28)}$$

Aranda et al. [111] also proposed metallic iron generation in the indirect gasification of biomass. As the iron is partially oxidised in the combustion zone, olivine with Fe_2O_3 is circulated to the gasification zone [112]. Moreover, oxygen, which is obtained from the combustion zone, is employed for partial oxidisation of gaseous products in the gasifier [113-114]. In the gasification zone, under reduction atmosphere, iron oxides are converted to metallic catalytic iron (R2.29-R2.31).

$$3Fe_2O_3 \rightarrow 2Fe_3O_4 + \frac{1}{2}O_2 \quad \text{(R2.29)}$$

$$Fe_3O_4 \rightarrow 3FeO + \frac{1}{2}O_2 \quad \text{(R2.30)}$$

$$FeO \rightarrow Fe^{o} + \frac{1}{2}O_2 \qquad \text{(R2.31)}$$

The metallic iron distributes and segregates from olivine into the bed particles. During the reduction reactions, the essential quantity of iron (II) of (18–21%) rapidly redistributes inside the olivine lattice. The reduced iron formed from R2.29 and R2.30 transfers later to the combustion zone to be recovered to Fe_2O_3 [111].

2.10.2 Dolomite Mechanism

Dolomite is a widespread inexpensive mineral that forms in rocks over a huge underground area which can exist in different colours. It is a common tar conversion catalyst that is composed of calcium magnesium carbonate $CaMg(CO_3)_2$ [80]. The composition of dolomite may vary depending on the geographical location [115]. However, the major compounds found in dolomite are calcium oxide (CaO), magnesium oxide (MgO), and CO_2 [116]. Dolomite may also contain minor species such as silica (SiO_2), aluminium oxide (Al_2O_3), and Fe_2O_3 with different percentages [117].

The content of CaO and MgO in dolomite determines the catalytic activity; the higher the content of calcium and magnesium oxides, the better the efficiency of the catalyst [118]. The tar cracking efficiency increases as the ratio of Ca/Mg increases. It enhances the tar cracking through promoting the water-gas reaction (R2.10) [119]. The tar elimination in the presence of dolomite can attain 100% as demonstrated by Simell et al. [80].

The calcination of raw dolomite enhances the efficiency of the catalyst in tar conversion. Zhang [120] pointed out that about 73% and 88% of tar conversion was achieved using raw and calcinated dolomites, respectively, in the air gasification of rice husk. Also, calcinated dolomite, in air gasification of mixed plastic wastes, promotes the tar conversion to 73%, compared with silica sand, as reported by Cho et al. [121]. Dolomite calcination includes the formation of MgO and CaO by thermal cracking [116]. The following chemical reactions describe the calcination of dolomite over two ranges of temperatures [122]:

$$MgCa(CO_3)_2 \leftrightarrow Ca(CO_3)MgO + CO_2 \qquad (T > 600℃) \qquad \text{(R2.32)}$$

$$Ca(CO_3)MgO \leftrightarrow CaO.MgO + CO_2 \qquad (T > 900℃) \qquad \text{(R2.33)}$$

As can be seen in the reactions, the equilibria of calcination are sensitive to CO_2 gas release [123]. The partial pressure of CO_2 is preferred to stay under the equilibrium pressure to avoid the catalyst deactivation [123]. Besides the process pressure, temperature plays a crucial role in controlling the calcination and carbonation reactions, as shown in Figure 2-11 [124]. Several factors influence the calcination process such as heating rate, the quantity of catalyst, and particle size [125]. The purpose

of dolomite calcination is to increase the size of the catalyst pores which is then responsible for mass transfer enhancement. The time and temperature of calcination increases the surface area of the catalyst, hence the efficiency increases [126].

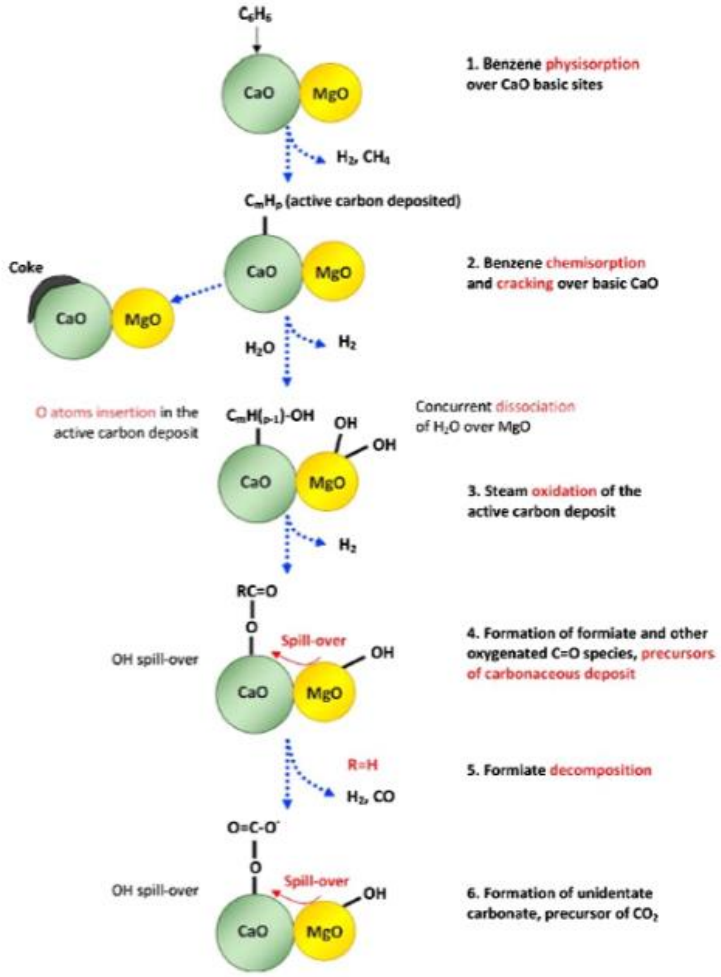

Figure 2-11 Mechanism of dolomite catalysis according to various studies [127]

The catalysis mechanism of dolomite in benzene tar elimination is presented in Figure 2-11 based on the work done by Hervy et al. [128] and other studies in the literature. Gas products and an active carbon deposit (C_mH_p) are formed when a benzene ring incorporates on the active sites of CaO. The active carbon deposit undergoes a reaction with steam, or ends with coke formation on CaO. MgO breaks the hydrogen bonding in water, forming OH which is absorbed on the active sites of MgO. The OH group then combines with the remaining active carbon to form formate. A spill-over of OH takes place leading to decomposition of formiate to syngas and removal of coke [129-130]. Herman et al. [131] reported that the metal oxides in the bottom ash such as SiO_2, Fe_2O_3, CaO, MgO, and Al_2O_3 have a catalytic influence on gasification of the biomass. The presence of Al, Ca, Mg, Si, Ti and Fe confirms the ability of bottom ash to be utilised as the gasification process catalyst. CaO decreases the CO_2 content increasing the product gas yield while Fe_2O_3 reduces the tar formation.

2.11 Fluidised bed gasifiers

In many cases sand is used as a bed material in bubble fluidised bed gasifiers where a gasifying agent of air or steam is introduced to the gasifier to make the sand particles more randomly fluidised. The feedstock is introduced from the upper part and then mixed with hot sand, which produces syngas and small amounts of char [132]. The remaining char is reduced into a smaller particle size by the mechanical attrition with sand due to a dynamic atmosphere in the fluidised zone before being separated using cyclones. In an indirectly heated gasifier, the fluidised content is moved to a secondary gasifier where the char is burnt as the temperature of the sand rises. The sand is transferred back to the primary gasifier to fluidise new feedstock. The fluidised bed gasifier has temperatures of 700 to 1000 ºC and residence times depend on biomass particle size. The main difference between a bubbling fluidised bed gasifier and a circulating fluidised bed gasifier is the recirculation of solids into the circulating bed gasifier after separation in the cyclone. The system is also identified as a circulating bed (as shown in Figure 2-12) when the materials move from one chamber to another [133].

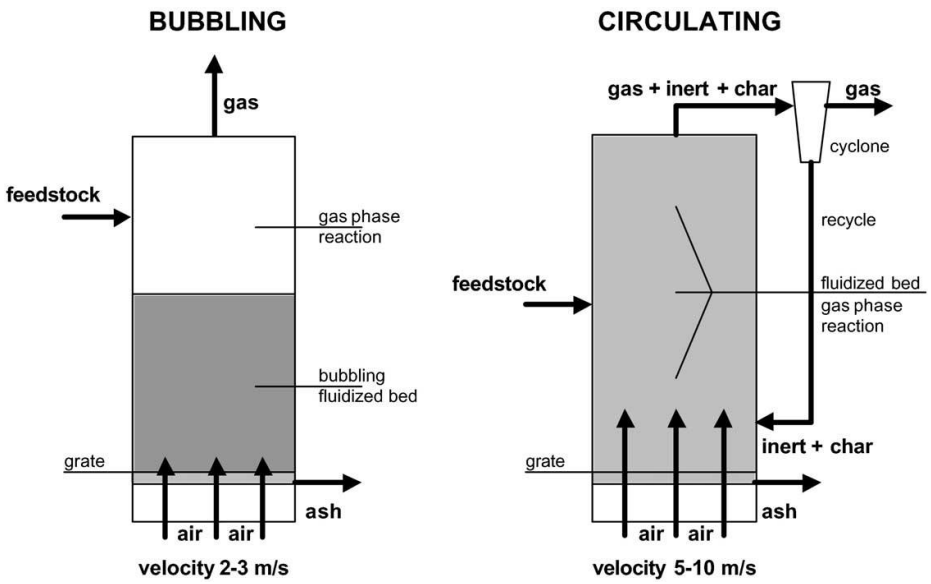

Figure 2-12 Fluidised bed gasifiers [132]

The fluidised bed gasifier is suitable for industrial use (> 1 MW_{Th} scale) because it has shorter residence times. The major advantages of fluidised bed gasifiers are their ability to deal with non-uniform particle sizes and shapes, and their fuel flexibility brought about by good mixing of feedstock and oxidant, and this ensures efficient mass and heat transfer [70].

2.12 Factors affecting the gasification process

The first factor that affects gasification is the feedstock composition [134]. In most cases, the feedstock entails something that can be vigorously combustible. For instance, dry biomass would be much better than high-moisture biomass, which will result in consumption of energy in evaporating the moisture from the wood. Reaction temperature also affects the gasification process. Higher temperatures are sufficient to form the required conditions that are good for syngas formation due to

tar conversion [135]. However, when the temperatures go too high it leads to the combustion of biomass and formation of flue gas. Thus, the resultant gas is lower in calorific value.

The heating rate of feedstock should be somewhat constant to ensure that the biomass is heated uniformly to avoid some sections not being heated uniformly and more so to ensure that the heat does not dissipate with time [136]. Residence time will determine the time it takes for biomass to stay in the reactor before complete conversion has been achieved. The higher the residence time, the better the quality of the gases being produced and the lower temperature the required for complete conversion. A poor quality syngas is characterised by low HHV and residence time. Different studies have reported several factors that affect biomass residence time that is present in the fluidised beds. An increase in gasifying agent velocity and bed height leads to a wider residence time distribution of solid particles. Big biomass particles have longer mean residence time and lower descending vertical velocity [137].

Gasifying agent (Air, O_2, steam, CO_2) is another factor that affects the gasification process. The quality of the syngas being produced depends on the type and quantity of the gasifying agent. The best gasifying agent is air since it is cheap and available in the atmosphere. On the other hand, oxygen is very expensive and thus will increase the cost of production of the gas [138].

Another factor that affects the gasification process is the reactor design. It is critical that the reactor design should be according to a conceptual approach that reduces the capital cost and facilitate the maintenance [139].

2.13 Summary

Biomass is a sustainable source of energy in which feedstock is converted into a useful and clean fuel to meet increasing energy demand with the lowest environmental emissions. Biomass conversion technologies are classified into thermochemical conversion and biochemical conversion. Thermochemical conversion, which is more efficient in large-scale production, includes pyrolysis, gasification and combustion. Pyrolysis and combustion can be occurred in the reactor during biomass gasification. Therefore, these processes have to be simultaneously studied under different conditions and catalyst ratios.

Some reported studies have focused on biomass obtained from wood, sewage waste, poultry litter, and agricultural products. However, non-recyclable MSW product such as paper and plastics has been received little attention in the literature. The mixture of plastics and papers waste fractions is converted into a solid fuel pellet known as Subcoal™. The combustion of Subcoal™ alongside fossil fuel in cement and power plants have been investigated. However, the gasification and kinetics of Subcoal™ thermochemical conversion to fuel gases is not well understood. Developing such knowledge will contribute to the better design of reactors for Subcoal™ gasification which helps to reduce the energy cost and the ecological footprint. In addition, this technology will reduce the

landfilling of MSW and support Qatar national vision 2030. In this work, the kinetics of pyrolysis, gasification and combustion of Subcoal™ will be examined using the TGA. Also, air-gasification of pellet and pulverised Subcoal™ will be investigated under different operating conditions using FBGR. The literature points to the existing gap as studies of gasification of Subcoal™ are limited. Knowledge on this field, is thus inadequate. To close this gap, comprehensive studies in this field must be conducted. From this requirement and need, this study will conduct experiments to understand the gasification of Subcoal™.

Chapter 3: Methodology

3.1 Introduction

In the present chapter, the methodology of Subcoal™ characterisation and preparation for TGA and FBGR experiments is described. The determination of sample composition and properties was a crucial step in the evaluation of gasification reaction. The proximate analysis was carried out first to determine the content of volatiles, ash, moisture, and fixed carbon which is essential to determine the fuel/air ratio in the gasification process. Then, an ultimate analysis was performed to determine the percentage of C, H, N, S and O (by difference) in sample. The findings of the proximate and ultimate analysis were also used to predict the mass balance and producer gas composition. Sand bed material and Subcoal™ bulk density were estimated for gasifier design. Moreover, calorific value and carbon/sulphur content were determined. Also, pellets reduction size and catalyst preparation were demonstrated. The methods of pyrolysis, CO_2 gasification, and combustion using TGA are highlighted. The XRF analysis method was highlighted to identify the rest of the trace elements in sample. Then, the XRD technique was used to determine the crystallinity proportion in Subcoal™ powder, sand and ash. Finally, the particle size distribution of silica sand and sample powder was evaluated using a Malvern Mastersizer 3000. The dominated particle size is an important factor for the design of FBGR.

3.2 Proximate analysis

Proximate analysis is a typical and simple technique that has been used for more than a century to determine the content of volatile matter, moisture, ash, and fixed carbon contents in biomass. Such an analysis is very crucial in biomass fuel degradation processes to figure out the process characteristics. The amount of ash formed, process conditions, and the generated gaseous products can be determined with reference to proximate analysis. The measurements of moisture, ash, volatiles, and fixed contents of sample indicate the amount of energy stored in the fuel [140]. The proximate analysis of the sample in this work followed relevant British Standards (BS).

3.2.1 Moisture content

Moisture content is the quantity of water in biomass that can be found in two forms, namely: free water in solid fuel and as a chemically bonded water molecule to the fuel structure. The presence of moisture in biomass leads to a reduction in temperature during the first stage of the gasification process [132]. The reduction in temperature may affect the rate of endothermic reaction between steam and char, in addition to the devolatilisation process. The moisture content, therefore, should be minimised to 5-10 wt.% of the original feedstock. The moisture content was determined using a furnace (BINDER, Germany), according to BS ISO 18134-3:2015 standards [141].

Evaporation of the moisture from sample was carried out in the furnace at 105 ºC for two hours. The analysis was performed minimum three times to ensure the result's repeatability and quantify potential uncertainty. Three empty crucibles dishes that have lids are inserted in the oven and at a temperature of 105 ºC. After that, the three clean and dry crucibles dishes with lids were weighed. Then, one gram of the sample powder was evenly placed in each dish. Both the fuel and dish were weighed before the heating process. The three dishes with sample were consequently placed in the furnace free of cover. The lids were also put inside the furnace, but not on the dishes. After two hours of heating, the lids were placed on dishes, removed from the furnace, and placed in a desiccator to cool to room temperature before being weighed again. The lids were used to prevent the biomass from absorbing moisture from the surrounding environment. The mass of an empty crucible dish and lid m_1, the total mass of the biomass, crucible dish and lid prior heating m_2, and the total residue mass, crucible dish and lid once heating is completed m_3 were used to calculate the moisture content according to the following equation [142]:

$$\mathrm{M_{ad}} = \left(\frac{\mathrm{m_2 - m_3}}{\mathrm{m_2 - m_1}}\right) \times 100 \tag{3.1}$$

3.2.2 Volatile matter content

The volatile matter in biomass includes C, H, N and O. The content of volatile matter was measured based on BS EN ISO 15148:2009 standards [143]. The overall test methodology consists of three individual tests to run simultaneously. First, three empty and clean crucibles of the fused silica along with lids are put in the furnace and subjected to a temperature of 900 ºC for 7 minutes to eliminate contaminants that may affect the test. The crucibles were then taken out of the furnace and given time to cool such that they could reach ambient temperature before being introduced into a desiccator. At this stage, the weight of the empty crucible and lid m_1 were evaluated. Then, one gram of sample was distributed in each crucible with a lid on it, and the weight was evaluated again m_2. To make sure the heating was equally distributed, the crucibles were placed on racks. The main test started when the three filled crucibles were put into the furnace at a temperature of 900 ºC for 7 minutes. After heating, the filled crucibles with lids were removed and cooled down and finally weighed to obtain m_3. Based on the knowledge of the weights of the samples, the volatile matter content was estimated for each sample using the formula below [143]:

$$\mathrm{V_d} = \left[\frac{100(\mathrm{m_2 - m_3})}{\mathrm{m_2 - m_1}}\right] \tag{3.2}$$

3.2.3 Ash content

Ash is a substance residue from the combustion process which comprises of inorganic material. The higher the ash content in the biomass, the lower the calorific value of a fuel. Ash content is

represented as a percentage of the dry mass of the fuel [142]. The formation of ash post combustion results in several operational and design issues such as slagging, corrosion fouling, and particulate fouling. The surface deposition of an ash layer may reduce heat transfer efficiency. Moreover, during the combustion of char, ash affects the diffusion of oxygen to the fuel surface. These issues retard the process performance and treatment of syngas [144].

The content of ash was measured according to BS EN ISO 18122:2015 [145]. The test was performed a minimum three times to confirm the repeatability of the results. Three empty crucible dishes were placed in a furnace at 550 ± 10 ºC for 60 minutes to remove the volatile contaminations. The crucibles then were removed from the furnace and cooled down for 5-10 minutes before being transferred to a desiccator for further cooling to attain ambient temperature. The crucible dish that is empty has its weight taken. Subsequently, 0.1 mg of the sample was placed in each dish, and the total weight was recorded. The dishes loaded with sample were placed in the furnace as shown in Figure 3-1.

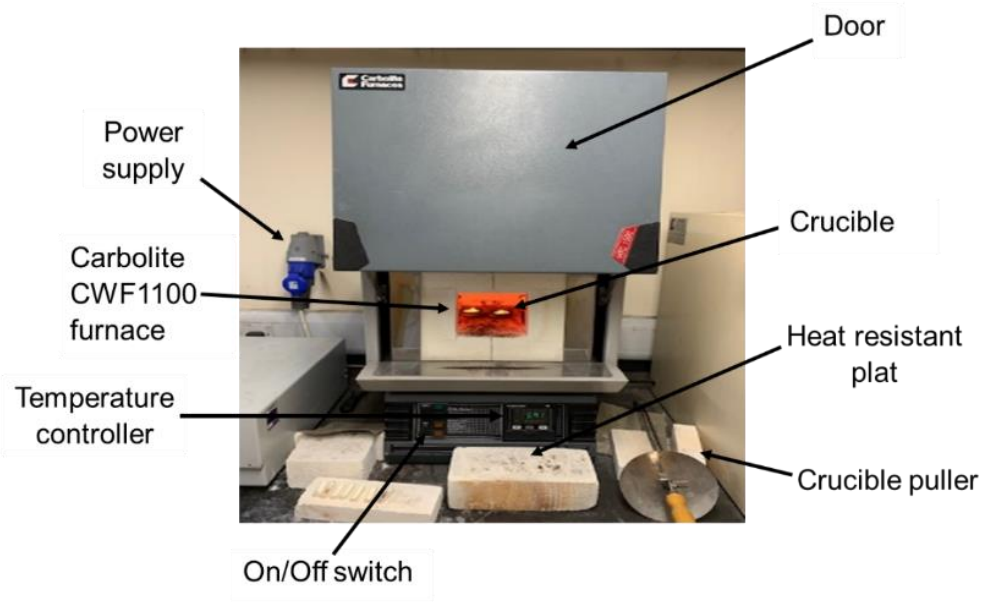

Figure 3-1 Ash content test setup

In the first stage, the temperature and time on the furnace control panel were set to 250 ºC and 30–50 minutes, respectively, to obtain a heating rate between 4.5 to 7.5 ºC/min to eliminate any volatiles before the ignition step. Then, the temperature was raised to 550 ºC for 30 minutes at a heating rate of 10 ºC/min. Once the temperature reached 550 ºC, it was constantly maintained for 120 minutes to ensure complete combustion was achieved. At the end of the process, the crucible dishes were removed from the furnace and placed on a heat resistant plate for 10 minutes to be cooled down before being cooled in a desiccator. The final weight was evaluated when the sample temperature settled at the ambient temperature. The ash content (%) was determined using the following formula [145]:

$$A_d = \left(\frac{m_3 - m_1}{m_2 - m_1}\right) \times 100 \quad (3.3)$$

Where m_1 is the mass of the empty crucible dish, m_2 is the initial total mass of the crucible dish and test biomass sample, and m_3 is the final total mass of the crucible dish and ash. The value obtained was the average of the three sample repeats.

3.2.4 Fixed carbon content

Another primary component of biomass was the fixed carbon content (FC %), which is the combustible solid residue that forms after the combustion of biomass where all volatiles and moisture were removed. The FC % was determined by difference because it depends on the amount of volatile matter released from biomass under specific conditions. Therefore, it provides valuable information about the amount of char formation and the size of the gasifier. The FC was determined using the following formula:

$$FC\ \% = 100 - [M_{ad} - V_d - A_d] \quad (3.4)$$

Where M_{ad} is the moisture content, V_d is the volatile matter, and A_d is the ash content of the sample. The crucible dishes used in the determination of M_{ad}, V_d and A_d are presented in Figure 3-2.

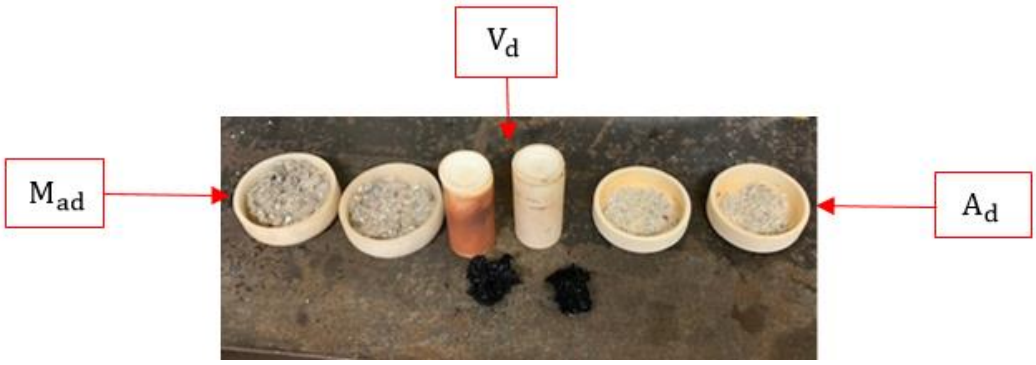

Figure 3-2 Crucibles used in the estimation of the ash, volatile matter and moisture content

3.3 Ultimate analysis

Ultimate analysis offers the biomass primary elements composition, such as CHNSO (carbon, hydrogen, nitrogen, sulphur, and oxygen). The ultimate analysis gives more inclusive information in comparison to proximate analysis. This analysis was essential to estimate the air/fuel equivalence ratio in terms of complete combustion. For the current study, the process of ultimate analysis of the sample was carried out in Pennine Analytical Laboratories. The results of the ultimate analysis of Subcoal™ are presented in Section 5.2 and Table 5-1.

3.4 Sand bulk density

Bulk density (or apparent density) is considered to be the property of powders that is defined as the mass of bulk solid that is contained in a unit volume including the voidage volume between particles. As it has powder properties, the determination of biomass fuel bulk density is crucial in identifying the energy density [146]. The density of the bed particles is an essential parameter in the fluidisation process that determines with particle size the relevant Gartland classification of particles. Gartland classification describes the behaviour of the fluidised bed. The density of silica sand (500-600 µm) ranges between 1400 and 4000 kg/m^3. In this case, the bubble appears (Umb) = minimum fluidisation Umf, and they are widely used in industrial applications due to their ease of fluidisation. The bulk density of silica sand was measured according to the BS 1337-9:1990 by using a piece of equipment comprising of two sections [147]. The first section was a pouring cylinder with a cone-shaped base and the second section was a calibration container, as illustrated in Figure 3-3. The mass (m_1) in kg, and volume (m_3) of an empty calibration container was measured. Then, the mass of the sand bed (m_2) that occupied the conical section was determined. The long cylinder subsequently was filled with silica sand (500-600 µm). The valve was opened, and the sand poured into the calibration cylinder as well as the cone space. The mass of the equipment and sand was defined as (m_3). Finally, the mass of a sand sample in the calibration container (m_4) was determined by difference as written below [138]:

$$m_4 = m_3 - m_2 - m_1 \tag{3.5}$$

Thus, the bulk density of silica sand was calculated as follows:

$$\text{Bulk density} = \frac{m_4}{\text{volume}} \tag{3.6}$$

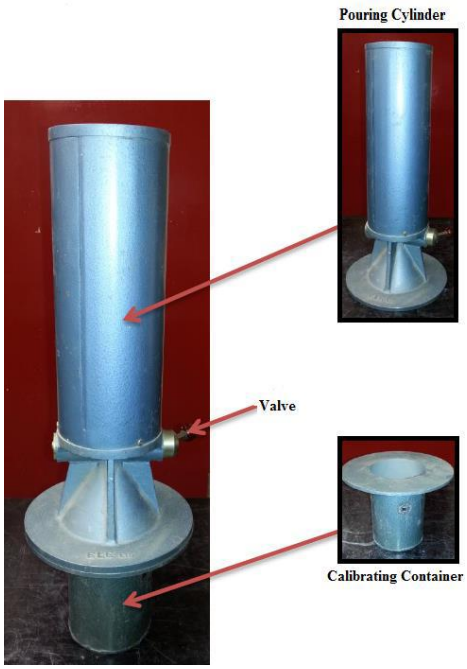

Figure 3-3 Apparatus for determination of bulk density of sand, container for calibrating and cylinder for pouring [138]

3.5 Subcoal™ bulk density measurement

The bulk density of the sample as received from N+P company was 150 kg/m^3, and the moisture content was 12%. The analysis of bulk density is considered to be an essential parameter, which is used in calculations of the fluidised bed hydrodynamics. Due to the sample property, it was not feasible to perform Subcoal™ powder bulk density using the calibration cylinder in Section 3.4. Therefore, the Subcoal™ measurement was carried out following BS EN 15103:2009 [148]. To reduce the uncertainty, the measurements were repeated three times. The test setup consists of a hollow cylinder with a known volume that meets the measurement specification requirements (height to diameter ratio: 1.25 to 1.5). This cylinder was fixed underneath a funnel where the sample particles were placed. The funnel was fixed by a metal clamp, as displayed in Figure 3-4. The bulk density of the sample particle size < 3 mm was calculated based on the following equation:

$$D_d = D_{ar} \times \frac{100 - M_{ar}}{100} \tag{3.7}$$

Where D_d depicts sample mass bulk density with reference to dry mass in kg/m^3, D_{ar} is the received bulk density in kg/m^3, and M_{ar} is the moisture content, as received, as a percentage by mass. The value of D_{ar} can be calculated using equation (3.8):

$$D_d = \frac{(m_2 - m_1)}{V} \tag{3.8}$$

Where m_2 is filled container mass in kg, m_1 is the empty container mass in kg, and V is the measuring container net volume in m^3.

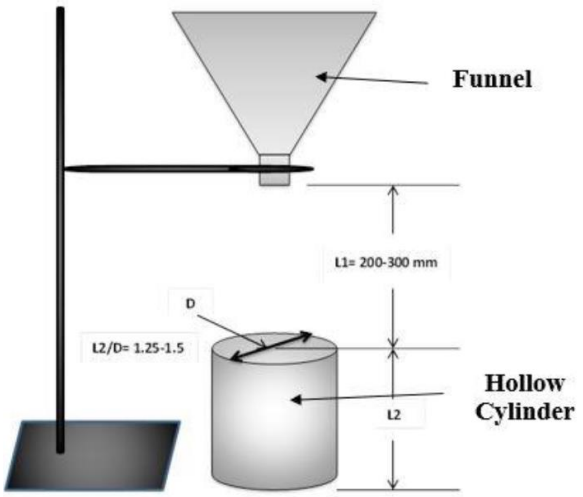

Figure 3-4 Schematic of the apparatus of Subcoal™ bulk density measurement

3.6 Calorific value

Calorific value (or heating value) is the amount of heat released from the complete combustion of a unit volume of the biomass fuel in the presence of oxygen [149]. The calorific value can be expressed in two ways, namely: high heating value (HHV) or low heating value (LHV). In the high heating value (or gross calorific value), the latent heat of vaporisation of water was considered, while this was not the case in the low heating value [150]. The HHV were determined in the laboratory according to BS EN 14918 using a bomb calorimeter (Parr 6100) from Parr Instrument Company, as presented in Figure 3-5 [151].

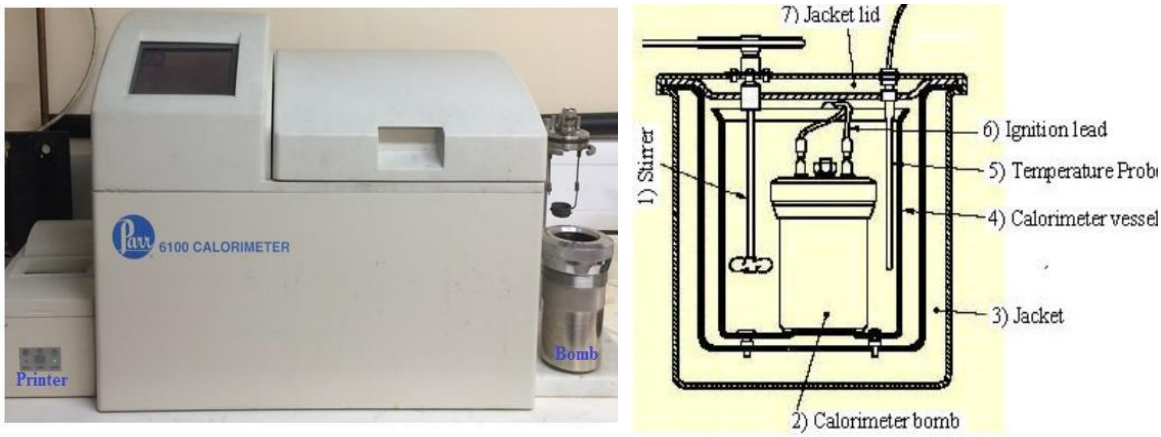

Figure 3-5 Labelled schematic drawing of bomb calorimeter (right) and the bomb calorimeter (Parr, model No. 6100) (left)

The test ran when the sample burned under controlled conditions of the oxygen-rich environment in a pressurised vessel. Calibration of the bomb calorimeter occurred before testing with three pellets of benzoic acid. Next, about 0.5 gram of Subcoal™ sample was placed in the calorimeter vessel, then sealed and pressurised with oxygen to 30 bar before being electrically ignited. The calorimeter vessel

was immersed in 2000 ml of distilled water inside a jacket made of stainless steel. The function of the jacket was to absorb the excess heat, which the fuel sample releases from combustion. The increase in water temperature was recorded and the energy released was defined as HHV [152]. After the test completed, the excess pressure in the bomb was released. The test was performed a minimum three times to confirm the repeatability of the results. LHV was estimated by subtracting the value of steam latent heat from the HHV as well as taking the moisture content into account based on the following equation:

$$\mathrm{LHV} = \mathrm{HHV} - \mathrm{h}_g \left(\frac{9\mathrm{H}}{100} + \frac{\mathrm{M}}{100} \right) \tag{3.9}$$

Where H is the hydrogen percentage, M is the moisture percentage, and h_g is the latent heat of steam (h_g= 2.26 MJ/kg).

3.7 Sulphur (S) and carbon (C) content

The content of S and C in the Subcoal™ were evaluated through the use of a LECO SC-144DR analyser, as presented in Figure 3-6. The testing procedure was adopted from the analyser user manual. The sample was placed into a boat dish and then introduced to the combustion chamber to burn it in the oxygen-rich environment at a temperature of 1500 ºC. Consequently, carbon dioxide (CO_2) and sulphur dioxide (SO_2) gases were released from the complete combustion reaction of the sample. Infrared (IR) detection cells were then employed to measure the concentration of the two gases, thus C and S content can be determined as percentages. The test was launched and controlled using Windows-based software [153]. This analyser can detect the trace of S and C at a precision of ± 5.0 ppm and ± 25.0 ppm, respectively. The device was linked to software that converts the product gas concentration from PPM to mass percentage in the original sample. The test was performed three times to ensure repeatability in results.

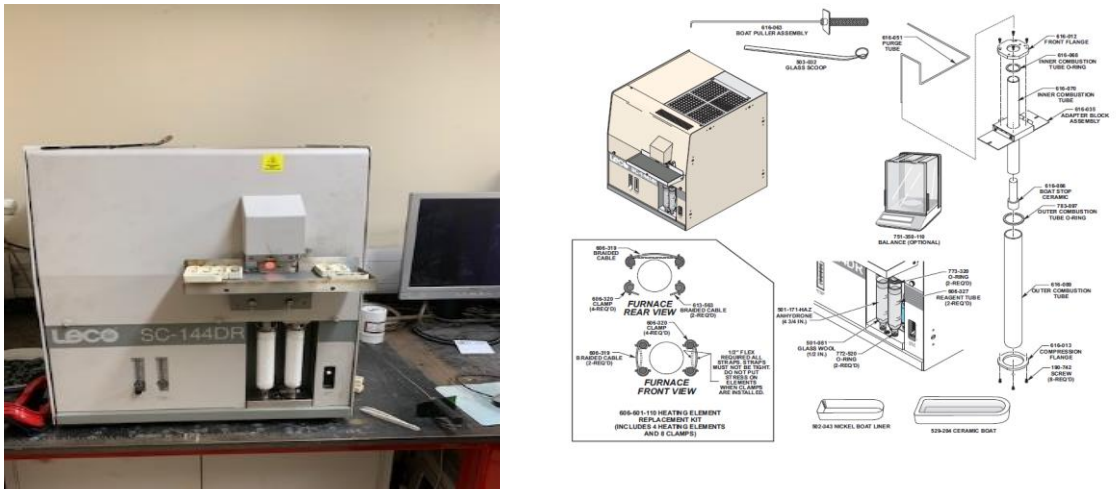

Figure 3-6 Representation of analyser labelled components (right), and an image of the SC-144DR analyser (left)

3.8 XRF analysis

Subcoal™ comprises of different trace elements other than those detected by the techniques mentioned above. The X-ray fluorescence (Innov-X System, model X-5000) technique was used to measure the content of the trace elements in the sample. The analysis procedure was adopted from the XRF operating manual using a 3-beam method, namely: alloy, mining plus, and soil. These methods are suitable for the analysis of sample, chars, and ashes. The 3-beam method operates with three voltage levels of 50, 35, and 15 kV, which are applicable in detecting the common elements [154]. Figure 3-7 shows the XRF analyser used in the present test.

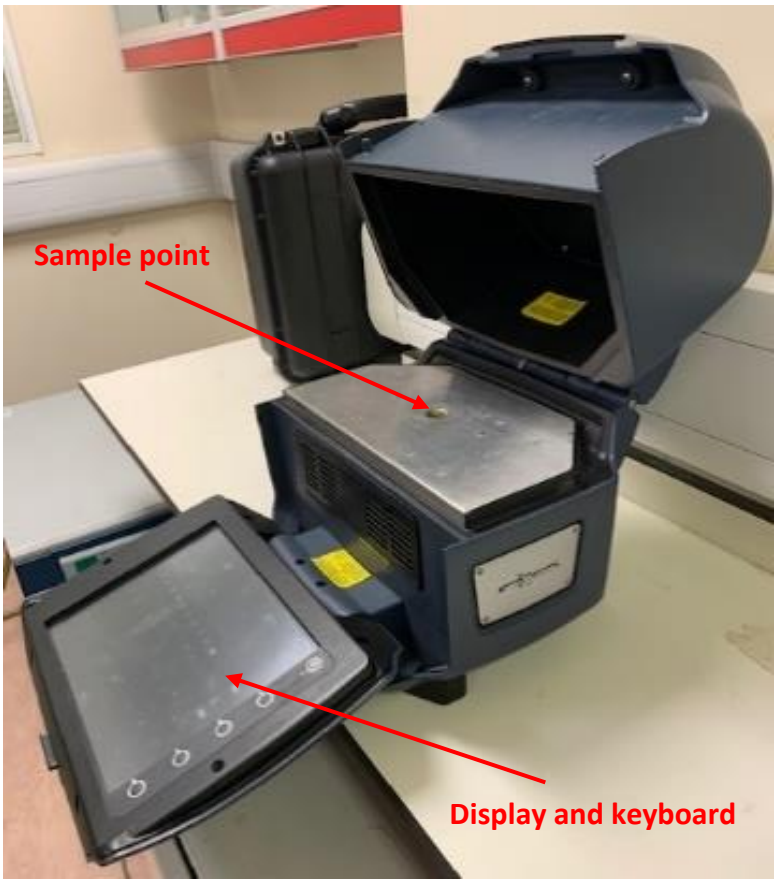

Figure 3-7 XRF analyser (Innov-X System, model X-5000)

Before running the test, the analyser was calibrated with a sample of stainless steel 316 alloy. In the sample preparation, a new thin-film sample support was attached to a clean sample holder. Then, about 1 g of the sample powder or ash was distributed on the holder using a spatula to at least 3 mm thickness. The sample holder was placed at the sample point and the lid was closed. The required sample data were inserted into the analyser system. The "Mining Plus, Soil, Alloy" modes were selected to run the test. When the test was completed, the sample was removed and the result in ppm was saved in the device. The test was repeated three times to ensure repeatability in results.

3.9 XRD analysis

3.9.1 Background

X-ray diffraction (XRD) is the most widely used non-destructive technique for providing information on atomic and molecular structure and phase of a material. It is also capable of measuring some morphological parameters such as crystal size, strain, crystallinity, and crystal defects [155]. The XRD technique was commonly used to characterise minerals and their polymorphic phase in coals due to the capability of this analysis of evaluating the crystalline structure of solid mixtures [156-157]. However, significant noise was observed in the XRD analysis of coal and char by Gupta [158] due to the presence of amorphous carbonaceous species.

In the XRD characterisation, the sample of material was exposed to monochromatic X-ray radiation produced from a cathode ray tube. In the sample, the ray radiation was scattered by the sample in different directions. The diffracted beams then were collected by a detector. However, a signal resulting from a beam striking a sample at a certain angle may lead to constructive interference. Figure 3-8 represents the working principle of XRD.

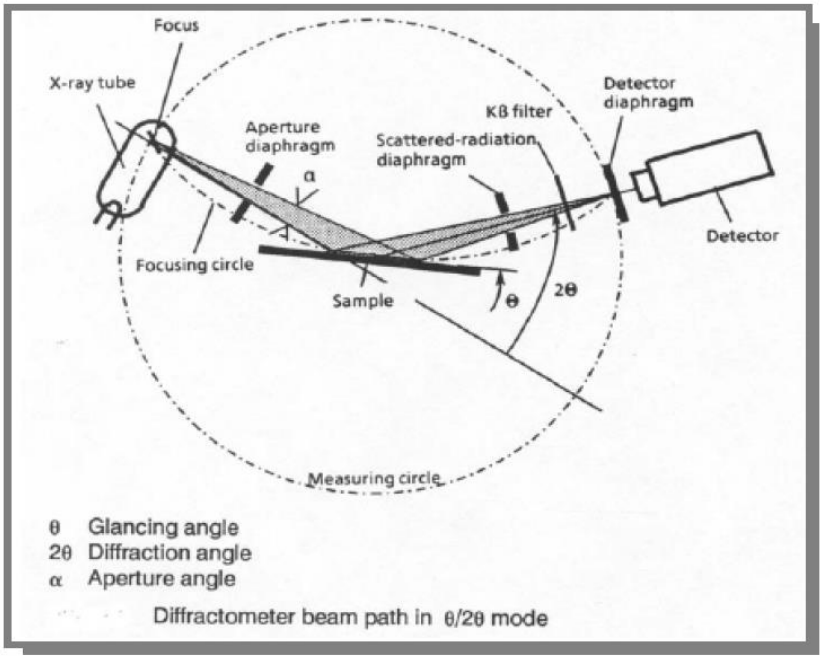

Figure 3-8 Schematic representation of the XRD working principle [159]

The energy and angle of an incident beam of X-rays were known and controllable from the source. The energy and angle (θ) of the scattered beam can be estimated by a detector which was used later to estimate the intensity of the beam. The energy of an incident beam was partially absorbed by the material being tested. Therefore, the energy of a diffracted beam was lower than that of the incident beam. Concerning beam angle and energy, the compound identity, composition, and crystalline phase can be inferred. The XRD unit was linked to a computer and the software plots the intensity data as

a function of (2θ) angle. Based on a crystallography database, the peaks graph can be further analysed to identify the peaks structure and crystalline phase [160].

The interaction between X-rays and sample creates secondary diffracted beams to spacings of interplanar based on the powder that is crystalline with reference to Bragg's law, which is a mathematical relation illustrated below:

$$n\lambda = 2d \sin\theta \tag{3.10}$$

Where n depicts the reflection order, λ is the incident ray wavelength, d is the interplanar spacing of the crystal, and θ is the angle of incidence and reflection of the incident ray. The wavelength of incident X-ray can be estimated from the energy of radiation. In contrast, the angle of diffraction was determined based on the position of the detector. X-ray data were recorded in terms of 2θ (x-axis) vs. intensity (y-axis).

3.9.2 XRD analysis method

A dry powder of Subcoal™< 3 mm, silica sand (500-600 µm) and ashes were analysed in the XRD Diffractometer D5000, as displayed in Figure 3-9. The sample was mounted on the diffractometer sample holder in a flat layout. A typical sample holder is a 2-mm thick plate with a 20-mm square hole in the center. The proportion of the crystalline components in the fuel (crystallinity) was determined according to standard test method ASTM D5758 and results evaluated using the following formula [161]:

$$\text{Crystallinity } \% = \frac{A_c}{A_c + A_a} \times 100 \tag{3.11}$$

Where A_c is the area under the peaks representing the total crystalline region, and A_a is the area under the peaks representing the total amorphous region [161].

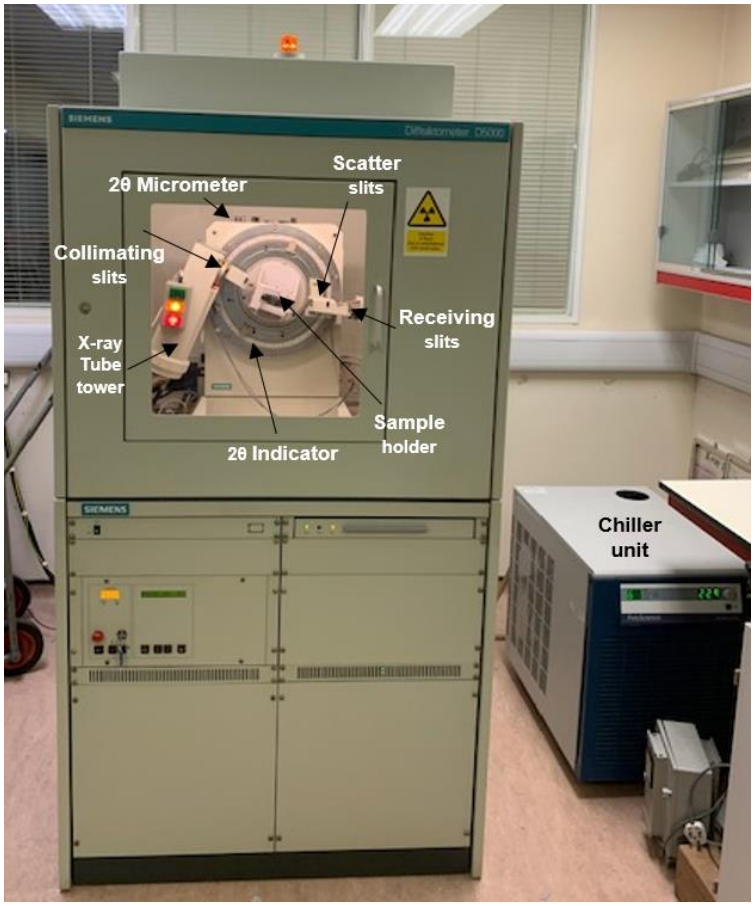

Figure 3-9 Labelled image of an XRD machine (Siemens, Diffractometer D5000)

In addition, the sample was placed onto the holder in the machine sample stage and compressed using a glass slide to obtain a flat and even surface. The holder was transferred into the XRD goniometer and the door was closed. The chiller unit and XRD unit were then switched on, respectively. The default power was set at 200 W (20 mA and 10 kV), which was increased to 1400 W (35 mA and 40 kV). The shutter door kept open to allow X-rays to reach the sample. Then, the scanned data was inserted in computer-based software (Panalytical X'Pert HighScore Plus) that organises the scanning process. Finally, the scan program was sent to the XRD machine and the scan commenced. The results were transferred to OriginPro® software and the crystallinity of the sample was calculated.

3.10 Malvern Mastersizer 3000

3.10.1 Background

The particle size of bed material is one of the key parameters required in the design calculations of a fluidised bed gasifier reactor. The Mastersizer 3000 (Malvern Instruments, UK) is a commonly used particle sizing instrument that is able to measure a size range of 10 nm to 3.5 mm. Figure 3-10 displays the operating parameters of the Malvern Mastersizer 3000. The Mastersizer 3000 instrument comprises of four essential units, namely: disperse unit, optic unit, measurement cell, and computer-based software [162]. Figure 3-11 shows an image of a Malvern Mastersizer 3000 instrument.

Parameter	Specification
Pump speed range	0-3500 rpm †
Pump speed resolution	+/- 10 rpm
Pump speed accuracy	+/- 50 rpm
Maximum flow rate	1.7L/min †
Sonication power & frequency	40W max, 40kHz (nominal) †
Volume	250mL / 600mL / 1000mL (using lab beaker)
Materials in contact with sample	316 stainless Borosilicate glass Tygon® FKM (cell seal only - FFKM available) PTFE PEEK Titanium Nitride
Maximum particle size	2100µm ††
Minimum time between measurements	less than 60 sec ††
Dimensions	220mm x 150mm x 300mm (L x W x H)
Mass	4kg
† Dispersant dependent †† Sample dependent	

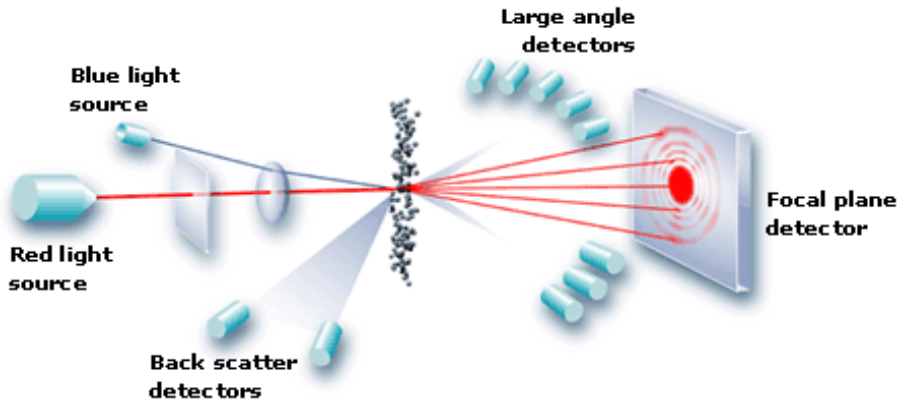

Figure 3-10 Operating parameters and diagram of laser diffraction method of the Malvern Mastersizer 3000 [163]

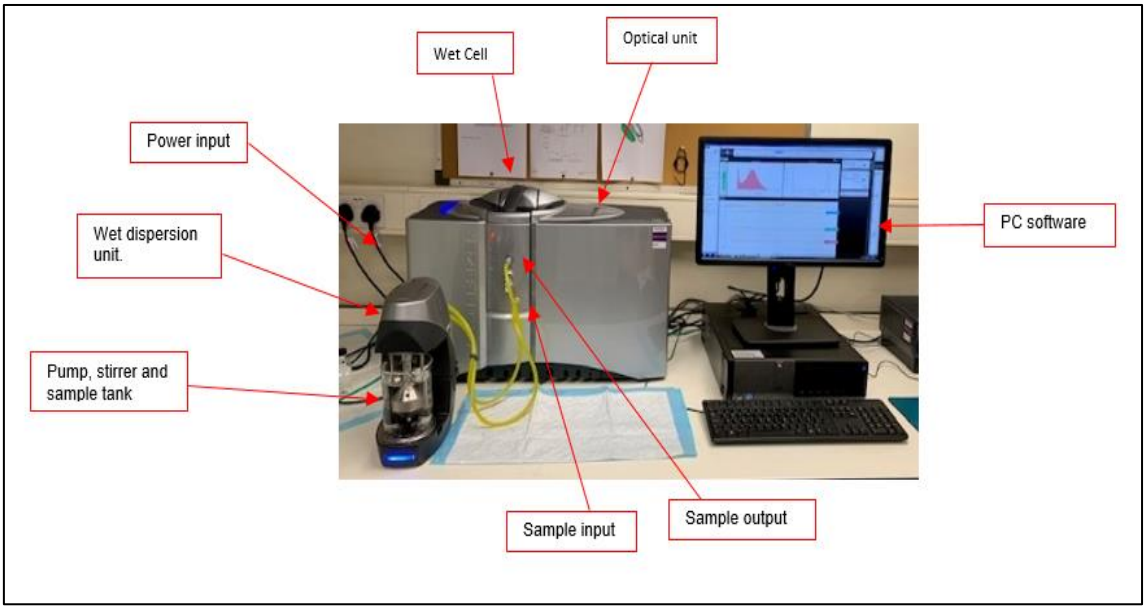

Figure 3-11 Malvern Mastersizer 3000 instrument

This particle sizing instrument provides information on the particle size distribution of a mixture of particles, as well as mean particle sizes. The working principle of the device is based on the diffraction of laser light on particles of different sizes, as shown in Figure 3-10. The method of laser diffraction is utilised in distribution measurement of the particle size for its broad dynamic range (from nanometers to millimeters) and rapid measurements [162]. A beam of laser light was applied on a dispersed particulate sample that scatters on the dispersed particles of different sizes. The angular variation and energy of the scattered light were measured. As the particle size increases, the scattering angle decreases. Based on the obtained angular scattering data, the particle size can be estimated utilising the Mie theory of light scattering. The particle size data was subsequently interpreted in terms of volume equivalent sphere diameter. Inherent assumptions in the Mie scattering theory are the spherical particles with radius on the same order of magnitude as the laser light with a single scattering [164]. These assumptions may affect the accuracy of the size distribution measurements. The calculations of size distribution were calculated using the following equation:

$$\mathrm{dp} = \Sigma \mathrm{xi} \times \mathrm{dpi} = 1 \qquad (3.12)$$

Where dp is the mean particle diameter, xi is the mass fraction, and dpi is the diameter of particle size.

3.10.2 Method

The silica sand was sieved in a range of particle sizes measuring 500-600 μm, and Subcoal™ powder with a particle size of < 3 mm was prepared as shown in Section 3.12. The experimental procedure was obtained from the Malvern instrument operating manual [165]. At startup, the instrument must

be connected to all accessories and dried. The power was supplied and a measurement file was created in the software. A sample was placed in the wet dispersion unit. Once the test was completed, the report result was saved. Finally, the dispersion unit was emptied of a sample and cleaned.

3.11 Catalyst preparation

The effect of mineral catalyst concentrations on Subcoal™ pyrolysis, gasification, and combustion was evaluated. Dolomite and olivine were supplied by Tarmac company from Port Talbot in form of powder with particle size of < 1 mm. A ring mill machine (Labtech Essa 100100, Australia) was used to reduce the catalyst through grinding machine, as shown in Figure 3-12.

(a)

(b)

Figure 3-12 a) Grinding and crushing machine (Labtech Essa 100100, Australia), b) dolomite left and olivine right side

The catalyst sample was placed in a metal bowl and fixed by a pneumatic clamp. Then, the machine cabinet was closed and secured. The pneumatic air isolation ball valve was opened. The on/off push button was activated to start the machine for 3 to 6 minutes. Finally, the machine was stopped, the milled catalyst was sieved according to BS 1377-9 1990 to 106 μm and packed in a dry container.

3.12 Subcoal™ pellets size reduction

Pulverised Subcoal™ pellet (pellet B) were supplied by N+P company with dimensions of 14-27 mm length and 8 mm diameter. To study the effect of heating rate and catalyst ratio on sample by TGA, the pellet B were reduced and milled by using a knife type mill (Fritish model 55743, GmbH, Idar-Obersten, Germany), as shown in Figure 3-13. This mill uses special curvature mesh trays with different sizes.

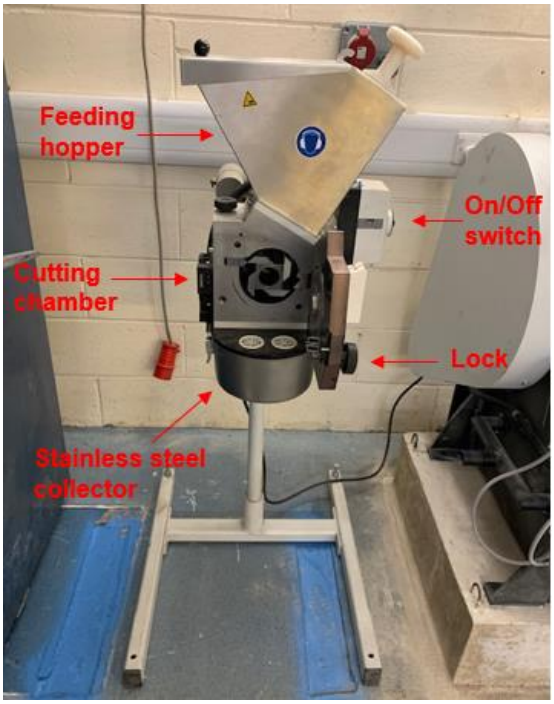

Figure 3-13 Fritish GmbH grinding and crushing machine

As soon as the mill was activated, an amount of sample (50 g) was placed into the machine hopper. The flow of the feed particles to the cutting chamber was controlled by a gate. The cutting chamber consists of several sharp stainless steel knives which are fixed radially on a stainless steel cylindrical shaft. An electrical motor rotates the knife shaft at a controlled speed. The mill design provides a clearance distance between the knives and a curvature mesh tray to press the sample cuttings through the mesh tray. At the bottom of the cutting chamber, a stainless steel container was located to collect the cut particles. Finally, the milled product was called pulverised alternative fuel (PAF) with particle size < 3 mm is shown in Figure 3-14 were packed and stored in sealed bags.

Figure 3-14 Subcoal™ PAF

The difficulty of sieving the PAF leads to only one size being produced. To analyse the effect of pellets particle size of sample in FBGR, the pellet B was reduced by using scissors to (10-6.3 mm), as illustrated in Figure 3-15 and the selected pellets sizes were obtained by sieving according to BS 1377-2:1990.

(a) (b)

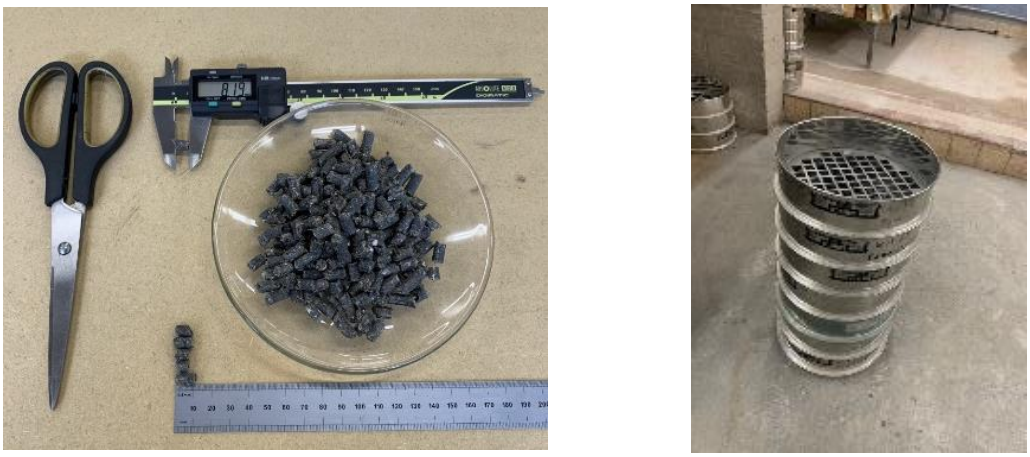

Figure 3-15 Pellet (B) reduction size (a) tools and sieves (b)

3.13 Thermogravimetric analysis

Thermogravimetric analysis (TGA) and derivative thermogravimetry (DTG) were performed in a Mettler Toledo analyser (AG TGA/SDTA 851e) with a temperature range of 25 to 900 ºC. The experiment was performed following BS EN ISO 11358:1997 [166]. Figure 3-16 shows the TGA instrument and components.

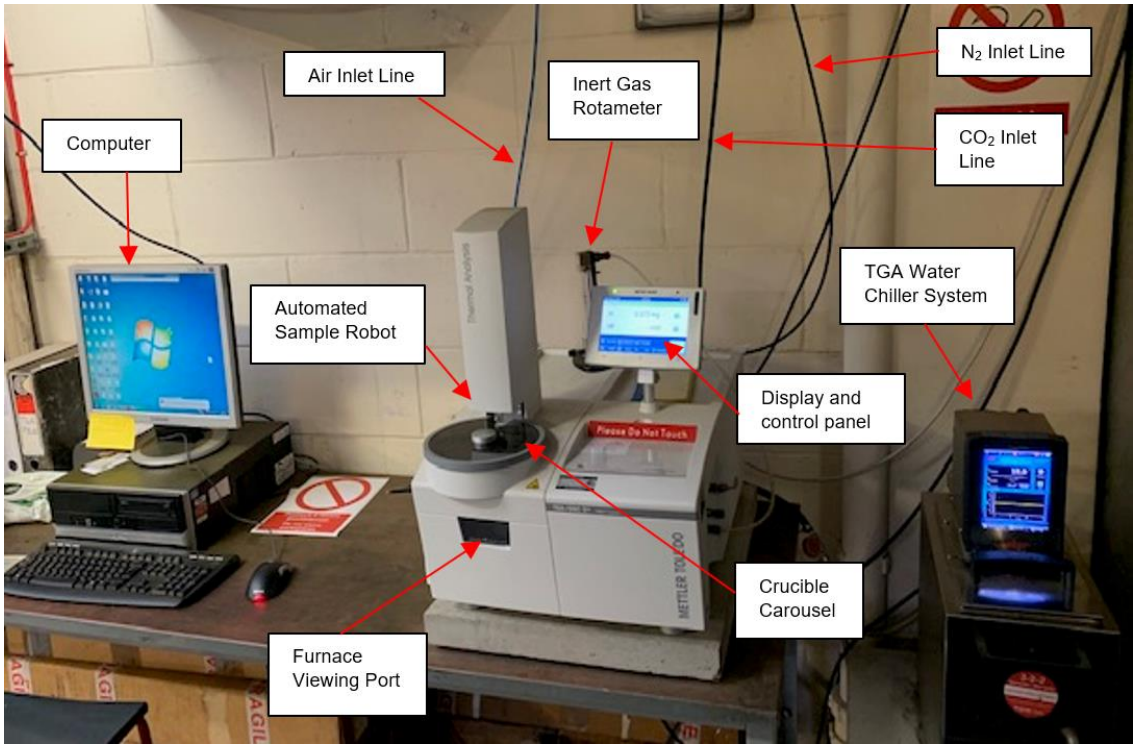

Figure 3-16 Labelled TGA device

The thermal degradation and kinetics of the non-isothermal process were studied in the presence and absence of a catalyst. Subcoal™ PAF was used as a milled product as a powder<3 mm particle size. The mass loss data was acquired with temperature change for different conversion degrees ranging from 20 to 80 wt.%. The model-free method was used to evaluate the E_a behaviors of the sample without catalyst at different heating rate 5, 10, 15, and 20 ºC/min, while the CR model fitting method was selected to determine the kinetic parameters with catalyst at a constant heating rate of 20 ºC/min. Dolomite and olivine (106 μm particle size) were employed with different concentrations 0, 5, 10, 15 and 20 wt.%. However, low loadings of the catalyst (e.g., 1 wt.%) were not used in this study due to insignificant changes in the gasification performance that is due to poor mixing with Subcoal™ and the gasification agent.

The experimental procedure began when 10 ± 5 mg weight of the sample was placed into a crucible made of alumina. To make sure the sample was well distributed, the crucible was gently tapped on a solid surface. The crucible was then transferred and loaded onto the TGA carousel using tweezers. Once the crucible was automatically placed into the furnace, a program comprising four heating rates was digitally run, with N_2 gas with a volumetric flow rate of 50 ml/min adopted to provide an inert atmosphere for the pyrolysis process, while 100 ml/min CO_2, and 100 ml/min of air were used for the gasification and combustion atmosphere. The flow rate setting for different gases was chosen based on the optimum operating condition of the TGA instrument and to compare the result with the literature. In all experiments, sample weight loss was continuously recorded against the temperature and time to obtain the TGA curve, which was derived later for first-order derivative to obtain a DTG

curve. In DTG curves, T_m was observed when the maximum decomposition of solids takes place. As reported previously, the model-free method is sensitive to measurement errors. Therefore, all experiments were performed a minimum three times to confirm the repeatability of the results and minimise the effect of experimental errors. The trend of the TGA curve, as well as the width of the DTG peak, determine the thermal decomposition behaviour [167]. The obtained data was exported to a Microsoft Excel® sheet when the test was completed for thermal and kinetic statistical analysis.

3.14 Bubbling Fluidised bed gasifier reactor (BFBGR)

The BFBGR rig was designed by Al-Farraji [138] and constructed in a combustion laboratory at the School of Engineering in Cardiff University. However, the biomass feeding system in this study was modified to provide a high heterogeneous gasification reaction and smooth pellets fluidisation as shown in Figure 3-17. Also, a condenser installed on the producer gas outlet for liquid tar removal. Figure 3-18 displays P&ID and experimental rig equipment.

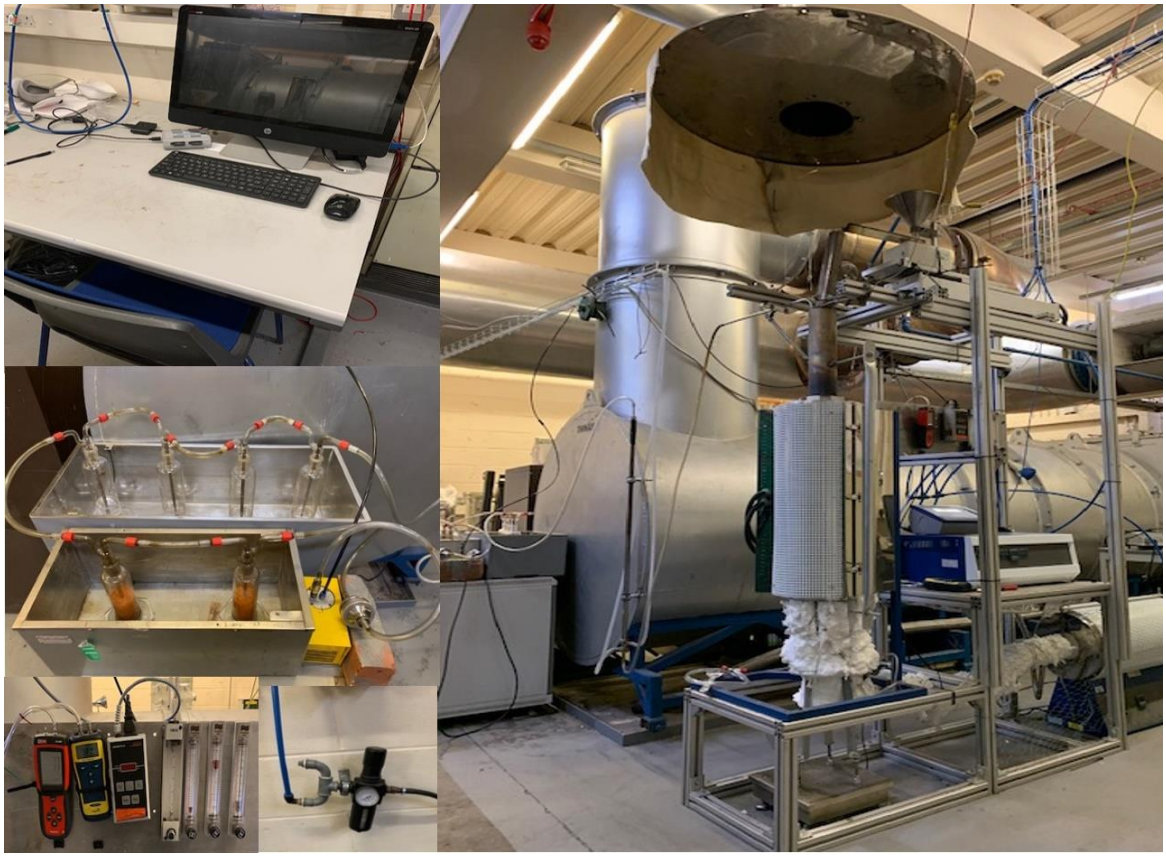

Figure 3-17 Experimental rig

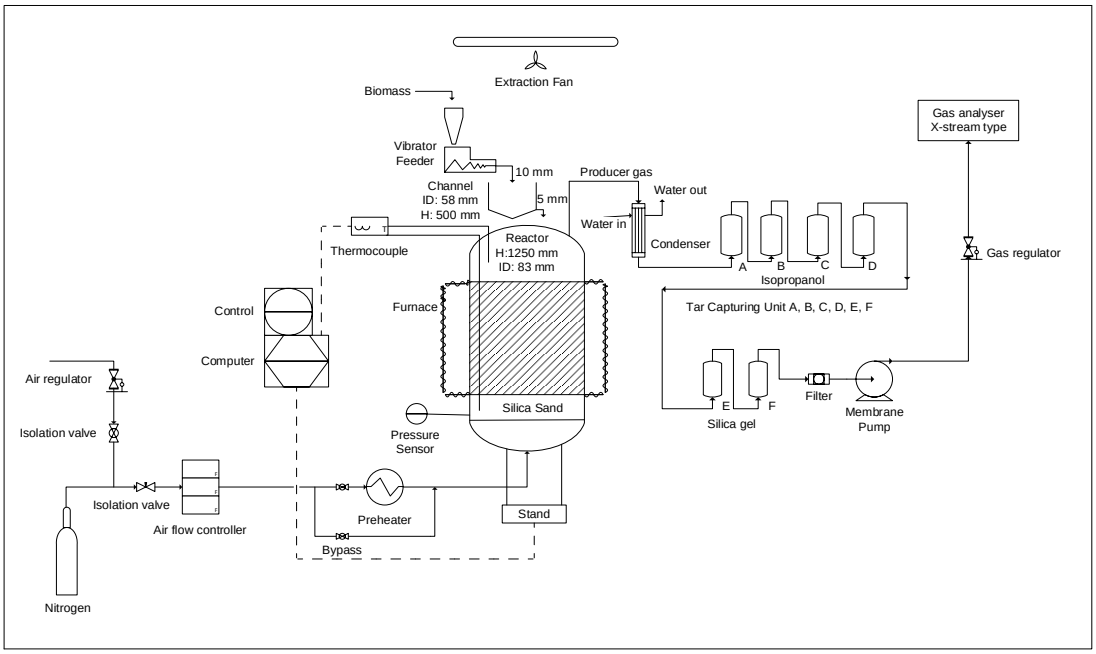

Figure 3-18 Schematic P&ID diagram of BFBGR

3.15 FBGR experimental rig procedure

1. Before starting the experiment, all safety procedures should be followed as described in the Appendix A: Kinetic Theory and Feedstock, for example, wearing PPE, making sure compressed air valves were closed, electrical connection was ready, no dangerous chemical surrounding the rig and extracting fan was started for toxic gas ventilation.
2. The freezer was turned on a day prior to the gasification experiment, and an ice cube bag was placed in the freezer.
3. Cold/hot gasification test run was performed to check pellets fluidisation behaviour and parameters were working correctly.
4. 100 ml of isopropanol was poured into each of the 250 ml Drescher bottles in the tar capture unit located inside the stainless steel box. Then ice cubes were installed in the stainless steel box with the tar capture unit and temperature was maintained at -10 °C and this was verified with a thermocouple.
5. The Chiller unit started to supply cooling water to the condenser, and the temperature was maintained at 15 °C.
6. The gas analyser was zero calibrated and the description of the gas analyser is provided in Section 4.7.12.
7. Based on the static bed height H_s and reactor diameter D (Hs/D) ratio, an amount of silica sand with a particle size 500-600 μm and a density of 2650 kg/m^3 was added as bed material to the gasification column.
8. The air blower, split surface, and preheater were switched on and the temperatures were monitored using a data logger. The superficial velocity was kept constant at 40 L/min, i.e. two times the value of U_{mf}.

9. The activation of the indicator of multifunction temperature and data logger occurred after switching the computer on.
10. The vibrating feeder was then calibrated for each mass flow rate depending on equivalence ratio (ER) by direct weighing of the biomass for five minutes. The mass flow rate of biomass varies with the given ER. The air flow rate was held constant by rotameter during the experiment. The description of ER is provided in Section 4.7.2.
11. When the gasifier reached the optimum operating temperature, the biomass feeder was switched on. It was observed that the biomass feeding time required to achieve equilibrium was less than two minutes, therefore, five minutes was chosen as the experimental time. This procedure was repeated minimum three times to ensure reproducibility.
12. Once the experiment was completed, the air flow was replaced by inert N_2 gas and the flow was maintained at a minimum flow rate to ensure a dominant environment for the bed materials, and to cool down the gasifier as quickly as possible.
13. Gas composition analysis was transferred to Microsoft Excel® for analysis.

Proximate and ultimate analysis, bulk density, calorific value, and TGA experiments followed the relevant British Standards. Furthermore, XRD, XRF, Malvern Mastersizer 3000, gas analysis and milling procedures were carried out following the equipment operating manual. Studies reported in the literature proved that these methods provided accurate measurements and safe practices [168-170,138, 157].

To study the kinetics of Subcoal™ and thermal degradation (DTG), the thermogravimetric analysis (TGA) and laboratory-scale fluidised bed gasifier reactor (FBGR) were used. The TGA was chosen to investigate the pyrolysis, gasification, and combustion of Subcoal™ under different heating rates and catalyst loadings. The TGA is an inexpensive and easy-to-use technique that provides a rapid measurement of weight loss as a function of time or temperature. This experimental data from TGA can be used to evaluate reaction kinetics using one of the model-free or model-fitting methods. The air gasification behaviour was also examined in laboratory-scale FBGR. The FBGR is widely used to study biomass gasification due to various advantages over fixed bed gasifier such as low tar formation, good temperature distribution, high fuel throughput and high carbon conversion efficiency [171]. The quality and composition of producer gas can be determined by different catalysts, equivalent ratio, temperatures, bed particle material and properties, and gasifying agent. It is also simulating the fluidised bed gasifiers in the industry in terms of the chemical and physical changes.

3.16 Summary

Subcoal™ was subjected to different examinations to evaluate the operating conditions required in the pyrolysis, gasification, and combustion process. Proximate analysis was performed to measure the volatile matter, moisture, ash, and fixed carbon content in the sample. The content of volatiles in biomass determines the amount of product gas. Other important constituents are ash and fixed carbon which affect the calorific value of a fuel. The ultimate analyses determine the element composition

of the sample CHNSO. Sand and sample bulk density methods were described, which was crucial to identifying the energy density. The measurement of the calorific value of the sample was essential to estimate the amount of heat released during the combustion which was needed to provide the endothermic reactions in the gasification reaction. Sulphur and carbon content were determined using a LECO SC-144DR analyser with a precision of ± 5.0 ppm for sulphur, and ± 25 ppm for carbon. The XRF test method was illustrated to estimate the content of the trace elements in the sample. XRD procedure was carried out using Diffractometer D5000 to deduce the crystallinity percentage of Subcoal™, silica sand and ash. The particle size distribution method was determined using a Mastersizer 3000. The catalyst preparation and pellets grinding for size reduction were presented. Finally, TGA and FBGR experimental preparation and procedure were described.

Chapter 4: Kinetic Theory and Experimental Rig Overview

4.1 Introduction

In this chapter, kinetic theory and evaluation methods are demonstrated. According to the kinetic principle, each reaction has temperature-independent parameters, namely: pre-exponential factor (A) and the activation energy (E_a). The experimental findings for given values of conversion (X) would be employed to determine these parameters, which in turn are needed to assess the energy barrier for each reaction. The analysis of reaction kinetics includes processing the TGA data using model-free and model-fitting methods. Each method poses a unique mathematical model and procedure leading to minimise error in the uncertainty of calculations. The FBGR experimental rig setup and the associated reactor operating conditions have been discussed. Also, important parameters that have an impact on the process of gasification performance, as well as producer gas quality, are described. The typical ranges of the key operating conditions and feedstock properties such as temperature, pressure, residence time and flowrate have been presented. A detailed description of the experimental methodology including the essential design parameters such as fluidisation velocity and equivalence ratio (ER) have been reported. Gasification effectiveness theory for producer gas composition and material balance are discussed.

4.2 Fixed bed thermogravimetric analysis

Thermogravimetric analysis (TGA), or thermogravimetry (TG), is a technique that monitors the mass of a material as a function of time and temperature where a sample of a substance is subjected to a controlled temperature variation program [172]. The TGA provides an understanding of the physical and chemical phenomena that are causing mass changes. The physical processes are defined as vaporisation, sublimation, gas adsorption and desorption, while chemical phenomena are decomposition, cracking reactions, chemisorption, and gas-phase reactions. The mass of the specimen may fluctuate with time and temperature due to the physical and chemical processes.

Commercial TGA instruments typically work with temperature ranges from ambient to more than 1000 ºC. A purge inert gas such as N_2, argon, or helium is used in TGA to create an atmosphere in a mass balance. Oxidising gases like air, CO_2 or reducing gases like hydrogen-nitrogen mixture could also be adopted [173]. Using the oxidising atmosphere at slow heating rates may lead to mass gain due to oxidation deposition. Another mechanism that describes the mass gain is the adsorption or absorption phenomena. Therefore, the selection of gasifying agent type and catalyst will affect the TGA measurements.

A typical TGA instrument consists of a precision balance with a sample pan placed inside the furnace alongside a programmable temperature controller. For gasification or pyrolysis applications the temperature is controlled with a constant mass loss for the thermal degradation reaction. The

chemical reactions occur within a spectrum of atmosphere consisting of air, N_2, CO_2, vapours of liquids, corrosive gases, self-generated atmosphere, carburising gases, vacuum and reduction gases. Furthermore, this also includes a broad variety of pressures, consisting of high pressure, high vacuum, and controlled pressure [173].

A schematic drawing shown in Figure 4-1 displays typical TGA temperature sensor locations. The instrument is fully automatic with two underlying systems, namely, a magnetic suspension/balance system and a vapour dosing system that supplies gases to the reaction zone [174]. The balance system operates based on a null-balance principle in which a current is applied if a change in the mass occurs. Different parameters may affect the accuracy of the balance such as position, layout, and temperature range.

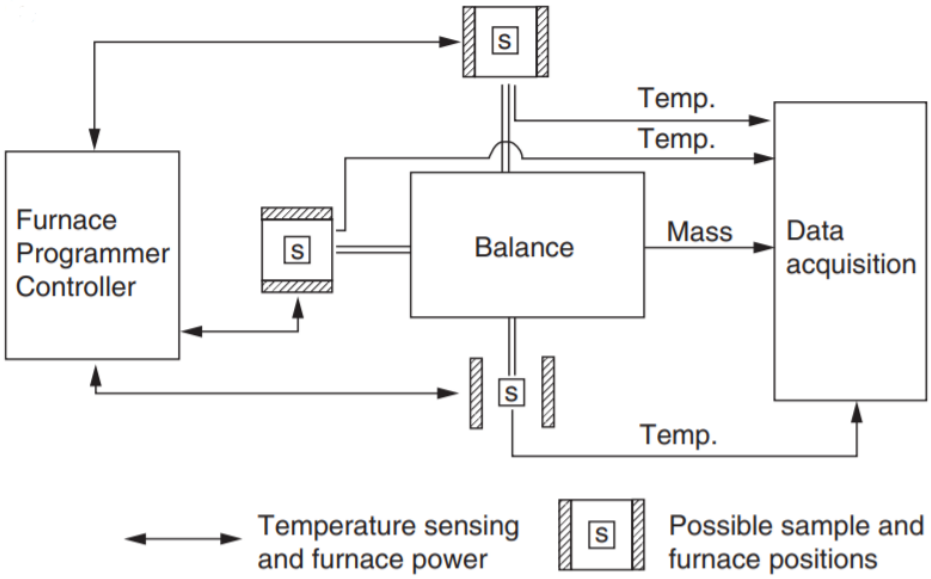

Figure 4-1 General schematic representation of thermobalance [175]

TGA measurements can be influenced by various experimental factors and conditions. Disturbances in the evaluation of substance mass arise from three sources: electrical impacts, atmospheric considerations, and secondary reactions. Factors affecting mass results are buoyancy and thermal expansion, condensation, intermediate reactions, electrostatic and magnetic forces, and atmospheric turbulence [173]. Buoyancy is a phenomenon that occurs as a result of a reduction in the atmospheric density, especially at the early stages of heating. Therefore, the apparatus performance depends on the specimen volume, specimen support, and purge gas flow properties. The temperature measurements also are influenced by thermal conductivity, heating rate, the heat of reaction, and specimen–furnace–thermocouple configuration [173].

Controlled rate TGA (CRTGA) is the common operation procedure that comprises three sub-modes. In the first mode, the data of mass change per time change is used to control the furnace temperature. The decomposition reaction takes place at a constant temperature. The equilibrium temperature of

degradation is related to the partial pressure of the volatile products. A second mode, which is also referred to as 'auto-stepwise', is a gradual non-isothermal method in which the upper and lower limits of mass change are pre-set. The last approach is known as dynamic rate Hi-Res™ TGA. This approach is based on changing the heating rate during the analysis to enhance the separation of mass at multiple degradation stages [173].

The TGA curve is a smoothed curve on the graph and the first order derived thermogravimetric known as the DTG curve that helps to determine the inflection points to establish in-depth analysis and differential thermal analysis at different stages [174]. This analyses the material characteristcs by interpretation of decomposition patterns. Thus, the TGA can record the loss of weight of the sample by continually increasing the temperature at a uniform rate and yielding a useful comparison of the reaction parameters, heating rate, and temperature. In this thesis, thermal and kinetic reactions of Subcoal™ PAF were evaluated using a Mettler Toledo TGA (Mettler Toledo, UK). In addition, the first mode was used to study the influence of catalysts at constant heating rate. While the second mode (Hi-Res™) was performed without catalyst at different heating rates.

4.3 Kinetics of chemical reaction

Reaction kinetics is a vital branch of physical chemistry in which understanding of reaction mechanisms can be achieved. Kinetics of chemical reaction determines how the reaction responds to the change in the reactant concentrations, temperature, pressure, and presence of other foreign species such as catalysts and solvents. Moreover, reaction kinetics can provide information on the reaction pathway such as whether a reaction is reversible or irreversible, as well as the intermediate steps [176]. The kinetics of a thermal reaction can be understood by performing experimental thermodynamics measurements under different operating conditions.

Parallel and series reactions take place during the gasification process. The reaction mainly occurs between a biomass molecule and a gasifying agent such as air, O_2, CO_2, and steam. Heterogeneous reactions subsequently follow to form target and inert products [74]. The kinetics of pyrolysis, gasification and combustion reaction can be investigated by determining the reaction rate parameters for biomass. Parameters such activation energy (E_a), pre-exponential factor (A), reaction rate constant (k), overall reaction order, as well as the heat of reaction, need to be estimated for a full understanding of kinetics. The present section gives an insight into the kinetics of chemical reactions. The mechanisms and kinetic evaluation methods are briefly reported. An explicit description of the estimation of kinetic essential parameters is given.

Among reaction kinetics components, the rate of reaction, which describes the reaction speed, is the most important. The reaction rate is the change of reactant quantity as a function of time or temperature. It mostly relates to the reactant's mass and reaction temperature [177]. However, based on the overall reaction order, the rate of reaction depends on the reaction temperature. The rate of reaction (r) is expressed as follow:

$$r \propto [B]^n \tag{4.1}$$

Where $[B]$ is a reactant concentration and n the overall reaction order. The rate of reaction is proportional to the reaction constant (k):

$$r = k[B]^n \tag{4.2}$$

$$\frac{d[A]}{dt} = k[B]^n \tag{4.3}$$

The rate of reaction in Eq. 4.3 can be given as a function of fractional conversion:

$$-[B]_o{}^{1-n}\ \frac{dx}{dt} = k[1-x]^n \tag{4.4}$$

A chemical reaction between molecules/particles takes place based on the theory of collision [178]. A new product molecule forms when two or more reactant molecules collide. However, collision does not always end with a new product. To ensure that the reaction is feasible, the molecules must have E_a exceeding or equal to the reaction energy barrier [179]. The E_a of reaction determines the reaction rate changes with temperature or time. The E_a, as well as reaction temperature, affects the reaction rate by changing the reaction constant (k). The functional form of the mathematical relationship between the reaction k, E_a and absolute temperature ($\bar{T}$) was proposed by Arrhenius in 1889 [176]:

$$k = A\ e^{\frac{-E_a}{RT}} \tag{4.5}$$

Both A and E_a are independent of temperature. Where R is the universal gas constant. By combining Eq. 4.4 and Eq. 4.5, the following equation is obtained:

$$-[B]_o{}^{1-n}\frac{dx}{dt} = \left[A\ e^{\frac{-E_a}{RT}}\right][1-x]^n \tag{4.6}$$

Which simplifies to Eq. 4.6 can be written as follows:

$$\frac{dx}{dt} = \left[A\ e^{\frac{-E_a}{RT}}\right] f(x) \tag{4.7}$$

4.4 Analysis of reaction kinetics

In order to perform an optimised chemical and mechanical design of the gasification process, acquisition and evaluation of thermal degradation and kinetics data are needed. Data obtained from dynamic experiments should be processed through the analysis process to estimate kinetic parameters such as effective E_a and A [180]. The most common experimental techniques are TGA and DTG. The data from these experiments can be analysed using a model-free method, namely: Ozawa–Flynn–Wall (OFW) [181], Kissinger-Akahira-Sunose (KAS) [182], Tang (TA) [183], Starink (ST) [184], and a model-fitting method, Coats-Redfern (CR) [185].

The data obtained from TGA is defined as the change of fractional conversion to temperature or time. The rate of reaction is indicated as the result of the contribution of reactant concentration and the process temperature which increases the reaction constant [186]. However, to estimate the kinetic parameters either reactant concentration or temperature should be assumed as a constant. In this experimental study, the process was assumed to be non-isothermal for TGA in which the reactant conversion rate was measured as a function of temperature according to Eq. 4.7. The sample mass loss is used to calculate the conversion based on the following formula:

$$x = \frac{m_o - m_t}{m_o - m_f} \tag{4.8}$$

Where $m_o, m_{t,}$ and m_f are the sample mass at the reaction initial stage, at any point of reaction, and the end of the reaction, respectively. The TGA is set to work at a constant heating rate (β) which can be introduced to Eq. 4.9 for non-isothermal conditions:

$$\beta = \frac{dT}{dt} \tag{4.9}$$

Then,

$$-[B]_o{}^{1-n}\frac{dx}{dT} = \frac{A}{\beta}\, e^{\frac{-E_a}{RT}}\,[1-x]^n \tag{4.10}$$

Integration of Eq. 4.10 from an initial to final value of temperature ($T_i \; and \; T_f$) and conversion ($x_i \; and \; x_f$) allows the E_a in the equation to be estimated as described below:

$$-[B]_o{}^{1-n}\int_{x_i}^{x_f}\frac{dX}{[1-x]^n} = \frac{A}{\beta}\int_{T_i}^{T_f} e^{\frac{-E_a}{RT}}\,dT \tag{4.11}$$

Eq. 4.11 can be solved using one of kinetics evaluation methods which are described in detail in Section 4.4.1.1. This thesis used model-free and fitting methods to evaluate kinetic reactions at different conditions.

4.4.1 Model-free methods

4.4.1.1 Ozawa–Flynn–Wall (OFW) method

One of the most popular thermal degradation analysis and kinetic methods is known as Ozawa–Flynn–Wall (OFW) [187]. It is an isoconversional integral method that includes measuring the temperature at given values of conversion and various heating rates. In this method, Eq. 4.11 is integrated utilising Doyle's approximation to determine the E_a. The empirical equation developed by Doyle is illustrated below:

$$P(x) = 7.03 \times 10^{-3} e^{-x\,B(x)} \tag{4.12}$$

Where $B(x)$ is ranged between -1.195 and -1.034 based on the conversion value, therefore, -1.052 is considered as an average value and rearranged as below:

$$g(x) = \frac{A\,E_a}{R\,\beta} 7.03 \times 10^{-3} e^{-1.052x} \tag{4.13}$$

By taking natural logarithms for Eq. 4.12 and 4.13 sides:

$$ln(\beta) = \ln\left(\frac{A\,E_a}{R}\right) - \ln g(x) - 4.9575 - 1.052\frac{E_a}{RT} \tag{4.14}$$

$$ln(\beta) = C - 1.052\frac{E_a}{RT} \tag{4.15}$$

Where C is the integration constant that can be determined from the y-intercept. This constant comprises the following terms:

$$C = ln\left(\frac{A\,E_a}{R\,g(x)}\right) - 4.9575 \tag{4.16}$$

Where $g(X)$ is the integral reaction model for fixed values of conversion. By plotting ln(β) versus $\frac{1}{T}$ in Eq. 4.15, the E_a of reaction can be estimated for specified values of conversion. The estimation of A is dependent of the Doyle approximation adopted in the E_a calculations [188]. The following relationship can be used to determine A for the first order reactions and for known value of E_a:

$$A = \frac{-\beta R}{E_a} (ln[1-x]) \ 10^a \tag{4.17}$$

Where *a* is a numerical integration constant based on the Doyle approximation, as listed in Table A-1 in the Appendix A.

4.4.1.2 Kissinger-Akahira-Sunose (KAS)

Kissinger (1956) proposed a mathematical procedure, which was later developed to the Kissinger-Akahira-Sunose (KAS) method, to determine the E_a in various non-isothermal chemical processes at various heating rates and given values of a conversion. The KAS method is well-known as one of the best isoconversional, linear, and integral methods used without any knowledge concerning the kinetic information [189]. Among all kinetic evaluation methods, KAS applies the Murray and White approximation of *P(x)* which supports the results accuracy as shown below:

$$p(x) \cong \frac{e^{-x}}{x} \tag{4.18}$$

The KAS method considers in the derivation the T_m at the maximum reaction rate value to oversimplify temperature approximation. Eq. 4.10 is rearranged to define the integral kinetic function $g(x)$ for the initial condition of $X=0$ and $T=T_o$:

$$\int_0^{X_f} \frac{dX}{f(x)} = g(x) = \frac{A}{\beta} \int_{T_o}^{T_f} e^{\frac{-E_a}{RT_m}} dT \cong \frac{-E_a A}{\beta R} p\left(\frac{-E_a}{RT_m}\right) \tag{4.19}$$

This procedure presumes that A and E_a are independent of T and X, therefore, Eq. 4.19 can be integrated as follows:

$$\ln g(x) = \ln\left(\frac{E_a A}{R}\right) - \ln \beta + \ln p\left(\frac{-E_a}{RT_m}\right) \tag{4.20}$$

According to the Murray and White approximation in Eq. 4.18, the equation above becomes:

$$p\left(\frac{E_a}{RT_m}\right) \cong \frac{e^{\frac{-E_a}{RT_m}}}{\frac{-E_a}{RT_m}} \tag{4.21}$$

From Eq. 4.19 and 4.21, a final form is given:

$$\ln\frac{\beta}{T_m^2} = \ln\left(\frac{R\,A}{g(x)E_a}\right) - \frac{E_a}{R}\cdot\frac{1}{T} \tag{4.22}$$

For a progressive value of conversion degree, the term $\ln\frac{\beta}{T_m^2}$ is plotted against $\frac{1}{T}$ to give a straight line slope of $\frac{E_a}{R}$, hence the apparent E_a can be determined. Once the value of E_a is obtained, the A at each heating rate can be estimated as follows:

$$A\,(\beta) = \frac{\beta\,E}{R\,T_m^2}\,e^{-\frac{E_a}{R\,T_m}} \tag{4.23}$$

Where T_m is the highest value in the curve of $\frac{dx}{dT}$ vs T which is known also as a maximum peak temperature.

4.4.1.3 Tang (TA) method

A highly accurate approximate formula for estimating the kinetic parameters of non-isothermal processes has been developed by the Tang method [183]. This approach has been approved as having higher accuracy and reliability than other methods [190].

$$\ln\left(\frac{\beta}{T^{1.894661}}\right) = Const. - 1.00145033\,\frac{E_a}{R\,T} \tag{4.24}$$

$Const.$ includes the following terms:

$$Const. = 3.63504095 - 1.89466100\,\ln E + \ln\left(\frac{E_a\,A}{R\,g(x)}\right) \tag{4.25}$$

By plotting $\ln\left(\frac{\beta}{T^{1.894661}}\right)$ versus $\frac{1}{T}$ in Eq. 4.24, the E_a of reaction can be estimated for given values of conversion. Then, Eq. 4.23 can be used to determine the *A* value.

4.4.1.4 Starink (ST) method

Linear integral methods like KAS and OFW employ temperature integral approximations such as the Doyle approximation and the Murray and White approximation. These approximations showed a significant inaccuracy in the estimation of E_a for a wide range of temperatures. Starink developed a highly precise representation of the temperature integral using a linear isoconversional method and summarised the source of errors such as approximation of temperature integral, measuring temperature, and non-constant β in KAS and OFW methods. The expression of KAS and OFW methods can be considered into a general form of a linear equation [184]:

$$ln(\frac{\beta}{T^r}) = C - D\frac{E_a}{RT} \quad (4.26)$$

Where r=2, D=1 for the KAS method, and r=0, D=0.4567 for the OFW method. After a further deep study of the discrepancy of findings [191], Starink found that the parameters can be adjusted to be r=1.92, D=1.0008 which gives higher accuracy over the other methods, as described:

$$ln(\frac{\beta}{T^{1.92}}) = C - 1.0008\frac{E_a}{RT} \quad (4.27)$$

The E_a can be determined by fitting a straight line of $\ln(\beta/T^{1.92})$ versus *1/T* plot. The *A* value is estimated for a fixed value of conversion using Eq. 4.23.

4.4.2 Model-fitting method

4.4.2.1 Coats-Redfern (CR) method

The Coats-Redfern (CR) method is an integral model-fitting method, which involves the expansion of the asymptotic series that approaches the integral of temperature for Eq. 4.11. The knowledge of reaction mechanism (overall reaction order) is essential in the determination of E_a. This approach is developed by modifying the conventional form of CR in Eq. 4.25 [192] to be effective for single or multiple heating rates:

$$ln\left(\frac{ln(1-x)}{T^2}\right) = ln\left[\frac{R\,A}{\beta\,E_a}\left(1-\frac{2\,R\,\bar{T}}{E_a}\right)\right] - \frac{E_a}{R\,T} \quad (4.28)$$

Where $\bar{T}$ is the mean experimental temperature. In the conventional equation, CR assumed that the reaction is first order (i.e. $g(x) = \ln(1-x)$). Later, the equation was generalised to be compatible with different reaction mechanisms. It was also assumed that the term $\frac{2\,R\,\bar{T}}{E_a} \ll 1$ to simplify the equation, hence the general form of the method becomes:

$$ln\left(\frac{G(x)}{T^2}\right) = ln\left[\frac{R\,A}{\beta\,E_a}\right] - \frac{E_a}{R\,T} \quad (4.29)$$

The E_a from the equation above can be achieved by plotting the term $ln\left(\frac{G(x)}{T^2}\right)$ against $\frac{1}{T}$. The thermal decomposition mechanism function $G(x)$ can be approximated from 19 rate law models, as a listed in Table 4-1 (where $x = \alpha$). The accuracy of this method largely depends on the selection of the mechanism function. However, if the E_a is known, the reaction kinetics can be obtained. The y-

intercept of the E_a curve gives the value of term $ln\left[\frac{R\,A}{\beta\,E_a}\right]$ which can be rearranged to obtain the A value as follows:

$$A = \frac{\beta\,E_a}{R}\,e^{y-intercept} \tag{4.30}$$

Table 4-1 Types of kinetic mechanism models in the literature, (LN: 5235900730034) [193].

Symbol	Reaction mechanism	f(x)	G(x)
G1	One-dimensional diffusion 1D	$1/2x$	x^2
G2	Two-dimensional diffusion (Valensi)	$[-\ln(1-x)]^{-1}$	$x+(1-x)\ln(1-x)$
G3	Three-dimensional diffusion (Jander)	$1.5(1-x)^{2/3}[1-(1-x)^{1/3}]^{-1}$	$[1-(1-x)^{1/3}]^2$
G4	Three-dimensional diffusion (G-B)	$1.5[1-(1-x)^{1/3}]^{-1}$	$1-2x/3-(1-x)^{2/3}$
G5	Three-dimensional diffusion (A-J)	$1.5(1+x)^{2/3}[(1+x)^{1/3}-1]^{-1}$	$[(1+x)^{1/3}-1]^2$
G6	Nucleation and growth (n=2/3)	$1.5(1-x)[-\ln(1-x)]^{1/3}$	$[-\ln(1-x)]^{2/3}$
G7	Nucleation and growth (n=1/2)	$2(1-x)[-\ln(1-x)]^{1/2}$	$[-\ln(1-x)]^{1/2}$
G8	Nucleation and growth (n=1/3)	$3(1-x)[-\ln(1-x)]^{2/3}$	$[-\ln(1-x)]^{1/3}$
G9	Nucleation and growth (n=1/4)	$4(1-x)[-\ln(1-x)]^{1/3}$	$[-\ln(1-x)]^{1/4}$
G10	Autocatalytic reaction	$x(1-x)$	$\ln[x/(1-x)]$
G11	Mampel power law (n=1/2)	$2x^{1/2}$	$x^{1/2}$
G12	Mampel power law (n=1/3)	$3x^{2/3}$	$x^{1/3}$
G13	Mampel power law (n=1/4)	$4x^{3/4}$	$x^{1/4}$
G14	Chemical reaction (n=3)	$(1-x)^3$	$[(1-x)^{-2}-1]/2$
G15	Chemical reaction (n=2)	$(1-x)^2$	$(1-x)^{-1}-1$
G16	Chemical reaction (n=1)	$1-x$	$-\ln(1-x)$
G17	Chemical reaction (n=0)	1	x
G18	Contraction sphere	$3(1-x)^{2/3}$	$1-(1-x)^{1/3}$
G19	Contraction cylinder	$2(1-x)^{1/2}$	$1-(1-x)^{1/2}$
Note: A-J: Anti- Jander; G-B: Ginstling-Brounshtein			

4.5 Method comparison

The features/advantages and disadvantages/limitations of each method of analysis are included in Table 4-2 as a summary.

Table 4-2 Features and limitations of kinetics evaluation methods.

#	Method	Features/advantages	Disadvantages/limitations
1	Standard Isoconversional	• Simplicity • Easy procedure	• Low accuracy • High variation in E_a
2	Friedman	• No limitations to any temperature range • Valid for multiple-step reactions	• Variation in E_a • Sensitive to the experimental noise • At least two sets of experimental data are needed
3	OFW	• No need for parallel reaction steps • Determination of each reaction point • Most precise E_a	• Suitable only for dynamic tests • Requires positive heating rates • Measuring temperature errors
4	KAS	• No need for parallel reaction steps • Determination of each reaction point • Most precise E_a	• Requires positive heating rates • Suitable only for dynamic tests • Approximation *p(x)* errors
5	TA	• Most precise E_a • Valid for parallel intermediate reactions	• Measuring temperature errors
6	Kissinger	• Free of approximation • E_a is not calculated for progressive conversion values	• Limited to dynamic measurements • Experimental errors require performing a series of runs
7	ST	• Highly precise representation of the temperature integral • Overcome approximation *p(x)* uncertainty	• No uniform model • Requires positive heating rates
8	CR	• Excellent accuracy for knowing the reaction model • If the E_a is known, the reaction mechanism can be obtained • Needs only a single set of experiments	• Need for reaction mechanism knowledge • High variation in parameters if the incorrect model is used

Model-free schemes follow the isoconversional principle which excludes the need for an already available kinetic model or generating a modify model which mitigates occurrence of errors linked to selection of a kinetic model. The conversion (X) consequently is an independent reaction at a given value of temperature. The isoconversional methods consider the dependency of the E_a on the conversion degree [194]. Not all approaches of model-free strategy are isoconversional; For example, the Kissinger method makes an assumption that E_a is independent of conversion [195]. However,

for non-isothermal processes, repeating the experimental procedure at different heating rates is required to eliminate errors.

Model-fitting methods rely on fitting different kinetic models to the data to obtain the most optimised statistical fit model in order to determine E_a and A for non-isothermal and isothermal reactions [196]. Most analysis of TGA and DTG data can be done by model-fitting methods which are able to estimate Arrhenius parameters from a single conversion curve. However, the inability to determine the appropriate model, especially for non-isothermal processes, is one of the drawbacks. Therefore, different reaction mechanisms (G1-G19) are highly recommended to identify E_a and the highest correlation coefficient (R^2).

4.6 Gasification process and operating conditions overview

The gasifier operating conditions depend on the properties of biomass and the design of the experimental rig. Gasifiers can be classified based on the flow direction of the biomass fuel and gasifying agent. Table 4-3 displays a comparison of feedstock and design for different types of gasifiers.

Table 4-3 Comparison of feedstock and design for different types of gasifiers [197].

Parameters	Fixed/moved bed	Fluidised bed	Entrained bed
Feed size	51 mm and below	8 mm and below	0.15 mm and below
Tolerance for fines	Limited	Good	Excellent
Tolerance for coarse	Very good	Good	Poor
Gas exit temperature	450-650 ^{0}C	800-1000 ^{0}C	1260 ^{0}C
Feedstock tolerance	Low-rank coal	Low-rank coal and excellent for biomass	Any coal including caking but unsuitable for biomass
Oxidant requirements	Low	Moderate	High
Reaction zone temperature	1090 ^{0}C	800-1000 ^{0}C	1990 ^{0}C
Steam requirements	High	Moderate	Low
Nature of ash produced	Dry	Dry	Slagging
Cold-gas efficiency	80%	89%	80%
Application	Small capacities	Medium-sized units	Large capacities
Problem areas	Tar production and utilisation of fines	Carbon conversion	Raw-gas cooling

The major challenge face by biomass gasification is achieving a good carbon content and efficient char elimination. To overcome these challenges, gasification reactions must be carried out at high temperatures which can be achieved by using superheated steam and from the energy released from the combustion zone [58]. High gasification temperature is also beneficial in enhancing char reactions to produce CO_2 and H_2O when a favourable gasifying agent is provided. Temperature also promotes the calcination of the catalyst which contributes to tar conversion [122].

Ash is composed of non-combustible minerals which depend on the process temperature. The operating temperature can be decided based on the presence of ash in the final product. A high temperature is required when molten ash is produced. The temperature over a range of 750-900 ºC prevents the fuel contaminants such as glass and metal from being fluidised. The presence of contaminants (metal or glass particles) retards the caloric energy of the fuel. However, running the process under low temperature (>600 ºC) causes tar formation that reduces the gasification efficiency. Moreover, the gasification of lignin, a refractory species of biomass, is unachievable at low temperatures [198].

4.6.1 Gasifying agent

The composition and LHV of the product gases are mainly determined by the selection of the gasifying agent. Gasifying agent which can be used includes steam, pure oxygen, air, CO_2, or a mixture of gases. It determines the selectivity and type of reactions that take place during the gasification [198]. Steam as a gasifying agent is used to obtain high LHV and H_2 content in the product gas. However, using steam leads to the formation of a higher amount of tar compared with other mediums. This adds further cost to the downstream tar capturing unit [72]. Also, steam is an indirect gasifying agent which produces less energy from the exothermic reactions which are needed to maintain the temperature in the gasification zone.

Air and pure oxygen are used as a direct gasifying agent that maintains the temperature in the gasifier as high as required. Air was chosen in this study as a gasifying agent in FBGR due to the availability in the atmosphere and contain good amount of oxygen [138]. However, the flowrate of air should be controlled to avoid shifting the process from gasification to combustion leading to the production of flue gas instead of syngas. Furthermore, most of the heat produced during the gasification process is produced by the exothermic reactions of complete and partial combustion. As a result, if the optimum flowrate of air is used as a gasifying agent, partial combustion occurs due to nitrogen dilution [199].

CO_2 was chosen in this study as a gasifying agent in TGA for two main reasons: (1) CO_2 can generate high volatiles content in a reactive char, and (2) CO_2 is a good substitute for N_2 in product gas as it can be recycled and recovered. The reaction of CO_2 with carbon in biomass is extremely endothermic, therefore, a mixture of CO_2 and oxygen, or CO_2 and steam as a gasification medium are normally used to compensate for the heat need [200].

4.6.2 Residence time

The time taken by biomass to flow and react through a gasifier is known as residence time which directly relates to the final product of the gasification [84]. It composes of two periods: solid residence time and volatile residence time. The solid residence time is defined as the time required for the fuel to leave the hot zone, whereas the period between volatiles generation and exiting the heated zone is called volatile residence time [201].

In the case of unpredictable residence time, the secondary reactions are highly affected by the residency time of fuel conversion in the gasifier. However, this enhances the quality of product gas due to increasing the content of H_2, CO, and minimising CO_2. The residence time of biomass in the gasifier can be controlled by manipulating the gasifying agent flow rate and the load of biomass [137]. The bed fluidisation influences the residence time distribution and the conversion efficiency of the biomass particles. Also, the residence time of biomass distribution in the gasifier increases as the gas velocity and bed height increase. The decreasing residence time increases the heat loss in the devolatilisation zone. However, the mean residence time reduces with the height of gasifier decrease and velocity of gas increase. The mean residence time and residence time distribution characterise the degree of mixing in a non-catalytic fluidised bed reactor [137].

4.6.3 Gasification pressure

Reactor pressure during the gasification process plays an important role as the reactions are lying in gas phase equilibrium. It promotes the secondary cracking reactions, thus better product gas quality. Commercial gasifiers can be operated at the atmospheric pressure or higher to obtain the desired products. For instance, by increasing the pressure to less than 2 MPa, insignificant changes in the gas composition quality as reported by Efika [100]. As the pressure increases, the amount of CH_4 and H_2 increases, while CO content decreases. Table 4-4 displays the gas composition at different operating pressures.

Table 4-4 Gas product composition at different pressures [202].

Operating pressure (MPa)	Composition (dry basis) (mol%)				Calorific value (MJ/m^3)
	CO_2	CO	H_2	CH_4	At operating pressure
0.1	18.97	49.19	31.83	0.01	2.26
2.0	18.91	43.82	36.62	0.65	62.48

Ruiz et al. [203] demonstrated that biomass gasification at high pressures is more effective than those at atmospheric pressure. The high gasifier pressure improves the efficiency of char reduction in the producer gas, hence enhancing the calorific value of product gas. However, running the gasifier at high pressures (>1 bar) demands modifications in the mechanical design of the gasifier reactor that increases the capital cost. It also has an impact on the syngas cleaning unit which may need optimisation for a stable process [202].

4.6.4 Reactor temperature

The rate of chemical reactions during the gasification process increases with temperature increase. Also, the thermodynamic equilibrium varies depending on the reaction energetics. The impact of temperature on the reaction rate depends on the E_a of that reaction. Therefore, the increase in temperature may increase the producer gas and tar conversion efficiency [138]. The high temperature in the gasification zone promotes secondary reactions such as cracking and reforming reactions of hydrocarbons. Efika [100] found that H_2, CO concentrations increased and CO_2, CH_4 contents

decreased when gasification temperature raised from 700 to 800 ºC [100]. Wilson et al. [204], investigated the effect of temperature on coffee husk gasification using a batch reactor and found that the increase in temperature reduces the amount of char, while CO content linearly increases with temperature.

4.7 Experiments rig setup

4.7.1 Fluidisation regime

The minimum fluidisation velocity (U_{mf}) is a critical factor in the design of fluidised bed gasifiers. The value of U_{mf} can be estimated based on the drag coefficient and turbulence intensity of the flow. The importance of U_{mf} lies in determining when the fluidisation starts. The fluidisation velocity can be estimated for a bed reactor by two methods: numerical and experimental approaches [205]. Pressure measurements are one of the experimental methods to evaluate the fluidisation velocity. The experimental approach of velocity estimation depends on system design, physical properties of fuel, and bed materials. It has been proved that determining the minimum fluidisation by the pressure drop across the bed is one of the common methods based on bed porosity, fluid and bed properties [48-49].

The pressure drop across the bed correlates to gas velocity through two regimes; fixed bed and fluidised bed, as shown in Figure 4-2. At low velocity, the gas flows through the pores of the static bed creating a pressure drop across the column. As the velocity increases, the bed begins to fluidise and the pressure drop linearly increases. The increase in the gas velocity leads to buoyancy forces and drag forces generated by the gas to overcome the weight of particles. Once the bed is completely fluidised, the fixed bed regime ends and the maximum pressure drop is reached. In the fluidised bed region, the pressure drop equals the gravity force, therefore no change is expected as the velocity increases.

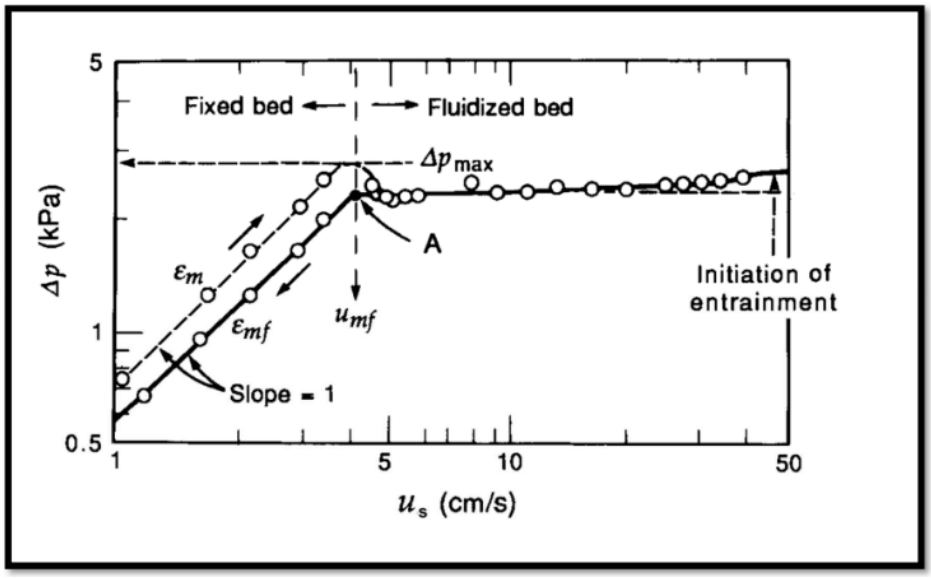

Figure 4-2 The relationship between the pressure drop and gas velocity for particles bed [206]

When the maximum pressure drop is reached, the bed is fully fluidised due to high drag forces applied on the particles against the frictional force. At the maximum pressure drop, the gas velocity is known as U_{mf} which is the minimum velocity to fluidise the bed. It also represents the transition point that occurs between the zone of fluidised bed and fixed bed [206]. The maximum pressure drop can be estimated from the bed weight (*W*) and the bed cross-sectional area (*A*) [138]:

$$\Delta P = \frac{W}{A} \tag{4.31}$$

The U_{mf} experimental setup, the operating parameters of the column and diffuser design, are reported in the thesis of Al-Farraji [138]. In the present work, silica sand of known mass (400 g) and particle size of 500-600 μm was placed on the diffuser plate at the bottom of the fluidised bed reactor as bed material.

The U_{mf}, which is commonly determined during reduction of the velocity of the air, has been estimated to be 0.064 m/s at H_s=D and H_s=0.5D at 300 °C [138]. Al-Farraji [138] reported that the value of U_{mf} is not impacted by the height of static bed (H_s), but it does affect the pressure drop. Also, one of the objectives in Al-Farraji [138] is to maintain the superficial velocity lower than the terminal velocity to ensure that there is no elutriation loss for the particles of the bed. The terminal velocity of gas was estimated using the equations below [207]:

$$d_p^* = d_p \left[\rho_g \left(\rho_s - \rho_g\right) g \, \mu\right]^{\frac{1}{3}} \tag{4.32}$$

$$u^* = \left[18 \, {d_p^*}^2 + 0.591 \, {d_p^*}^{0.5}\right] - 1 \tag{4.33}$$

$$u_t = u^* \left[\frac{\mu\left(\rho_s - \rho_g\right)g}{\rho_g^2}\right]^{\frac{1}{3}} \quad (4.34)$$

Where d_p is the mean particle size of sand, $dp*$ and $u*$ are dimensionless particle size and a dimensionless gas velocity, μ is the viscosity of air 0.00018 (g/cm^3), ρ_s is the density of solid particles 2.650 (g/cm^3), ρ_g is the density of air 0.001225 $(g/cm.s)$, g is gravity 9.8 (m/s^2), and u_t is the calculated terminal 0.89 (m/s) [138].

4.7.2 Equivalence ratio

The ratio of air-to-fuel mass flow rate, commonly known as the equivalence ratio (ER), is a critical parameter in the process of combustion. It determines the combustion performance as well as gas product composition. It can be mathematically expressed as a ratio of measured ratio to the theoretical ratio of air to fuel.

$$ER = \frac{(\text{air/biomass})_a}{(\text{air/biomass})_s} \quad (4.35)$$

Where *a* is the actual air biomass ratio and *s* is the stoichiometric ratio. The stoichiometric air flow rate is normally evaluated based on the combustion reactions of C, H_2, and S. However, N_2 is usually excluded from the calculations as the temperature is not sufficiently high to oxidise N_2 to NO_x. At low ER values (complete combustion), the heat produced from the combustion zone, as well as temperature, is also low due to low production of H_2 [208]. The ratio of air mass required to complete combustion to fuel mass is called the air-fuel ratio (AFR). Table 4-5 illustrates the amount of oxygen in the air required to achieve Subcoal™ combustion. The actual air-to-fuel ratio, AFR_a, can be calculated from stoichiometric AFR_s as follows [138]:

$$AFR_a = ER \times AFR_s \quad (4.36)$$

As the AFR_a is determined, the actual mass flow rate of fuel, $\dot{m}_f$, is given below:

$$\dot{m}_f = \frac{\dot{m}_{air}}{AFR_a} \quad (4.37)$$

The air mass flow rate, $\dot{m}_{air}$, can be estimated from the volumetric flow rate, $\dot{V}_{air}$, and density of air, ρ_{air}, using the following equation:

$$\dot{m}_{air} = \dot{V}_{air} \times \rho_{air} \quad (4.38)$$

The ambient temperature for the air has a density, which is 1.225 kg/m^3. The fraction weights utilised for O_2 and N_2 in estimations are 0.232 and 0.754. Table 4-5 and Table 4-6 shows the actual rate of air-mass flow and ratio of air-fuel required for different values of ER.

Table 4-5 Air-fuel ratio stoichiometry for gasification of Subcoal™.

Combustion equation	Fuel composition			Stoichiometric O_2 (g)
	Element	(wt.%)	Mass (g)	
$C + O_2 = CO_2$	C	45.72	0.4572	1.2192
$H_2 + 0.5O_2 = H_2O$	H_2	6.41	0.0641	0.5128
	O_2	35.26	0.3526	-0.3526
	N_2		0.0000	
$S + O_2 = SO_2$	S	0.2	0.0020	0.0040
Total		87.59	0.8759	
Total O_2 required				1.3834
Total air required				6.6191
Air-fuel ratio (by mass) [AFR]s = (total air required / total of mass)				7.5570

Table 4-6 The actual ratio of air-fuel for Subcoal™ gasification in various ER.

An air-fuel ratio under air atmosphere					
ER	0.15	0.2	0.25	0.3	0.35
(AFR) actual	1.134	1.511	1.889	2.267	2.645
(kg biomass/hr) with moisture $\dot{m}_f$	2.594	1.945	1.556	1.297	1.112

It has been reported that at an ER range of 0.15–0.4, high efficiency of syngas production is achieved, at which point the amount of air is perfect for partial oxidation rather than complete combustion [209]. An increase in ER leads to an increase in the heating value of the gas product stream. Nevertheless, to some extent, the increase in ER may reduce the heating value of the gas stream because of oxidation of CO and H to CO_2 and H_2O, respectively. The partial oxidation of char may lead to an increase of CO and H. Species like CH_4, C_2H_2, and C_2H_4 are independent of ER [210].

4.7.3 Feedstock system

The feeding system was modified by replacing the previous stainless steel hopper and internal feeding channel, which was designed to feed only small particle sizes of biomass at the bottom of the reactor with new channel. The new channel was designed to feed pellets and small particles from the top, with a pipe height (H) of 500 mm and an internal diameter (ID) of 58 mm, and was placed 18 mm above reactor freeboard at a 30° angle. Subcoal™ pellets were fed into the gasifier reactor using a vibrating feeder (Fritch, UK). The feeder was placed at the top of the gasifier and a stainless steel reactor channel located 10 mm below the vibration channel. The pellets flow rate depends on the frequency of the channel vibration which is controlled by the oscillation amplitude of the

electrical control system. The pellets flow down in counter-current with air flow through stainless steel pipe to the reactor tube. Then the pellets continuously fluidise at the bottom of the reactor until the complete gasification reaction is achieved. Nevertheless, the feeding system faces fewer challenges as it is contact-free with the hot bed material. The optimisation of the feeding rate of fuel is an essential parameter in gasification performance.

4.7.4 Fluidised bed reactor

The fluidised bed reactor is constructed of a stainless steel cylinder with an 83 mm internal diameter and 1250 mm height, giving a volume of 316 litres. The space, at the top of the column, between the exit gas and bed material surface, is defined as freeboard. The freeboard height should be greater than the height of the Transport Disengaging Height (TDH) to avoid the loss of fluidised bed [138].

4.7.5 Plenum

Below the diffuser plate, there is an air box known as plenum. The purpose of using a plenum is to evenly distribute the air and keep a fixed air flow rate at each hole in the diffuser plate. The air can be preheated before entering the reactor, and the plenum is made of a stainless steel alloy. The plenum design and dimension is described by Al-Farraji [138].

4.7.6 Diffuser plate

The diffuser plate is a stainless steel plate consisting of 151 drilled holes in the form of a triangular pitch. The plate holes have a uniform diameter of 1 mm and a plate thickness of 5 mm. There are two benefits of using the diffuser plate: to distribute the gas flow evenly over the whole bed, and to support the bed material.

4.7.7 Air supply system

The air supply system provides air at a pressure of 7 bar which can be regulated using a ball valve located upstream of rotameters. An air pressure regulator was used to prevent rotameter damage caused by high air supply pressure and to control air flow rate within the required limits. The air flow rate is manipulated and measured using three Platon flowmeters. The flowmeters had different capacities: 150 L/min, 50 L/min, and 12 L/min with an accuracy of ±1.25% of readings. A flexible stainless steel hose is used to deliver the air from the flowmeters to the plenum section of the gasifier. The pressure drop across the gasifier is assumed to be small, so the rotameters did not need to be re-calibrated to compensate for the slightly denser air.

4.7.8 Heating system

A horizontal preheater (LTF, model:12/100/940) is used to preheat the air/N_2 stream to maintain the stream temperature constant before entering the plenum section of the gasifier for isothermal measurements. A vertical split furnace (model: PSC 12/100/900) is employed to provide the gasifier with the required heat to achieve uniform temperature over an extended section. It has been split into three sections providing a set temperature of around 1200 ℃. A split tube is employed for equal distribution of heat around the furnace that averts the experimental errors. Temperature variation within the uniform zone is typically ± 5 °C, according to the Lenton manual. To confirm the accuracy with the furnace temperature controller set point, two calibrated thermocouples were used to monitor the temperature at the bottom and top of the gasifier. The split furnace and preheater have the same rated power output of 4.5 KW.

4.7.9 Measurements of pressure and temperature

K-type thermocouples are used to measure the temperatures over the experimental time. The thermocouples are placed in two sections: one in the bed section and the second in the freeboard space. A data acquisition system (Omega, UK) is used to convert the thermocouple analogue signal to digital to be stored in a computer as a spreadsheet. DAQ software was used to record and transfer the data to the Multiple Channel Data Acquisition Module (OM-DAQ-USB-2401), Then, collected data was exported to Microsoft excel® for calculation. The pressure drop in the FBGR indicate the bed conditions and performance at certain air flow rate. The pressure transducer in the plenum is linked to an external digital pressure meter (model: Digitron PM-20) through a plastic hose. In both cold and hot experiments test runs, the pressure drop between the transducer and the orifice at air flow rate 40 l/min was very small and considered negligible. The main specifications of the Digitron PM-20 are shown in Table 4-7.

Table 4-7 illustrates Digitron PM-20 main specifications.

Features	Specifications
Pressure measurement	0-130 mbar
Accuracy	±0.2% of reading ±0.2% of full scale ±1 digit
Resolution	0.01 range of resolution to 19.99 mbar and auto ranges between 0.1 and 130 mbar
Operating Temperature	–10°C to 50°C/+14°F to 122°F (Ambient)
Calbration	PM 20 gauge comes complete with traceable calibration certificate
Design	Twin 8mm tube connection
Display	12.7mm/0.5” custom LCD
Environmental	Water Resistant

The real-time dynamic mass measurements also indicate the status of the bed; a sharp increase of mass predicts that the bed particles get agglomerated due to mass accumulation in the furnace. This, therefore, leads to a reduction in the particle fluidisation. The bed agglomeration results in the air flowing in channels instead of fluidising the bed, which reduces the mass and heat transfer to/from the fuel particles, hence lower gasification efficiency.

4.7.10 Condenser

A shell and tube condenser made of stainless steel is connected to the gas outlet of the gasifier by a flexible hose. The condenser is a crossflow type and uses water as a coolant agent. The purpose of the condenser is to condense tar and other impurity contents associated with syngas into liquids before entering the tar capturing unit. After each run, the condensate should be drained and collected in a glass bottle. Figure 4-3 shows the chiller unit for the condenser cooling water system.

Figure 4-3 Chiller unit

4.7.11 Gas cleaning system

Besides the tar condenser, the gas cleaning system comprised four isopropanol (99.8 vol%) Drescher bottles that connect in series and known as tar capturing unit. These bottles were placed inside a freezer at a temperature of -10 ºC. The product gas was passed successively through the isopropanol bottles before being treated in two silica gel bottles. The purpose of silica gel is to absorb moisture (water) from the gas stream. A fibre filter is placed after the silica gel bottles to remove any contaminants from gas. The treated gas was pumped to a gas analyser using a membrane pump that compensated the pressure drop that may occur during the process. Figure 4-4 illustrates a schematic of a gas cleaning system.

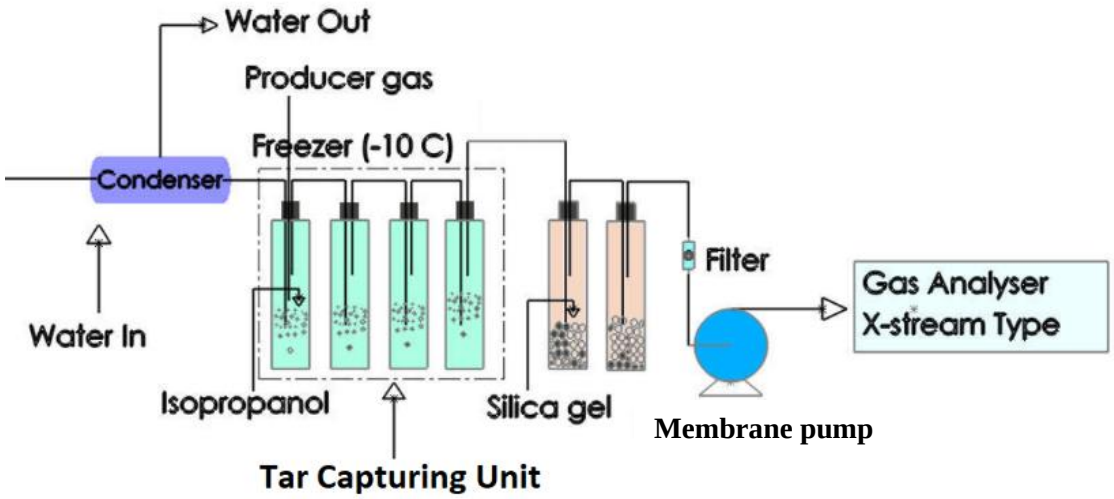

Figure 4-4 Schematic of the downstream tar capturing unit

4.7.12 Gas analyser

Following the product gas being treated by the gas cleaning system, it was introduced for analysis using an Emersion X-Stream gas analyser (Model: XEA04303555317) as shown in Figure 4-5. A lab-scale rotameter is used to control the gas flow rate and keep it below 1 l/min. This analyser detected and measured up to five different gases (CO_2, CH_4, H_2, O_2, and CO) as a function of time, and relies on mechanisms for analysis that include:

- Non-dispersive infrared analysis (IR) for CO, CO_2 and CH_4 measurements
- Electrochemical and paramagnetic oxygen analysis (eO_2 and pO_2)
- Paramagnetic oxygen and Electrochemical analysis (pO_2 and eO_2)
- Analysis using thermal conductivity H_2

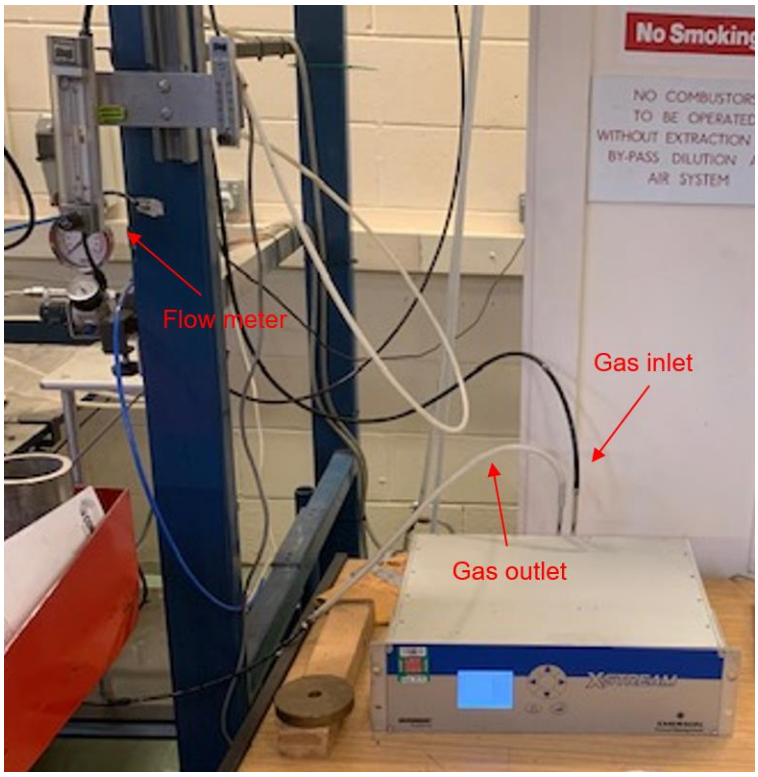

Figure 4-5 Image of Emersion X-Stream gas analyser (Model: XEA04303555317)

Gas analyser for the presence of any impurities has high sensitivity. As such, all channels for gas calibrated to zero on N_2. Further, air needs to be supplied by the span of the gas mixture. The calibration of gas analyser has a standard mixture of gas, which is composed of CH_4, CO_2, H_2 and CO where the concentration on volume basis is 5%, 15%, 15%, and 15% respectively. The balance of this is N_2. The analyser is associated with outlet and inlet streams for producer gas. The stream of the outlet gas is connected to the extraction system. Thus, the provided data depicted percentage volume (vol%) of each gas composition as a function of time (seconds).

4.8 Gasification effectiveness

The higher heating value (HHV) of dry gas, carbon conversion efficiency (η_c) and cold gas efficiency (η) were utilised in the examination of the process of biomass gasification effectiveness. The HHV of dry gas is determined based on the composition of gas as given below [138]:

$$HHV = \frac{12.63[CO] + 12.75[H2] + 39.82[CH4] + \cdots}{100} \tag{4.39}$$

The concentration of syngas is in mol% and the HHV is in MJ/Nm^3. The content of higher hydrocarbons (C>2) is low in the product gas, therefore, it can be neglected in the calculations. The material balance of nitrogen in the air was considered to estimate the yield of dry gas (Y) as follows [138]:

$$Y = \frac{Q_a \times 79\%}{\dot{m}_f \, N_2\%} \tag{4.40}$$

Where Q_a is the volumetric air flow rate, $\dot{m}_f$ is the mass flow rate of solid fuel, and $N_2\%$ is the volumetric percentage of N_2 in solid fuel (0.6% in Subcoal™). The carbon conversion efficiency (μ_c) can be estimated based on volume percentages of product gas components [138]:

$$\mu_c = \frac{Y\,(CO\% + CO_2\% + CH_4\%) \times 12}{22.4\,C\%} \times 100\% \tag{4.41}$$

Where *C%* denotes carbon percentage in mass according to biomass ultimate analysis. The cold gas efficiency (η) is a vital index that determines biomass gasification process performance. It is defined as the ratio of the heating value of product gas to the heating value of biomass fuel excluding the heat released from the condensable compounds such as tars, as given in the following expression [138]:

$$\eta = \frac{HHV_g \times Y}{HHV_f} \times 100\% \tag{4.42}$$

Where HHV_f is the higher heating value of biomass fuel, and HHV_g is the higher heating value of the fuel gas.

4.9 Summary

Kinetic reactions of biomass pyrolysis, gasification, and combustion can be understood by performing experimental thermochemical measurements under different operating conditions. Kinetics of chemical reaction determines how the reaction responds to the change in the reactant concentrations, temperature, pressure, and presence of other foreign species such as catalysts and solvents. The experimental data of pyrolysis, CO_2 gasification, and combustion reactions obtained from TGA can be used to estimate the kinetics parameters adopting different methods. The kinetics analysis methods are classified into isothermal and non-isothermal in terms of operating conditions, and into model-free and model-fitting regarding the calculation procedure. The model-fitting method include CR, while, the model-free methods involve OFW, KAS, TA and ST. Model-free schemes follow the isoconversional principle which excludes the need for an already available kinetic model. However, model-fitting methods rely on fitting different kinetic models and mechanisms to the data to obtain the most optimised statistical fit model.

Gasifying agents such as steam, pure oxygen, air, CO_2 or mixture of gases is a vital component in the gasification process by which the composition and LHV of the gaseous product are determined. The three main operating parameters in the gasification process are temperature, pressure, and

flowrate of biomass. The residence time, that changes as a function of flowrate, is an important parameter in the kinetics and conversion of biomass. The particle size of biomass determines the rate-determining step whether it is chemical reaction-controlled or diffusion-controlled. Besides residence time, U_{mf} and pressure drop across the column are important parameters in the design of FBGR. The calculations of U_{mf} and ER made based on the experimental setup are presented. The ER is important factor to determines whether the reaction is complete or incomplete. The FBGR equipment includes feedstock system, reactor, air supply system, heating system, gas analyser, tar capture unit, and condenser. The measurement procedure associated with the gasifier includes evaluation of product gas composition, mass balance, temperature, and pressure.

This chapter presents the theoretical and experimental methods used in the research. The main focus of the work is on the kinetics and performance of thermal degradation (combustion, pyrolysis and gasification) of a unique solid fuel (Subcoal™). As a result, the methods and equipment to achieve the work objectives were described in this chapter. The experimental methods and rigs are well established at Cardiff University with a good track record of substantial experiments. While the kinetics analysis methods are well-known in the literature for such purpose. In summary, the methods and rig systems mentioned in this chapter were used to study the thermal conversion of Subcoal™ and explore the potential to establish such technologies in Qatar to reduce MSW landfill.

Chapter 5: TGA Results and Discussion

5.1 Introduction

In this chapter, a detailed analysis of feedstock properties and TGA results was carried out. From the present chapter, two journal papers have been published in the ChemEngineering journal [211-212]. First, proximate analysis was conducted to measure moisture content, volatile matter, ash, and fixed carbon of Subcoal™. Then, ultimate analysis was used to determine the elemental composition (CHNSO) of Subcoal™ to estimate the mass balance on a gasifier and syngas composition. In addition, carbon and sulphur content in Subcoal™ was determined by a LECO (SC-144DR) analyser. The bulk density of Subcoal™ and silica sand were also measured in the laboratory. The particle size distribution of bed sand and Subcoal™ PAF particles were evaluated using Malvern Mastersizer 3000. The particle size distribution analysis measured the Sauter mean diameter, volume mean diameter, specific surface area, actual density, and the width of the size distribution. As the ash is a critical component in biomass conversion, trace element analysis of residual ash from Subcoal™ PAF combustion was carried out using XRF analyser. Also, XRD analysis of Subcoal™ powder, ash and bed sand were performed to indicate sample crystallinity. TGA thermal degradation results and discussion also have been presented. The effect of heating rate and catalysts loading (0, 5, 10, 15, 20 wt.%) on the thermal decomposition of Subcoal™ PAF in the pyrolysis, CO_2 gasification, combustion has been determined.

5.2 Feedstock characterisation

The characterisation outcomes of Subcoal™ are presented and discussed in this section. The results of the proximate and ultimate analysis are listed in Table 5-1. The results show that the volatile matter forms most of the Subcoal™ mass with 77.6 wt.%. The volatile matter content determines how easily the biomass fuel can be ignited. The higher the volatile matter content the more homogenous ignition and the higher flame stability. Moreover, the higher the volatile matter content the greater the LHV [213]. The fixed carbon content in Subcoal™ was 7.5 wt.% which is the amount of fuel that burns in solid state after the volatiles have been taken off and 11.8 wt.% of ash. The test reveals that the moisture content is as low as 3.1 wt.%. Low moisture content offers two benefits: low energy of combustion is needed, and easier pellets fluidisation in a gasifier [213].

The ultimate analysis indicates that the fuel is composed of 45.7 wt.% carbon, 35.3 wt.% oxygen, and 6.4 wt.% H. These elements are essential for the gasifier design which is involved in the combustion process to produce syngas. The content of oxygen determines the amount of gasifying agent required. The sulphur content is found to be as low as 0.2 wt.% in the fuel. This reduces the amount of hydrogen sulphide (H_2S) and sulphur oxides (SO_x) which contribute to particulate matter pollution and affect the analysis of the calorific value [214]. Finally, the content of nitrogen is 0.6

wt.% which is also beneficial as this correlation to the nitrogen oxides (NOx) emissions. The bulk density of Subcoal™ and silica sand bed are represented in Table 5-2. The method of the bulk density estimation is described in details in Section 3.5.

Table 5-1 Proximate and ultimate analysis of Subcoal™.

Proximate Analysis (wt.%)		Ultimate Analysis (wt.%)	
Moisture content	3.1 ± 0.4	C	45.7 ± 2.7
Ash	11.8 ± 0.5	H	6.4 ± 0.2
Volatile matter content	77.6 ± 1.4	S	0.2 ± 0.06
Fixed carbon	7.5 ± 1.4	N	0.6 ± 0.2
Gross calorific value, (MJ/kg)	23.1 ± 2.8	O (by difference)	35.3 ± 1.9
Density, kg/m^3	450		

Table 5-2 Bulk density of Subcoal™ and silica sand.

Bulk density (g/cm^3)	
Subcoal™	0.43
Silica Sand	1.54

5.3 Particle size distribution analysis

5.3.1 Silica sand

The particle size distribution was obtained for the silica sand (SiO_2) bed using a Malvern Mastersizer 3000 from two different angles to meet the requirement of different particle shapes. The surface area was calculated based on the spherical shape of particles. The analysis findings are presented in Figure 5-1. The key parameters are summarised in Table 5-3.

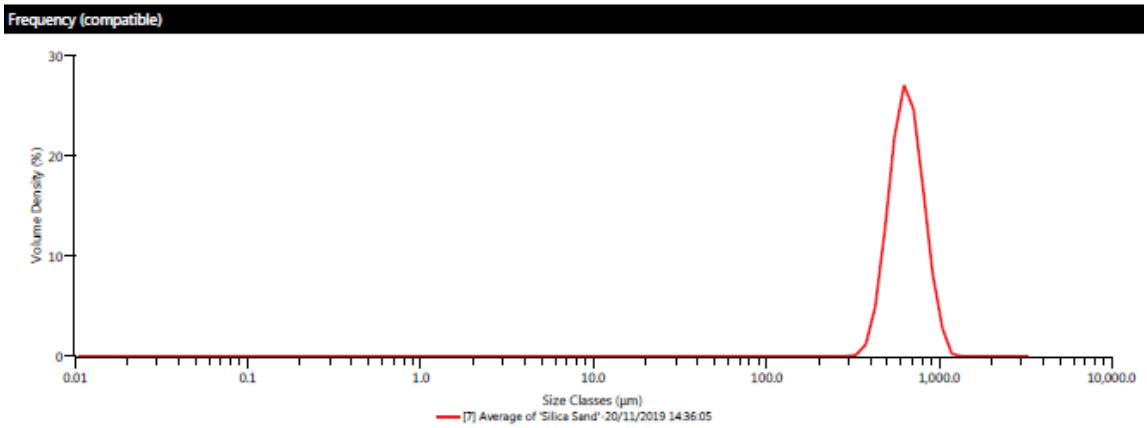

Figure 5-1 Particle size distribution analysis for silica sand

The analysis shows that the Sauter mean diameter D [3,2] and volume mean diameter D [4,3] are 630 µm and 658 µm, respectively. The curves show a consistent, monomodal, normal distribution of the data. The accumulative size analysis indicates that the sizes below which 90% (Dv0.9), 50% (Dv0.5), and 10% (Dv0.1) of particles tested are 850 µm, 643 µm, and 485 µm, respectively. Span is

a parameter that determines the width of the size distribution based on a volume-based size distribution as stated in Eq. 5.1 [168].

$$\text{Span} = \frac{\text{Dv0.9} - \text{Dv0.1}}{\text{Dv0.5}} \tag{5.1}$$

Employing very small size bed particles could affect biomass fluidisation and leads to slug flow which consequently causes fuel blockage in a gasifier. 'The slug flow (slugging regime) forms in bed fluidisation when bubbles grow considerably large that their shapes are determined by the diameter of the reactor. Moreover, the size distribution plays a significant role in the bed agglomeration tendency [215]. However, the increase in bed particle size leads to an increase in the char yield during the gasification of biomass.

Table 5-3 Silica sand particle size distribution key findings.

Particle name	Sand
Silica sand density	2.65
Particle Refractive Index	1.4
Particle Absorption Index	0.01
Dispersant Name	Water
Dispersant Refractive Index	1.33 g/cm^3
Scattering Model	Mie
Analysis Model	General purpose
Weighted Residual	1.02 %
Laser Obscuration	9.1 %
Concentration	0.7721 %
Span	0.567
Uniformity	0.173
Specific Surface Area	3.666 m^2/kg
D [3,2]	630 µm
D [4,3]	658 µm
$D_{v0.1}$	485 µm
$D_{v0.5}$	643 µm
$D_{v0.9}$	850 µm

5.3.2 Subcoal™ particle size

The Malvern Mastersizer 3000 was used to determine the particle size distribution for Subcoal™ particles with a diameter of less than 3 mm, as shown in Figure 5-2. The key parameters from the characterisation are summarised in Table 5-4.

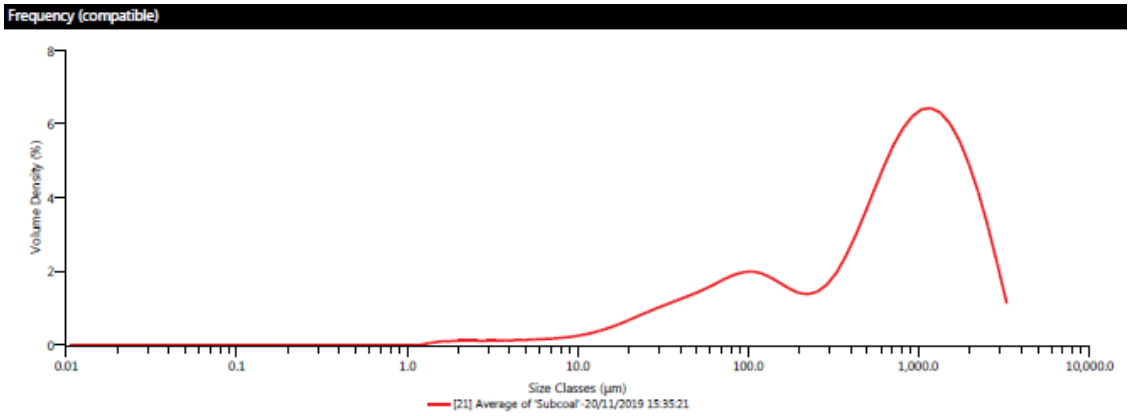

Figure 5-2 Particle size distribution analysis for Subcoal™ powder

Table 5-4 Subcoal™ distribution key findings.

Particle name	Subcoal™
Subcoal™ density	1.09 - 1.14 g/cm^3
Particle Refractive Index	2.4
Particle Absorption Index	0.01
Dispersant Name	Water
Dispersant Refractive Index	1.33
Scattering Model	Mie
Analysis Model	General purpose
Weighted Residual	0.80%
Laser Obscuration	6.72%
Concentration	0.0779%
Span	2.417
Uniformity	0.847
Specific Surface Area	65.45 m^2/kg
D [3,2]	91.7 µm
D [4,3]	890 µm
$D_{v0.1}$	49.7 µm
$D_{v0.5}$	731 µm
$D_{v0.9}$	2030 µm

As can be seen in Figure 5-2, bimodality appear in the analysis of Subcoal™. This is owed to the presence of two types of particles, namely plastics and papers. The volume density of the first and second peaks are 1.36% and 5.37%, respectively. The test demonstrates that the Sauter mean diameter D [3,2] and volume mean diameter D [4,3] are approximately 91.7 µm and 890 µm, respectively. As can be seen in Figure 5-2, the values of D [3,2] and D [4,3] are highly different. This implies that the particles with similar surface area and volume ratios are much smaller than those that contain the majority of the volume. The accumulative size analysis indicates that the sizes below which 90% (Dv0.9), 50% (Dv0.5), and 10% (Dv0.1) of particles tested are 2030 µm, 731 µm, and 49.7 µm, respectively. The particle size of biomass fuel has a pronounced influence on the performance of a gasifier. Luo et al. [216] reported that the carbon conversion efficiency, H_2 production rate, and dry gas yield increase as the biomass particle size decreases. Moreover, the decreasing biomass particle size reduces char and tar content.

5.4 Sulphur and carbon analysis

The LECO analyser was used to determine the Sulphur and carbon content of Subcoal™. The analysis results are presented in Table 5-5 and Figure 5-3. The weight percentage of sulphur obtained from three runs varies from 0.16% to 0.25% which indicates that the sulphur presents in Subcoal™ in different forms. Sulphur profiles similar to that in Figure 5-3 were used to identify the fine differences between the test repeats. The variation in sulphur content occurs due to the low wavelength of sulphur, which is prone to misdetection [214]. The content of sulphur determined by this analysis and ultimate analysis is identical, which is low when compared with other biomass. The content of sulphur in biomass should not exceed 1%. Besides the environmental concerns, these gases can cause equipment corrosion which might be accelerated by a high temperature [217].

Table 5-5 Analysis results of sulphur and carbon content in Subcoal™ by LECO.

Element	Run 1	Run 2	Run 3	Average
Carbon (wt.%)	33.19	22.32	25.61	27.04
Sulphur (wt.%)	0.25	0.16	0.19	0.20

The sulphur may also react with carbon in biomass forming other gases such as carbonyl sulphide (COS) and carbon disulphide (CS_2) [217]. These gases are flammable and release a high amount of heat during combustion with oxygen leading to SO_2 formation. The contents of COS and CS_2 were not considered in the present work. However, the mechanisms of COS and CS_2 formation and combustion elaborate the rapid release of sulphur in the presence of carbonaceous material.

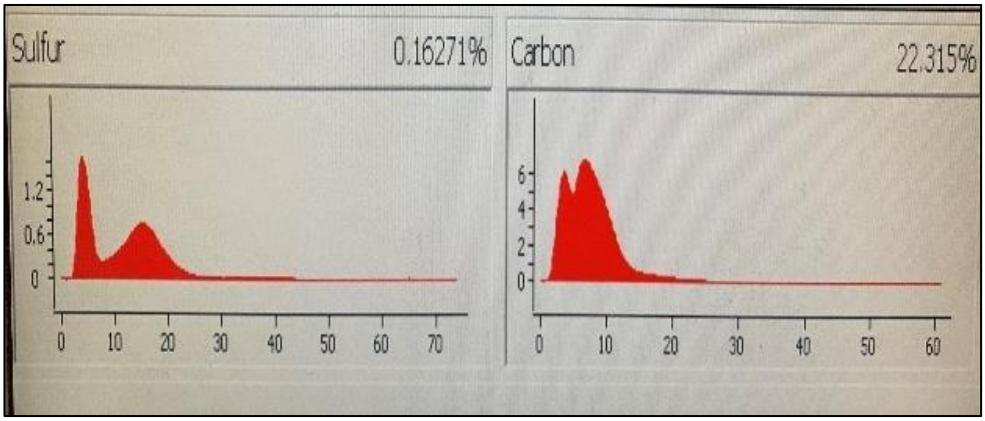

Figure 5-3 LECO Analysis Profile of sulphur and carbon content in Subcoal™

5.5 XRF ash analysis

The trace element analysis of residual ash from Subcoal™ combustion was carried out using the XRF analyser. The results from the ash analysis are shown in Table 5-6. The analysis results show that Fe, Ti, Al, Ca, S, and Cl have recorded the highest content among the mineral and soil elements. Ca and Al contents can reach up to 28% in paper and plastic ashes in the form of calcium oxide and aluminium oxide as the most versatile metals [218]. Ash may contain contaminations that lead to serious environmental issues. Ash from biomass is an alkaline residue of combustion that can reach

up to 20% of the fuel mass. The ash alkalinity reduces the fusion point of ash causing fouling and slagging [219]. The increase in the ash content of Ca, K, and P decreases specific energy production, cold gas efficiency, and low heating value of syngas. Some elements in ash such as sulphur may cause catalyst poisoning and deactivation and hence reduction in the reaction rate.

Table 5-6 Results of trace elements XRF analysis of Subcoal™ ash.

Alloy				
No	**Element**	**Symbol**	**(ppm)**	**Deviation (±)**
1	Chromium	Cr	5.0E-02	1.0E-02
2	Copper	Cu	2.3E-02	1.2E-02
3	Iron	Fe	1.5E+00	4.9E-01
4	Manganese	Mn	4.0E-02	2.0E-02
5	Nickel	Ni	1.1E-02	5.5E-03
6	Titanium	Ti	1.9E+00	6.3E-01
7	Zinc	Zn	4.9E-01	1.9E-01
8	Zirconium	Zr	7.6E-03	5.0E-04
Mining Plus and Soil				
9	Aluminium	Al	4.1E+00	9.9E-01
10	Antimony	Sb	3.6E-10	7.1E-09
11	Barium	Ba	1.2E-09	1.4E+00
12	Calcium	Ca	1.0E+01	1.3E+00
13	Chlorine	Cl	3.8E+00	7.2E-01
14	Lead	Pb	5.1E-07	4.5E-03
15	Molybdenum	Mo	2.0E-08	3.0E-08
16	Phosphorus	P	2.5E-09	1.0E-10
17	Potassium	K	3.5E-05	6.5E-02
18	Silicon	Si	8.9E-08	1.3E+00
19	Silver	Ag	6.0E-07	1.0E-08
20	Strontium	Sr	1.1E-05	4.9E-06
21	Sulphur	S	3.5E+00	1.4E+00
22	Arsenic	As	3.9E-02	3.0E-02
23	Thorium	Th	1.9E-02	4.1E-02
24	Vanadium	V	1.3E-02	2.5E-03
25	Tin	Sn	1.2E-02	1.5E-03
26	Gallium	Ga	9.9E-03	2.6E-03
27	Germanium	Ge	4.0E-03	2.0E-03
28	Tungsten	W	3.2E-07	2.5E-07
29	Rubidium	Rb	9.0E-05	1.5E-05
30	Cobalt	Co	5.0E-05	1.5E-05

Biomass ash comprises of several minerals and elements. Table 5-7 lists the potential mineral content in Subcoal™ ash. The presence of mineral compounds in the ash could be responsible for issues

regarding gasifier design. The minerals and elements in ash may pose an inhibiting or catalytic effect on the gasification reactivity [220]. For instance, each of K, Na, and Mg had a catalytic impact, while Si and P had an inhibiting impact on the gasification reactions [221]. Jing et al. [221] emphasised that increasing contents of Fe, Ca, and sodium oxide (Na_2O) in ash reduce the deformation, flow and softening temperatures of gasification and combustion. This led to minerals formation and transformation.

Table 5-7 XRF analysis of major mineral elements in Subcoal™ as received.

Elements	Al_2O_3	CaO	Fe_2O_3	K_2O	SiO_2
wt%	18.3	38	2.7	0.1	22.7

5.6 XRD analysis

The XRD analysis of Subcoal™ powder sample and ash were carried out to identify the crystallinity and composition of the sample and ash. Also, XRD analysis was performed on silica sand with particle size of 500-600 µm. The analysis of Subcoal™ powder produced a large peak of amorphous compounds at 2θ of 23° with intensity of 240 a.u. composing of barium (Ba) and calcium (Ca), as shown in Figure 5-4.

(a)

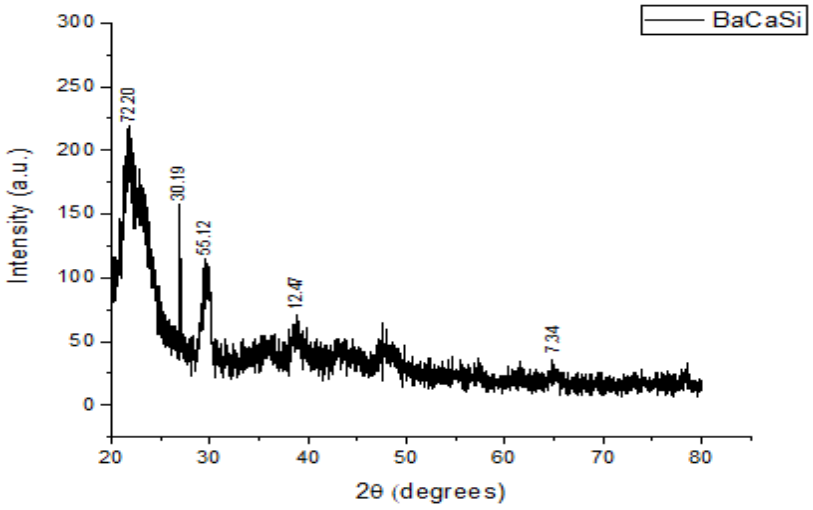

(b)

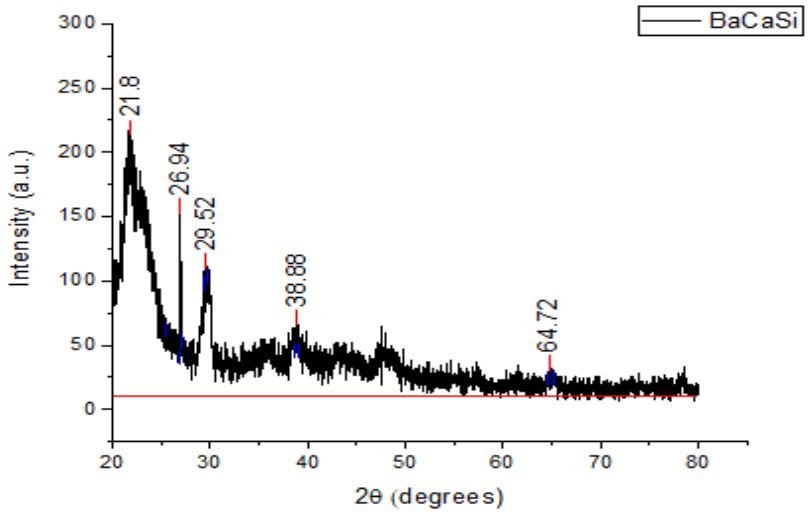

Figure 5-4 XRD analysis of Subcoal™ powder showing peak height (a) and peak area (b). The red line has been added to calculate the area under the curve

Thus, it can be concluded that the amorphous compounds consist mainly of Ba, Ca, and silica (Si). The first amorphous peak compounds consist mainly of Ba, Ca, and Si. The next peak is confirming a crystalline compound at 27° with an intensity of 161 a.u. while the second amorphous peak appears at 30°. Previous research in this area, specifically in relation to the analysis of polymers with XRD, Marsh [222] have found that amorphous peaks are dominant as shown by their defined peaks. However, the amount of crystalline matters in plastic and paper waste exceeds the randomly distributed amorphous ones.

Small crystalline peaks appear at 2θ of 40° and 65° with the intensity of 75.5 and 26.5 au., respectively, that consist of trace elements. It has been found that the crystallinity proportion in Subcoal™ powder based on the total area of all peaks is 42%. The XRD is also a substantial tool for the semi-quantitative evaluation of crystalline phases and mineral components in ash [223]. The content of amorphous materials in the biomass sample or ash determines the decomposition temperature. The higher the glass (amorphous) content the lower the gasification temperature [224]. The non-crystallinity is attributed to the presence of amorphous aluminosilicate [225]. The analysis data is listed in Table A-2 in the Appendix A.

Figure 5-5 shows the semi-quantification of XRD analysis of Subcoal™ ash in terms of peak height and area. The area of a peak is calculated by multiplying the FWHM (full width at half maximum) times the height. The area under the peak provides information on the percentage of crystallinity. The height of the main peaks indicates the intensity of each polymorphic phase.

(a)

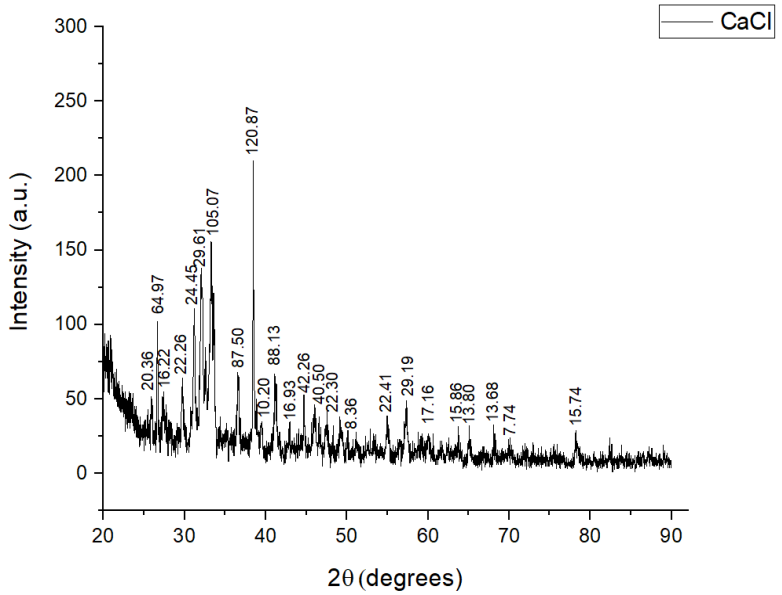

b)

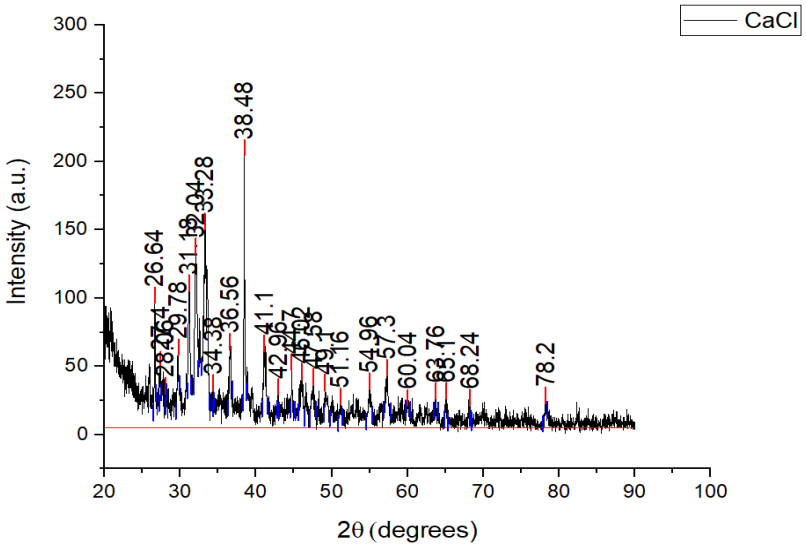

Figure 5-5 XRD analysis of Subcoal™ ash showing peak height (a) and peak area (b)

The largest crystalline peak of calcium chloride CaCl was obtained at 38.5° with an intensity of 245 au. Semi-crystalline peaks were also detected between 30° and 35°. The remaining signals include small crystalline peaks and experimental noise. The crystallinity percentage in ash based on the total area of all peaks was found to be 38%. In comparison with the Subcoal™ sample, the reduction in the crystallinity is attributed to the decomposition of crystalline cellulose fibers [226]. The crystalline minerals and metal oxides in the ash may behave as a catalyst of thermal decomposition reactions [227]. The analysis data is listed in Table A-3 in the Appendix A.

.

(a)

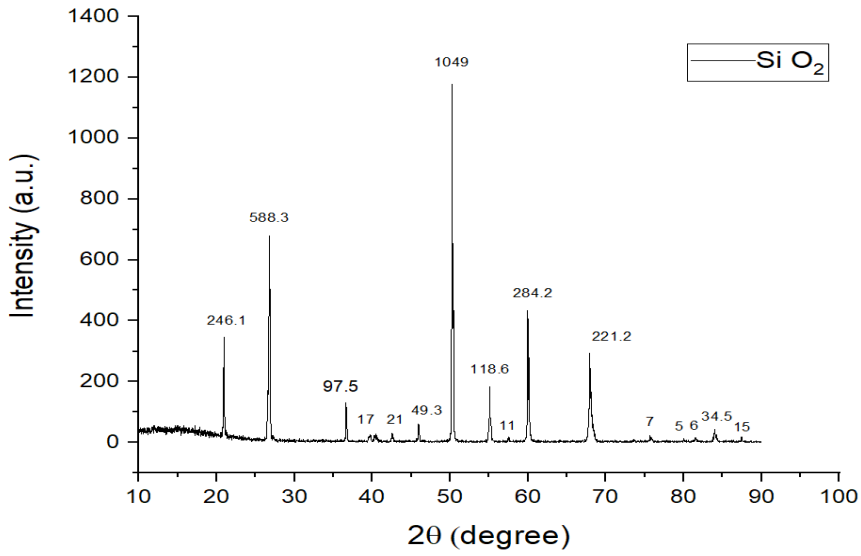

(b)

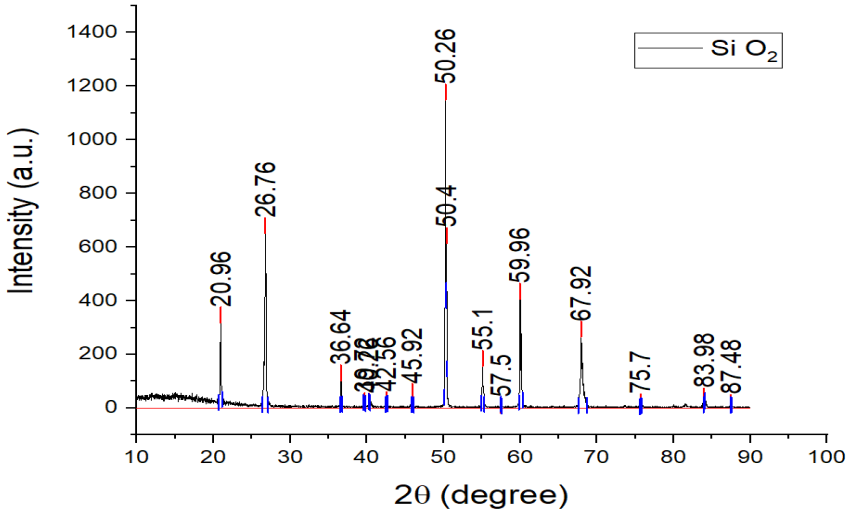

Figure 5-6 XRD analysis of silica sand showing peak height (a) and peak area (b)

Figure 5-6 shows the XRD analysis of silica sand with peak height (a) and area (b). The largest crystalline peak of silicon dioxide (SiO_2) was obtained at 50.3° with intensity of 1049 a.u. Medium crystalline peaks were also obtained at 20.9°, 26.8°, 60.0°, and 67.9° with intensity of 246.1, 588.3, 284.2, and 221.2 a.u., respectively. The remaining peaks are small crystalline peaks and experimental noise. The crystallinity of silica sand was found to be 46%. Silica exists in many different forms that can be crystalline as well as non-crystalline (amorphous). The proportion of crystalline phase (crystallinity) may vary depending on the source of the sample tested. As a result, crystallinity was reported at 32.7% in other studies [228]. The analysis data from XRD is listed in Table A-4 in the Appendix A. The findings show that the number of crystalline peaks phases in ash and silica sand are higher than in Subcoal™ powder. The ash inorganic minerals consist of crystalline and semi-crystalline amorphous phases. The porous black particulates of silicates, as observed by Vassilev et al. [229], is mostly of crystalline characters in ash. Tian et al. [230] observed that the relative intensity of XRD peaks changes with ash formation temperature due to formation of different minerals. The

crystalline peaks can be identified as sharp and narrow, while the amorphous ones have been seen as a broad pattern ‘’hump’’ [224]. The organic and inorganic materials in biomass transform to gaseous and amorphous solids during the gasification at high temperatures. Therefore, ash is commonly defined as a glassy ‘’amorphous’’ residual of combustion [231]. Moreover, the test handling and procedure, based on the spongy property of Subcoal™ powder, allows less accurate investigations by XRD.

5.7 TGA kinetic results and discussion

5.7.1 Effect of heating rate on pyrolysis

The effect of four different heating rates on thermal decomposition of Subcoal™ PAF pyrolysis without catalyst was investigated in TGA, as shown in Figure 5-7. Table 5-8 presents pyrolysis reaction parameters at different decomposition stages. The standard deviation (±) of the three experimental repeats is listed in Table B-1 in the Appendix B: TGA Conversion Repeatability.

(a)

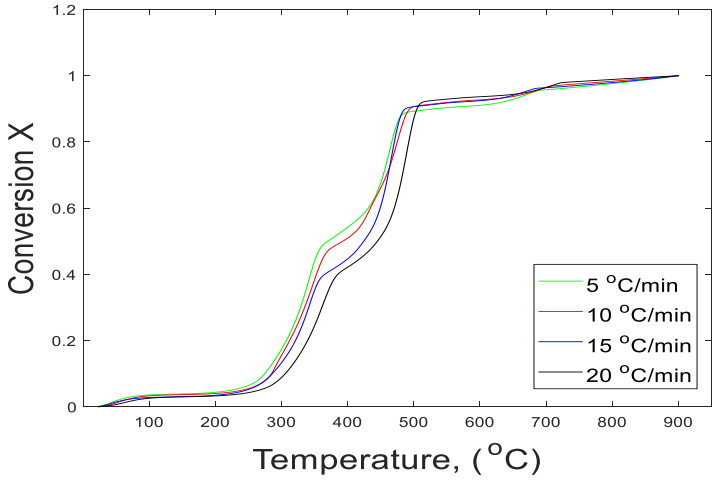

(b)

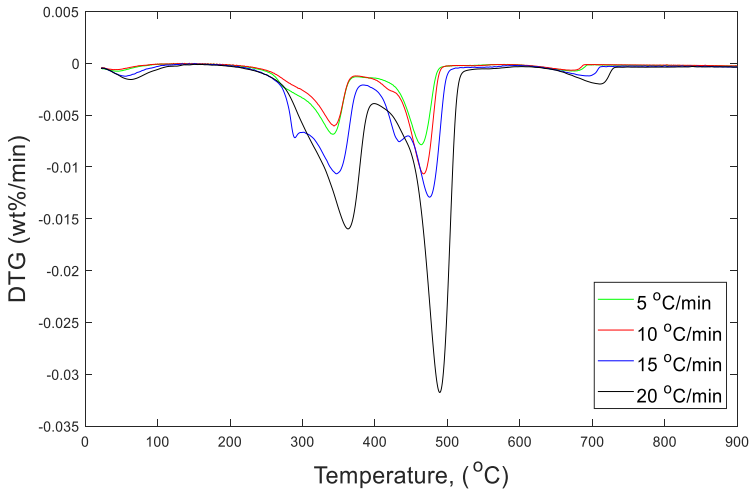

Figure 5-7 The effect of the heating rate on the pyrolysis process; (a) conversion degree (X), and (b) DTG curves

Table 5-8 Thermal decomposition parameters of pyrolysis.

	First stage			Second stage			Third stage		
β	Start*	End**	Wt***	Start*	End**	Wt***	Start*	End**	Wt***
ºC/min	(^{0}C)	(^{0}C)	(%)	(^{0}C)	(^{0}C)	(%)	(^{0}C)	(^{0}C)	(%)
5	28.2	156.9	3.6	233.5	376.3	34.2	376.3	471.4	41.4
10	28.8	156.5	4.7	233.5	378.6	35.6	378.6	493.8	42.6
15	28.1	157.3	4.9	233.5	395.6	37.6	395.6	510.4	45.7
20	27.7	158.9	5.2	233.5	426.7	39.6	426.7	522.2	48.5
Average	28.2	157.4	4.6	233.5	394.3	36.8	394.3	499.5	44.3

	Fourth stage		
β	Start*	End**	Wt***
ºC/min	(^{0}C)	(^{0}C)	(%)
5	636.6	688.1	11.2
10	638.6	693.7	11.4
15	640.5	712.4	9.2
20	641.6	732.4	4.7
Average	639.3	706.7	9.1

* Start refers to start (onset) temperature of an indicated decomposition step. ** End refers to end (offset) temperature of an indicated decomposition step. ***Wt refers to weight loss %. It can be seen from Figure 5-7 (a) the decomposition of Subcoal™ rapidly increases as temperature increased from 200 to 550 ºC. The conversion curve represents four decomposition stages. In the first stage, the moisture leaves the sample with insignificant changes in the mass at 150 ºC, which is known as passive pyrolysis. This means the decomposition reaction is favourable at a temperature less than 150 ºC. Then, in the second and third stages a region between 200 and 550 ºC is known as active pyrolysis, in which devolatilisation of hemicellulose-cellulose causes the sample to lose most of its mass as reported by Slopiecka et al. [169]. In the final stage, lignin decomposition results in only ash and char being left of the sample mass [232].

The increase of heating rate shifts the curve of fractional extent conversion to a high temperature zone. The heating rate increases the initial temperature of decomposition (onset temperature) [186]. As the heating rate increases, the degradation rate within the sample increases which leads to an increase in the conversion to gaseous products. Moreover, the higher the heating rate the lower the reaction residence time and hence the greater amount of Subcoal™ PAF converts [233].

It can be seen from Figure 5-7 (b) as the heating rate increases the DTG peaks become larger. The initial and final temperatures of the pyrolysis stages drift as the heating rate increases. The results from DTG illustrate that the four peaks position is not fixed when the heating rate changes. The endothermic peaks, which are due to decomposition reaction, are observed in the DTG curves at each

tested heating rate [234]. Small peaks may appear in the first and fourth stages, especially at the higher heating rates. In the first stage, the peak is shown as a result of moisture evaporation, while, a high degradation rate occurs due to the melting process of the decomposition residues such as char and ash at the fourth stage [235]. The first stage peaks are observed in the temperature range of 28 to 160 ºC, and then in the fourth stage, the peaks appear in the temperature range of 630 to 710 ºC. However, in the second and third stages two large peaks are observed at a temperature range of 230 to 550 ºC. These peaks also shift as the heating rate increases [236].

Table 5-11 lists T_m values for different heating rates. During the pyrolysis process, T_m increase as the heating rate increases. The value of T_m increased from 471.1 ± 7 to 487.1 ± 1.1 ºC when the heating rate raised from 5 to 20 ºC/min. For these temperatures, the DTG increased from -0.0094 ± 0.0014 to -0.032 ± 0.0014 wt%/min.

The rate of DTG and T_m increased with the heating rate which is coherent with the literature [237]. The difference between T_m at 5 ºC/min and that at 20 ºC/min is 16 ºC. Moreover, the difference between the higher and lower temperatures of T_m increases with a heating rate increase that may lead to uniting the peaks at higher heating rates [237]. The limitation of heat transfer from the surroundings to the sample may explain the temperature shifting to higher values. At a high heating rate, the residence time of reaction is short, and the temperature required to devolatilise becomes greater. While, when the process occurs at a low heating rate the instantaneous thermal energy is high with a longer reaction time that makes the degradation reaction lower [238].

5.7.2 Effect of heating rate on CO_2 gasification

The CO_2 gasification of Subcoal™ PAF was performed at four different heating rates. Figure 5-8 (a) illustrates conversion curves, and (b) DTG curves as a function of temperature. Table 5-9 presents gasification reaction parameters at different decomposition stages. The standard deviation (±) of the three experimental repeats is listed in Table B-2 in the Appendix B: TGA Conversion Repeatability.

As in the previous pyrolysis experiment, the time needed to start the decomposition of the sample (induction time) decreases with a heating rate increase, as illustrated in Figure 5-8 (a). However, mass loss at 15 ºC/min and 20 ºC/min are close to each other and are overlapping in some points. This may explain the complexity of the decomposition process in the presence of CO_2. In this situation, the limitations of diffusion and heat transfer restrictions had a pronounced impact [239].

(a)

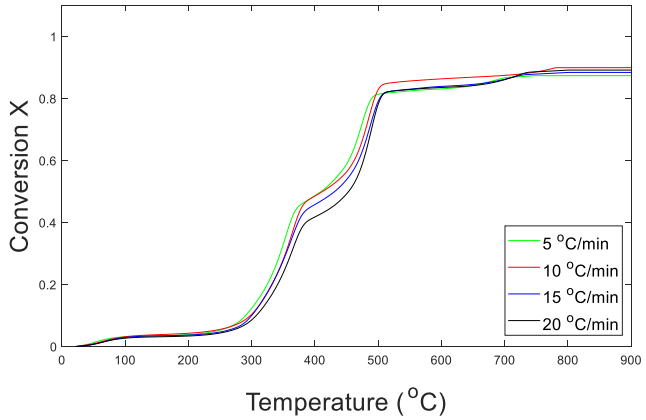

(b)

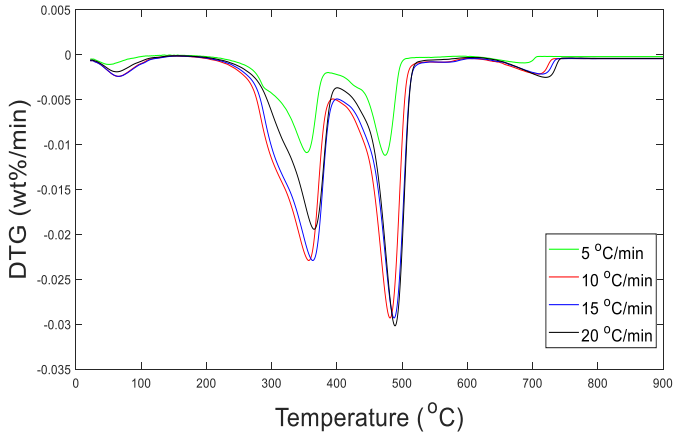

Figure 5-8 Effect of the heating rate on CO_2 gasification process; (a) conversion degree (X), (b) DTG curve

Table 5-9 Thermal decomposition parameters of CO_2 gasification.

	First stage			Second stage			Third stage		
β	Start*	End**	Wt***	Start*	End**	Wt***	Start*	End**	Wt***
°C/min	(^{0}C)	(^{0}C)	(%)	(^{0}C)	(^{0}C)	(%)	(^{0}C)	(^{0}C)	(%)
5	28.6	167.6	3.4	199.2	380.4	34.2	380.4	483.4	51.2
10	28.5	166.2	3.6	199.2	410.3	34.6	410.3	489.6	50
15	28.4	164.4	3.8	199.2	412.2	37.3	412.2	550.6	41.6
20	28.7	163.8	3.9	198.3	428.6	38.5	428.6	558.4	42.3
Average	28.6	165.5	3.7	198.9	407.9	36.2	407.9	520.5	46.3

	Fourth stage		
β	Start*	End**	Wt***
°C/min	(^{0}C)	(^{0}C)	(%)
5	622.2	658.3	3.8
10	622.2	692.2	3.9
15	622.2	708.9	4.4
20	623.4	792.7	5.5
Average	622.5	713.0	4.4

* Start refers to start (onset) temperature of an indicated decomposition step. ** End refers to end (offset) temperature of an indicated decomposition step. ***Wt refers to weight loss %. The effect of heating rate on the conversion is not obvious for CO_2 gasification. The findings show that the increase in heating rate causes an insignificant shift to higher temperatures with curves overlapping. Similarly, the CO_2 gasification process undergoes four decomposition stages.

The DTG graph in Figure 5-8 (b) also indicates two major T_m peaks in the second and third stages. As the heating rate increase, the T_m shifts to the high temperature. Therefore, increase the heating rate from 5 to 20 ºC/min causes T_m to raise from 466 ± 5.18 to 488.3 ± 1.15 ºC. For the same range of heating rate, the degradation rate (wt%/min) increased from -0.0097 ± 0.0014 to -0.0324 ± 0.0023 wt%/min.

The temperature difference in T_m at 5 ºC/min and that at 20 ºC/min is 20.3 ºC. From Figure 5-8 (b), it can be observed at second stage degradation that the first T_m peaks are wide and inconsistent, while the third stage peaks are narrow and tapered. The disorder of minimum DTG peaks occurs as a result of the consecutive reactions which take place simultaneously with the decomposition reaction [194]. Table 5-11 displays T_m and DTG values for three CO_2 experimental runs as well as the standard deviation average (±).

5.7.3 Effect of heating rate on combustion

The combustion of Subcoal™ PAF in TGA was carried out without catalyst at different heating rates. Figure 5-9 (a) illustrates conversion curves (*X*), and (b) DTG curves as a function of temperature. Table 5-10 presents combustion reaction parameters at different decomposition stages. The standard deviation (±) of the three experimental repeats is listed in Table B-3 in the Appendix B: TGA Conversion Repeatability.

(a)

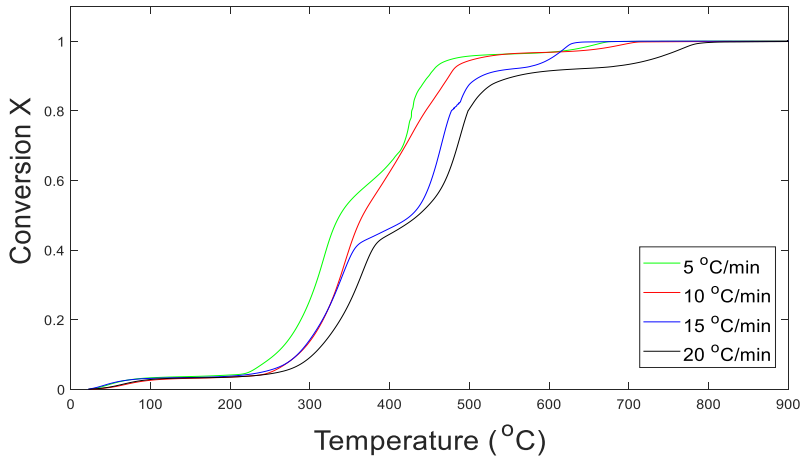

(b)

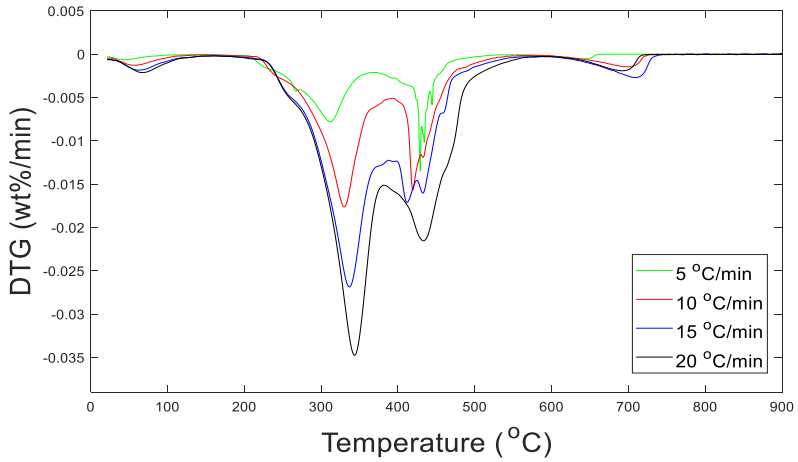

Figure 5-9 Effect of the heating rate on the combustion process; (a) conversion degree (X), (b) DTG curves

Table 5-10Thermal decomposition parameters of combustion.

	First stage			Second stage			Third stage		
β ^{0}C/min	Start* (^{0}C)	End** (^{0}C)	Wt*** (%)	Start* (^{0}C)	End** (^{0}C)	Wt*** (%)	Start* (^{0}C)	End** (^{0}C)	Wt*** (%)
5	28.4	140.3	4.3	214.2	332.5	33.4	332.5	478.6	52.7
10	28.2	150.4	4.6	214.2	347.5	34.3	347.5	524.6	52.1
15	28.6	150.2	4.4	214.3	358.3	35.3	358.3	534.5	42.3
20	28.2	160.4	5.3	214.5	385.1	38.9	385.1	546.2	42.6
Average	28.3	150.3	4.7	214.3	355.9	35.5	335.9	521.0	47.4

	Fourth stage		
β ^{0}C/min	Start* (^{0}C)	End** (^{0}C)	Wt*** (%)
5	615.5	655.3	3.2
10	615.5	690.2	3.7
15	616.3	705.9	4.5
20	617.5	745.8	5.4
Average	616.2	699.3	4.2

* Start refers to start (onset) temperature of an indicated decomposition step. ** End refers to end (offset) temperature of an indicated decomposition step. ***Wt refers to weight loss %.

The weight loss of the sample has the similar behaviour as the pyrolysis and gasification. However, the time required to initialise the decomposition process of combustion is shorter than pyrolysis and gasification [240]. Especially for the heating rate of 20 ºC/min, about less than 15% of the sample remained after the third stage decomposition. In some cases, the remaining amount of the sample ash or char depends on the size of the sample particles (passive stage) [194]. Like pyrolysis and gasification experiments, the combustion conversion curve shows four decomposition stages.

The DTG curves in Figure 5-9 (b) are divided into four sections: a small peak in the first stage, two big peaks in the second and third stages, and small peaks in the fourth stage. However, the degradation reaction in the combustion looks more complex than that in pyrolysis due to the chemical reaction between the sample and oxygen. The presence of oxygen promotes successive oxidation reactions which increase the degree of combustion conversion [241]. The lowest and highest T_m from the DTG analysis are shown in Table 5-11. Unlike pyrolysis and CO_2 gasification, the combustion reaction is faster and this can be seen in the second and third stages; the first peaks are greater than the second peaks, which is confirmed by Chen et al. [242] findings. Also, in the second stage, T_m is 317 ± 4.2 ºC at a heating rate of 5 ºC/min, and the degradation rate is -0.0072 ± 0.0009 wt%/min, respectively. While for the heating rate of 20 ºC/min, T_m is 340.3 ± 2.9 ^{0}C, and DTG is -0.032 ± 0.0037 wt%/min. The temperature difference for T_m at 5 ºC/min and that at 20 ºC/min is 22.9 ^{0}C.

Table 5-11Thermal degradation parameters under different streams.

	N_2		CO_2	
β	T_m	DTG_{Tm}	T_m	DTG_{Tm}
ºC/min	ºC	wt%/min	ºC	wt%/min
5	471 ± 7.0	-0.0094 ± 0.0014	466 ± 5	-0.0097 ± 0.0014
10	481 ± 6.7	-0.019 ± 0.0057	474 ± 6	-0.019 ± 0.0079
15	486 ± 4.8	-0.021 ± 0.0056	482 ± 5	-0.029 ± 0.0073
20	487 ± 1.1	-0.032 ± 0.006	488 ± 1.2	-0.032 ± 0.002
	Air			
β	T_m	DTG_{Tm}		
ºC/min	ºC	wt%/min		
5	317 ± 4.2	-0.0071 ± 0.0009		
10	328 ± 5.5	-0.015 ± 0.0024		
15	336 ± 2.0	-0.025 ± 0.0027		
20	340 ± 2.9	-0.032 ± 0.0037		

5.8 Thermal parameters with catalysts

5.8.1 Effect of dolomite on pyrolysis

The pyrolysis of Subcoal™ PAF was carried out in the presence of different concentrations of dolomite at a single heating rate of 20 ºC/min. Information on the properties and characterisation of dolomite were reported in Section 3.11. The pyrolysis findings in the presence of dolomite are shown in Figure 5-10 (a) and (b).

(a)

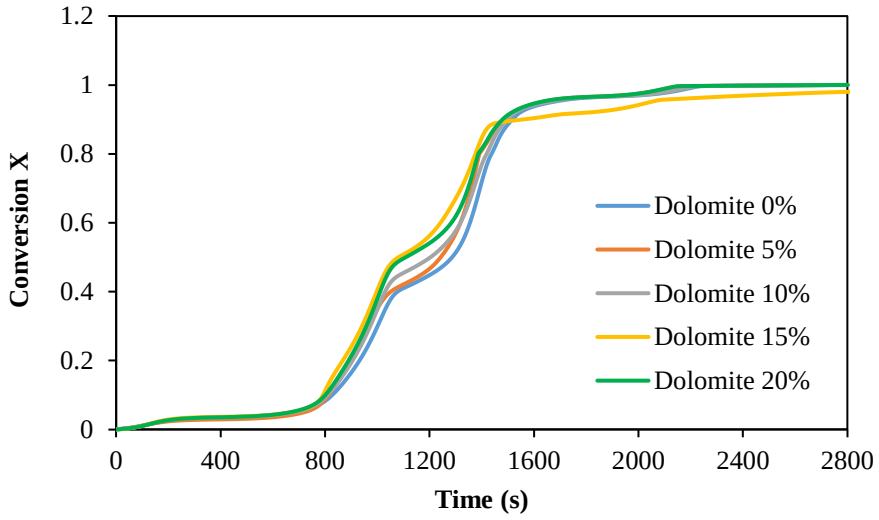

(b)

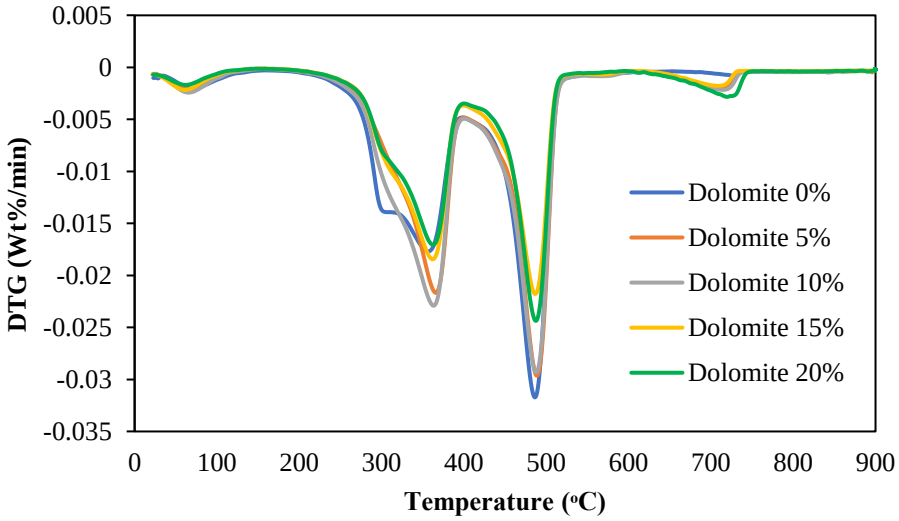

Figure 5-10 Effect of dolomite loadings on the pyrolysis; (a) conversion degree, and (b) DTG curves

Unlike the heating rate investigations, the thermal decomposition initiates at approximately the same time and the mass loss rapidly proceeds after about 12 minutes of the experiment start point. The mass of the sample degrades faster at dolomite ratio of 15 wt.% when compared with the other concentrations, as shown in Figure 5-10 (a) [232]. This will be analysed in greater detail below.

The conversion curve shifted to a lower decomposition temperature as the dolomite loadings increased [82]. The graph indicates that the catalytic cracking passes in two successive sub-stages; first, from 0.2 to 0.6 and then a sharp increase from 0.6 to 0.8 of conversion. The rate of catalytic cracking reaction in the second sub-stage (between 0.6 and 0.8) in the presence of dolomite is higher when compared with the case of no catalyst [243].

The analysis of DTG plots in Figure 5-10 (b) for pyrolysis with dolomite is divided into four stages. Two large peaks are identified in the second and third stages; the degradation rate for the first peak is lower than the second one. In the first peak, there is a low degradation rate corresponding to catalyst loadings. However, in the second peak (highest T_m), the mass loss per time increased as the dolomite loadings increased.

Table 5-12 shows the highest and lowest T_m as well as the DTG at each peak. T_m reduced from 487.4 to 472.5 ºC when the dolomite loadings increased from 0 to 15 wt.%. However, T_m peak increased at 20 wt.% due to overloading of catalyst.

Regarding the DTG, the peak decreased from -0.0392 to -0.0226 wt%/min as the dolomite ratio increased from 0 to 15 wt.%. The difference between the highest and lowest T_m is 14.9 ºC at dolomite content of 15% and 0%, respectively. This implies that Subcoal™ pyrolysis with dolomite needs a lower reaction time than without a catalyst to achieve complete conversion. The pyrolysis curves are more regular compared with olivine [232].

5.8.2 Effect of dolomite on CO_2 gasification

The thermal decomposition in CO_2 gasification of Subcoal™ PAF was carried out in the presence of different loadings of dolomite catalysts as shown in Figure 5-11 (a) and (b).

(a)

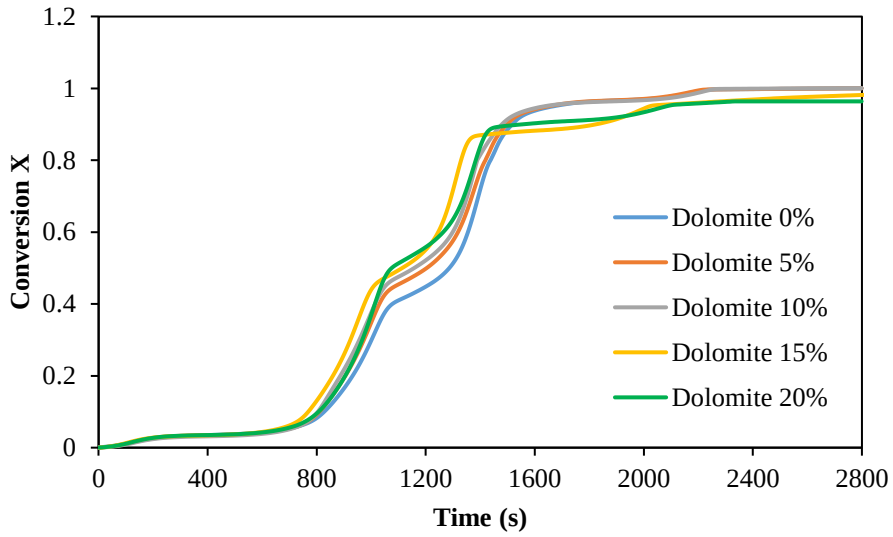

(b)

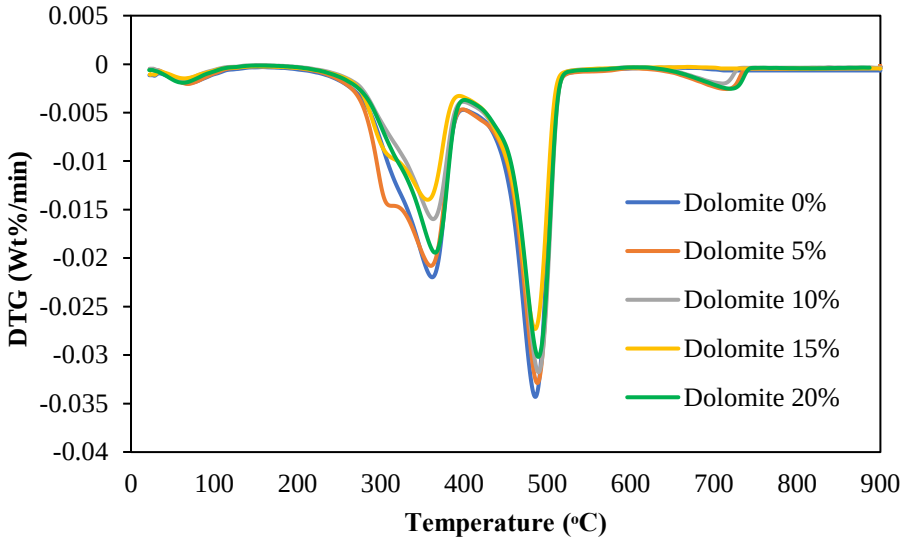

Figure 5-11 Effect of dolomite loadings on the CO_2 gasification; (a) conversion degree, and (b) DTG curves

The mass loss of sample indicates that the rate of decomposition with 15 wt.% dolomite increases much steeper than without catalyst, as shown in Figure 5-11 (a). Also, the conversion changes to lower temperature with the addition of the dolomite. The complete conversion reaction decreased from 792.7 ºC to 748.4 ºC as the dolomite loadings increased from 0 to 15 wt.%. The sample mainly decomposes in two sub-stages between 200 and 520 ºC. Dolomite shows good performance in promoting the reaction rate of CO_2 gasification. It enhances the cracking of tar and increases the production of syngas [121].

Table 5-12 lists T_m and thermal degradation DTG values. The degradation rate in the first and fourth stages is insignificant compared to the second and third stages (decomposition step). The T_m value reduces with the increase of the dolomite loading. T_m decreases from 489.3 to 477.2 ºC as the dolomite loading increased from 0 to 15 wt.%. The DTG at the lowest T_m and 15 wt.% dolomite is -0.0270 wt%/min.

5.8.3 Effect of dolomite on combustion

The combustion experiments were conducted in the presence of different concentrations of dolomite, as illustrated in Figure 5-12 (a, b). The results show that the dolomite has a positive effect on the decomposition reaction. This agrees with the results reported by Kim et al. [244].

(a)

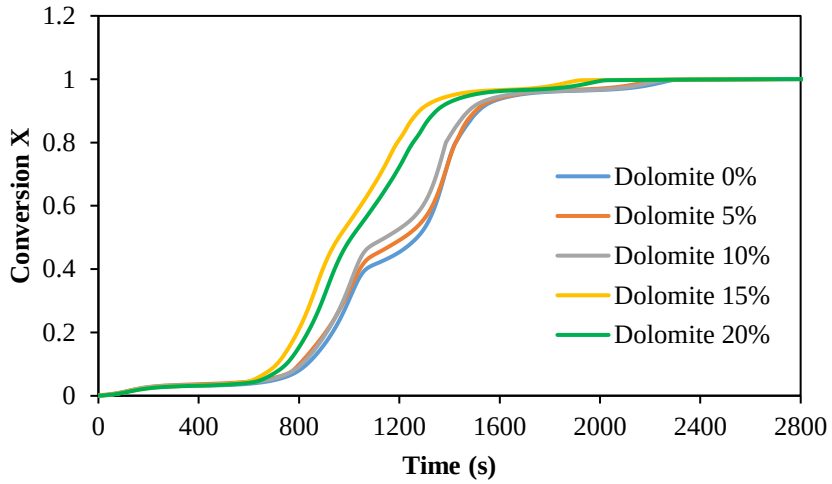

(b)

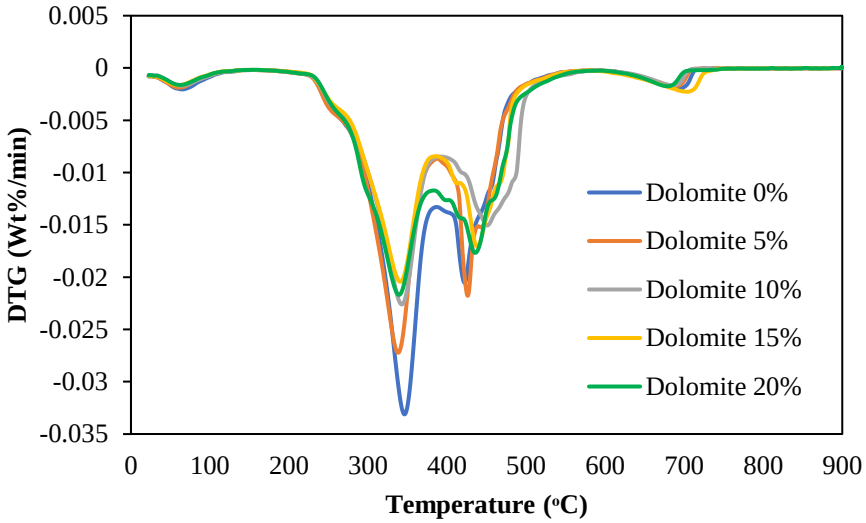

Figure 5-12 Effect of dolomite loadings on the combustion; (a) conversion degree, and (b) DTG curves

Figure 5-12 (b) illustrates DTG (wt%/min) curves of five peaks. When the dolomite loadings increased from 0 to 15 wt.%, the peak temperature of T_m reduced from 335.9 to 321.6 ºC. However, T_m peak increased at 20 wt.% to 324.3 ºC due to deactivation of dolomite. In terms of degradation rate, it decreased from -0.0331 to -0.0204 wt%/min as the dolomite ratio increased from 0 to 15 wt.%. In summary, the higher the concentration of dolomite the lower the peak of temperature degradation observed and the faster the conversion reactions [245]. However, overloading of dolomite ratio decreased the thermal degradation reaction and conversion efficiency. The difference between T_m is 14.3 ºC in the presence of 15 wt.% dolomite and without a catalyst, respectively.

Table 5-12 lists T_m and DTG rate for combustion with different dolomite ratio parameters.

Table 5-12 DTG and values of T_m of Subcoal™ PAF with different loadings of dolomite.

Dolomite	N_2		CO_2		Air	
	T_m	DTG_{Tm}	T_m	DTG_{Tm}	T_m	DTG_{Tm}
Wt.%	ºC	wt%/min	ºC	wt%/min	ºC	wt%/min
0	487.4	-0.0392	489.3	-0.0296	335.9	-0.0331
5	480.8	-0.0314	482.3	-0.0273	330.5	-0.0242
10	476.1	-0.0241	479.8	-0.0272	326.8	-0.0231
15	472.5	-0.0226	477.2	-0.0270	321.6	-0.0204
20	474.3	-0.0234	478.3	-0.0271	324.3	-0.0216

5.8.4 Effect of olivine on pyrolysis

The Subcoal™ PAF pyrolysis was performed in TGA to investigate the effect of olivine loadings on the reaction conversion. In the presence of 15 wt.% olivine, the rate of decomposition increased rapidly, as shown in Figure 5-13 (a) and (b).

(a)

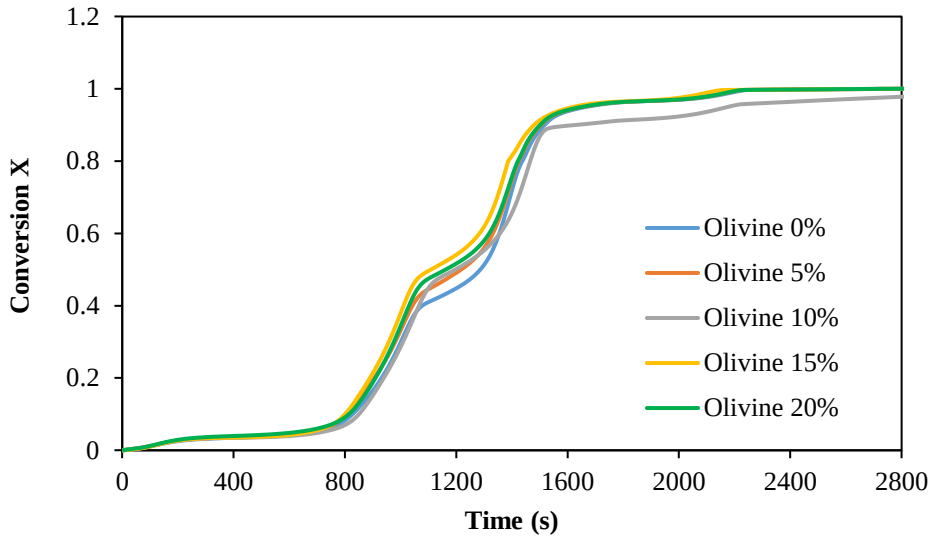

(b)

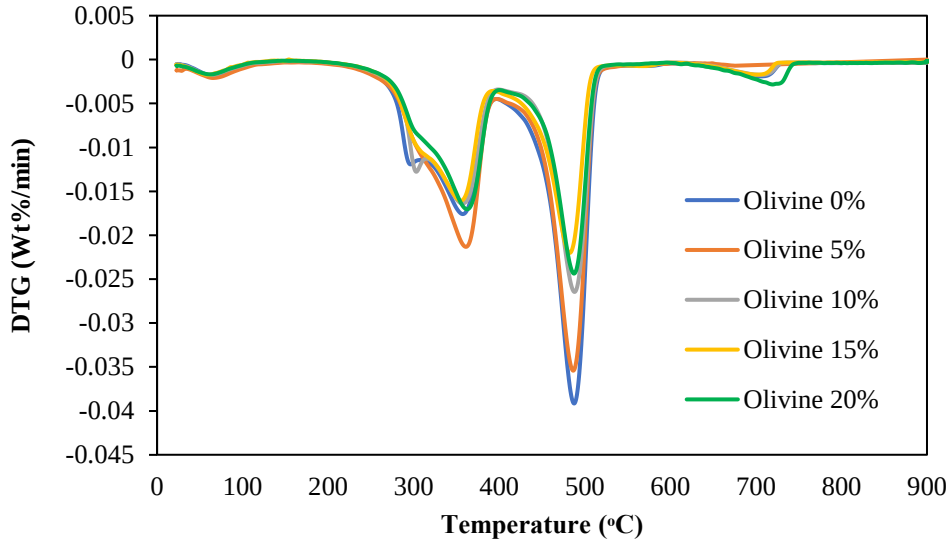

Figure 5-13 Effect of olivine loadings on the pyrolysis; (a) conversion degree, and (b) DTG curves

The presence of olivine makes the mass of the sample drop linearly until it reaches the final stage. In terms of conversion, olivine concentration shifts the decomposition curves to the lower temperature, especially in the second and third stages in the temperature range of about 280 to 550 ºC. In comparison with dolomite, olivine exhibits approximately similar performance.

It can be observed from the DTG curves in Figure 5-13 (b) that there are two main degradation peaks in the second and third stages. The second one is more regular and less fluctuated than the first one. Again, the irregularity is owed to complex reactions promoted by Subcoal™ PAF with olivine.

DTG parameters are listed in Table 5-13. T_m reduced from 487.4 to 477.6 ºC when the olivine loadings raised from 0 to 15 wt.% respectively. For these temperatures, the DTG decreased from -

0.0392 to -0.0268 wt%/min. Olivine at 15 wt.% concentration lowers the peak of temperature degradation and makes the pyrolysis reaction more favourable.

5.8.5 Effect of olivine on the CO_2 gasification

CO_2 gasification was conducted in the presence of different loadings of olivine. The decomposition and DTG reaction are plotted as a function of temperature in Figure 5-14 (a) and (b).

(a)

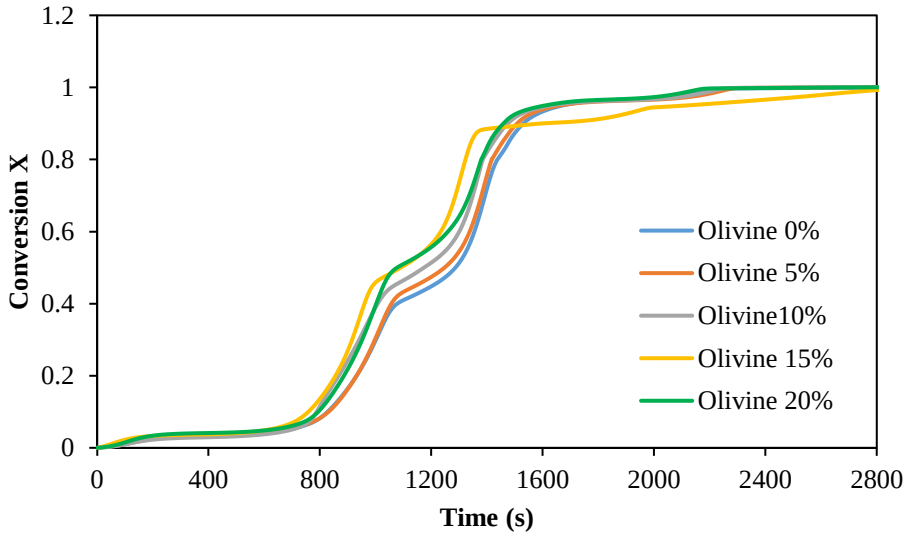

(b)

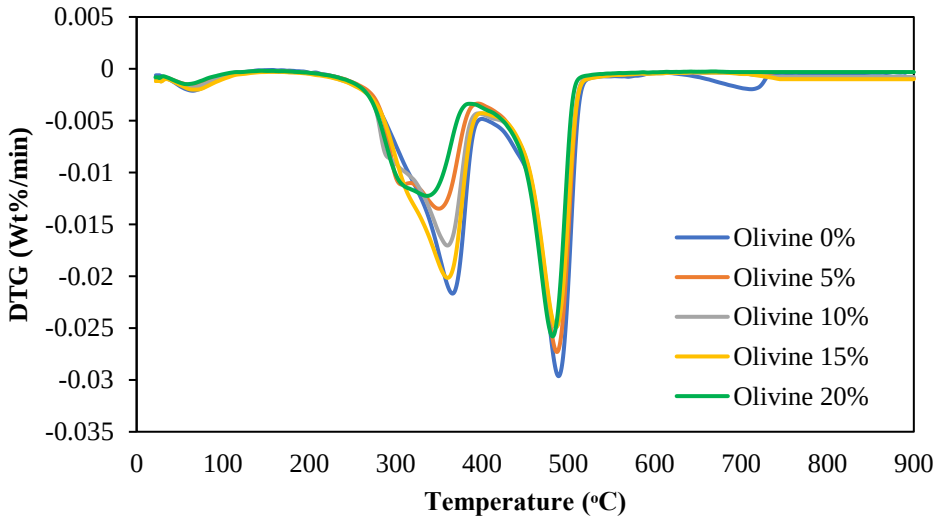

Figure 5-14 Effect of olivine loadings on the CO_2 gasification; (a) conversion degree, and (b) DTG curves

The olivine in CO_2 gasification exhibits a similar performance as that in dolomite. The olivine also promotes the decomposition of biomass. It can be seen from Figure 5-14 (a) that the reaction time decreases as the catalyst loading increases. The complete conversion reaction decreased from 792.7 °C to 767.7 °C as the olivine concentration increased from 0 to 15 wt.%. The conversion curve also shows two regimes of decomposition; the first is between 0.2 and 0.45, and then from 0.45 to 0.8.

However, the final conversion temperature increased to 772.5 ºC at 20 wt.% due to deactivation reaction between Subcaol™ and olivine.

In terms of the DTG analysis, the curves drift to a lower temperature as the loading of olivine increased. However, the overloading of olivine caused deactivation in the reaction and increased the T_m peak. The DTG parameters are listed in Table 5-13. The value of T_m reduces from 489.3 to 483.8 ºC as the catalyst loading increases from 0 to 15 wt.%. Regarding the degradation rate, the peaks decreased from -0.0322 to -0.0285 wt.%/min. The difference between the highest and lowest values of T_m is 5.5 ºC at catalyst loadings of 15 wt.% olivine and 0 wt.%. The concentration and conditions, dolomite catalyses the CO_2 gasification reaction slightly better than olivine [102].

5.8.6 Effect of olivine on combustion

Combustion of Subcoal™ PAF was carried out at different concentrations of olivine. For both 5 and 10 wt.% of olivine, the curves of decomposition were not significantly alternated. However, olivine at 15 wt.% increases the mass loss of the sample sharply in a linear relationship as displayed in Figure 5-15 (a) and (b).

(a)

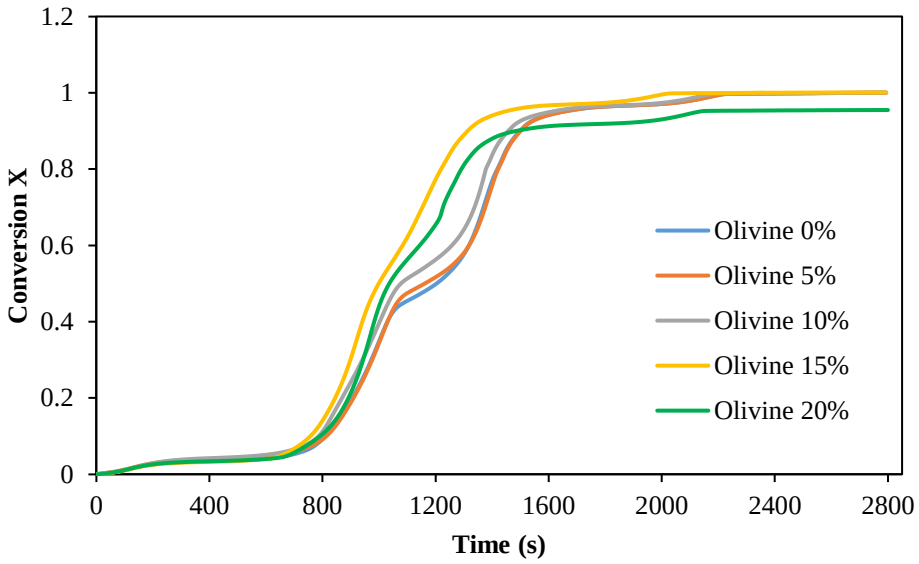

(b)

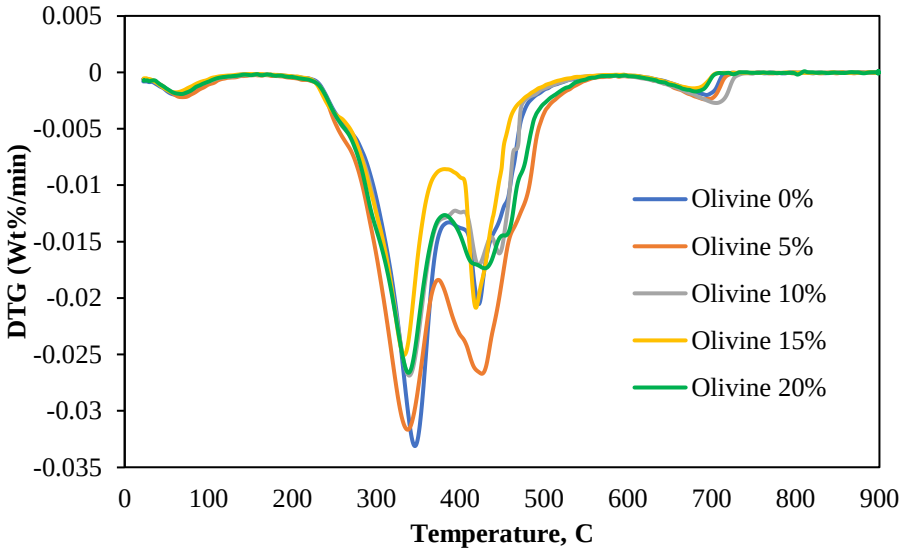

Figure 5-15 Effect of olivine loadings on the combustion; (a) conversion degree, and (b) DTG curves

Combustion with olivine shows that the decomposition process starts earlier than gasification and pyrolysis at a lower temperature. Table 5-13 lists the DTG parameters at various olivine ratios. The findings indicate there is an obvious trend regarding the effect of catalyst content. However, it can be seen in the second stage T_m and DTG decreased as olivine loadings increases. The irregularity of the peak shapes in the third stage is owed to the catalytic oxidation reactions due to the presence of oxygen and olivine as demonstrated in the work of Zan et. al. [241]. Different reactions impose different temperatures which affects the stability of the measurements.

When the olivine loadings increased from 0 to 15 wt.%, T_m reduced from 346.3 to 335.9 ºC. In terms of degradation rate, the peaks decreased from -0.0331 to -0.0261 wt%/min. However, T_m values increase to 338.1 ºC at 20 wt.% due to overloading of olivine ratio. The difference between the highest and lowest T_m value is 10.4 ºC at an olivine content of 15 and 0 wt.%, respectively. The addition of olivine improved the combustion degradation performance and speed up the reaction lowering T_m. Comparing the current results to that of olivine, it can be determined that 15 wt.% dolomite has a better performance on the combustion reaction.

Table 5-13 DTG and values of T_m of Subcoal™ PAF with different loadings of olivine.

Olivine	N_2		CO_2		Air	
	T_m	DTG_{Tm}	T_m	DTG_{Tm}	T_m	DTG_{Tm}
Wt.%	ºC	wt%/min	ºC	wt%/min	ºC	wt%/min
0	487.4	-0.0392	489.3	-0.0322	346.3	-0.0331
5	482.4	-0.0336	488.4	-0.0315	339.7	-0.0327
10	480.7	-0.0273	485.5	-0.0292	338.6	-0.0272
15	477.6	-0.0268	483.8	-0.0285	335.9	-0.0261
20	479.3	-0.0271	484.3	-0.0288	338.1	-0.0270

5.9 Discussion

5.9.1 TGA thermal analysis

The thermal behaviour of Subcoal™ PAF is described as a complex reaction. The TGA results of pyrolysis, CO_2 gasification, and combustion showed a similar general pattern of the process. The process of pyrolysis or gasification, or combustion in TGA passes in three sequential steps and four decomposition stages. The first step is known as the dehydration stage in which the free water (moisture) in a sample vaporises. In addition, the first step (stage I) is for a temperature range between ambient temperature and about 150 ºC and no significant change in the sample mass can be noticed. The second step (stage II and III) include the devolatilisation process of volatile organic components in the sample and decomposition to gaseous products. Most of the mass loss/conversion occurs in these stages in the temperature range of 250 to 550 ºC. The volatile products are divided into condensables such as oils, and non-condensable CO, CO_2, CH_4, H_2, and N_2 [246]. The final step (stage IIII) is where the char and ash forms and is degraded into volatile gases in the temperature range of 600 to 750 ºC with small variation in the mass loss [237].

The temperature range in the final stage is known as a critical temperature due to an insignificant change of mass with a continuous increase in temperature [247]. The heating rate plays a vital role in the thermal degradation of Subcoal™ PAF. The results indicate that the increase in heating rate leads to an increase in the reaction rate of decomposition and reduces the time required to start the degradation stage. Also, the lower the heating rate the greater the time needed to initiate the degradation. The combustion process began earlier than the pyrolysis process. This fact occurs because the pyrolysis was performed in the absence of oxygen. Instead in combustion, a high amount of oxygen can help and accelerate the heating process. However, the CO_2 gasification received high variation with the heating rate change. This can be explained by the high variation of temperature in the sample which leads to slower decomposition reaction [233].

At lower heating rates, the residence time in TGA will be longer. Thus, fewer molecules convert to products and slow decomposition reaction occurred [248]. Moreover, when the lower heating rate is applied, more time is needed to achieve the equilibrium, therefore, it was shifted to a higher temperature region due to slow heat diffusion [249].

In all experiments, mass loss curves at 15 and 20 ºC/min are close to each other and are overlapping at some points. This may explain the complexity of the Subcoal™ PAF decomposition process, especially in the presence of CO_2.

Olivine and dolomite catalysts have a good impact on the conversion rate when compared with the heating rate impact. The presence of a catalyst reduces the induction time of the thermal decomposition. It also shifts the conversion curve to a lower temperature as catalyst concentration increases which indicates shorter decomposition reaction time. The increase of catalyst loading to 20

wt.% reduced the thermal degradation efficiency and conversion rate due to deactivation reaction. TGA plots of conversion in the presence of a catalyst are divided into two main regimes; generally, from 0.2 to 0.45, and then from 0.45 to 0.8 which can be explained by the successive reactions of decomposition. Dolomite exhibits a better thermal degradation performance than olivine at 15 wt.% concentration in pyrolysis, CO_2 gasification, and combustion.

5.9.2 DTG analysis

In the DTG analysis, the degradation rate in wt%/min is plotted against the temperature. Four peaks appear in the graph showing the amount of degradation that occurred at a specific temperature. The value of DTG and T_m determine the performance of the pyrolysis, CO_2 gasification, and combustion process in TGA. The results show that two small T_m peaks correspond to degradation in the first and fourth stages, respectively, as well as two large peaks in the second and third stages [235]. For the effect of heating rate, T_m increase as the heating rate increases from 5 to 20 ºC/min. However, the DTG increases with a heating rate increase as well [234]. T_m peaks overlap and the irregularity of peak shape indicates the occurrence of simultaneous reactions, especially in the CO_2 gasification reactions [250]. The thermal stability is achieved with pyrolysis more than that with CO_2 gasification due to the absence of oxidation reactions [251]. In DTG combustion curves, the temperature peaks are more regular and the degradation occurred in lower T_m values compared with pyrolysis and CO_2 gasification. This is due to the presence of O_2 in the air that may promote decomposition reactions.

In the presence of catalysts at a constant heating rate of 20 ºC/min, the pyrolysis, CO_2 gasification and combustion process reactions were evaluated according to T_m value. The higher the concentration of catalysts, the lower the T_m peak obtained [232]. However, overloading of catalysts ratio to 20 wt.% increased the T_m peak and reduced conversion efficiency. In the combustion of Subcoal™ PAF with different dolomite concentrations, there were measurable changes in peaks which indicates that high catalysts affect the degradation reaction compared with CO_2 gasification and pyrolysis. The abnormality of DTG peaks appearing under CO_2 atmosphere is due to the presence of O_2 and reaction mechanism with catalyst [241]. The DTG analysis for the combustion, CO_2 gasification, and pyrolysis showed that insignificant change in the peak temperatures, and with dolomite loadings increase, the T_m shifts to lower temperature.

Replacing the dolomite with olivine to catalyse the pyrolysis, CO_2 gasification and combustion of Subcoal™ PAF also result in a good impact on the DTG curves. The temperature peaks look smoother and have less fluctuation. T_m for olivine is slightly higher than that for dolomite which may confirm that the dolomite has a better degradation performance at constant catalyst concentration than olivine. The DTG analysis with olivine is quite organised and sharpened compared to the dolomite case [252]. The performance of combustion with olivine was more affected compared with pyrolysis and CO_2 gasification. Also, the DTG rate is reduced as the olivine ratio increases.

Comparing Subcoal™ PAF results from TGA to the literature, Gerassimidou et al. [253] found that the pyrolysis of SRF T_m=500 ºC and for paper waste T_m=575 ºC, at 20 ºC/min. Also, the pyrolysis results for paperboard T_m=732 ºC while the oxidation of SRF results shows T_m=600 ºC. This result proves that thermal degradation of Subcoal™ PAF pyrolysis and oxidation is lower than SRF, paper waste, and paperboard [253]. Subcoal™ PAF is decomposed in a wider temperature range at lower levels compared to fossil fuels due to its low fixed-carbon and high volatile matter. Thus, combining Subcoal™ PAF with other biomass, or fuels such as coal, can mitigate emissions and provide some economic solutions to energy sectors.

5.10 Summary

In this chapter, Characterisation of Subcoal™ and TGA results have been reported in this chapter. The proximate test results showed that the Subcoal™ primarily comprises of volatile matter with 77.6 ± 1.4 wt.% and moisture with 3.1 ± 0.4 wt.%, respectively, which are in a suitable range for gasification technology. In addition, the ultimate analysis reported that the fuel is composed of 45.7 ± 2.7 wt.% carbon which indicates that the product gas will contain a high proportion of CO, CO_2 and CH_4. The bulk density of Subcoal™ and silica sand identified as 0.43 and 1.54 g/cm^3, respectively.

The particle size distribution findings for silica sand showed that the Sauter mean diameter D [3,2] and volume mean diameter D [4,3] are 630 μm and 658 μm, respectively. The accumulative size analysis of sand particles indicates that 90% of the particles have a mean size of 850 μm, 50% of the particles fit with 643 μm, and 10% of the particles were found to have a size of 485 μm. The specific surface area and span for silica sand bed are 3.67 m^2/kg and 0.57, respectively. The mean size of the particles determines the efficiency of mass and heat transfer as well as the flow pattern. The smaller the bed particle size the higher the pressure drop across the bed.

For Subcoal™ powder<3 mm, the Sauter mean diameter D [3,2] and volume mean diameter D [4,3] is approximately 917 μm and 890 μm, respectively. The accumulative size analysis indicates that 90% of the particles have a mean diameter of 2030 μm, 50% of the particles fit with 731 μm, and 10% of the particles were found to have a size of 49.7 μm. The specific surface area and span for the powder particles are 65.45 m^2/kg and 2.71, respectively. The gasifier bed and biomass particle characterisation are essential to identify the effect of particle size on the gasification process. The biomass particle size is desirable that ensure good gasification performance and particles bed stability against gases flow.

The sulphur and carbon contents in Subcoal™ have been measured using a LECO analyser based on three experimental trials. The concentration of sulphur found with an average content of 0.2 wt.% which is relatively lower than that in other types of MSW reported in the literature. While carbon content has been found as 27 wt.% which shows a lower value than carbon obtained from ultimate

analysis due to complexity of paper and plastics mixture in Subcoal™. A trace element analysis of the residual ash has been performed using XRF analyser. The analysis results show that Fe, Ti, Al, Ca, S, and Cl have recorded the highest content among the mineral and soil elements. The elements are forming the mineral compounds that contribute to catalysis process of the gasification.

The XRD analysis of Subcoal™ powder<3 mm, residual ash and silica sand particles were conducted. The results showed that the crystallinity content in Subcoal™ powder, residual ash and silica are 42.02%, 37.67%, and 46.1%, respectively. In comparison with the Subcoal™ sample, the reduction in the crystallinity of ash is attributed to the decomposition of crystalline cellulose fibers. The crystalline minerals and metal oxides in the ash may behave as a catalyst of thermal decomposition reactions.

TGA non-isothermal analysis of pyrolysis, CO_2 gasification, and combustion of Subcoal™ PAF without catalyst has been conducted at different heating rates (5, 10, 15, 20 ºC/min). The outcomes were presented in terms of the TGA and DTG curves. The increase of heating rate shifts the TGA curve to a high temperature region. From the DTG curves, the value of T_m increases as the heating rate raised from 5 to 20 ºC/min. Generally, the TGA curves showed three thermal degradation steps and four decomposition stages. The first stage is the dehydration zone for moisture removal that is up to 150 ºC. The second and third stages are the devolatilisation zone between 200 and 550 ºC. The final stage is the lignin decomposition zone between 600 to 750 ºC, which results in only ash and char being left of the sample mass. The gasification curves exhibit relatively higher complexity than pyrolysis and combustion due to the presence of CO_2. However, the reaction of combustion is faster at a lower degradation temperature of the devolatilisation stage than that in pyrolysis and CO_2 gasification due to the high ignition point of Subcoal™ PAF. Two common mineral catalysts have been used in this study, namely dolomite and olivine. The conversion curve shifted to a lower temperature region as the catalysts loadings increased which refer to a shorter reaction time. The T_m peak reduced when the catalyst loadings increased from 0 to 15 wt.%. However, the T_m values increased at catalyst loading 20 wt.% and caused deactivation to the thermal reaction. At dolomite 15 wt.%, the best thermal degradation reactions were obtained for all experiments.

Chapter 6: Kinetics Analysis

6.1 Introduction

In this chapter, TGA kinetics results and discussion are presented. The effect of four different heating rates (5, 10, 15, 20 °C/min) on the kinetics parameters are identified using model free methods. In addition, The CR model fitting method was used to estimate kinetic mechanisms for each reaction model at different dolomite or olivine loading (0, 5, 10, 15, 20 wt.%) and constant heating rate (20 °C/min). In addition, the kinetic parameters were estimated for the devolatilisation stages of degradation, where the conversion varies from 0.2 to 0.8, at fixed and multiple heating rates. As all methods adopt linear relationships to estimate the E_a and A. The R^2 was calculated to assess the strength of kinetic parameters between 0.85 and 1. The findings of TGA show that the reactions under heating rate 20 °C/min and dolomite (15 wt.%) play a vital role in thermal degradation and E_a parameters. Both kinetic methods vary in their accuracy based on the mathematical approach adopted.

6.2 Model free kinetic findings

6.2.1 OFW parameters

The E_a was graphically estimated from the slope of Eq. 4.15 by plotting (ln(β)) versus (1/T) for different values of conversion. The OFW kinetics evaluation is displayed in Figure 6-1. The A value was determined using Eq. 4.17 and Table 6-1 shows the kinetic parameters and R^2 values.

(a)

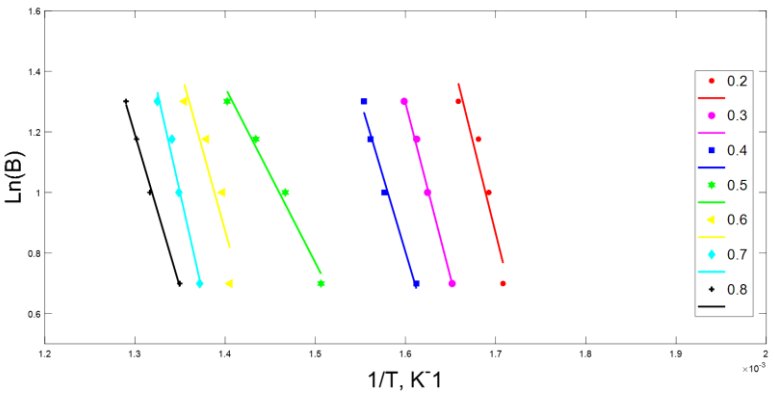

(b)

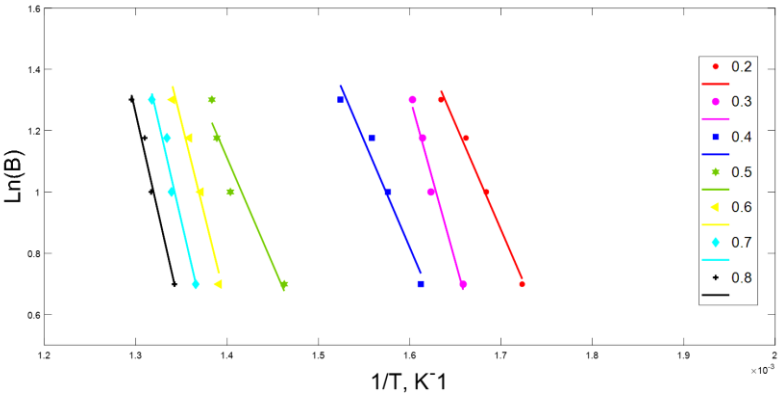

(c)

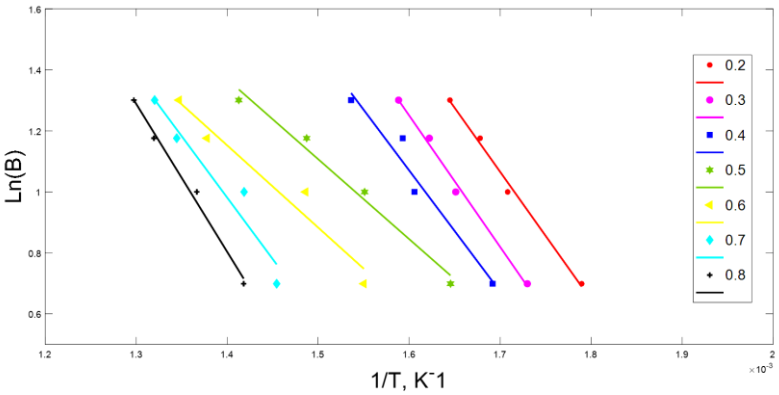

Figure 6-1 OFW plot of pyrolysis (a) CO_2 gasification (b) combustion (c) for given values of degrees of conversion at heating rates

Table 6-1 Comparison between kinetic parameters obtained by OFW method at different heating rates.

	N_2			CO_2		
X	E_a	R^2	A	E_a	R^2	A
/	(kJ/mol)	/	(min^{-1})	(kJ/mol)	/	(min^{-1})
0.2	118.9	0.802	2.7E+09	139.2	0.988	1.5E+11
0.3	142.5	0.995	1.6E+11	216.5	0.977	6.4E+10
0.4	161.9	0.996	2.7E+13	140.4	0.959	5.1E+10
0.5	71.9	0.966	6.9E+04	139.6	0.934	4.1E+09
0.6	165.4	0.970	2.7E+11	241.4	0.968	1.4E+09
0.7	207.2	0.857	2.4E+14	259.5	0.967	1.1E+09
0.8	264.2	0.931	2.4E+18	264.6	0.981	9.5E+08
Average	161.7	0.931	3.4E+17	200.2	0.968	4.0E+10
E_a	161.7 ± 24.7			200.2 ± 33.6		
	Air					
X	E_a	R^2	A			
/	(kJ/mol)	/	(min^{-1})			
0.2	84.6	0.993	2.7E+06			
0.3	86.8	0.993	2.2E+06			
0.4	80.0	0.957	2.2E+06			
0.5	52.8	0.981	2.0E+06			
0.6	54.2	0.951	1.0E+06			
0.7	81.1	0.934	4.6E+05			
0.8	97.7	0.991	3.5E+05			
Average	76.7	0.971	1.6E+06			
E_a	76.7 ± 15.4					

The E_a and A of the overall pyrolysis reaction are 161.7 ± 24.7 kJ/mol and 3.4E+17 ± 4.0E+19 min^{-1}. Also, the E_a and A of gasification are 200.2 ± 33.6 kJ/mol and 4.0E+10 ± 7.1E+05 min^{-1}. While the E_a and A of combustion reaction are 76.7 ± 15.4 kJ/mol and 1.6E+06 ± 7.1E+05 min^{-1}, respectively. The value of E_a pyrolysis obtained by OFW is slightly greater than that obtained by ST, TA, and KAS methods which may be caused by some improper integration approximation [169, 194]. On the other hand, the value of E_a for combustion is closer to ST with high accuracy analysis. The standard deviation (±) of the three experiments as listed in Appendix C: Model Free Kinetic Repeatability in Tables C-1, C-2 and C-3 is coherent with those estimated by KAS, ST, and TA methods. The slight differences in average are caused by the improper approximation of temperature integration. These findings are confirmed by Guida et al. [237].

6.2.2 KAS parameters

The KAS was used to estimate the E_a according to Eq. 4.22. Table 6-2 shows that the KAS method provides more stable parameters than OFW methods, as displayed in Figure 6-2. In addition, the result shows the high accuracy of kinetics parameters with R^2 ranging from 0.922 to 0.986. The plot of E_a estimation was executed and straight lines are almost parallel to each other that confirm the unsophisticated reaction mechanism and reliable mathematics. The experimental repeatability parameters are listed in Tables C-4, C-5 and C-6 in the Appendix C: Model Free Kinetic Repeatability.

(a)

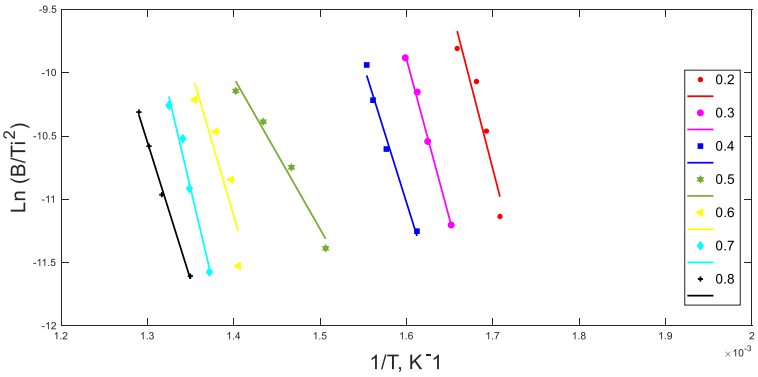

(b)

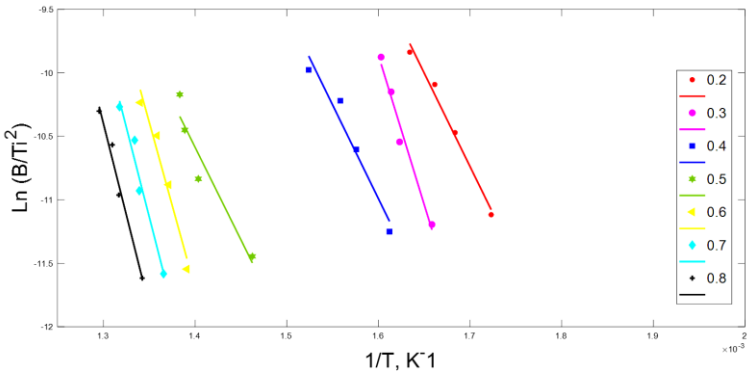

(c)

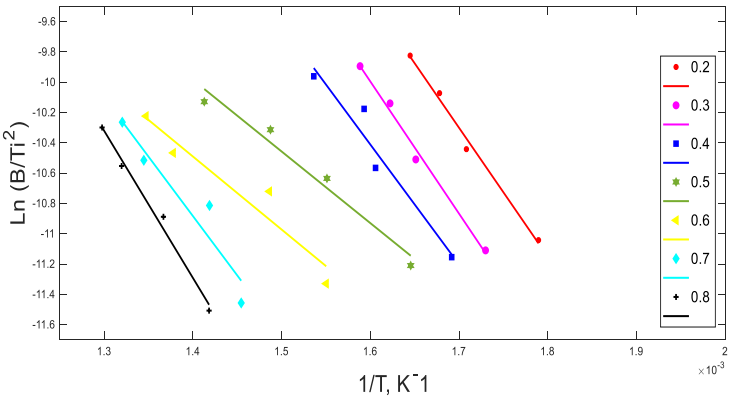

Figure 6-2 KAS plot of pyrolysis (a) CO_2 gasification (b) combustion (c) for given values of degrees of conversion at different heating rates

Table 6-2 Comparison between kinetic parameters obtained by KAS at different heating rates.

	N_2			CO_2		
X	E_a	R^2	A	E_a	R^2	A
/	(kJ/mol)	/	(min^{-1})	(kJ/mol)	/	(min^{-1})
0.2	103.2	0.771	1.8E+08	122.5	0.986	4.8E+07
0.3	125.3	0.994	2.0E+10	195.7	0.974	1.1E+13
0.4	143.9	0.996	9.8E+11	122.9	0.952	5.2E+07
0.5	57.1	0.951	9.4E+03	121.1	0.922	3.8E+07
0.6	145.3	0.965	1.3E+12	217.4	0.964	3.9E+14
0.7	184.7	0.840	4.9E+15	234.8	0.963	6.6E+15
0.8	238.8	0.924	3.7E+20	239.5	0.979	1.4E+16
Average	142.6	0.920	5.3E+19	179.6	0.963	3.1E+15
E_a	142.6 ± 23.5			179.0 ± 31.9		

	Air		
X	E_a	R^2	A
/	(kJ/mol)	/	(min^{-1})
0.2	46.9	0.957	9.9E+02
0.3	53.6	0.958	4.3E+03
0.4	59.3	0.977	1.5E+04
0.5	57.6	0.918	1.1E+04
0.6	62.5	0.914	3.0E+04
0.7	107.9	0.856	5.0E+08
0.8	109.3	0.927	6.8E+08
Average	71.0	0.925	1.7E+08
E_a	71.0 ± 4.4		

The E_a and A of the overall pyrolysis reaction are 142.6 ± 23.5 kJ/mol and 5.3E+19 ± 8.3E+29 min^{-1}. Also, the E_a and A of gasification are 179.0 ± 31.9 kJ/mol and 3.1E+15 ± 1.7E+28 min^{-1}. While the E_a and A of combustion reaction are 71.0 ± 4.4 kJ/mol and 1.7E+08 ± 7.9E+07 min^{-1}, respectively. The E_a value for pyrolysis lies in the middle between those obtained by the OFW and TA methods. Also, the E_a value for gasification is closer to that obtained by the ST, more than that obtained by the OFW methods, but it is larger than combustion. However, the fluctuation in the OFW data is more obvious than with the KAS method. By comparing KAS kinetic analysis of gasification to combustion, conversion lines in combustion are more parallel. This explains that the reaction mechanism in the presence of CO_2 is more complex than air. The mathematics variation of KAS E_a values is lower than OFW which is attributed to the overall integral analysis of KAS [254]. Also, the E_a and A in this method almost increase as the conversion increases [169]. In sum, the KAS showed high numerical stability in terms of E_a and A when compared with OFW method.

6.2.3 ST parameters

The ST was used to evaluate the E_a according to Eq. 4.27 and presented in Figure 6-3. The E_a results exhibit high mathematical accuracy and R^2 values as displayed in Table 6-3. The experimental repeatability parameters are listed in Tables C-7, C-8 and C-9 in the Appendix C: Model Free Kinetic Repeatability.

(a)

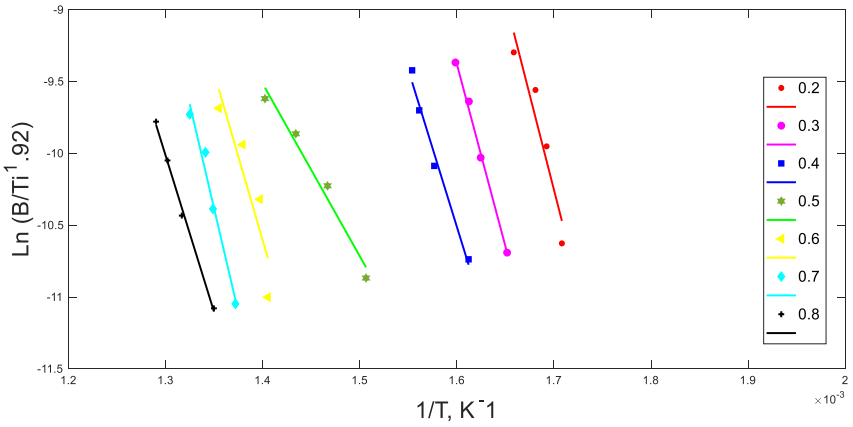

(b)

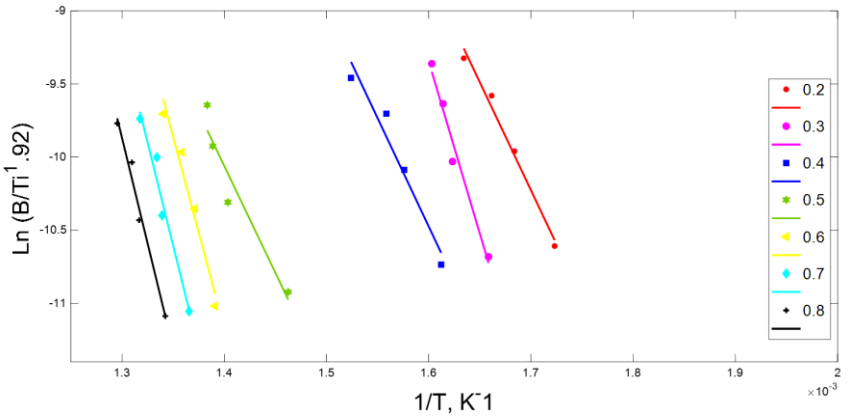

(c)

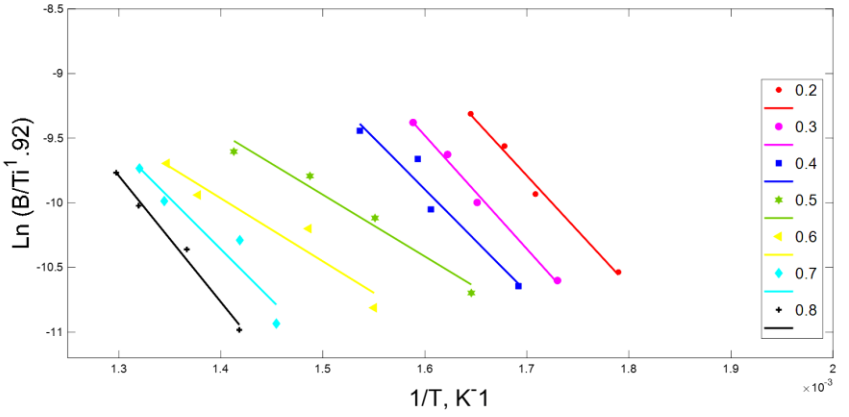

Figure 6-3 ST plot of pyrolysis (a) CO_2 gasification (b) combustion (c) for given values of degrees of conversion at different heating rates

Table 6-3 Comparison between kinetic parameters obtained by ST method at different heating rates.

	N_2			CO_2		
X	E_a	R^2	A	E_a	R^2	A
/	(kJ/mol)	/	(min^{-1})	(kJ/mol)	/	(min^{-1})
0.2	103.6	0.772	2.0E+08	122.9	0.986	5.2E+07
0.3	125.7	0.994	2.1E+10	196.2	0.974	1.1E+13
0.4	144.4	0.996	1.1E+12	123.3	0.952	5.6E+07
0.5	57.6	0.952	1.0E+04	121.6	0.922	4.1E+07
0.6	145.8	0.966	1.4E+12	217.9	0.964	4.3E+14
0.7	185.2	0.841	5.4E+15	234.9	0.963	7.2E+15
0.8	239.3	0.924	4.1E+20	239.7	0.979	1.6E+16
Average	143.1	0.921	5.8E+19	179.5	0.963	3.3E+15
E_a	143.1 ± 23.5			179.5 ± 31.9		

	Air		
X	E_a	R^2	A
/	(kJ/mol)	/	(min^{-1})
0.2	47.3	0.958	1.1E+03
0.3	53.9	0.959	4.7E+03
0.4	59.7	0.977	1.7E+04
0.5	58.0	0.919	1.1E+04
0.6	62.9	0.915	3.3E+04
0.7	108.4	0.827	5.5E+08
0.8	109.8	0.927	7.5E+08
Average	71.44	0.926	1.9E+08
E_a	71.4 ± 4.3		

The E_a and A of the overall pyrolysis reaction are 143.1 ± 23.5 kJ/mol and 5.8E+19 ± 8.9E+29 min^{-1}. Also, the E_a and A of gasification are 179.5 ± 31.9 kJ/mol and 3.3E+15 ± 1.9E+28 min^{-1}. While the E_a and A of combustion reaction are 71.4 ± 4.3 kJ/mol and 1.9E+08 ± 8.7E+07 min^{-1}, respectively. As shown in Table 6-3, the estimated E_a is approximately like the one obtained by the KAS method. This method is developed to overcome the limitations of KAS and OFW methods such as variable heating rate and approximation of temperature integral [255]. However, the plotted lines are not completely parallel to each other for combustion, especially those for the conversion of 0.5 and 0.6 due to the presence of O_2. The role of O_2 in this reaction is to minimise the energy required to initiate the chemical reaction. Excellent agreement is obtained between the kinetic parameters estimated by ST and KAS methods due to the consistency of analysis and mathematic techniques. This agreement is coherent with the literature [256].

6.2.4 TA parameters

The TA method is a highly precise formula for estimating the kinetic parameters which was recently developed by Tang [183]. The kinetic parameters were evaluated according to Eq. 4.24. and illustrated in Figure 6-4. The E_a and R^2 values are reported in Table 6-4.

(a)

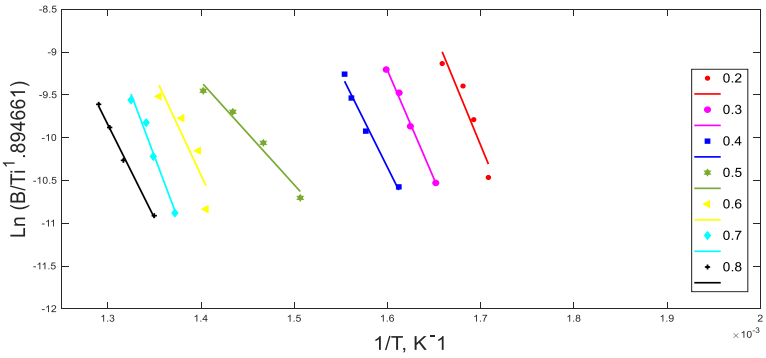

(b)

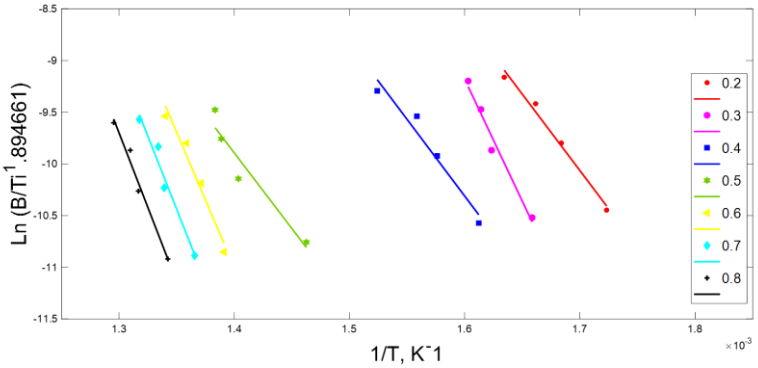

(c)

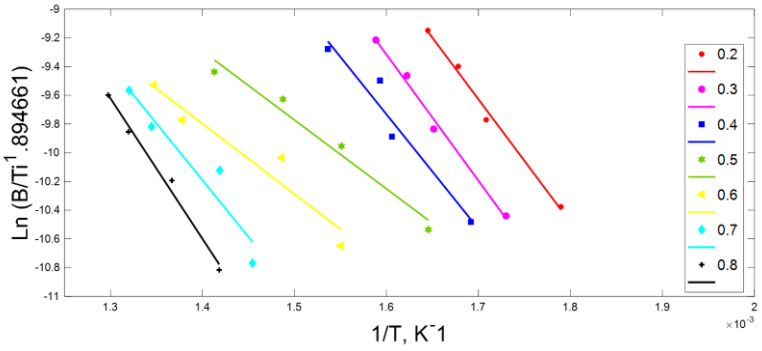

Figure 6-4 TA plot of pyrolysis (a) CO_2 gasification (b) combustion (c) for given values of degrees of conversion at different heating rates

Table 6-4 Comparison between kinetic parameters obtained by TA method at different heating rates.

	N_2			CO_2		
X	E_a	R^2	A	E_a	R^2	A
/	(kJ/mol)	/	(min^{-1})	(kJ/mol)	/	(min^{-1})
0.2	102.7	0.871	102.7	123.0	0.986	5.3E+07
0.3	116.5	0.881	116.5	196.3	0.974	1.2E+13
0.4	126.6	0.909	126.6	123.5	0.952	5.7E+07
0.5	121.9	0.948	121.9	121.8	0.922	4.3E+07
0.6	135.5	0.849	135.5	218.1	0.964	4.4E+14
0.7	212.6	0.691	212.6	235.1	0.963	7.4E+15
0.8	230.4	0.855	230.4	239.8	0.979	1.6E+16
Average	149.5	0.858	149.5	179.7	0.963	3.4E+15
E_a	149.5 ± 20.6			179.7 ± 47.7		

	Air		
X	E_a	R^2	A
/	(kJ/mol)	/	(min^{-1})
0.2	47.4	0.958	1.1E+03
0.3	54.1	0.959	4.8E+03
0.4	59.9	0.977	1.7E+04
0.5	58.2	0.919	1.2E+04
0.6	63.1	0.916	3.4E+04
0.7	108.5	0.827	5.7E+08
0.8	109.9	0.927	7.7E+08
Average	71.6	0.926	1.9E+08
E_a	71.6 ± 4.34		

The E_a and A of the overall pyrolysis reaction are 149.5 ± 20.6 kJ/mol and 149.5E+29 ± 9.2E+29 min^{-1}. Also, the E_a and A of gasification are 179.7 ± 47.7 kJ/mol and 3.4E+15 ± 3.6E+27 min^{-1}. While the E_a and A of combustion reaction are 71.6 ± 4.3 kJ/mol and 1.9E+08 ± 9.0E+07 min^{-1}, respectively. This value of E_a is almost similar to the one obtained by KAS and ST methods. However, it is inconsistent with E_a estimated by the OFW method, especially at the higher conversion degrees [257]. The linear plots of each conversion degree within the second and third stages are approximately in parallel. However, the values of the E_a vary with conversion indicating the occurrence of a complex multistep mechanism as listed in Tables C-10, C-11 and C-12 in the Appendix C: Model Free Kinetic Repeatability [169]. The mathematics accuracy is owed to the validity of this method for parallel reactions and approximation of temperature integral.

6.2.5 Comparison of E_a obtained from model-free methods.

The E_a from each model-free method was plotted against the conversion degree from the average of three experimental repeats as listed in the appendix C of each method with higher linearity coefficient

R^2, as shown in Figure 6-5. The connection points on the curves represent the value of E_a at each conversion between 0.2 to 0.8.

(a)

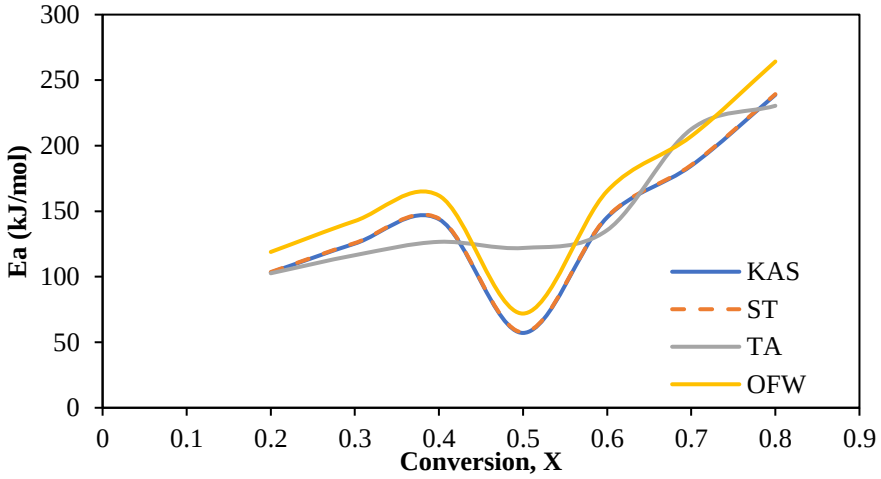

(b)

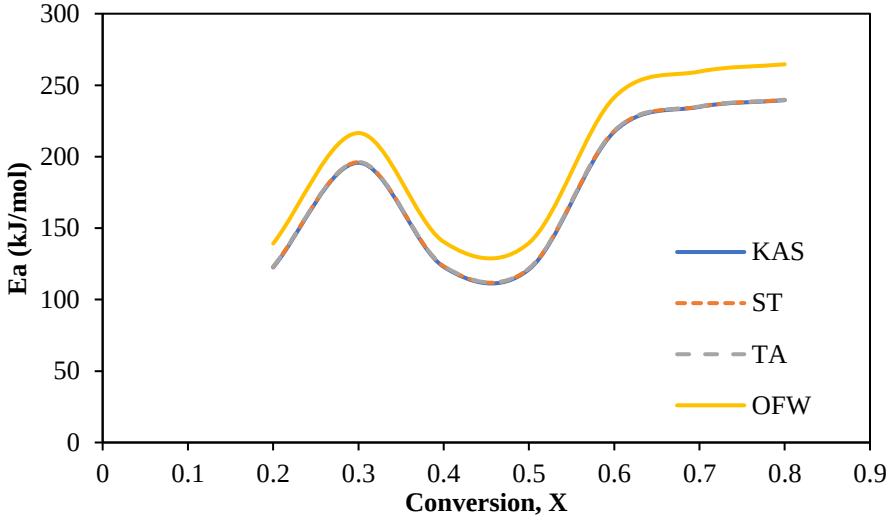

(c)

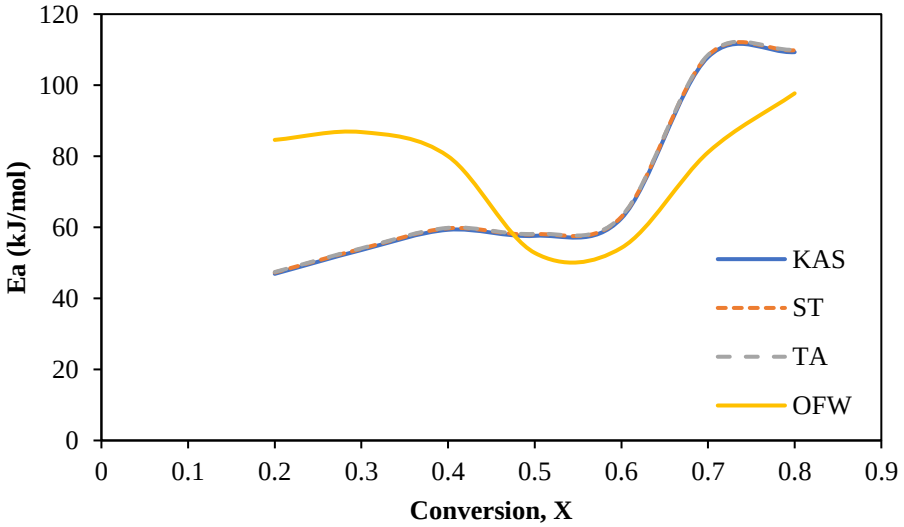

Figure 6-5 The variation of E_a of pyrolysis (a), CO_2 gasification (b), combustion (c) as a function of degrees of conversion estimated by KAS, ST, TA and OFW methods

The curves of all methods are identical in the trend but different in the values. All methods indicate that the reaction mechanism is a complex multi-step reaction. The difficulties in comparing between model free kinetic data arises from the different mathematics methods and the heterogeneous nature of the Subcoal™. The E_a plots for pyrolysis, CO_2 gasification, combustion shows that the OFW method produced a slightly higher value of E_a at fixed conversion as compared with ST, KAS, and TA. The complexity in the gasification reaction mechanism is more obvious than that in pyrolysis. The KAS, ST, and TA methods exhibit excellent agreement due to the similar kinetic mathematics estimation.

Comparing E_a of Subcoal™ PAF results with the literature, Singh, et al. [258] found the pyrolysis of MSW of E_a 294.8 kJ/mol [258]. While 313.77 kJ/mol for polyethylene was reported by Gou et al. [259]. Chen et al. [260] found the E_a of MSW in CO_2 gasification for polyester fabrics is 211 kJ/mol, and polyethylene (PE) is 221 kJ/mol [260]. Also, Azam [261] identified the E_a of MSW combustion as 116.1 kJ/mol [261]. However, the E_a of RDF and SRF combustion are 203 kJ/mol and 86.8 kJ/mol, respectively [262]. In addition, the E_a of RDF and SRF pyrolysis are 252.5 kJ/mol and 238.3 kJ/mol, respectively [263]. These results prove that the E_a of Subcoal™ PAF is lower than other biomass from the literature.

6.3 Model fitting kinetics evaluation with catalysts

6.3.1 Effect of dolomite

The CR method was selected to determine the kinetic parameters of pyrolysis, CO_2 gasification and combustion in the presence of dolomite at different concentrations (0, 5, 10, 15, 20 wt.%). As the CR is a model-fitting method, different mechanism models (G(x)) were attempted to estimate the appropriate kinetic parameters using Eq. 4.29 and Eq. 4.30, respectively. In addition, the mathematical formula of all models is provided in Section 4.4.2.1, Table 4-1. Figure 6-7 shows the most fitting models (G15) conversion as a function of temperature. The pyrolysis plotted lines are not linear at some conversion rates referring to the complexity of the reaction mechanism in the present of dolomite, as shown in Figure 6-6. Table D-1 in Appendix D: CR Method Kinetic Parameters lists the kinetic parameters of pyrolysis with R^2 values for each mechanism model tested, and Figure 6-8 displays a comparison of E_a.

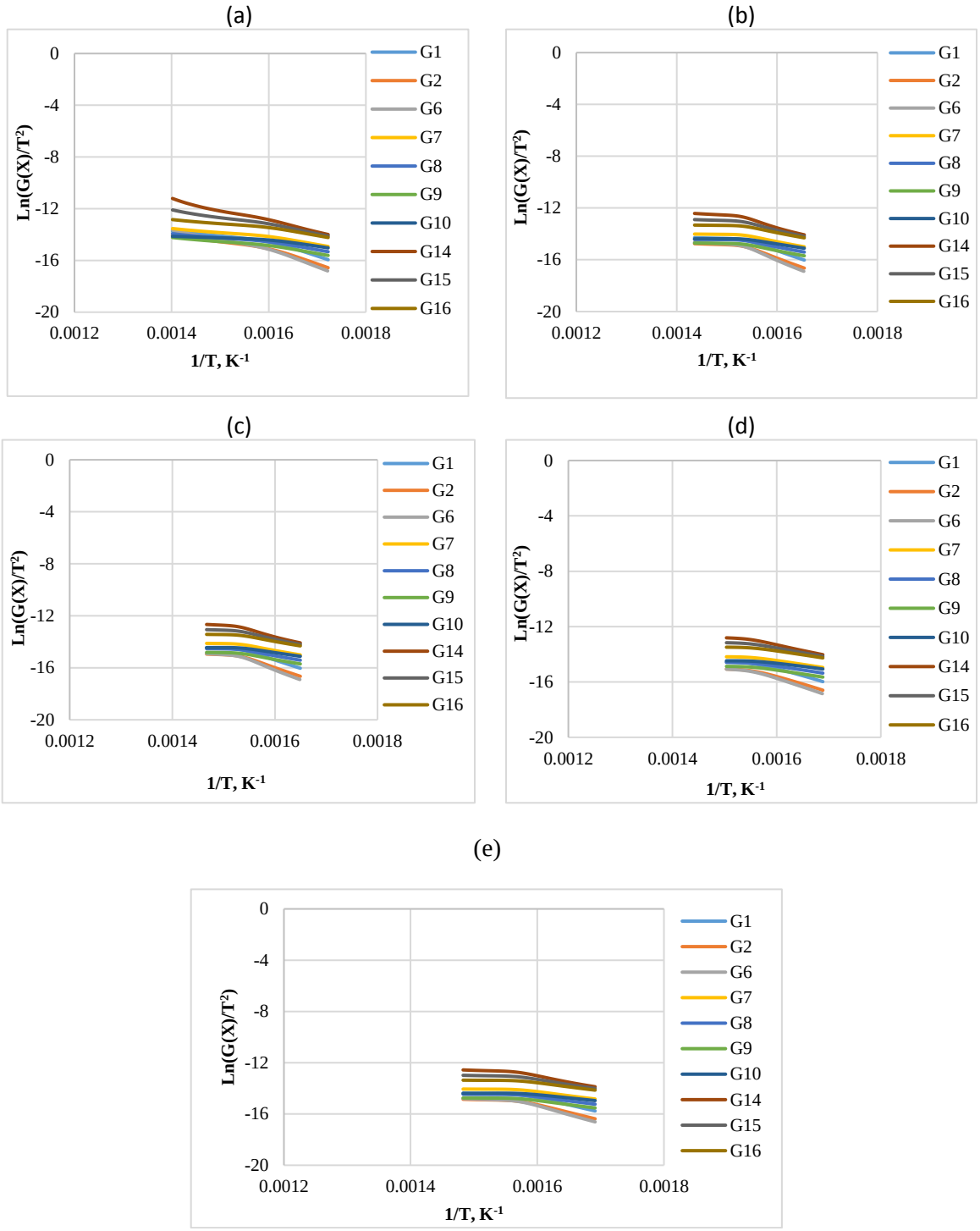

Figure 6-6 The CR method plots for pyrolysis at different dolomite loadings; (a) 0 wt.%, (b) 5 wt.%, (c) 10 wt.%, (d) 15 wt.% and (e) 20 wt.%

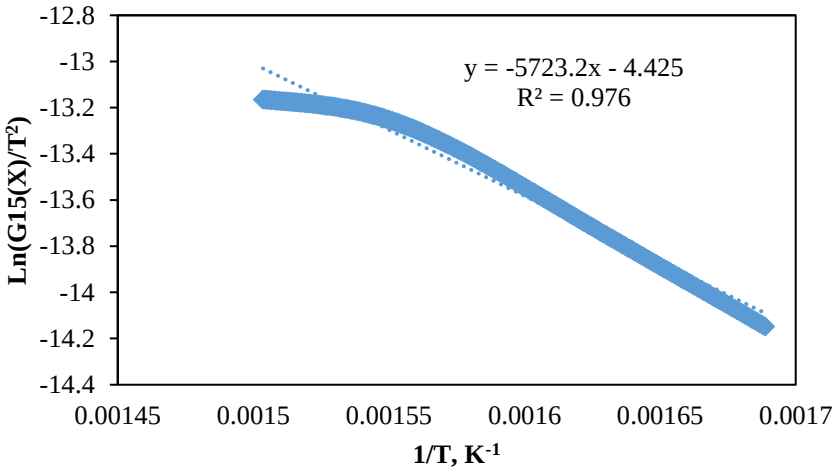

Figure 6-7 plot of the conversion function for the best CR fitting model (G15) Vs reciprocal of temperature for Subcoal™ PAF pyrolysis with 15 wt.% dolomite

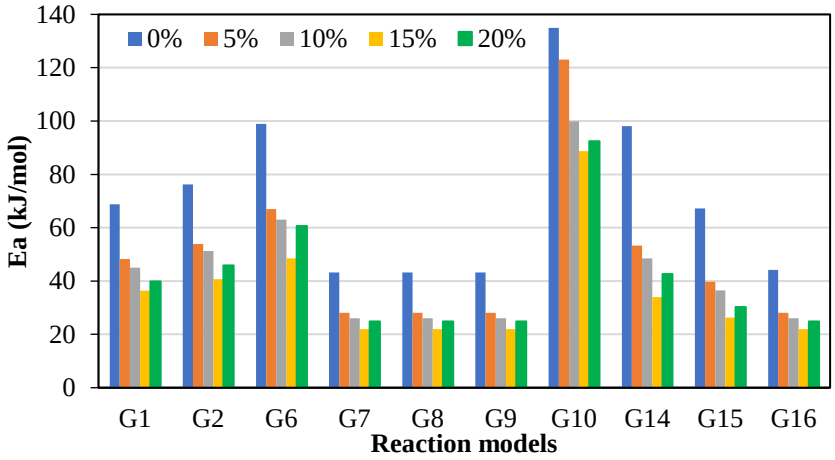

Figure 6-8 E_a from the most fitting reaction models of pyrolysis at different dolomite loadings

It can be seen that the E_a of each model decreases as the concentration of catalyst increases from 0 to 15 wt.%. Also, the best fitting model with 15 wt.% dolomite is G15 (Chemical reaction (n=2)) with E_a = 26.3 kJ/mol, A = 31.2 min^{-1}, and R^2 = 0.976. However, the E_a increases at 20 wt.% of dolomite due to carbon deposition on the surface of the catalyst as described in detail in Section 2.10.2. The presence of dolomite promotes the pyrolysis intermediate reactions and it reduces the energy barrier of reaction, hence reducing the E_a based on Maxwell-Boltzmann theory. The reduction in E_a leads to an increase in the overall rate of reaction [264].

The effect of dolomite loading on the CO_2 gasification kinetic parameters were evaluated as listed in Table D-2 in Appendix D: CR Method Kinetic Parameters. The table also includes the goodness of fit coefficient to the regression model (R^2) value based on E_a value to demonstrate the appropriateness of the model fitting. Figure 6-9 and Figure 6-11 show the approximated curves of the CR method for different reaction models (G(x)) and a comparison of E_a.

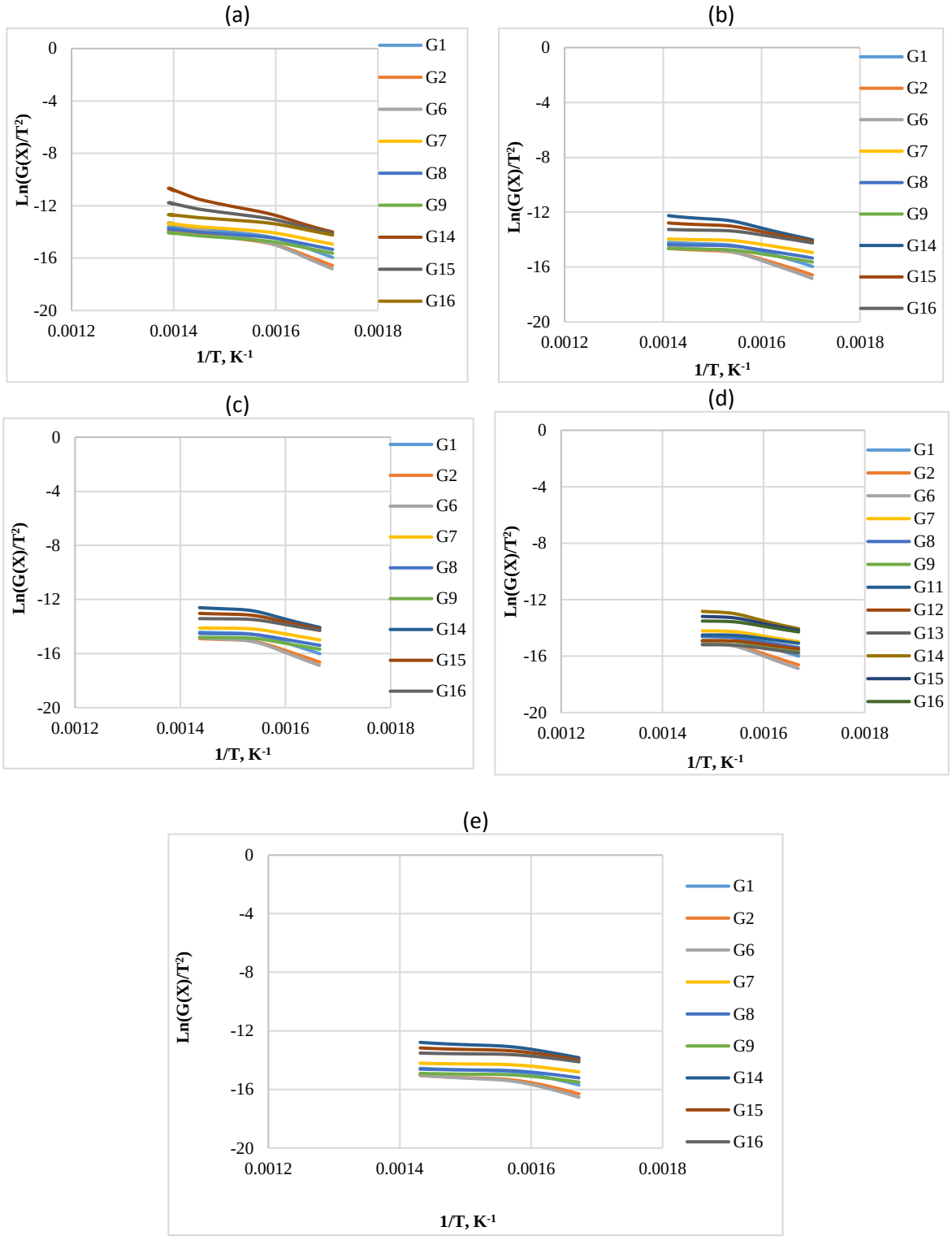

Figure 6-9 The CR method plots for CO_2 gasification at different dolomite loadings; (a) 0 wt.%, (b) 5 wt.%, (c) 10 wt.%, (d) 15 wt.% and (e) 20 wt.%

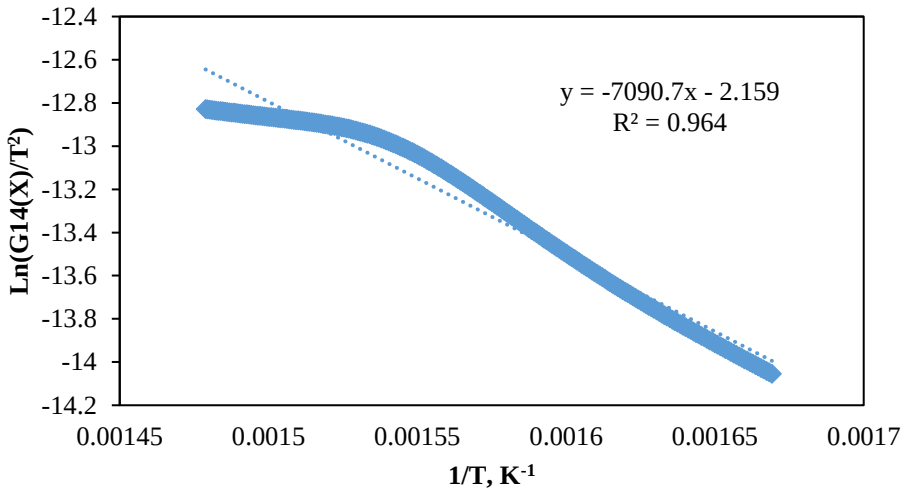

Figure 6-10 plot of the conversion function for the best CR fitting model (G14) Vs reciprocal of temperature for Subcoal™ PAF CO_2 gasification with 15 wt.% dolomite

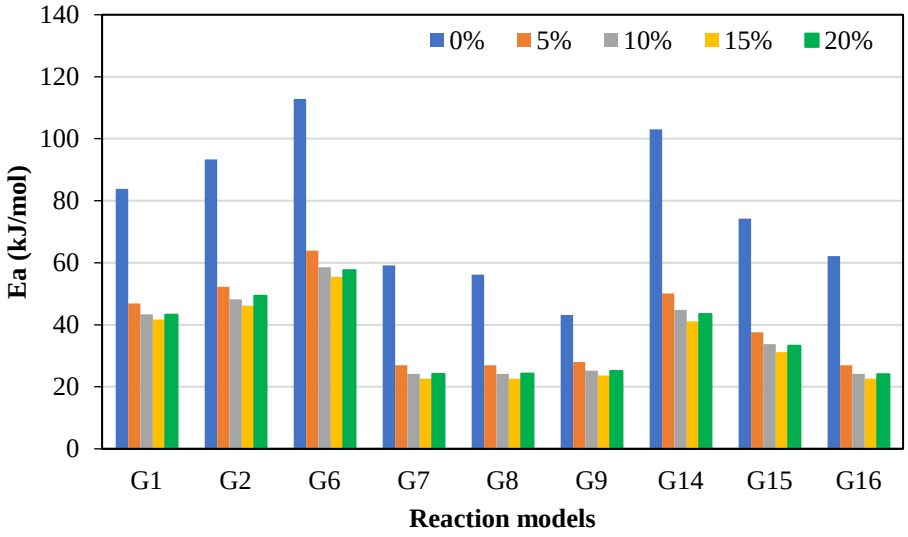

Figure 6-11. E_a from the most fitting reaction models of CO_2 gasification at different dolomite loadings

The linear relationship between ln(G(X)/T^2) and 1/T implies a single mechanism reaction. Figure 6-10 shows the best fitting models (G14) conversion as a function of temperature. However, most curves in Figure 6-9 demonstrate that the reaction takes place based on complex mechanism. Furthermore, as the catalyst ratio increased from 0 to 15 wt.%, the reaction lines for all models decreased due to a shorter reaction time, as shown in Figure 6-9. The calculated E_a and A values with the highest coefficient values (R^2= 0.964) are 41.1 kJ/mol and 370 min^{-1} found using G14 (Chemical reaction (n=3)) at 15 wt.% of dolomite loading, as shown in Table D-2 in the Appendix D: CR Method Kinetic Parameters. However, the other models also show high R^2 with different values of E_a due to the complexity of the Subcoal™ PAF gasification reactions, and the inhomogeneity of the material. The variation in the E_a was obtained due to the reaction mechanism models, as reported by by Aboulkas and El Harfi [265].

The effect of dolomite loadings on the combustion kinetic parameters were investigated, as plotted in Figure 6-12. Figure 6-14 displays a comparison of E_a. Figure 6-13 shows the best fitting models (G14) conversion as a function of temperature. Table D-3 in the Appendix D: CR Method Kinetic Parameters lists the kinetic parameters for different mechanism models of combustion.

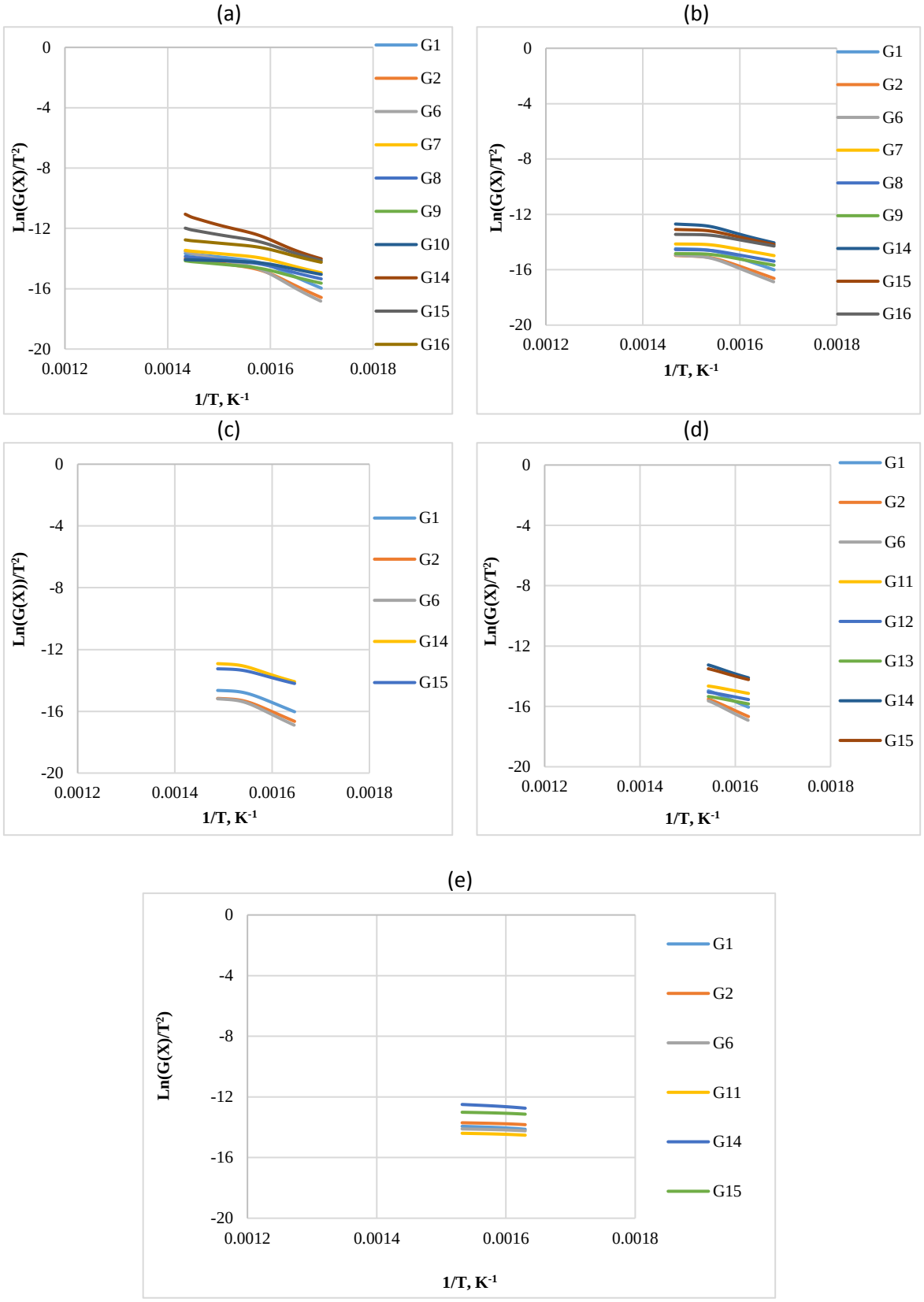

Figure 6-12 The CR method plots for combustion at different dolomite loadings; (a) 0 wt.%, (b) 5 wt.%, (c) 10 wt.%, (d) 15 wt.% and (e) 20 wt.%

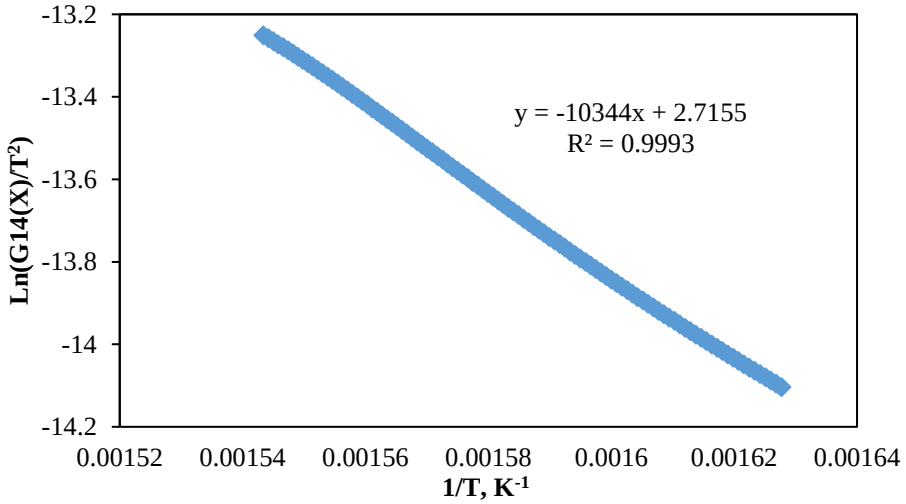

Figure 6-13 plot of the conversion function for the best CR fitting model (G14) Vs reciprocal of temperature for Subcoal™ PAF combustion with 15 wt.% dolomite

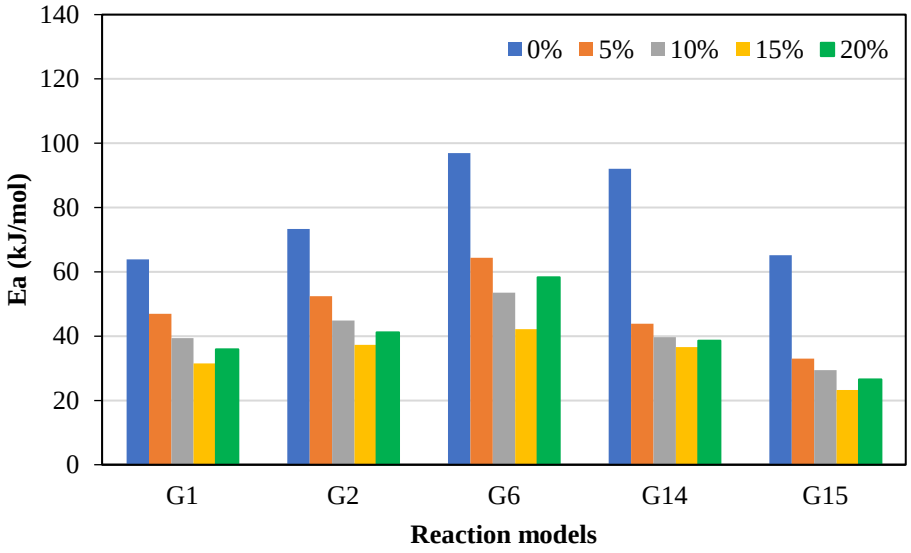

Figure 6-14 E_a from the most fitting reaction models of combustion at different dolomite loadings

As a result of non-linear relationships, some mechanism models are negligible due to low R^2 value, such as G11 (Mampel power law (n=1/2)), G12 (Mampel power law (n=1/3)), and G13 (Mampel power law (n=1/4)). The best fitting model of E_a and A values are found in G14 (Chemical reaction (n=3)) with 15 wt.% of dolomite 36.6 kJ/mol, 80 min^{-1} and R^2 = 0.999. The E_a obtained by CR at G2 (Two-dimensional diffusion (Valensi)) and G15 (Chemical reaction (n=2)) without catalyst are the closest value to E_a obtained by model-free methods.

6.3.2 Effect of olivine

The influence of olivine on the E_a for pyrolysis was examined, as illustrated in Figure 6-15 and Figure 6-17. Figure 6-16 shows the best fitting models (G14) conversion as a function of temperature. Table D-4 in the Appendix D: CR Method Kinetic Parameters lists the kinetic parameters for different reaction models.

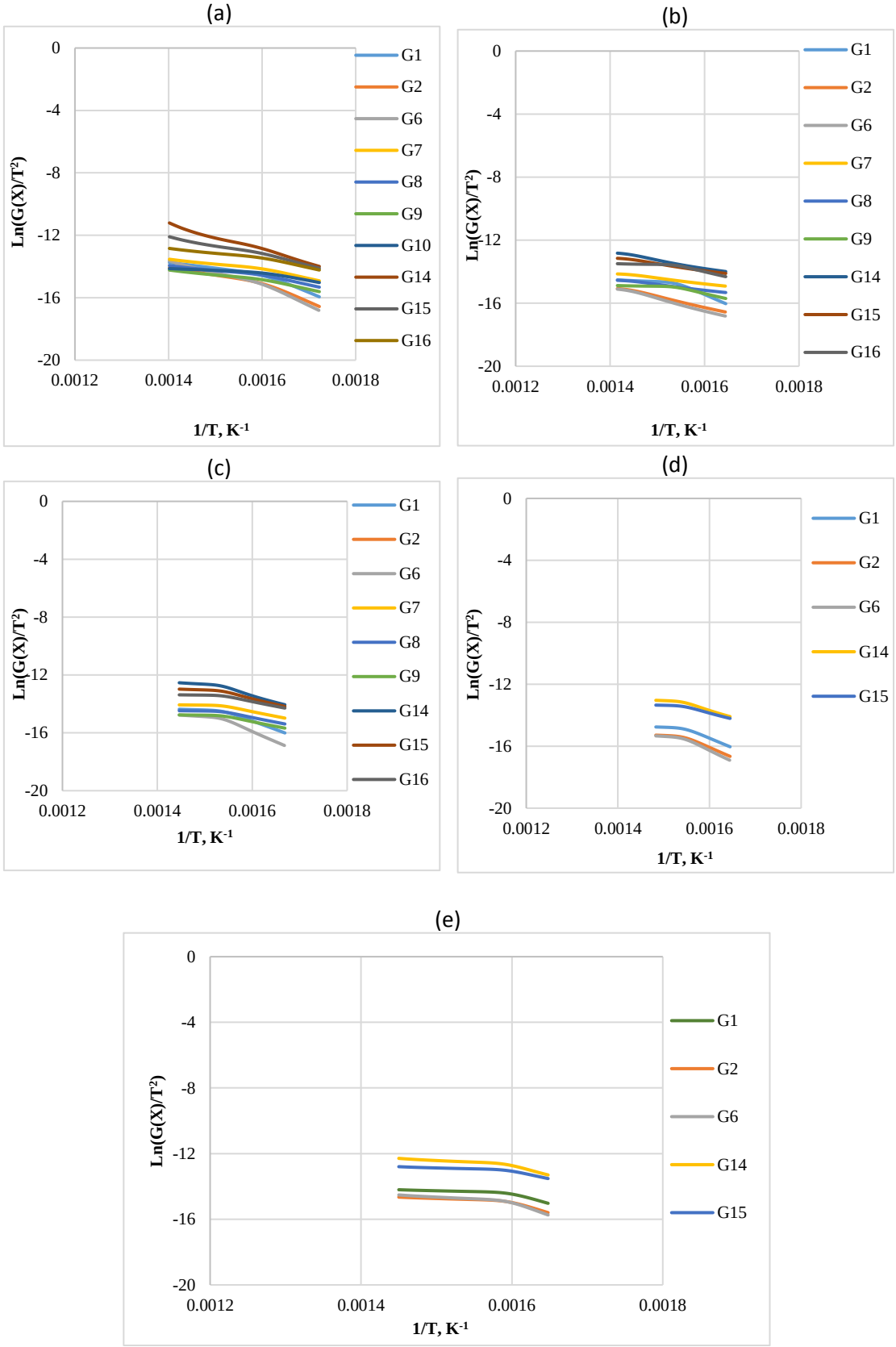

Figure 6-15 The CR method plots for pyrolysis at different olivine loadings; (a) 0 wt.%, (b) 5 wt.%, (c) 10 wt.%, (d) 15 wt.% and (e) 20 wt.%

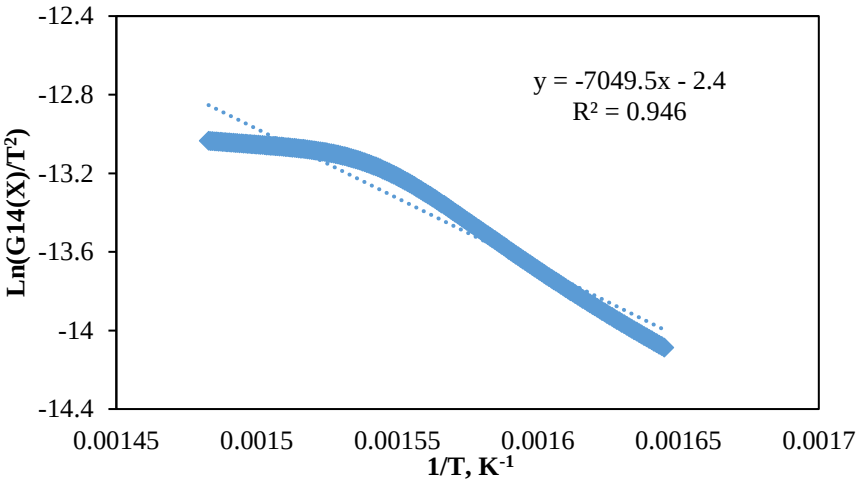

Figure 6-16 plot of the conversion function for the best CR fitting model (G14) Vs reciprocal of temperature for Subcoal™ PAF pyrolysis with 15 wt.% olivine

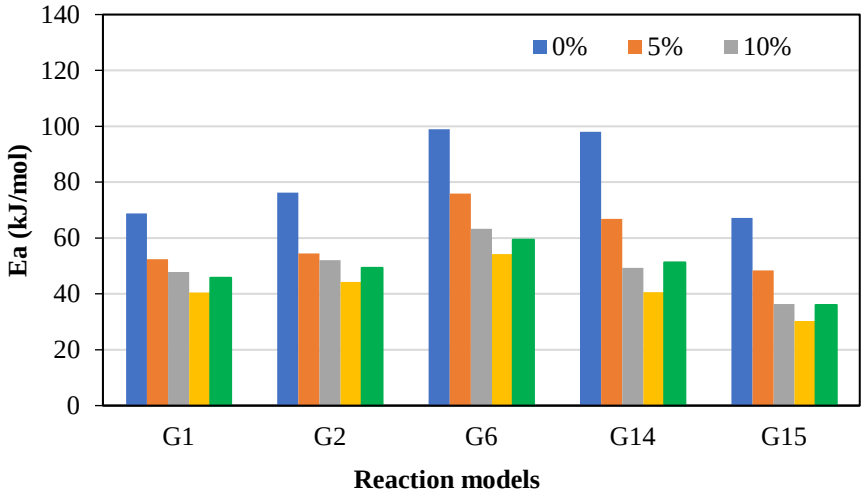

Figure 6-17 E_a from the most fitting reaction models of pyrolysis at different olivine loadings

The model which yields high linearity plots in the presents of 15 wt.% of olivine is G14 (Chemical reaction (n=3)). The presence of olivine has low attrition resistance when compared with dolomite, promotes several secondary reactions making the mechanism more complex [266]. Considering the models G1 (One-dimensional diffusion), G2 (Two-dimensional diffusion), G6 (Nucleation and growth (n=2/3)), G14 (Chemical reaction (n=3)), G15 (Chemical reaction (n=2)), the E_a decreases with olivine loadings increase from 0 to 15 wt.% and slightly increased at 20 wt.%, as listed in Table D-4 in the Appendix D: CR Method Kinetic Parameters. The best fitting model with 15 wt.% olivine is G14 with E_a = 40.6 kJ/mol, A = 80.4 min^{-1}, and R^2 = 0.946.

Figure 6-18 displays reaction kinetic graphs of gasification at different loadings of olivine loading. Figure 6-19 shows the best fitting models (G15) conversion as a function of temperature. Figure 6-20 below shows E_a comparison and Table D-5 in the Appendix D lists the kinetic parameters for different reaction models.

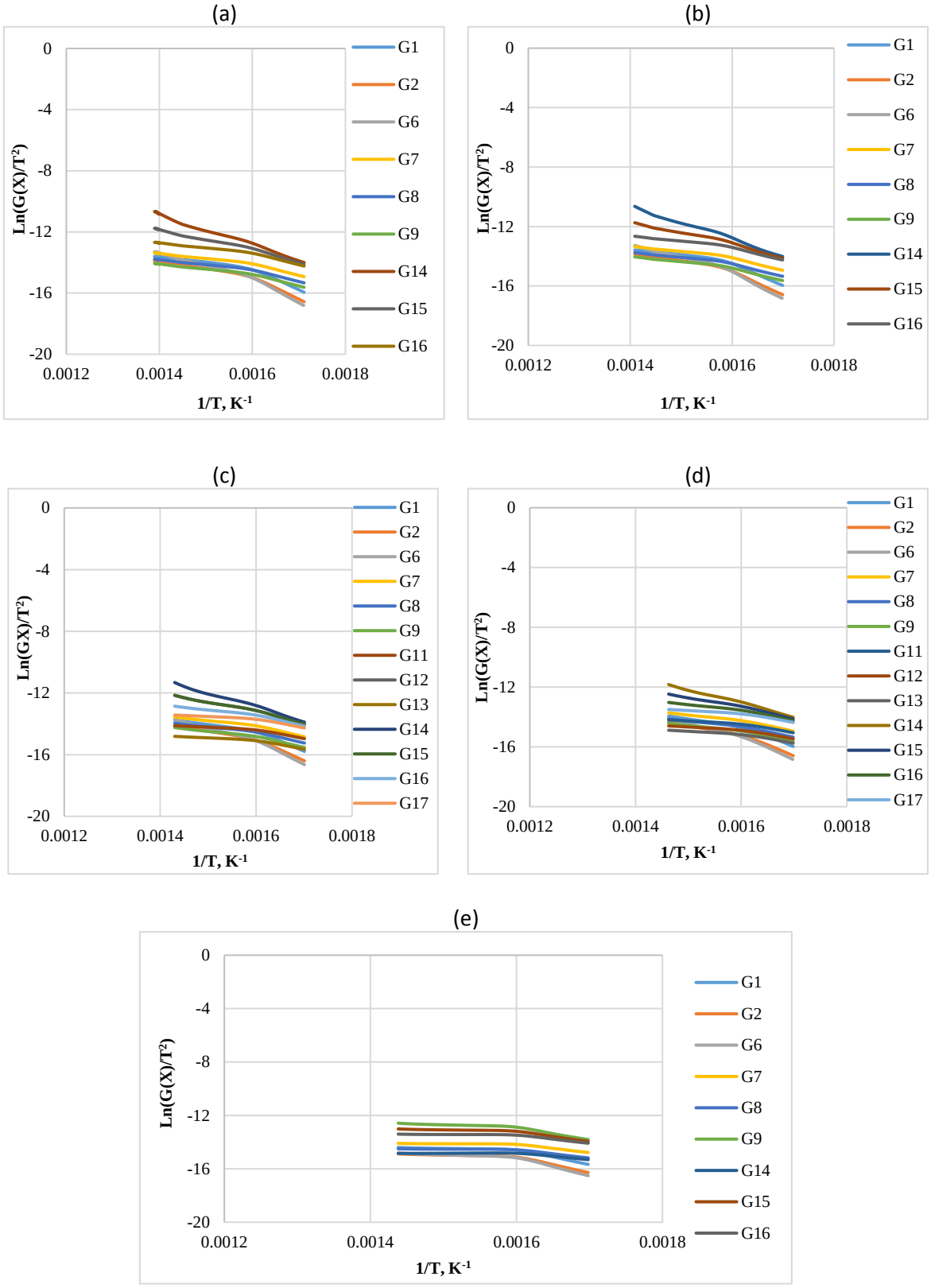

Figure 6-18 The CR method plots for CO_2 gasification at different olivine loadings; (a) 0 wt.%, (b) 5 wt.%, (c) 10 wt.%, (d) 15 wt.% and (e) 20 wt.%

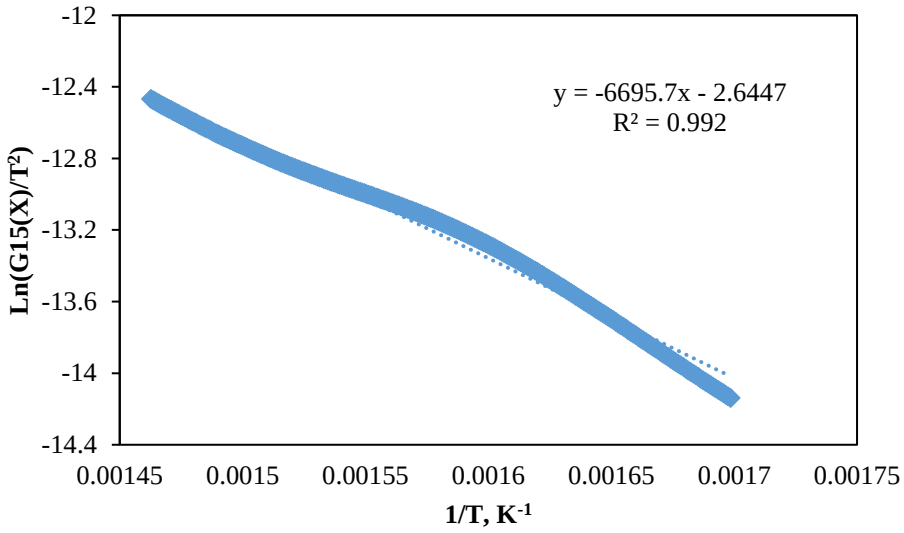

Figure 6-19 plot of the conversion function for the best CR fitting model (G15) Vs reciprocal of temperature for Subcoal™ PAF CO_2 gasification with 15 wt.% olivine

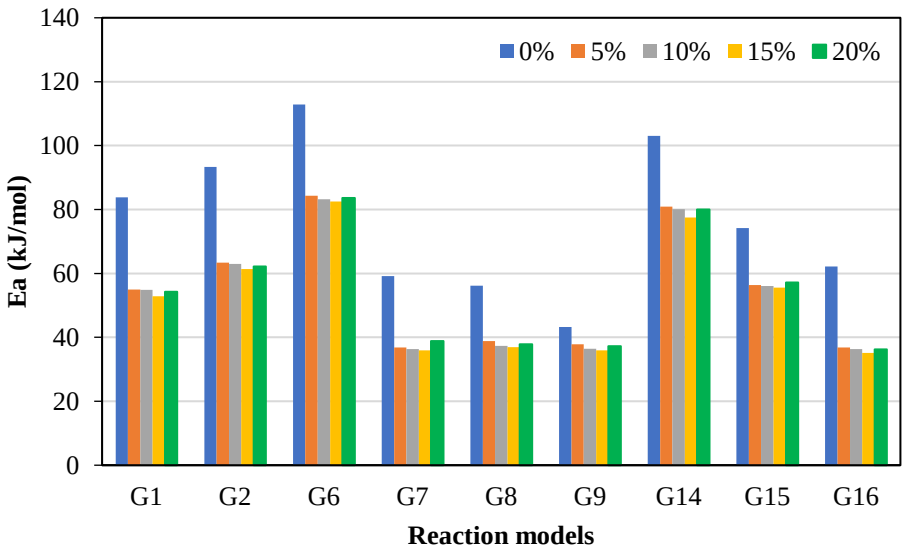

Figure 6-20 E_a from the most fitting reaction models of CO_2 gasification at different olivine loadings

The graph trends and layout of the gasification with olivine is closer to pyrolysis than combustion. Model G15 (Chemical reaction (n=2)) at 15 wt.% olivine exhibits excellent linearity with the highest R^2 value of 0.992, which makes it a good candidate for estimation E_a= 55.6 kJ/mol and A = 1.4E+04 min^{-1}. However, model G6 (Nucleation and growth (n=2/3)) yields in the absence of dolomite are the closest kinetic parameters to those estimated by the model-free methods.

Figure 6-21 shows a kinetic plot of the combustion reaction of the effect of olivine loading on the kinetic parameters. In addition, Figure 6-22 shows the best fitting models (G2) conversion as a function of temperature. Table D-6 in the Appendix D: CR Method Kinetic Parameters lists the kinetic parameters and Figure 6-23 illustrates a comparison between E_a for different reaction models.

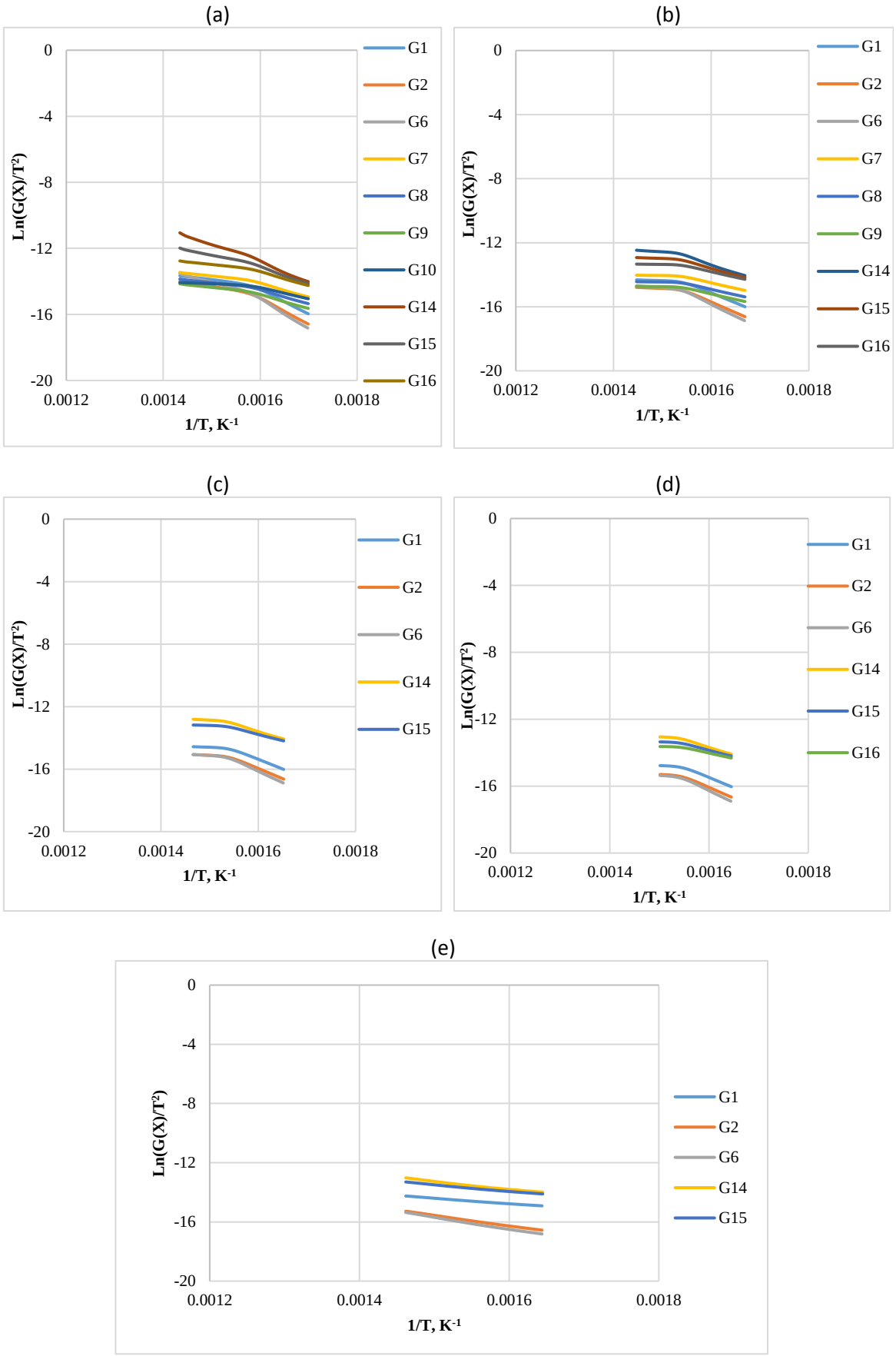

Figure 6-21 The CR method plots for combustion at different olivine loadings; (a) 0 wt.%, (b) 5 wt.%, (c) 10 wt.%, (d) 15 wt.% and (e) 20 wt.%

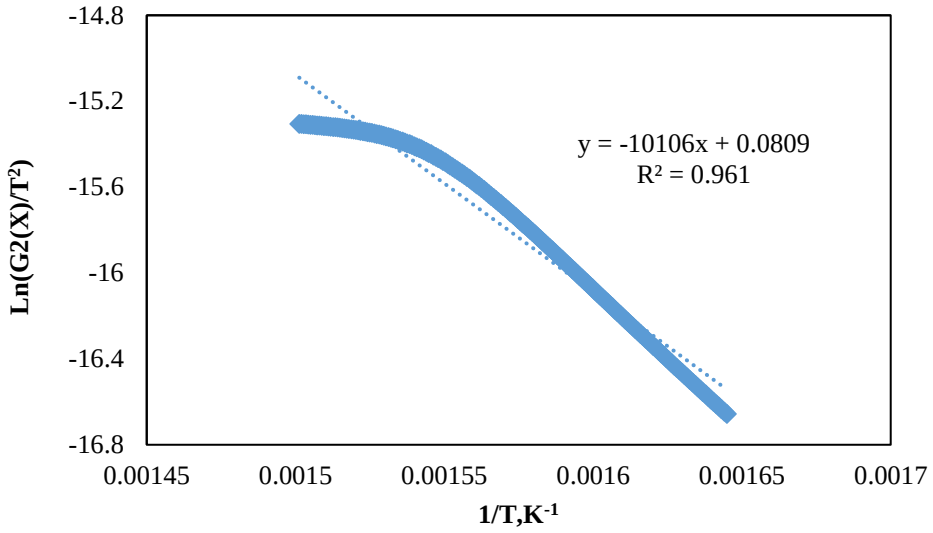

Figure 6-22 plot of the conversion function for the best CR fitting model (G2) Vs reciprocal of temperature for Subcoal™ PAF combustion with 15 wt.% olivine

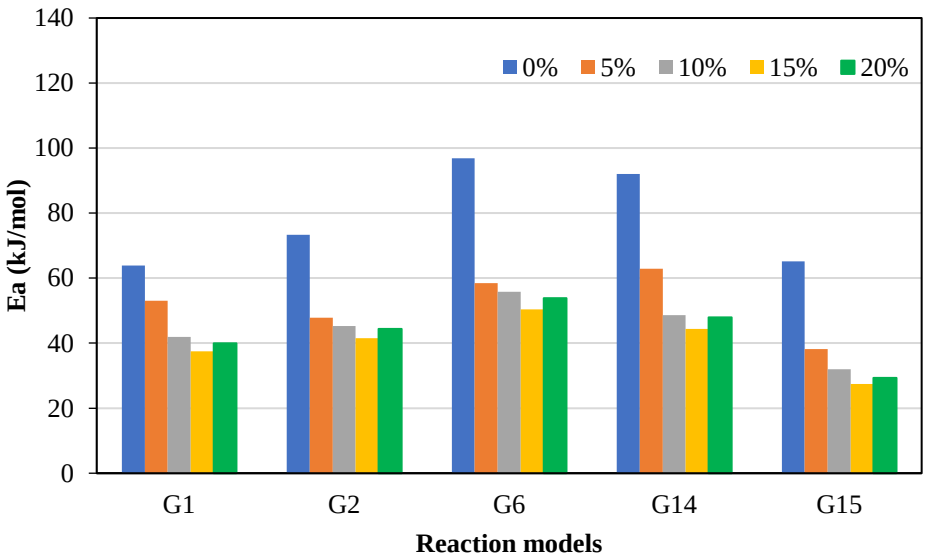

Figure 6-23 E_a from the most fitting reaction models of combustion at different olivine loadings

Different reaction models were fitted and obtained a linear relationship. Some models did not yield linear relationships and were therefore ignored. The best fitting reaction model with the lowest calculated E_a and A values was found in G2 (Two-dimensional diffusion) for combustion with 15 wt.% of olivine ratio as 41.5 kJ/mol, 32.2 min^{-1} and R^2 = 0.961.

6.4 Kinetics discussion

The kinetics parameters theoretically have a significant impact on the decomposition process investigations. It can be employed to the reaction mechanisms of the chemical decomposition, which especially occur in heterogeneous and non-isothermal conditions. In terms of practice, the kinetics parameters are essential to estimate the required design parameters such as reactor volume and the

operating conditions. Moreover, the relationship between time and temperature, storage conditions, and the shelf life for products can be predicted using the kinetics parameters [233]. Therefore, the validity of different kinetic evaluation methods was compared to estimate the E_a and A for pyrolysis, CO_2 gasification, and combustion of Subcoal™ PAF based on TGA data. The TGA data were obtained for four different heating rates (5, 10, 15, 20 ^oC/min) to avert the compensation impact in the estimation of kinetic parameters without catalyst [267]. The kinetic evaluation is very important for identifying the operating conditions of pyrolysis, gasification, and combustion processes for particular feedstock. The E_a was estimated based on overall devolatilisation reaction in which the removal of H_2, bounded surface water, as well as the structural degradation of Subcoal™ was executed [233].

The kinetic parameters obtained by KAS, ST and TA show more accurate E_a results with high R^2 values when compared to those obtained from OFW method. Also, the KAS plots in pyrolysis are more parallel to each other than those in gasification and combustion. This explains that the reaction mechanism in the presence of CO_2 as a gasifying agent is more complex [83]. The E_a obtained by ST and TA methods were much closer to KAS. There are slight differences in average E_a of OFW which are caused by the improper approximation of temperature integration. These findings are confirmed by Guida [237]. In all model free methods, the E_a value of Subcoal™ PAF combustion is less than gasification and pyrolysis. The presence of O_2 promotes the oxidation reaction and reduces the E_a. A series of oxidative reactions occur by O_2 which leads to an increase in the gasification rate [268].

The CR method was used to assess the influence of olivine and dolomite catalysts on the kinetic parameters. This method evaluates E_a mechanism for each reaction model at a fixed heating rate (20 ^oC/min) and low experimental error (± 2). For pyrolysis and CO_2 gasification without catalyst, G14 (Chemical reaction (n=3)) model could be the best appropriate model for this complex reaction. While for combustion, G16 (Chemical reaction (n=1)) model obtained a high R^2 value. On the other hand, pyrolysis, CO_2 gasification, and combustion with 15 wt.% dolomite shows G15, G14, and G14 are the best fitting reaction models. While for pyrolysis, CO_2 gasification and combustion with 15 wt.% olivine was G14, G15 and G2. The results obtained by CR method showed lower uncertainty when compared with the other model-free methods and good agreement with the experimental data [138]. However, some models were not considered due to low R^2 value [269]. The range of E_a achieved in CO_2 gasification is wider than pyrolysis which indicates that the thermal stability of pyrolysis is higher. Therefore, the E_a required by pyrolysis is found to be lower than that in CO_2 gasification [260]. The results showed that dolomite has a better performance in comparison with olivine in catalysing pyrolysis, CO_2 gasification, and combustion reactions. In the presence of dolomite or olivine, the E_a was significantly reduced with the increase of catalyst loadings 0, 5, 10 and 15 wt.% [264]. While the E_a for all experiments increased at 20 wt.% of olivine or dolomite. The main reason for catalyst ineffectiveness at 20 wt.% is an increase in carbon deposition on the

surface of the catalyst due to the rise in the percentage of hydrogen removal, which causes pore blockage, reduces surface area, and thus inhibits the work of the catalyst [117].

The results of CR exhibited that the reaction is a chemical reaction controlled in the first stage of degradation (reaction extent less than 0.2). In the second stage of degradation, when the reaction extent is between 0.2 and 0.8, the reaction is controlled by three-dimensional diffusion and chemical reaction. Finally, at a reaction extent greater than 0.8, the reaction is solely controlled by the three-dimensional diffusion mechanism [270].

The kinetic analysis of all tested methods shows a significant variation of E_a as a function of conversion. This illustrates that the reaction mechanism of Subcoal™ PAF is complex and it occurs in a multistage thermal decomposition. The higher the complexity of the dehydration mechanism, the greater the variation of E_a [271]. The findings of the isoconversional methods state that the E_a is dependent on conversion and measures the overall reaction. While model-fitting methods identified that the E_a is based on each reaction model. Heating rate is an essential parameter in the estimation of the E_a and A using the non-isothermal TGA data. An inaccurate determination of the heating rate may lead to imprecise estimation of the kinetic constants. Therefore, 20 ºC/min was the optimum heating rate for Subcoal™ PAF and was used to evaluate the influence of the catalyst experiments. Miscalculation of the heating rate is one of the significant sources of error in the kinetic evaluation as described in Section 4.2. The assumption of the actual heating rate, or more explicitly, the programmed heating rates, is the main reason for the heating rate miscalculation. Other factors that may contribute to inaccurate determination of heating rate are self-heating/cooling, and purge gas cooling. The potential experimental errors can be reduced by conducting experimental repeatability [272].

6.5 Summary

In this chapter, the reaction kinetics were evaluated using model free and model-fitting methods. Both approaches showed kinetics analysis results with some variation of E_a due to mathematical evaluation method and sample reaction complexity. However, the CR method is preferred over other methods because it does not necessitate experimental repetitions and investigates the reaction mechanisms with lower error (± 2) than model free methods. The influence of olivine and dolomite loading (0 to 20 wt.%) on the behaviour of thermal conversion of the sample was determined at a constant heating rate (20 ºC/min).

The increase in the heating rate has an impact on the reaction kinetics which leads to an increased degradation rate. The influence of different loadings of dolomite and olivine ratio on Subcoal™ PAF showed a reduction in the E_a from 0 to 15 wt.%. While the E_a increased for both catalysts at 20 wt.% due to an increase in carbon deposition on the surface of the catalyst. In comparison with olivine, dolomite at loading 15 wt.% produces a lower E_a value and makes the degradation reaction more

favourable. In addition, Subcoal™ with 15 wt.% dolomite shows better kinetic performance than olivine. These findings have been supported by some studies from the literature. It is expected that at catalyst loadings above 15 wt.%, no significant change in the E_a may occur due to supersaturation conditions of the catalyst. In the comparison of the results of the model-free methods, KAS, TA, ST have produced a more accurate kinetics analysis than OFW method. Also, the lowest E_a obtained was for combustion which is due to the role of O_2 and sample properties. The CR method showed that G15 is the best appropriate model for describing the reaction of pyrolysis in the presence of 15 wt.% dolomite. However, G14 provided the best fitting reaction model for CO_2 gasification and combustion at 15 wt.% dolomite with high R^2 values.

Chapter 7: BFBGR Results and Discussion

7.1 Introduction

In this chapter, the gasification of Subcoal™ pellet A and pellet B in the bubbling fluidised bed gasifier reactor (BFBGR) was studied. Cold and hot test runs of the fluidised bed were carried out to investigate the parameters in the presence and absence of the heating source under isothermal conditions. Also, the CO_2 gasification process was carried out in the TGA at different loadings of sand bed material to investigate the effects of sand on Subcoal™ gasification. The effects of ER, bed temperature, particle size and catalysts on the air gasification process using FBGR has been discussed. In addition, the findings detail the characteristics of the producer gas and chemical reactions. The assessment of product gas quality from the FBGR includes gas composition, high heating value (HHV), carbon conversion efficiency (CCE), cold gas efficiency (CGE), char and dry gas yield (Y). The effectiveness of olivine and dolomite at various loadings (5, 10, 15, 20 wt.%) was identified. The findings obtained from the FBGR have been compared to TGA results concerning the operating temperature and catalysts concentration. Finally, material balance calculations on the FBGR were carried out.

7.2 Experimental test run

7.2.1 Cold run

In the combustion laboratory of Cardiff School of Engineering, the cold experimental rig was built to study cold bubbling fluidised bed hydrodynamic parameters. The cold experiment was performed to investigate the hydrodynamic design parameters of fluidised bed reactor using sand at different air flow rates. The behaviour of the bed fluidisation and pressure across the bed were checked against the data reported by previous researcher Al-Farraji [138] who successfully used this setup to evaluate FBGR performance. The components of the rig are illustrated in Figure 7-1 below. The current rig comprises a regulator for air pressure, air box, diffuser plate, transparent pipe, and three rotameters for feeding the required flow rate to the fluidised bed column.

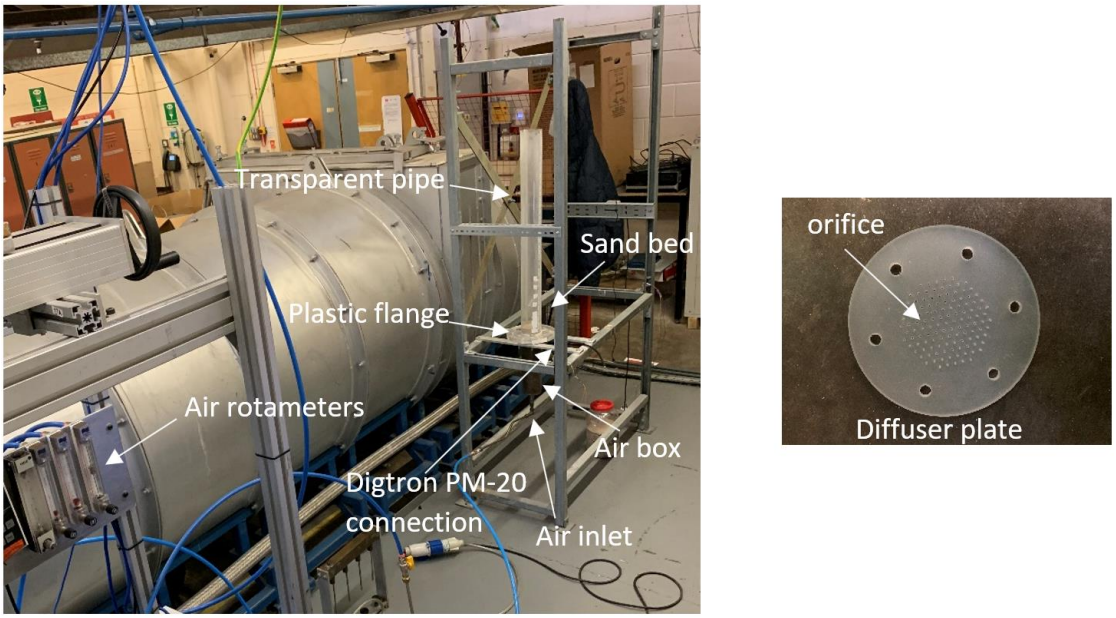

Figure 7-1 Cold bubble fluidised rig

The fluidised bed column has a distributer plate where pressure drop was measured using a digital manometer (Digtron PM-20). This was linked to the section of the air-box pipe and it joins the manometer positive point. The second point illustrated through the use of the multi-points is situated at the transparent column for the fluidised bed on top of the distributor plate and it joins the manometer negative point. Standard fittings are also included in the cold rig to ascertain that connection occurs between various components using PVC tubes. As illustrated in Figure 7-1, a plastic acrylic diffuser plate was included that contains similar specifications to the external diameter of the stainless-steel metal plate used in the gasifier rig.

The bed material was composed of 400 g of silica sand (500-600 µm particle size), with the air flow rate varied between 10 l/min and 40 l/min. As the compressed air moved via the distributor holes to the packed sand bed, sand particles moved through the free space column, forming an environment of fluidised bed. The air flow rate and type of the distributor determine the bed expansion size. The sand bubble fluidisation onset was at 1 bar pressure and 40 l/min. In the diffuser plate, smooth fluidisation was confirmed after adding 43 g pellet of Subcoal™ (14-27 mm). The recording of the pressure drop was very small across the plate in the interval of 40 l/min and neglected. The cold experiment is an exact representation of an actual case of experiments on hot rig gasification taking into account variation in gas flow velocity due to temperature change.

7.2.2 Hot run

The hot isothermal test was also carried out to examine the relationship between air flow rate and pressure, as well to determine the behaviour of pellet fluidisation under heating condition. By conducting hot isothermal test runs in air-sand between 500-600 µm as singled bed material of FBGR at 300 °C, the fluidisation behavior of sand in the air flow rate range of 10 l/min to 40 l/min was examined. A thermal equilibrium was established between the preheater and rig furnace set to

experimental conditions of the temperature under investigation. An increase of air flow was provided until the point of detection of bed fluidisation occurred at the bottom of the gasifier. Between 30 l/min and 40 l/min, the first observation was made for the air bubbles. The lab extraction fan was started after attaining a steady-state gasifier condition. The membrane pump was then activated to ensure that product gases were directed to the gas analyser. The vibrator feeder then started providing an ER = 0.2 to ascertain a consistent flow of delivery 43 g of Subcoal™ pellets (27-14mm) from the top of the gasifier.

At the lower part of the gasifier, there was a stable hydrodynamic fluidisation behaviour of sand and pellets at 40 l/min. A thermocouple was used to measure the temperature changes at the top and bottom of the gasifier reactor. The thermocouple system is described in detail in Section 4.7.9. The gas was discharged to the gas analyser using the membrane pump after cleaning the product gas in the tar capturing unit. In real time, recordings were made by the gas analyser to monitor the gas reaction (vol%) as a function of time (5 minutes). The gas analyser calibration method is described in Section 4.7.12. Once the test was completed, the gasifier was shutdown and time was provided for cooling down to room temperature. The time taken for the cooling processes was 5 hours and the next test was conducted after replacing the sand. Finally, N_2 was purged to the gasifier and gas analyser re-calibration was conducted. After each experiment, the producer gas stainless steel pipe and pump filter were replaced to ensure no blockages or tar content before the next run.

7.3 Effect of sand

The effect of various loading of silica sand on Subcoal™ PAF CO_2 gasification was experimentally derived using TGA at a constant heating rate (20 ^{0}C/min) and flow rate of 100 ml/min. The conversion of the decomposition reactions are plotted as a function of temperature in Figure 7-2.

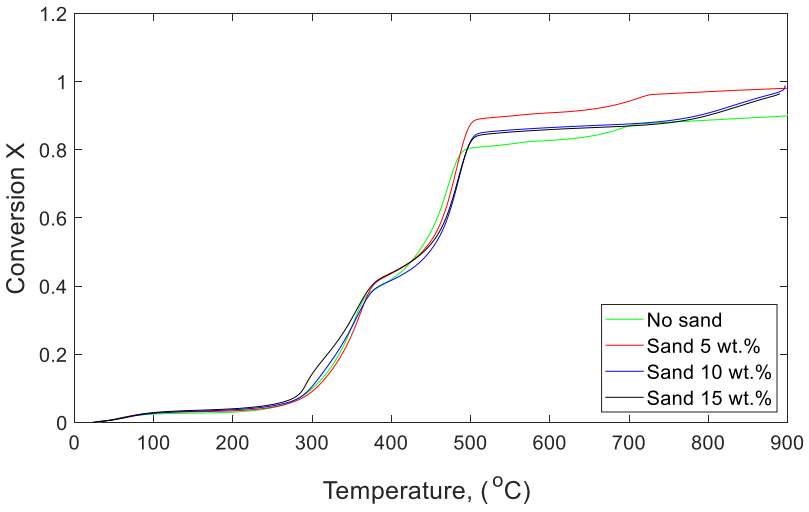

Figure 7-2 Effect of sand loadings on the CO_2 gasification conversion curve

Insignificant variation was observed in the conversion among the different loadings of sand. The degradation of Subcoal™ with different loadings of silica sand was observed at four decomposition

stages, based on the relationship between conversion and temperature in Figure 7-2. The conversion performance at the various weight of sand illustrated the same behaviors compared with the gasification reaction without sand. This confirms that there is no chemical interaction between the silica sand and Subcoal™ at various loadings. As a result, it was deemed suitable to be used as a bed material for gasification experiments in the FBGR. In addition, silica sand was suitable for gasification in the presence of catalyst and Subcoal™.

7.4 Gas composition analysis

7.4.1 Effect of Equivalence ratio

The effects of ER on the gas composition, heating value, and yield of the producer gas were evaluated in the experiments described herein. The experiments were performed at 750 °C for an ER range of 0.15 to 0.35 using a constant air flowrate of 40 l/min gasifying agent. Figure 7-3 shows the change of gas composition as a function of the ER. The volume fraction of H_2 and CO decreased in the outlet gas as the ER increased. The produced CO and H_2 were oxidised to CO_2 and H_2O as the ER increased [273]. The CO, CH_4, and H_2 content of the producer gas was observed to drop from 16.2 vol %, 7.2 vol %, and 9.1 vol % at an ER of 0.15 to 10.4 vol %, 4.5 vol %, and 5.1 vol % at an ER of 0.35, respectively. However, the CO_2 content slightly increased from 10.4 vol% at an ER of 0.15 to 14.1 vol % at an ER of 0.35.

With the ER increase, the char was completely oxidised to CO_2 instead of CO and the H_2 oxidised to steam according to reactions (R2.8 and R2.2). However, the decrease in the ER lead to dilution of product gas, hence H_2 and CO concentration product according to (R2.6, R2.7, R2.9, and R2.10) [274-275]. However, at ER 0.3 the concentration of CO_2 slightly decreased and CH_4 increased in the producer gas. This is due to an enhancing effect of temperature on the boudouard and methanation reactions (R2.9 and R2.5), as reported by Upadhyay et al. [276]. The obtained optimum gasification parameters, gasification parameters and gas composition at different ER's are listed in Tables E-1, E-2 and E-3 in the Appendix E: FBGR Parameters.

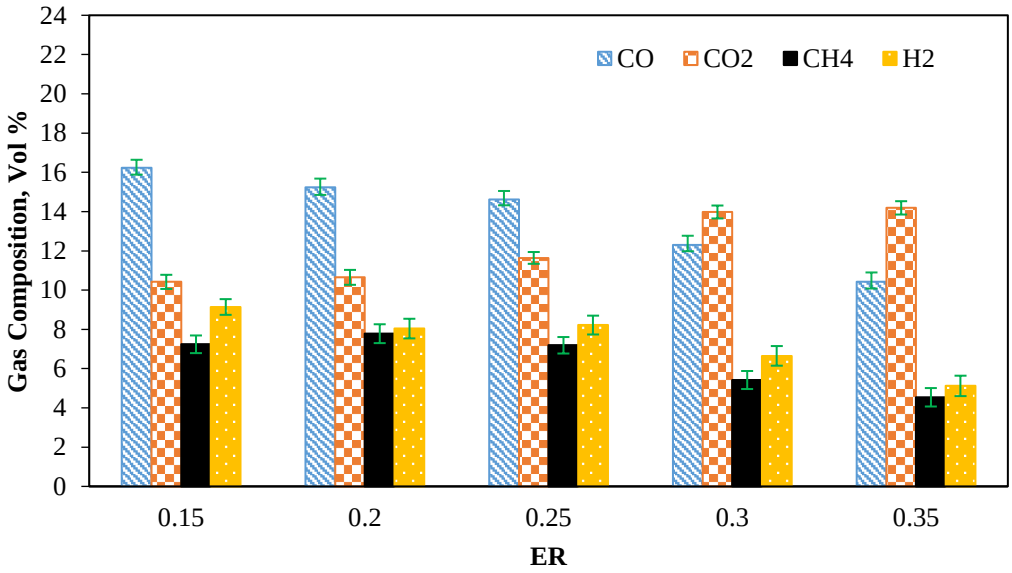

Figure 7-3 Effect of ER on product gas composition

Figure 7-4 (a) displays the effects of ER on the HHV and Figure 7-4 (b) demonstrates the CCE. Increased ER reduced the HHV of the producer gas due to increasing the proportion of N_2 in the gas which incombustible gas. The combustion of carbon (R2.8) and oxidation of CO (R2.2) reactions (as described in Section 2.8) are enhanced with oxygen amount increase leading to increasing the yield of CO_2 that is also incombustible gas. On the other hand, the smaller the ER the higher yield of combustible gases such as H_2, CH_4, and CO [277]. However, ER increase the CCE due to increase of oxygen amount and elevated rate of oxidation. The increase in ER means more N_2 in the producer gas as well as more CO_2 and water due oxidation of CO and H_2 to CO_2 and H_2O which was confirmed by studies in the literature [278, 279]. CCE is essential to evaluate the processing time and gasification performance regardless of the producer gas composition. It also reduces the need for recycling the unreacted solid fuel. The composition of producer gas can be manipulated by operating conditions and catalyst.

(a)

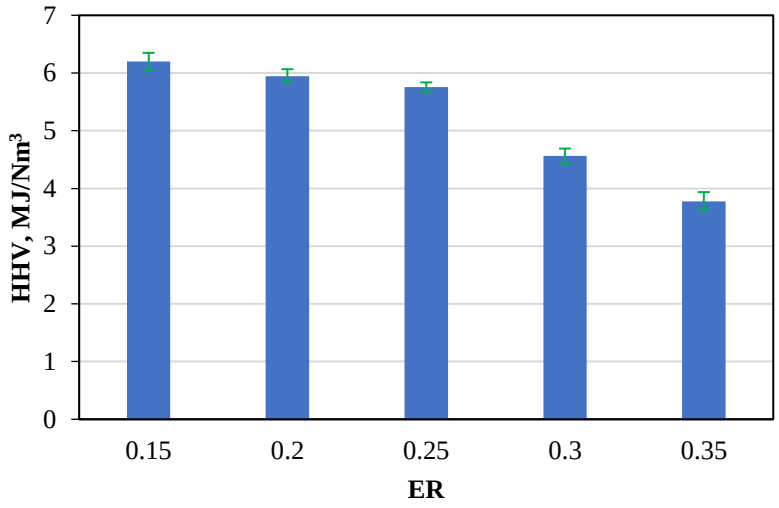

(b)

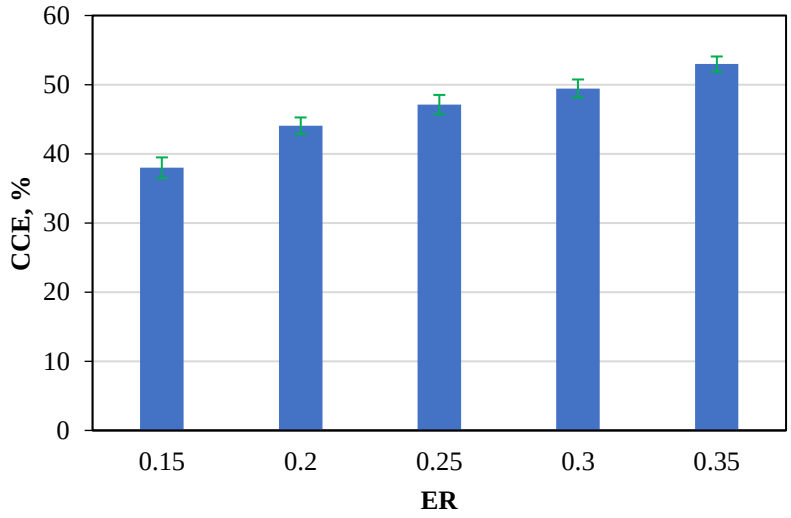

Figure 7-4 (a) Effect of ER on the HHV and (b) effect of ER on the CCE

The increase in the ER lead to a reduction in the CGE as shown in Figure 7-5. The reduction in the CGE as ER increased can be explained by the reduction in the combustible gases in the product gas such as CO and H_2 due to reactions R2.2 and R2.4. However, at an ER of 0.15, the CGE increases to 33.9% due to the conversion of char by CO_2 and H_2O to syngas by Boudouard (R2.9) and water-gas shift reaction (R2.11), respectively. Similarly, the declining char rate as ER decreases is owed to R2.7 and R2.9 as described in Section 2.8. As the gasification energy flow is dependent on the syngas and methane yield in the product gas, it decreases as ER increased [280-281].

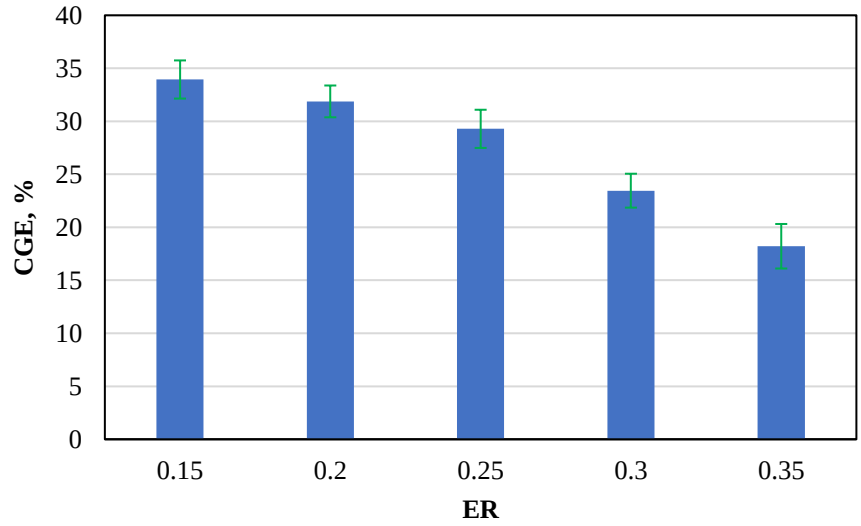

Figure 7-5 Effect of ER on the CGE

The volumetric yield of the dry gas per unit mass of the fuel increases with ER increase as shown in Figure 7-6. This finding is consistent with the combustion and oxidation reaction theory. The increase in the oxygen amount in the feed lead to increases in the rate of combustion and oxidation reactions, hence the volume of the producer gas raised. These results are in good agreement with the findings of wood biomass gasification reported by James, et al. [282]. However, the increase in the yield of gas is associated with a reduction in HHV (Figure 7-4 a). Therefore, a balance must be established between the gas yield and quality.

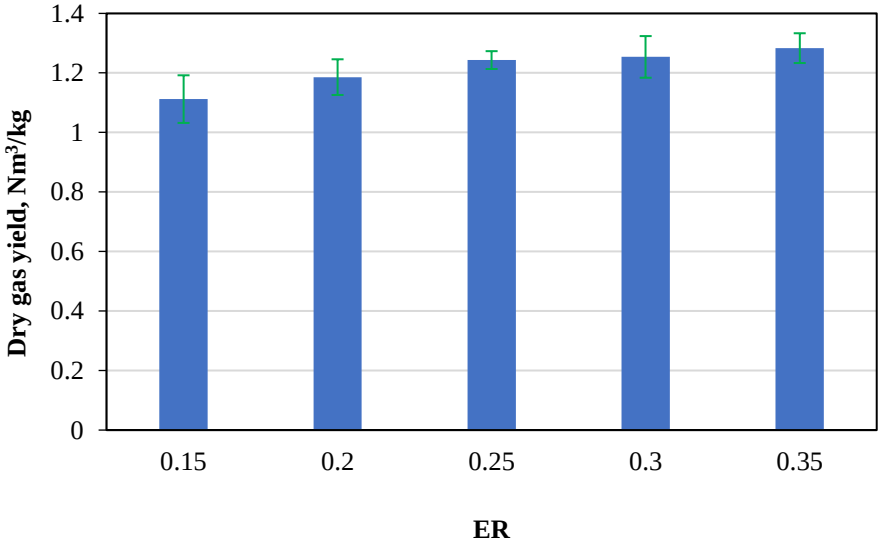

Figure 7-6 Effect of ER on the dry gas yield

7.4.2 Effect of temperature

Temperature is a crucial parameter for the biomass gasification process that affects the rate of reactions based on the heat of reaction. In the present study, the bed temperature was changed from 350 to 750 °C at a fixed ER of 0.15 for both pellet A and pellet B. The influence of bed temperature

on the syngas composition is presented in Figure 7-7 and Figure 7-8. The concentration of syngas increases with temperature due to an increase in the decomposition rate of char. For both feedstocks, at a temperature of 750 °C, the highest yield for all producer gases was obtained.

The yield of CO, CO_2, H_2, and CH_4 increases with bed temperature. The gas composition increased 16.8 vol% CO, 10.9 vol% CO_2, 9.6 vol% H_2, and 7.4 vol% CH_4 at the temperature of 750 °C for pellet A. From the experiment of the pellet B, the gas composition was found similar to pellet A with 17.1 vol% CO, 10.7 vol% CO_2, 9.6 vol% H_2, and 7.4 vol% CH_4 at a temperature of 750 °C. However, comparing pellet B with pellet A gasification reaction, pellet B exhibited a shorter reaction time than pellet A due to highes shredding grads. As a result, the gasification temperature of 750 °C was chosen as an optimum feedstock and operating temperature for FBGR experiments.

The raise in temperature is favourable for the formation of H_2 and CO. The endothermic reactions in Section 2.8 such as boudouard reaction (R2.9) and water-gas reaction (R2.10) are promoted as temperature increased [283]. However, it is noted that temperature increase may lead to some operational issues such as bed agglomeration and operating costs. Fuchs et al. [284] reported that the yield of H_2 could reach 70 vol% for a temperature range between 600 and 700 °C in the gasification of biomass.

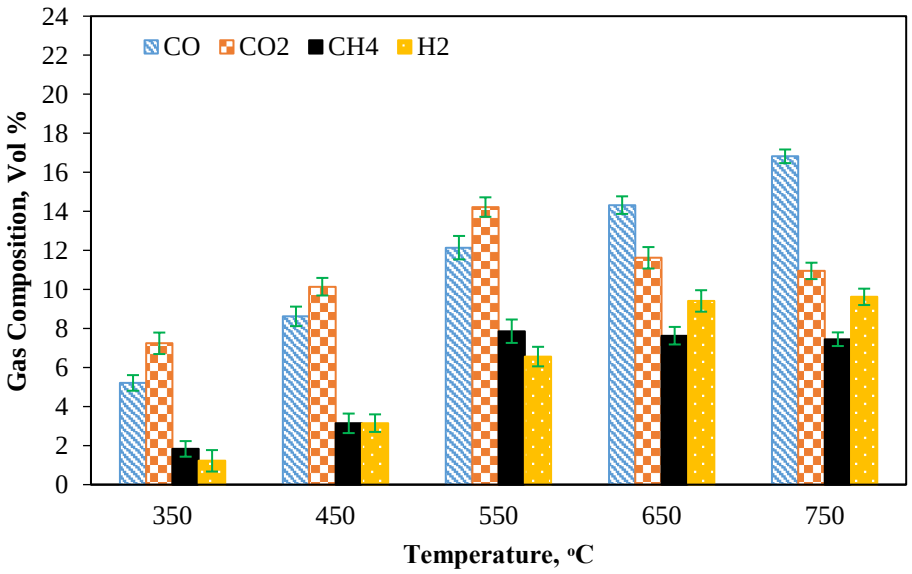

Figure 7-7 Effect of bed temperature on the gas composition for pellet A gasification

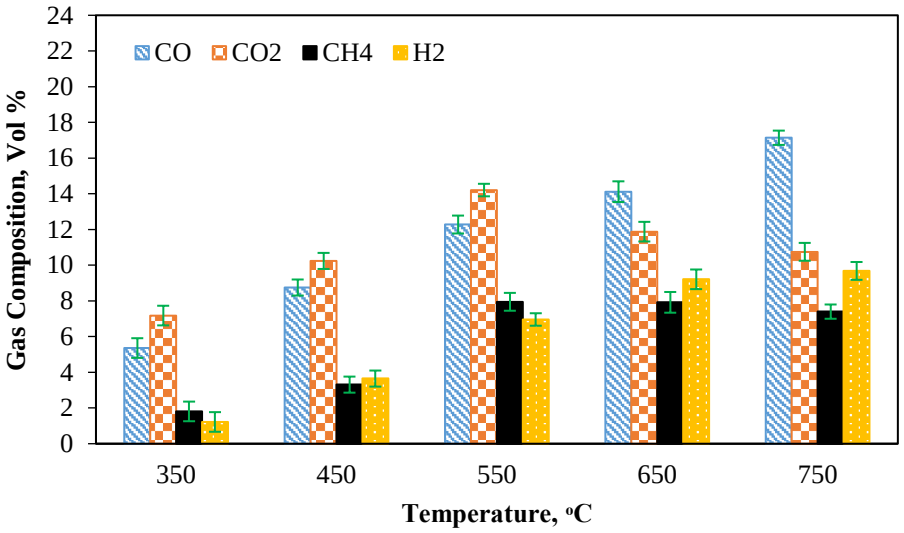

Figure 7-8 Effect of bed temperature on the gas composition for pellet B gasification

Figure 7-9 and Figure 7-10 show the change of HHV and CCE as a function of temperature for pellet A and pellet B. The value of HHV increased from 1.5 to 6.3 MJ/Nm^3 for pellet A and pellet B as temperature increased from 350 to 750 °C. Enriching of producer gas with combustible gases such as CO and H_2, according to R2.9 and R2.7, enhanced the HHV of the product gas [275, 285]. The CCE for both fuels increased with temperature due to the gasification rate increase according to reactions R2.6, R2.9, R2.10, R2.12, and R2.14 in Section 2.8 [283].

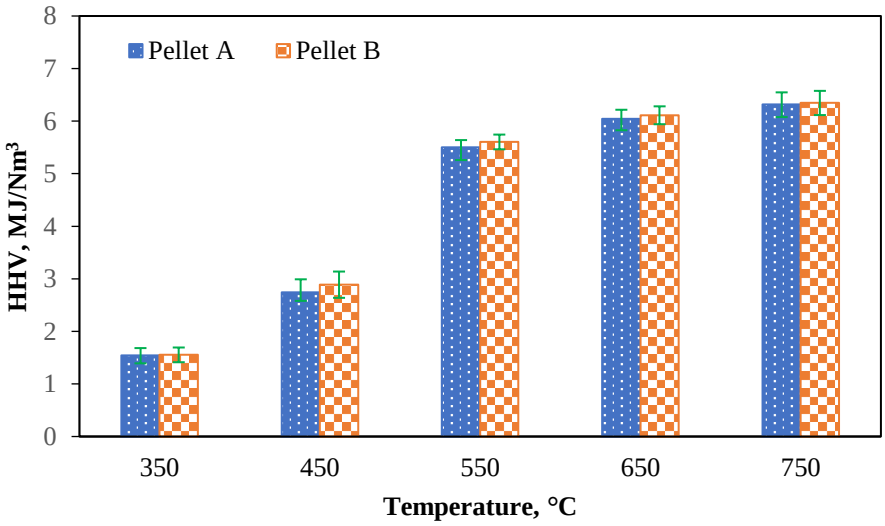

Figure 7-9 Effect of temperature on HHV of pellet A and pellet B

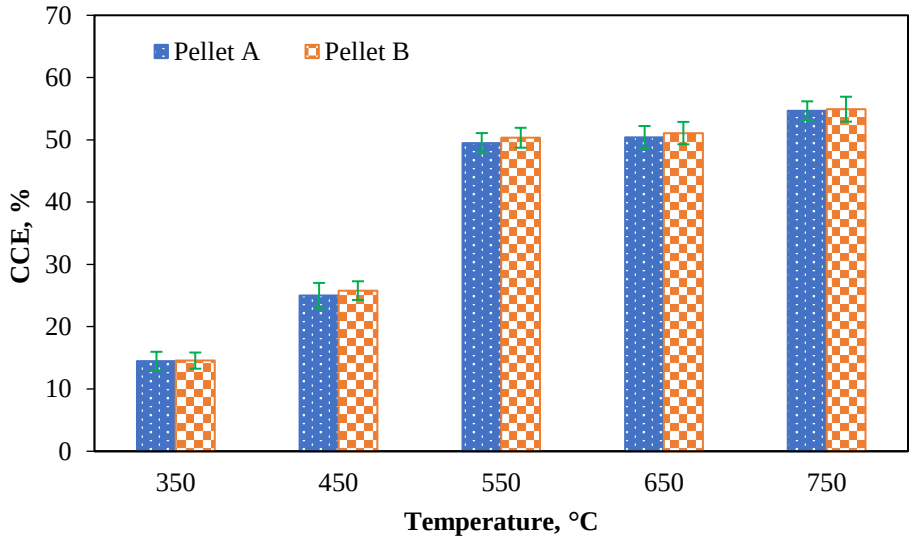

Figure 7-10 Effect of temperature on CCE of pellet A and pellet B

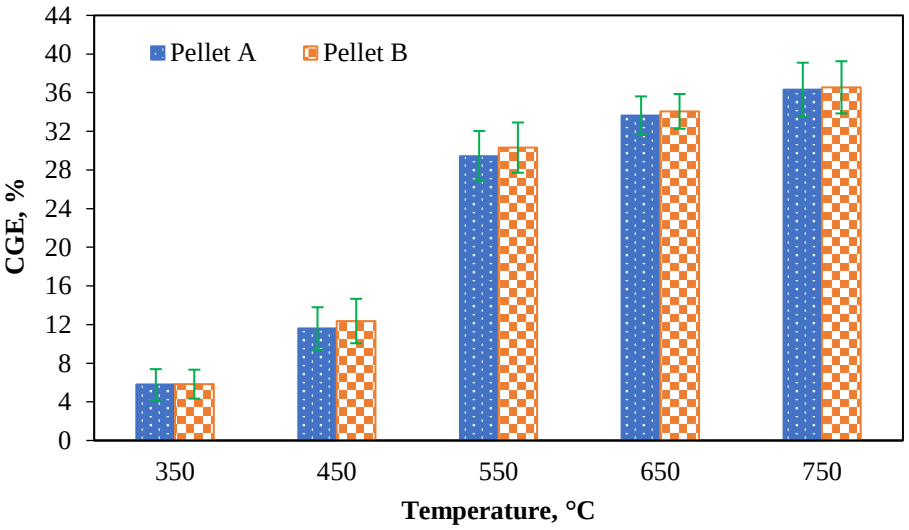

Figure 7-11 Effect of temperature on CGE of pellet A and pellet B

In Figure 7-11, the CGE increases with the temperature of gasification due to the increasing calorific value of the product gas [286-287]. The CGE for pellet A and pellet B at 750 °C is about six times that at 350 °C. The yield of char exhibits a reduction as temperature increased from 350 to 750 °C that is caused by the promoted rate of char endothermic reactions (R2.9, R2.10, R2.14) at high temperatures [287]. The heat produced from the process consequently increases with temperature and heating value increases. The rise in the production of syngas leads to an increase in the yield of product gas to 1.3 m^3/kg at 750 °C for both feedstocks, as shown in Figure 7-12.

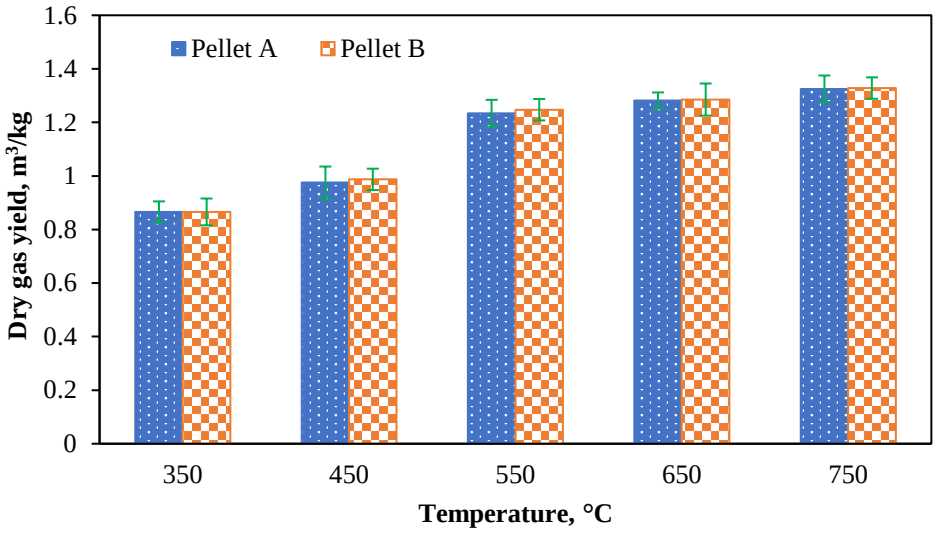

Figure 7-12 Effect of temperature on dry gas yield of pellet A and pellet B

The gasification data from the temperature effect experiment for pellet A and pellet B are listed in Tables E-4, E-5, E-6, E-7 and E-8 in the Appendix E: FBGR Parameters. From Figure 7-9 to Figure 7-12, it can be seen that insignificant variation in the results of pellet A and B were obtained. The pellet A and B come at almost same size and shape. The only difference is that pellet B is relatively a high shredded grade of Subcoal™. This may affect the packing structure in pellet B. The completion time of pellet A and B gasification in FBGR was measured using a stopwatch. The longest and shortest pellet A gasification reaction times were about 23 and 10 minutes at 350 and 750 °C, respectively. However, the longest and shortest pellet B reaction times were about 11.1 and 7.9 minutes at 350 and 750 °C, respectively. The time of gasification is an influential factor in determining the cost of the gasification process. The longer the gasification time the higher the operating cost hence pellet B is preferable.

7.4.3 Effect of catalyst on gasification

The effect of olivine and dolomite catalysts on the producer gas composition is presented in Figure 7-13 and Figure 7-14, respectively. The purpose of the investigations was to identify the appropriate catalyst type and loading %. The loading of olivine and dolomite was changed from 0 to 20 wt.% in increments of 5 wt.% at the optimal temperature of 750 ^{0}C and ER of 0.15. The temperature was selected for the catalyst study based on economic and operational considerations from the pellet B gasification temperature investigations. The present experiments were repeated a minimum of three times with a % error of less than ±0.5 vol%. The gasification data from different catalysts loading are listed in Tables E-9-E-15 in the Appendix E: FBGR Parameters.

For both catalysts, the producer gas content of H_2 and CO increased with catalyst loading until reaching the peak at 15 wt.% catalyst loading. At 20 wt.% catalyst, the content of H_2 and CO decrease in comparison with 15 wt.% loading. Dolomite shows a better performance than olivine in catalytic

cracking reactions. With dolomite, the proportion of CO and H_2 increased by about 2% compared to olivine at the same loading. This makes dolomite a desired choice over olivine. However, the catalysing capability could be dependent on the feedstock nature and properties [102].

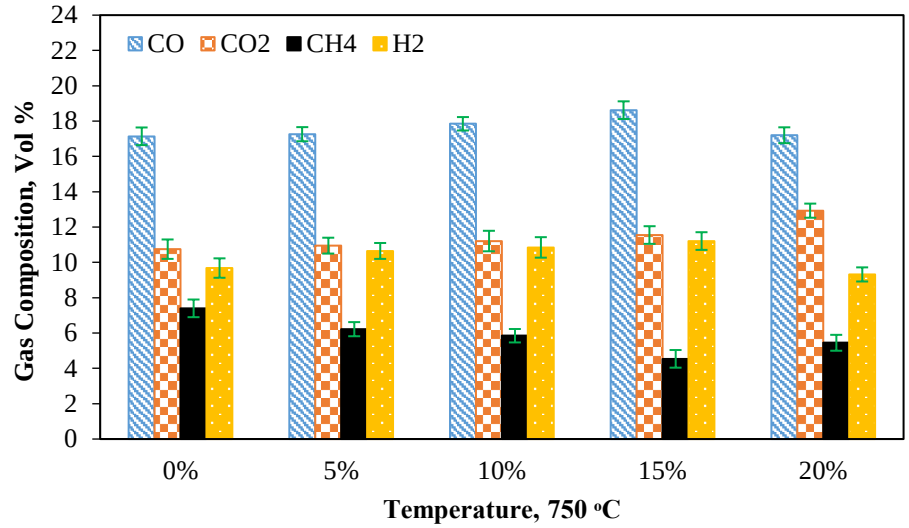

Figure 7-13 Effect of olivine loadings on the composition of the producer gas

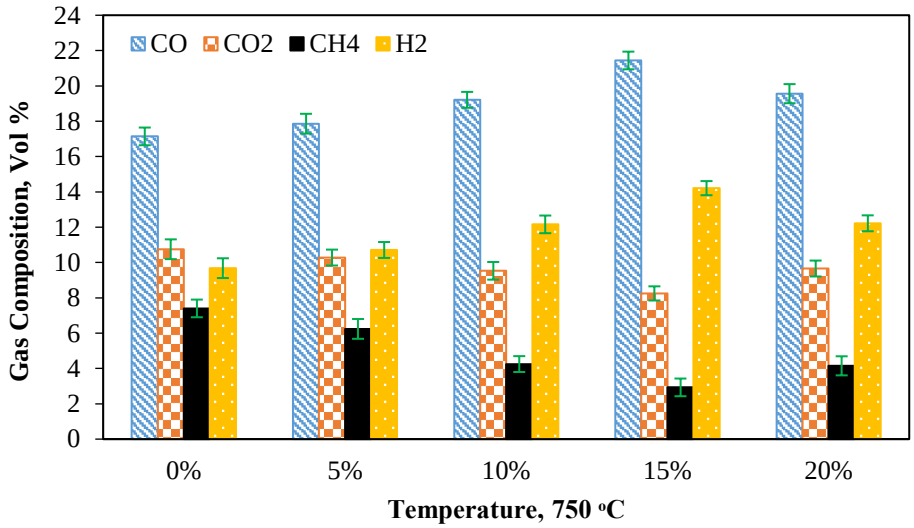

Figure 7-14 Effect of dolomite loadings on the composition of the producer gas

The completion time of pellet B gasification in the presence of 15 wt.% dolomite was measured using a stopwatch. The time of degradation time was reduced from 7.9 to 3.5 minutes when compared with gasification without catalyst. At the temperature of 750 °C, the presence of olivine and dolomite reduce the reaction time at high temperatures, and this is confirmed by TGA results using 15 wt.% catalyst at 20 °C/min which provided the lowest E_a, which decreased the reaction time. Dolomite catalyses the gasification process by enhancing the hydrocarbon reformation and acting as an oxygen carrier from the combustion to the gasification zone [116]. Dolomite plays a positive role in water gas-shift (WGS) and tar cracking reactions due to the presence of iron in its structure [288]. However, the calcination of olivine makes a pronounced difference in catalyst performance [112]. From the

results of temperature and catalyst, it can be concluded that the gasification optimum temperature with the catalyst is 750 °C. Pellet B was chosen for catalyst investigation due to shorter residence and reaction time than pellet A. The effectiveness of catalysts was tested between 600 and 750 °C. The findings from various temperatures and ER tests show that the optimum gasification performance is obtained at 750 °C.

The influence of catalysts on the gas composition is shown in Figure 7-15 and Figure 7-16. The effect of temperature without using a catalyst is displayed in Figure 7-17. The highest yield of product gas was achieved at 750 °C with 15 wt.% for both dolomite and olivine [289]. For dolomite and olivine, the volume fraction of H_2 and CO in the dry gas increased with temperature, explaining the role of temperature in reaction rate kinetics and tar cracking according to R2.10, R2.14, and R2.15 in Section 2.8. However, the CO_2 yield with olivine is greater than that for dolomite as a result of the olivine reaction mechanism that enhances the rate of char hydrocracking reactions (R2.11 and R2.13) [290].

The content of CO, H_2 in the presence of 15 wt.% olivine increases from 11.1 and 3.8 to 18.6 and 11.2 vol%, while CO_2 and CH_4 content decreased from 15.4 and 5.4 to 11.5 and 4.5 vol%, respectively, when the temperature is raised from 600 to 750 °C. For dolomite, the producer gas composition change was 12.2 to 21.4 vol% for CO, 14.2 to 8.2 vol% for CO_2, 4.2 to 14.2 vol% for H_2, and 5.1 to 2.9 vol% for CH_4. Therefore, pellet B gasification with 15 wt.% dolomite was more effective in tar cracking than olivine.

Comparing the dolomite experiment results with the case without catalyst, the CO and H_2 increased by 4.3 vol% and 4.52 vol% at 750 °C. However, the change in temperature with dolomite and olivine makes more significant increases in the syngas in comparison with the same change of temperature without a catalyst. This concludes that the activity of dolomite increased as the temperature increased.

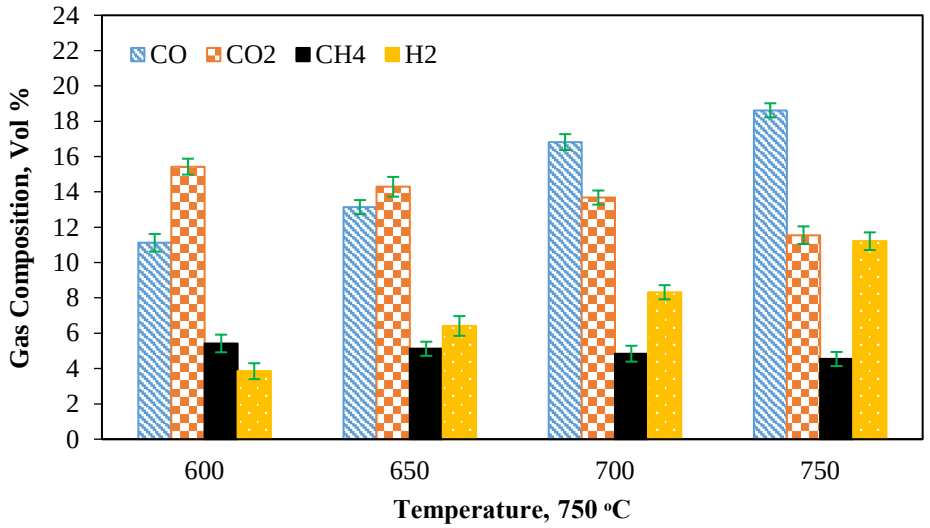

Figure 7-15 Effect of olivine (15 wt.%) on the gas composition of pellet B at different temperature

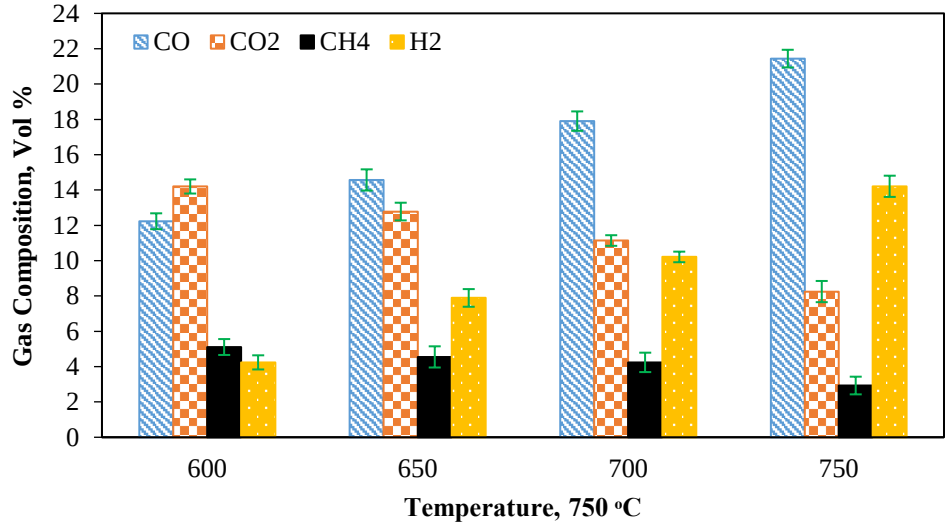

Figure 7-16 Effect of dolomite (15 wt.%) on the gas composition of pellet B at different temperatures

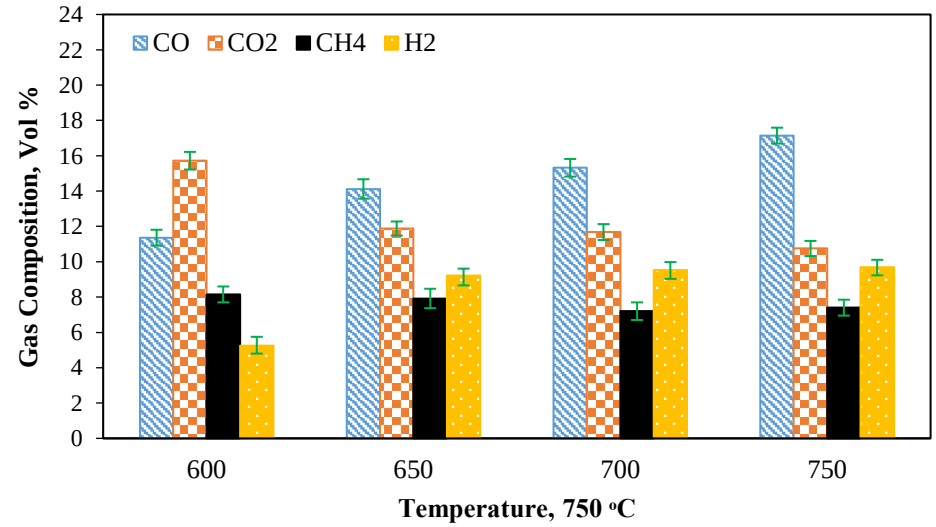

Figure 7-17 Effect of temperature on the gas composition of pellet B without catalyst

The results also exhibit that olivine has a significant impact on CO_2 production rate and a slight influence on CH_4. Corella et al. [291] pointed out that the dolomite reaction mechanism is capable for reducing the content of tar 1.4 times greater than olivine and enhancing the yield of syngas. It speeds up hydrocarbon reforming reactions such as R2.10, R2.14 and R2.15, leading to an increase in syngas formation. It also acts as an oxygen carrier that transfers O_2 from the combustion stage to the partial oxidation stage which explains the CO_2 yield decrease. This argument is supported by the findings in Figure 7-18 which compares the gas composition at 750 °C. However, in some cases such as high catalyst loading, the reduced effectiveness of dolomite may be attributed to coke deposited on the surface of the catalyst [292]. Dolomite reduces CO_2 production by more than 2 vol% in the small scale reactor.

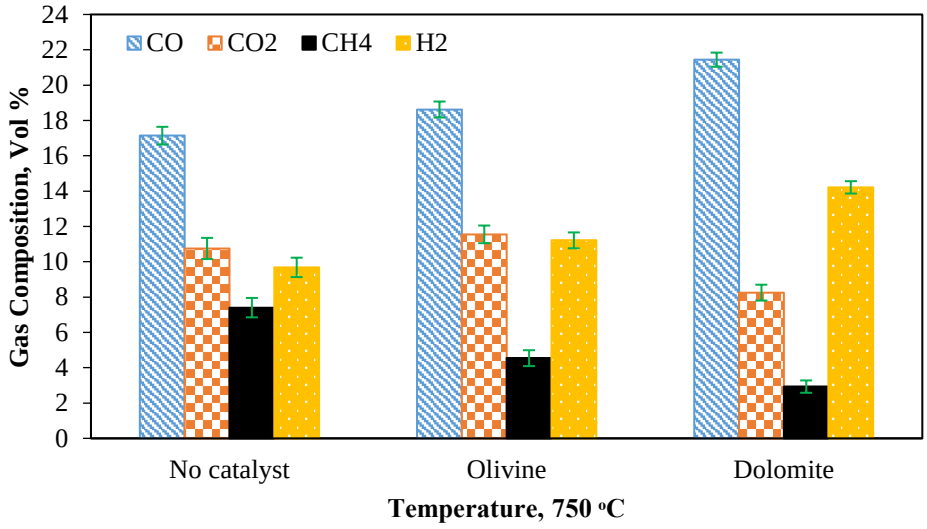

Figure 7-18 Gas composition comparison between catalyst and no catalyst at 750 °C

The HHV of producer gas in the presence and absence of catalyst was evaluated at a temperature range of 600 to 750 °C, as illustrated in Figure 7-19. The findings show that there is a slight variation in the HHV value between all cases. However, the HHV of the dolomite is higher than olivine and the case without catalyst. This might be explained by the high content of H_2 and CO in the presence of 15 wt.% dolomite with pellet B. Another parameter is that the concentration of CO_2 for olivine is consistently higher than that for dolomite [290].

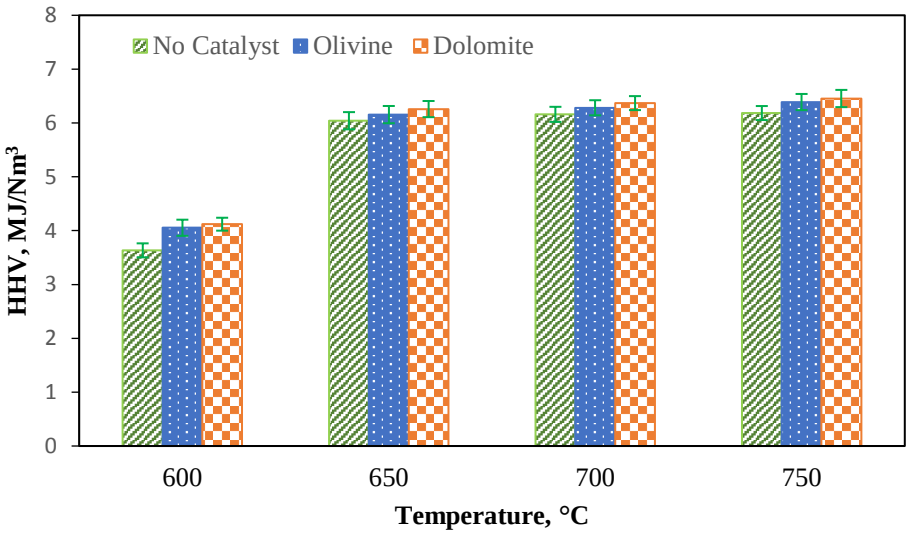

Figure 7-19 Effect of catalysts on HHV at various gasification temperatures

Figure 7-20 displays the CGE for pellet B gasification with 15 wt.% olivine and dolomite and no catalyst at different temperatures. The results show that the CGE for olivine increased from 20.3 to 34.8% when temperature increased from 600 to 750 °C as a result of syngas quantity increase. While for dolomite the CGE also increased from 20.3 to 36.9%, respectively. However, there is an insignificant variation in CCE and CGE in the presence of olivine and dolomite, as reported by Ma et al. [293]. The increase in CH_4 content may affect the production rate of H_2 that then affects the CGE value [290].

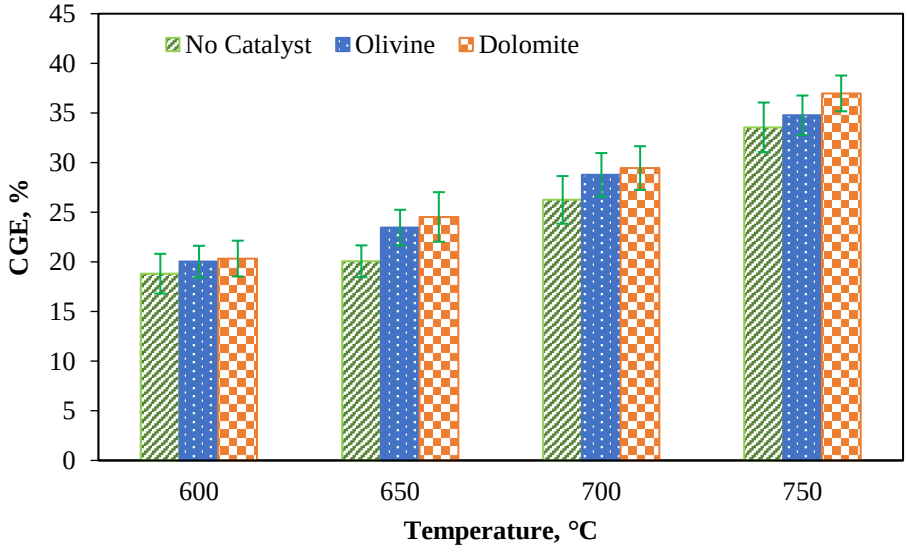

Figure 7-20 Effect of catalyst on CGE at various gasification temperatures

Figure 7-21 shows the variation of CCE with temperature and catalysts. Dolomite shows good effectiveness in promoting the conversion of carbon to gases over olivine at the same operating conditions [294]. The catalytic activity of dolomite is found to be towards tar conversion and water-gas reactions (R2.14, R2.15, R2.10) in Section 2.8. It has been stated that the performance of olivine is dependent on the different oxidation states of the segregated iron at the catalyst particle surface

[104]. The metallic iron is the responsible element in olivine that can be extracted from the olivine structure by calcination under reducing conditions.

As the carbon conversion from char increased in the presence of the catalyst, the yield of dry gas increases with dolomite more than that with olivine, as shown in Figure 7-22. The presence of CO_2 in high concentrations may result in the catalyst deactivation [295]. The dolomite enhanced the partial oxidation reaction in the combustion zone of the gasifier and tar reduction according to R2.29-R2.31 in Section 2.10.1. The dolomite also may be responsible for enhancing the production of CO_2 through carrying the O_2 to the gasifier according to R2.32 and R2.33 in Section 2.10.2. As mentioned earlier, temperature improved the yield of product gas by increasing the endothermic reaction rates.

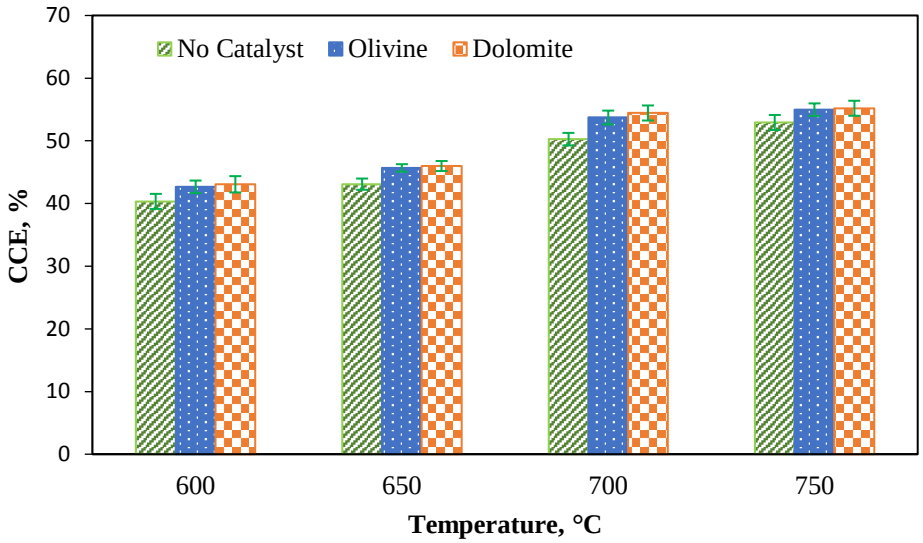

Figure 7-21 Effect of catalysts on CCE at various gasification temperatures

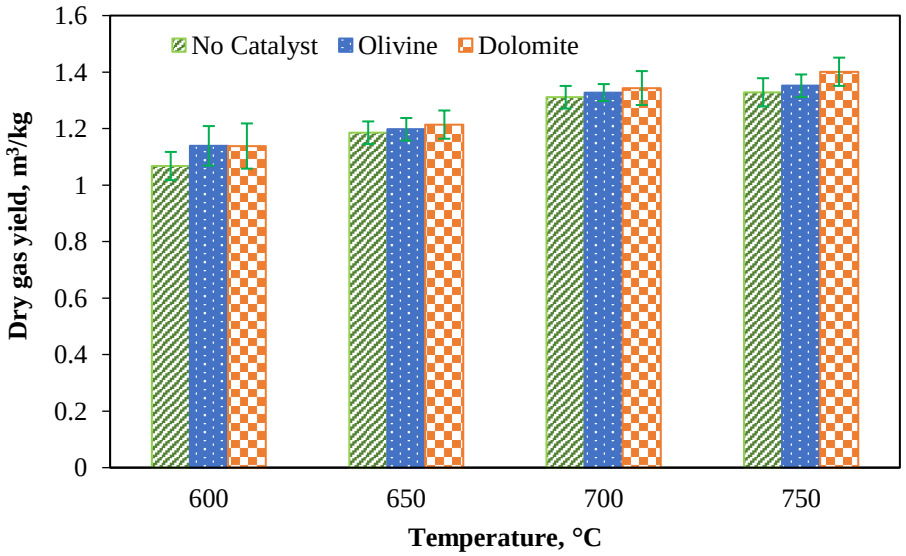

Figure 7-22 Effect of catalysts on total dry gas yield at various gasification temperatures

7.4.4 Effect of particle size

The pellet iron is the responsible element in olivine B size was reduced to 10-6.3mm and gasification was performed at 750 °C. The influence of particle size on the producer gas composition at constant temperature is presented in Figure 7-23. As stated by Wang [296], the small particles of biomass, which possess a high surface-to-volume ratio, increase the consumption rate of O_2 controlled by chemical reactions. The increased surface area of particles enhances the reaction rate between fuel particle and gasifying agent. However, the increase of accessible internal surface has a more significant effect as it is coupled with self-oxidation reaction. The fuel particle size effects the quality, yield, and LHV of the product gas. In large particles, the diffusion of the reacting gas is limited by the distance to the particle core and topography of the surface as well as the density of the chemical active sites. In this case, the particle size is affecting the apparent E_a of biomass conversion reactions [297].

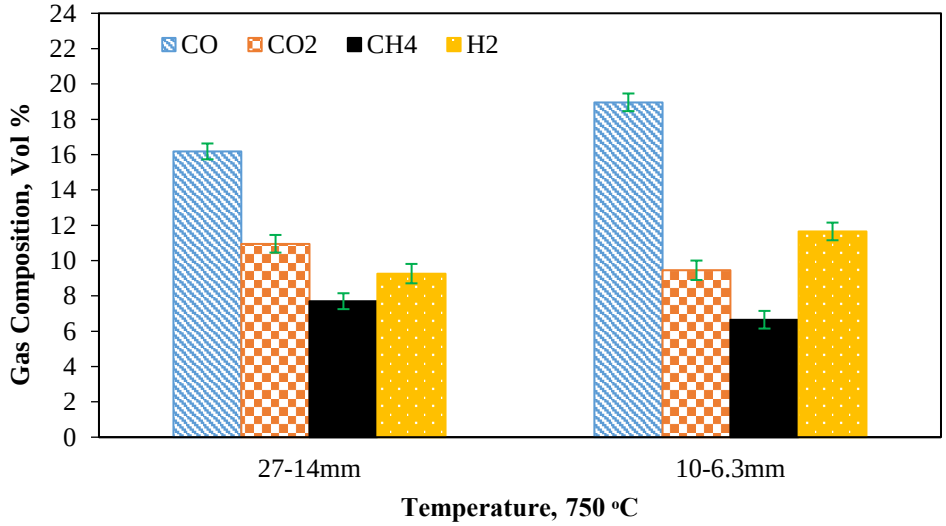

Figure 7-23 Gas composition comparison for different particle sizes

The smaller the particles the larger the surface-to-volume area. Therefore, a small surface area enhances the contact area with the gasifying agent in gasification reactions. Wang et al. [298] reported that as the particle size increased from 0.1 to 5 mm, the content of CO and H_2 decreased in the producer gas. Also, small particle size obtains high burning rates and ignition front speeds. Mohammed et al. [299] carried out a series of experiments to determine the influence of biomass particle size on the gasification of empty fruit bunch to produce H_2. The results showed that the smaller the particle size the greater the content of H_2, CO, and the less CO_2 in the gas product. As the particle size increased to 0.5 to 1 mm, the production rate of H_2 and CO decreased. Similar findings were obtained by Xiong et al. [209]. However, this comparison is made based on an assumption of that the biomass particles are nominally identical.

Table 7-1 demonstrates that all the gasification parameters at small pellet B size (10-6.3mm) shows higher values and better performance than bigger size (27-14). The gas yield at particle size 10-6.3

was 1.37 m^3/kg which is slightly higher than particle size 27-14mm. According to Table 7-1, small pellets have a slightly higher HHV (6.53 MJ/Nm^3) than larger pellets. The experiments were repeated a minimum three times to check the reproducibility.

Table 7-1 comparison parameters between different Pellet B sizes gasification.

Parameters	10-6.3 mm	27-14 mm
Temperature (°C)	750	750
HHV (MJ/Nm^3)	6.53	6.35
Gas yield (m^3/kg)	1.37	1.33
Carbon conversion efficiency (%)	56.35	54.93
Cold gas efficiency (%)	38.83	36.55
Char (%)	7.00	8.50

7.5 Material balance

Biomass gasification in the BFBGR produce two main products: volatile substances from the top, and solid char from the bottom, as illustrated in Figure 7-24. The volatile substances include CO, CO_2, CH_4, H_2 and N_2. While the solid products involve char mixed with sand, unreacted fuel particles, tar, ash, and fine particles of carbon. The tar in volatiles stream is also separated by a condenser and a tar capture unit. These streams and compounds were used to determine the mass balances in the gasifier based on the conversion of the Subcoal™ to gas products.

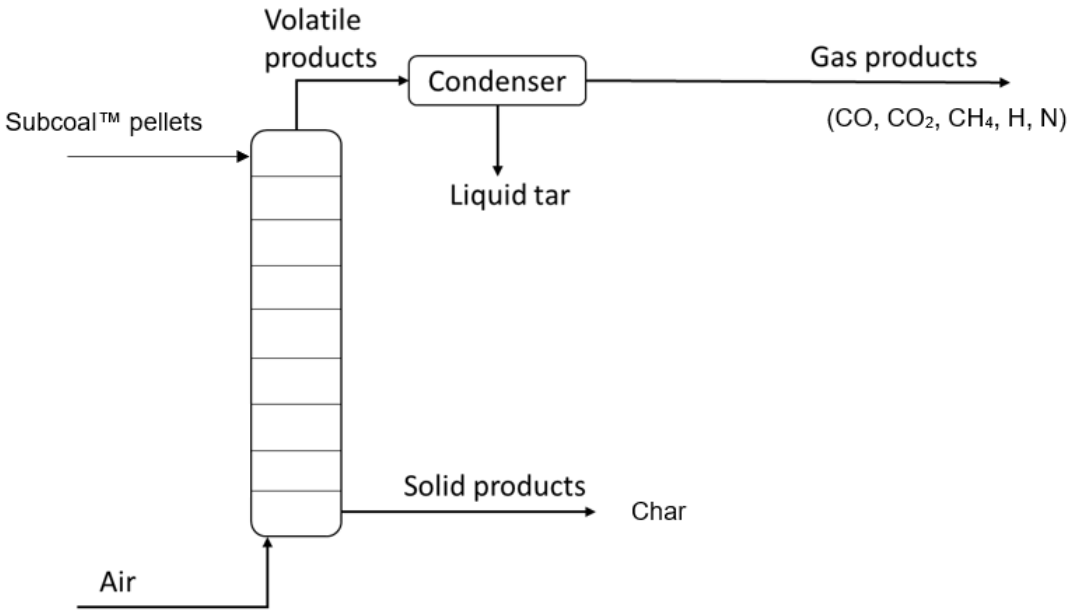

Figure 7-24 Schematic drawing of the mass balance flow for FBGR in the gasification

The overall mass balance on the system was determined according to Eq. 7.1.

$$\left[\dot{m}_{air} + \dot{m}_f\right]_{in} + Genergation = \left[\dot{m}_{gas} + \dot{m}_{solids}\right]_{out} + Consumption + Accumulation \quad (7.1)$$

$$\dot{m}_{air} = Q_{air} \times \rho_{air} \quad (7.2)$$

Where Q_{air} is the air volumetric flow rate in (m^3/min) and ρ_{air} is the density of air (1.2 kg/m^3) at ambient temperature. As the reactor runs at a steady state and there is no material accumulation inside the reactor, the term accumulation has been neglected. The terms generation and consumption were used based on the component assigned for calculations. The consumption rate of reactant and the generation rate is dependent on the conversion degree of the reaction. The mass flow rates of biomass entering the reactor was estimated using Eq. 4.37 and the product gas yield was calculated using Eq.4.40 in Chapter 4.

The initial quantity of biomass was determined using a scale in the laboratory, while the char product was weighed with a load cell linked to the gasifier. The individual gas product was determined using Eq. 7.3.

$$yi = Y \times X_i \quad (7.3)$$

Where Y, yi, xi are the total yield gas product in (Nm^3/kg feed of biomass), the individual product gas yield in (Nm^3/kg feed of biomass) and individual mole fraction. The composition of the gas product was determined using a gas analyser in volume per kg of biomass (y_i), except for N_2 that was estimated by difference. The fraction of the mass of each gas (z_i) per kg of biomass is based on ideal gas volume at standard temperature and pressure calculated as follows [138]:

$$z_i = \frac{y_i \times Mw_i}{22.4} \quad (7.4)$$

Where Mw_i donates for the molecular weight of each individual gas in the product, y_i is the gas yield of every gas product in ($\frac{Nm^3}{\text{kg biomass feed}}$) and $\dot{m}_{gas}$ is the mass flow rate of each gas in g/min:

$$\dot{m}_i = z_i \times \dot{m}_f \quad (7.5)$$

So, the total mass flow rate of the product gas is given in the following expression:

$$\dot{m}_{gas} = \sum_{n}^{i=1} \dot{m}_i \quad (7.6)$$

The conversion of Subcoal™ to products was evaluated in terms of carbon mass balance. An atomic carbon balance was carried out based on carbon in feedstock and products. In feedstock, Subcoal™ is the only source of carbon considered in the calculations. However, carbon exists in product gas and char for product side calculations. The carbon mass flow rate ($\dot{c}_f$) in the feedstock intel of gasifier was estimated from the total mass rate of fuel ($\dot{m}_f$) and carbon weight fraction (CC_f) in the ultimate analysis:

$$\dot{c}_f = CC_f \times \dot{m}_f \tag{7.7}$$

Carbon in product gas ($\dot{c}_g$) was estimated using a combination of Equations 7.4 and 7.5, as stated:

$$\dot{c}_g = \frac{y_i \times 12}{22.4} \times \dot{m}_f \tag{7.8}$$

The content of carbon in char (solid product) ($\dot{c}_{char}$) was estimated by the following expression:

$$\dot{c}_{gas} = \sum \dot{c}_i \tag{7.9}$$

$$\dot{c}_{char} = \frac{CC_{char} \times m_{char}}{t} \tag{7.10}$$

Where, CC_{char} is the weight percentage of carbon in the char, m_{char} is the total mass of char obtained from the process, and t is the processing time. The char is assumed to be carbon due to the low content of ash in the solid product. This assumption was made to avoid char-sand separation. By combining all terms together, carbon balance on the gasification of biomass would be:

$$\dot{c}_f = \dot{c}_{char} + \dot{c}_g \tag{7.11}$$

The quantities obtained from the overall mass balance and the carbon balance in the system can be used to determine the experimental error [138]:

$$\%\ error = \frac{input - output}{input} \times 100\% \tag{7.12}$$

The results from the mass balance calculations are presented in Table 7-2 and Table 7-3.

Table 7-2 Mass balance calculations for pellet B gasification at different ER at 750 °C.

ER	Total mass balance (g/min)			Carbon mass balance (g/min)		
	Inlet	Outlet	Error %	Inlet	Outlet	Error %
0.15	92.23	77.78	15.67	19.76	18.35	7.16
0.2	84.32	73.91	12.34	16.15	14.5	13.53
0.25	77.32	68.19	11.81	12.91	12.11	6.17
0.3	70.65	63.75	9.77	9.89	9.5	4.02
0.35	66.45	60.85	8.43	7.98	7.68	3.74

Table 7-3 Mass balance calculations for pellet B gasification at different temperatures.

Temperature (°C)	Total mass balance (g/min)			Carbon mass balance (g/min)		
	Inlet	Outlet	Error %	Inlet	Outlet	Error %
350	92.23	64.86	29.68	19.76	14.32	27.51
450	92.23	68.35	25.89	19.76	15.16	23.26
550	92.23	72.64	21.24	19.76	16.03	18.88
650	92.23	76.21	17.37	19.76	17.77	10.07
750	92.23	77.78	15.67	19.76	18.35	7.16

This mass balance includes two calculation approaches: molecular species mass balance, and atomic species mass balance based on the carbon atom. The total inlet and outlet mass flow rates in g/min, as well as the mass balance percentage errors, were determined based on the two approaches. The amount of carbon in the feed was estimated according to the ultimate analysis of Subcoal™. While the outlet carbon was estimated by producer gas analysis. From Table 7-2, the carbon leaving the reactor decreased from 18.35 to 7.68 g/min with ER increase from 0.15 to 0.35. This can be explained by the reduction in contents of CO, H_2, CH_4 and increase CO_2 as reported in Figure 7-3. Also, the total mass in the outlet increased from 60.6 to 77.8 g/min as a result of air excess with the decreasing ER. The results of mass balance calculations for Pulverised Subcoal™ pellet (pellet B) demonstrated that the total mass balance output increased with temperature and reduced the percentage error % that is owed to the indirect estimation of deposited char. The carbon quantity in the gasifier outlet increased with temperature. Moreover, the amount and composition of tar were not measured at the outlet which contributes to an error in the total mass and carbon mass balances. As the temperature increases, the tar may convert into measurable gases reducing the percentage error in the mass balance. Furthermore, a positive margin error percentage implies that the inlet material mass is greater than the outlet material mass. As a result, a negative % error margin is possible if the feeder unit had more biomass than was initially calculated in the reaction calculations, as this would increase the gas outlet.

7.6 Summary

The ER effect on the gas composition showed that the concentration of H_2, CO decreases and CO_2 increased as the ER increased from 0.15 to 0.35. In addition, as ER increased the HHV and CGE decreased while CCE increased. The influence of bed temperature was evaluated from 350 to 750 °C at ER of 0.15 for both pellet A and pellet B. The results showed that the syngas content of producer gas increases and char formation decreased with temperature. The optimum gasification temperature for both pellet (A/B) was found to be 750 °C with the highest dry gas yield. Also, HHV, CCE and CGE raised to a maximum at 750 °C. However, the pellet B showed an excellent gasification performance with a shorter reaction time than the pellet A due to high shredding grade.

The influence of olivine and dolomite at 15 wt.% each in the pellet B gasification has been investigated between 600 and 750 °C and at ER of 0.15. The findings showed that both catalysts reduce the reaction time required to reach the complete conversion. However, the highest yield of product gas has been achieved at 750 °C with dolomite. The time of complete pellet B gasification in the presence of dolomite reduces from 7.9 to 3.5 minutes when compare with gasification without catalyst at 750 °C. While complete pellet A degradation obtained at 5.5 minutes with 15 wt.% olivine. In terms of HHV, CCE and CGE, dolomite showed better performance than olivine in catalytic cracking reactions at the same operating conditions.

The effects of pellet B size reduction on the producer gas composition was examined. The outcomes showed that the smaller the particle size the better syngas yield and composition. However, in terms of the producer gas quality, the effects of particle size were insignificant in comparison with catalyst and temperature. Finally, the mass balance calculations on the process were presented. The increase of temperature reduces the percentage error attributed to deposited char inside the equipment.

Chapter 8: Life Cycle Assessment of Solid Recovered Fuel Gasification in the State of Qatar

8.1 Introduction

In this chapter a life cycle assessment (LCA) is carried out to assess current MSW handling in Qatar and to propose alternatives to reduce its environmental impact. As the current practice for handling MSW is landfilling with composting, the scenario is environmentally unsustainable. Therefore, in this chapter alternatives are presented that utilise biogas capture, SRF gasification, and the use of solar PV with gasification technology to provide electricity from MSW processing steps. This is the first reported LCA for Qatar that considers SRF gasification as an alternative to landfills which has been published in the ChemEngineering journal [300]. The chapter also includes a theoretical background and detail on the LCA methodology.

8.2 Background

Qatar's economy and power generation infrastructure are highly dependent on fossil fuel. It can be seen from Figure 8-1 that most of the output flows are accounted for exports of crude oil and natural gas. This Sankey diagram can be used to depict the process of any type of flow in which the width of each process represents the flow quantity. It is very important to show the process of complex information such a topic under consideration**.** In addition to this, electricity generation via thermodynamic cycles requires water-based cooling towers. Since Qatar does not have natural freshwater sources, it relies heavily on seawater desalination which is inherently an energy-intensive process. The same water, in addition to being used domestically, is used in the agricultural sector [301]. Therefore, the use of electricity generated by fossil fuels is at the heart of resource consumption.

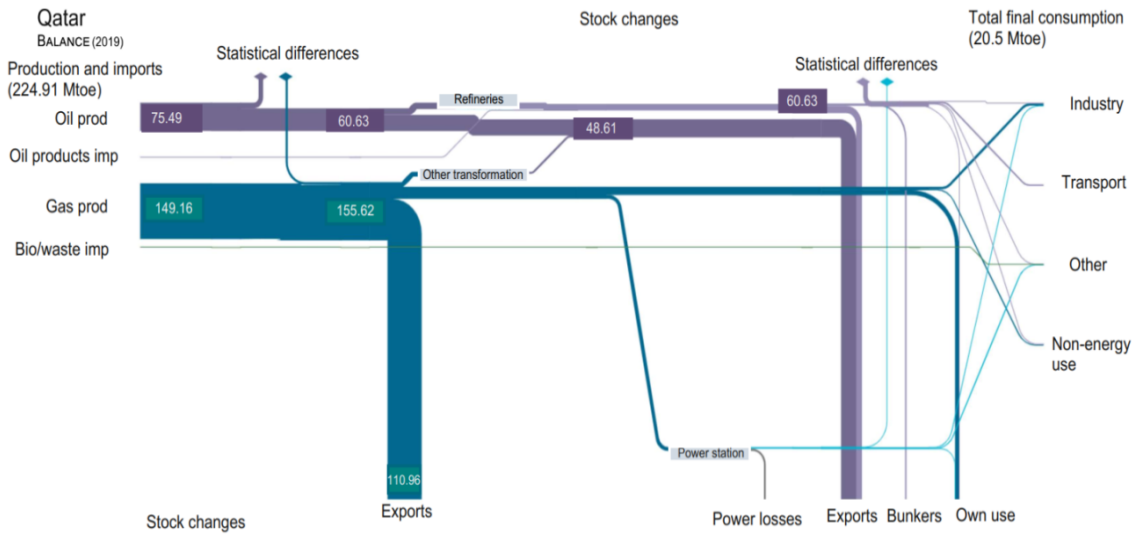

Figure 8-1 Energy balance for Qatar in the form of a Sankey diagram

Qatar created the Domestic Solid Waste Management Centre (DSWMC) facility to afford the treatment and supply of electricity to its grid system. The center turns the domestic waste into clean energy. This facility marks the first-ever to be created in the Middle East. The organic wastes are also be processed into other raw products to be used in other industries, for example, fertilizer. Approximately1000 tonnes of other wastes are estimated to be combusted within the environment, with less than 5% taken as landfill. To improve sustainability via the use of biogas, the Ministry of Municipality and Environment, in collaboration with Qatar University's College of Engineering, established another project to produce biomethane gas to power vehicles. This project was aimed at reducing the overdependence of fossil fuels in the transport sector. Biofuel is also estimated to reduce the cost of operating vehicles [302].

The growth in population and economic development of Qatar is expected to increase in the future [13], which will result in greater fossil fuel use unless sustainable development principles are pursued [32]. According to Kahramaa [303], the national body responsible for electricity, the annual electricity demand in Qatar increases at about 8% per year (at time of writing), which is among the highest growth rates globally. The total energy transmitted in 2016 was 39,667 GWh, an increase of 2.1% over the previous year [303]. Considering that Qatar currently generates almost all of its electricity using indigenous natural gas, the carbon emissions and environmental impact from this electricity generation are important considerations for the country's government [211]. In view of these challenges, the Qatar national vision 2030, as well as the national development strategy, highlights the sustainable use of natural resources as well as preserving the natural environment for future generations as key national objectives [304].

The environmental statistics of Qatar documents that the current major disposal route is landfilling with composting as a treatment being used to reduce a small amount of organic material. Table 8-1

shows the breakdown of the total waste in the country by type and the waste management facilities that process the waste. Overall, in the country the total waste arising is 5,946,811 tonnes for the year 2018, with 77,606 tonnes treated in waste management facilities. This accounts for only 11.9% of the total waste generated in the country being treated, while the rest is landfilled. The largest waste stream in Qatar is currently from the construction sector with total arisings of 3,006,287 tonnes in 2018. Of this, only 50,306 tonnes were processed by the different waste treatment facilities in Qatar, which is only 1.7% of this amount of construction waste.

Table 8-1 Environmental statistics on waste management in Qatar from 2013 to 2018 [305].

النفايات الوارده حسب النوع ومرافق إدارة النفايات

2018 - 2013

INCOMING WASTE BY TYPE AND WASTE MANAGEMENT FACILITY

2013- 2018

TABLE (249) (Unit:Metric tons) — جدول رقم (249) (الوحدة: طن متري)

Wastes by type	Waste management facility	2018	2017	2016	2015	2014	2013	مرفق إدارة النفايات	النفايات حسب النوع
Domestic	Umm AlOAfai (1)	0	0	0	0	0	0	أم الأفاعي (1)	نفايات منزلية
	Mesaieed	664,959	536,050	537,313	482,640	408,526	326,960	مسيعيد	
	DSWMC		648,337	618,156	613,226	639,522	603,703	مركز إدارة النفايات الصلبة المنزلية	
	Total Domestic	**664,959**	**1,184,387**	**1,155,469**	**1,095,866**	**1,048,048**	**930,663**	إجمالي النفايات المنزلية	
Construction	Raw dat Rashid/Income	2,010	140,402	1,998,853	3,806,745	6,433,372	8,893,750	روضة راشد/وارد	نفايات البناء
	Raw dat Rashid/Treated	50,306	177,969	485,657	459,857	539,631	0	روضة راشد/معالج	
	Umm AlOAfai	0	0	0	0	0	0	أم الأفاعي	
	Mesaieed	1,058,918	533,036	548,527	469,669	622,978	460,737	مسيعيد	
	Umm Thanytain	1,945,359	3,418,673	2,096,906	0	0	0	أم ثنيتين	
	Total Construction/Treated	50,306	177,969	485,657	459,857	539,631	0	إجمالي نفايات البناء/المعالجة	
	Total Construction/Income	**3,006,287**	**4,092,111**	**4,644,286**	**4,276,414**	**7,056,350**	**9,354,487**	إجمالي نفايات البناء/الواردة	
Bulky (2)	Umm AlOAfai	0	0	0	0	0	0	أم الأفاعي	نفايات ضخمة (2)
	Mesaieed	2,198,780	2,661,504	2,333,567	2,048,954	1,747,678	1,796,396	مسيعيد	
	Total Bulky	**2,198,780**	**2,661,504**	**2,333,567**	**2,048,954**	**1,747,678**	**1,796,396**	إجمالي النفايات الضخمة	
Tires	Raw dat Rashid/Income	39,406	37,186	37,824	36,297	31,605	16,448	روضة راشد/وارد	الإطارات
	Raw dat Rashid/Treated	27,300	15,062	17,739	12,933	18,172	0	روضة راشد/معالج	
	Umm AlOAfai/Treated	0	13	5,621	9,269	19,351	0	أم الأفاعي/معالج	
	DSWMC	0	0	0	0	0	8,943	مركز إدارة النفايات الصلبة المنزلية	
	Total Tires/Treated	**27,300**	**15,075**	**23,360**	**22,202**	**37,523**	**0**	إجمالي الإطارات/ المعالجة	
	Total Tires/Income	**39,406**	**37,186**	**37,824**	**36,297**	**31,605**	**25,391**	إجمالي الإطارات/ الواردة	
Other	Umm AlOAfai	0	0	0	0	0	0	أم الأفاعي	أنواع أخرى
	Mesaieed	37,379	171,912	213,022	207,367	12,540	10,064	مسيعيد	
	DSWMC	0	9,491	10,625	9,468	0	0	مركز إدارة النفايات الصلبة المنزلية	
	Total other	**37,379**	**181,403**	**223,647**	**216,835**	**12,540**	**10,064**	إجمالي الانواع الاخرى	
Total/Treated		**77,606**	**193,044**	**509,017**	**482,059**	**577,154**	**0**	**الإجمالي/المعالج**	
Total/Income		**5,946,811**	**8,156,591**	**8,394,793**	**7,674,367**	**9,896,221**	**12,117,001**	**الإجمالي/ الوارد**	

(1) From 2013 Umm AlOAfai has been Closed — (1) من عام 2013 أم الأفاعي مغلقة

(2) Bulky waste disposed only in Umm AlOAfai and Rawdat Rashid. — (2) النفايات الضخمة يتم التخلص منها في أم الأفاعي ومسيعيد فقط

Source: Ministry of Municipality and Environment — المصدر : وزارة البلدية والبيئة

It is therefore understandable that the Qatar government has set a target of treating 38% of the waste as these current practices are environmentally unsustainable and need to change [302]. The SRF considered within this LCA consists of wood waste, cardboard, paper, polyethylene plastic segregated from MSW and can be used as alternative solid fuel in gasification. The process of air gasification converts SRF into syngas by a thermal reduction process, which can subsequently be used to generate energy in a gas engine and thus reduce reliance on landfill [306].

8.3 LCA background

LCA is a tool that has been designed for measuring environmental impact due to human activity. It is a well-established analytical method that has been applied to various manufacturing industries, and is well suited to analyse different technological process chains and pathways. Example applications

are to the cement industry, acrylic fibre production, food products manufacturing, and buildings energy [307-308].

Conducting LCA involves four steps: goal and scope definition, inventory analysis, life cycle impact assessment (LCIA) and interpretation. The framework for LCA is conceptually depicted in Figure 8-2, and its procedures and principles have been standardised in ISO 14040 [307]. The double arrows in Figure 8-2 between the phases indicate the iterative nature of the LCA process. When conducting the assessment, it can become clear that certain information is missing which would require an improvement the inventory analysis. It may be possible that the interpretation of results is not clear and not straightforward to understand. This may mean expanding the goal and scope of the study so that the study objectives can be achieved. Therefore, in practice, LCA is not a linear process, rather an iterative process carried out for these four stages in order to arrive at credible results that address the study goal and objectives.

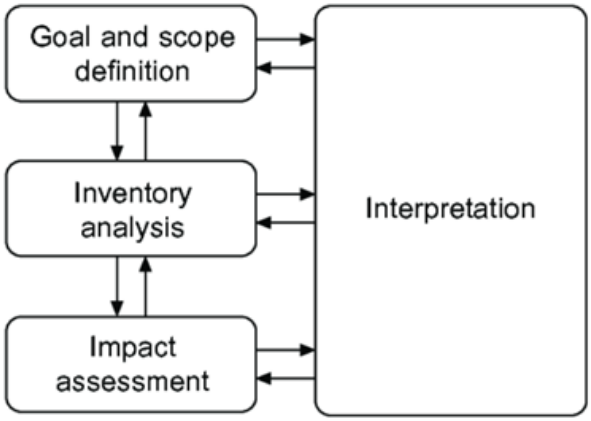

Figure 8-2 LCA framework [307]

LCA is typically conducted by modelling the energy and mass flows of the process that are to be considered. Similar to the system boundary issue, increasing rigour of the analysis is associated with increased challenges in data availability and accuracy, while reducing rigour is associated with many simplifying assumptions. Consequently, appropriate techniques are being increasingly developed that incorporate optimisation of engineering systems to address these challenges. As a result of its increasing use, different variations of the LCA methodology have been developed. For example, one variant is ExLCA (Exergy LCA) which incorporates the modelling of mass and energy flows in terms of exergy (this term can be defined as the amount of possible work that a system can produce in the thermodynamic equilibrium) [309-310]. While the LCA methodology was originally developed to act as a decision support tool for distinguishing products or product systems or services with an environmental impact perspective, it can be seen from the previous examples that its application has spun out into the areas of manufacturing, thus looking at process chains. Therefore, this is the analysis tool of choice and it is used in this chapter to assess the environmental impact of MSW treatment by SRF gasification technology. According to the ISO14040 standardised LCA methodology in Figure 8-2, the life cycle assessment of this study is carried out in four phases, which is described in the

following sub-sections to confirm the validation of the ReciPe2016 model and data analysis process. Results produced in the current work is validated with the findings of Al-Maaded et al. [40].

8.3.1 Goal and scope definitions

Defining the goal and scope is the first step of the LCA. This is a very important step that must take into account the objectives of the study at hand. Too big a system boundary can result in data requirements that would make the study unachievable. At the same time, too much of a simplified approach would result in loss of rigour and loss of credibility in the analysis due to the many assumptions that would need to be made, a point that has already been made. One of the first things is to define the system boundary in view of goal. Therefore, defining the study goal and the system boundary go hand-in-hand and may be defined in an iterative manner. In the LCA, the results are presented based on the 'functional unit', which is the unit of the product or process flow that forms the basis of the environmental impact that is to be assessed in the LCA. The functional unit is the performance characteristic based on which two or more products or processes can be compared. All data that is gathered within the phase of inventory is eventually related to the same functional unit to facilitate an objective comparison of the different scenarios, process, or products. Following this definition of the study scope and goal, the time consuming step of collecting all the data to allow the analysis to be conducted is performed, namely the inventory analysis [309].

8.3.2 Inventory analysis

This is the second and most involved stage of the LCA. At this stage, the process details and boundaries need to be refined in view of the data availability. Issues of data accuracy and validity need to be considered in order to conduct a reliable LCA. The result of this inventory phase is essentially input/output data that is reliable and should be referenced. Different software exists to facilitate this process. The most commonly used environmental databases are Ecoinvent [311] and GaBi Professional Database [308], This step of the life cycle includes data collection and treatment on the material consumption, and energy use in other phases of the life cycle. The data can be site specific, but it may also be more general. For example, data may be acquired for a process in general rather than for a specific location. This is the approach that has been taken in this chapter, where the energy and mass flow data for SRF gasification in general is taken, while the environmental impact associated with these energy and mass flows is calculated based on Qatar-specific characterisation factors (CF).

8.3.3 Impact assessment

This is the third step which comprises identifying and aggregating the burdens of environment quantified within the analysis of inventory to environmental impacts such as climate change. The shift to impact assessment from inventory analysis is a complex step in conducting LCA. The collection of data is the highly intensive activity for the LCA, especially when specific data is

required and may not be available in the literature. In many cases, data averaged from the literature or previous study are used. However, the problem with average data is that it may be some years old and may not represent the latest situation. The result of the data collection can be typically presented in an inventory analysis, presented succinctly, to be then interpreted as environmental impact categories [312].

8.3.4 Interpretation

Interpretation is the fourth phase of the LCA, where the results are analysed and understood regarding environmental impact. The procedure is systematic and it involves identification, checking and evaluation of the information obtained from the inventory analysis, and to present them in order to meet the requirements of the pre-defined study scope and goal. This may include an analysis of all the impact categories to judge the impacts that are the most significant. There is in line with the aim of interpretation, to reduce the amount of quantified data in the inventory analysis to facilitate decision making. After this evaluation of the process/product, conclusions are formed in view of the limiting assumptions. Finally, recommendations are presented towards reducing environmental impact. This step is important to improve the reporting and transparency of the study [307].

8.4 Methodology

LCA has been widely used to assess the environmental impact of biomass gasification and waste treatments [313]. Different LCA studies for Qatar have been previously conducted and have been published in the literature [30, 314-317]. The objective of reviewing previous studies is to provide background on the state-of-the-art of LCA in Qatar and to support this study [307] . To apply this process in Qatar, the environmental impact of the mass and energy flows were acquired from literature, government environmental statistic reports [318], and the ReCiPe2016 model database [319]. The environmental impact categories were obtained from ReCiPe2016 based on Qatar specific data and calculated using Microsoft Excel®. The theoretical framework and the study design were based on the ISO 14040 standard. This LCA aims to analyse the environmental impacts of SRF gasification on electricity generation using four scenarios:

1. MSW landfills only with no further treatment (baseline).
2. Biogas capture from landfill.
3. Biogas capture and SRF gasification.
4. Biogas capture and SRF gasification with solar technology.

These scenarios were compared with previously published work by Al-Maaded et al. [40]. The research herein is the first LCA that considers SRF gasification as an alternative method to reduce MSW landfills and produce sustainable energy in line with Qatar's national vision 2030.

This LCA methodology provides a harmonised characterisation method for calculating environmental impacts, known as midpoint and endpoint levels. Its predecessor (ReCiPe2008) only considered European characterisation factors, while this improvement included presenting the global scale [320]. Problem shifting is a vital issue that arises with LCA process that encompasses many different process stages, in that improving one stage may worsen another stage along the process chain. Concerning the scope and system boundary selection, the system boundary can be kept small to facilitate data collection, but it may introduce 'problem shifting' which needs to be tackled if a credible analysis is carried out. However, expanding the analysis boundary results in problems of availability of data and accuracy of the analysis [312]. The largest system boundary that could be considered is called 'cradle-to-grave' which includes the process of extracting resources from the earth, their transportation, manufacturing and utilisation in the process in question, and finally disposal again into the earth. Therefore, the challenge of data collection and availability needs to be considered hand-in-hand with study boundary selection to conduct a reliable LCA [321].

Out of the 18 midpoint impact factors, only five categories—climate change, terrestrial acidification, marine ecotoxicity, water depletion and fossil depletion—which had significant values relating to Qatar were considered. The endpoint stage was to reduce MSW landfills in Qatar by producing electricity from SRF gasification. In addition, the other impact categories with negligible values were neglected in this analysis due to an abundance of data in the literature; hence it was deemed that further analysis was not necessary. For this study, the midpoint impact factors are calculated based on medium-term (hierarchist) of 100 years impact [320]. Consequently, these impact categories are presented in the results, Section 8.4.2. The full list of indicators for the corresponding impact categories and associated reference substances is provided in Table 8-2.

Table 8-2 Reference substances for impact category representation [320].

Impact Category	**CF_m**	**Unit**
Climate change	Global warming potential	kg CO_2-eq to air
Terrestrial acidification	Terrestrial acidification potential	kg SO_2-eq to air
Marine ecotoxicity	Marine ecotoxicity potential	kg 1,4-DCB-eq to marine water
Water depletion	Water consumption potential	m^3 water-eq consumed
Fossil depletion	Fossil fuel potential	kg oil-eq

In order to calculate the midpoint impact category, the following formula was used:

$$Indicator\ result_{catagory} = \sum_{sub\ catagory} (CF \times Inventory\ result) \qquad (8.1)$$

The indicator result refers to the emission of a substance for any process, CF refers to the ReCiPe2016 characterisation factor, while the inventory result is the amount of emitted substance per year. For example, the indicator result can be the 'Global warming' impact category in kg CO_2-eq, the characterisation factors are given in Table 8-2, while the subcategory example is CO_2 and CH_4. Finally, the inventory result is the mass flow per year. Application of the above formula to each process, in each scenario results in calculating the impact for each ReCiPe2016 mid-point category per year.

8.4.1 Goal and Scope of the Current Study

The scope of this study is limited to the state of Qatar's geographical boundaries. As a result, the environmental impact of oil and gas exports beyond this boundary is unconsidered. The functional unit used in this analysis is environmental impact per tonne of dry MSW processed. While this is the functional unit, the results are presented for one year based on the waste disposal data from 2018 in Table 8-1 [305].

The main assumptions used in this study are as follows:

- The system boundary starts when the MSW is collected and delivered to the waste management plant (be it landfilling or further processing). The transport emissions from the city to the landfill site are not considered in all scenarios due to no relevant data available in the literature for Qatar. Therefore, it is more sensible to focus on the different environmental impacts associated with MSW processing, and as each scenario considers the transportation emissions will be nominally the same, so the comparison between all scenarios will be more reliable.

- According to Al-Maaded et al. [40], the bulk of the MSW comprises of paper and plastic. Glass and metals comprise 13% of the MSW, which have not been considered in this study. To conduct the analysis, a comparison has to be made between different scenarios within the case study goal and system boundary. Therefore, the goal of this analysis is to quantify the reduction in environmental impact caused by the implementation of MSW treatment to produce SRF for gasification technology; variables other than the additional waste treatment are kept constant. In this way, a certain improvement upon the baseline scenario can be compared objectively with the baseline case. Additionally, the baseline is selected to represent the actual MSW treatment situation in Qatar.

The following scenarios are defined for comparison:

Baseline: In this scenario, MSW landfilling only with no further treatment. The wastes are buried in a controlled environment known as a landfill [314]. The organic fraction of wastes in the landfill decompose under anaerobic conditions, releasing landfill gas, also known as biogas that mainly

comprises 58% CH_4, and 41% CO_2, which has an environmental impact and is accounted for in the baseline scenario [315].

Scenario 1: In addition to the baseline, this scenario adds biogas capture to the landfill. In this case, about 50% of the biogas is collected, treated and burnt to generate electricity, releasing only CO_2 to the environment. The remaining 50% is either burnt in flares or released into the atmosphere [316].

Scenario 2: In addition to the technologies deployed in Scenario 1, this scenario adds the production of SRF to generate electricity via air gasification. According to Al-Maaded et al. [40], the MSW in Qatar has paper and plastics that equate to 25–30% of the total waste. As a result, this MSW can be treated to produce SRF for gasification to generate electricity with lower environmental impact while reducing the need for landfill as shown in Figure 8-3. The treatment process starts with the incoming MSW to the primary material recovery facility (MRF), where separation and segregation of MSW into different categories can be performed, for example glass, plastics, paper, metals and cardboard. After that, the mechanical treatment unit shreds of waste to produce SRF pellets, while other trash that is not suitable for gasification at this stage is sent to a landfill. Then, the SRF is used as a solid fuel in air gasification to produce syngas and generate electricity. In addition, supply the power input to MSW treatment stages (primary, mechanical) and SRF air gasification unit. Finally, the organic residue part (70% of the MSW) is handled in the secondary MRF for further processing.

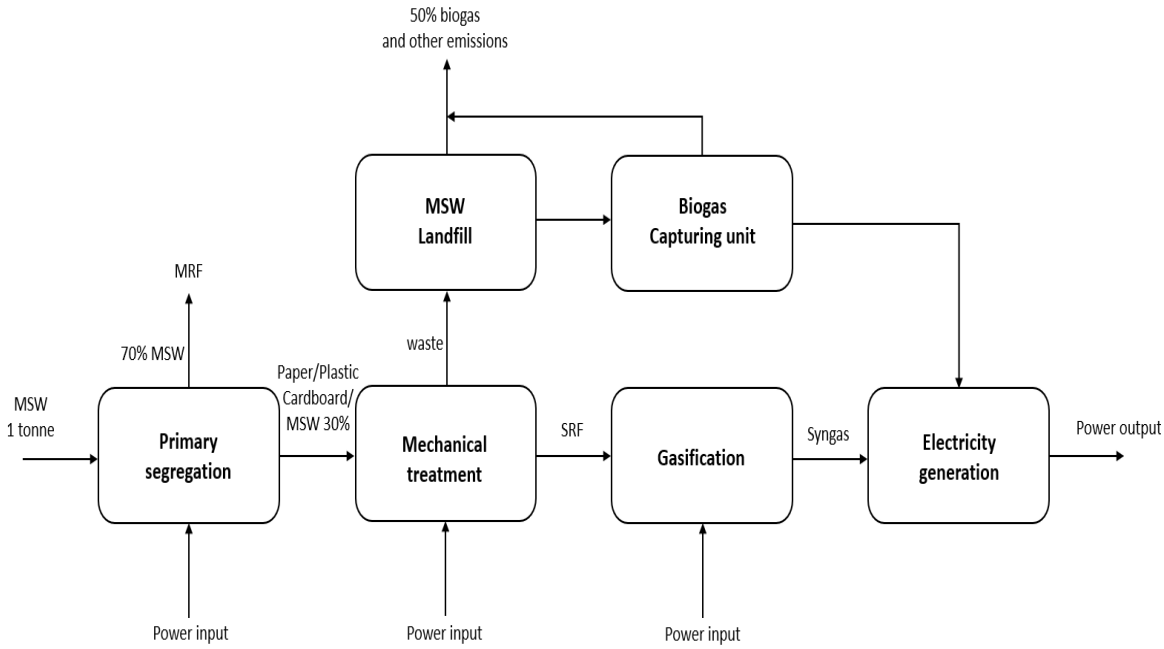

Figure 8-3 Energy and mass flows diagram for Scenario 2

Scenario 3: In addition to Scenario 2, here the electricity used by the MSW treatment processes in Figure 8-3 (power input) is supplied by solar PV with air gasification technology instead of using electricity from syngas combustion. It is assumed that electricity generated from the solar PV with gasification produces similar CO_2 emissions from the thermal treatment of the SRF process in

Scenario 2. However, the solar plant size and Qatar climate are the significant challenges in this process.

8.4.2 Inventory analysis of this study

MSW continues to grow due to increasingly wealthy lifestyles and continuing industrial and commercial development globe-wise. Biodegradable MSW, such as food waste, undergoes a series of complex biochemical processes which happen inside the landfill, resulting to waste decomposition, which in turn leads to the emission of biogas and the draining of material from the landfill. Though there is a global embrace of MSW, its challenges have encouraged the development of standby strategies to convert waste to energy. Despite the availability of various ways, gasification has been proposed as a superior and efficient technology. The treatment process of MSW in this study has followed the method provided by Abduli et al. [322], and listed in Table 8-3.

Table 8-3 Life cycle inventory for landfilling with composting for the functional unit of one tonne of MSW [322], (License N.: 5183000344643).

Property	Diesel	8.331 kg
Material Consumption	Electricity consumption	35.425 MJ/t
	Electricity recovery	−196.14 MJ/t
	Electricity consumption from leachate treatment	0.2436 MJ/t
	Land used	0.1283 m^2/t
Direct Emissions	CH_4	13.49 kg/t
	NOx	0.228 kg/t
	VOC	1.000111 g/t
	SOx	0.012 kg/t
	NH_3	0.182 kg/t
	Metal (air)	3.00E-5 g/t
	CO_2	35.749 kg/t
	HCFC	0.118 g/t
	SPM	2.1 g/t
Direct Water Emissions	COD	0.56525 kg/t
	T-N	1.4896 g/t
	T-P	2.352 g/t
	Cu	0.0621 g/t
	Cr	0.05683 g/t

	Zn	0.19193 g/t
	Pb	0.03697 g/t
	Cd	0.005799 g/t
	Ni	0.06779 g/t

This LCA process is mainly based on the work done previously by Al-Maaded et al. [40], Andric et al. [317], Huijbregts et al. [319], Cherubini et al. [315] and Abduli et al. [322]. The landfill statistics for 2018 were obtained from the Planning and Statistics Authority [317,305]. The MSW is treated, converted into compost, and a significant portion is landfilled. This landfilling is associated with environmental emissions from the mass and energy flows of the process [322]. These practices and data were taken for the baseline and MSW processing proposed in Scenarios 1–3 [322, 40].

The impact of depositing plastics in the Qatari context has been quantified by Al-Maaded et al. [40] as 8 kg CO_2 eq. (GWP 100 years), 7.8 kg DCB eq. (human toxicity potential CML 2001), 0.15 kg Sb eq. (abiotic depletion) and 0.029 kg SO_2 eq. (acidification potential CML 2001). Paper and plastic account for 25% of total MSW in Qatar; the MSW processing proposed in Scenarios 1–3 is based on this number [40]. Luz et al. [30] provide the energy and mass flow data of SRF production from MSW. It is important to note that while the baseline scenario is not associated with significant electricity usage, the alternative scenarios generate electricity that offsets grid supply. As the grid electricity is generated using indigenous natural gas with associated environmental impact, alternative scenarios to the baseline reduce these carbon emissions by offsetting this grid electricity. The energy and mass flow based on 1 tonne of MSW per hour have been assigned to Table 8-4. For the current case, the caloric value of SRF air gasification is 5.8 MJ/Nm^3 and the combined cycle gas turbine (CCGT), 400 kg CO_2 eq./MWh, are used to generate electricity [29, 323]. Qatar-specific impact characterisation factors are taken from the ReCipe2016 database are presented in Table 8-5, 6 and 7.

Table 8-4 Energy production and consumption of MSW to SRF to electricity generation [30], (L.N.: 5183000524754).

Sections/Equipment	Throughput Capacity (Tonne/Hr)	Electric Power Consumption (kW)
Primary Separation	16.7	176.6
Mechanical Treatment	2.0	99.30
Sections/Equipment	Thermal Energy Generation (kW/h)	Electric Power Consumption(kW)
Gasification and Gas Cleaning	1000	5.25
Sections/Equipment	Electric Power Generation (kVA/h)	Electric Power Consumption(kW)
ICE-Electric Generator	330	0

Table 8-5 Qatar-specific characterisation factors from the ReCiPe2016 database.

Acidification Potential (AP), Kg SO_2-eq-kg^{-1}			Endpoint Characterisation Factors, Species yr/kg		
Emitted Substance			Emitted Substance		
NOx	NH_3	SO_2	NOx	NH_3	SO_2
0.97	2.02	1.25	8.61×10^{-8}	2.85×10^{-7}	$2.14w \times 10^{-7}$
human Health Ozone Formation Potentials (hofp), (kg NOx-eq/kg)		Ecosystem Ozone Formation Potential (eofp), (kg NOx-eq/kg)			
Emitted Substance		Emitted Substance			-
NOx	NMVOC	-	NOx	NMVOC	-
1.17	0.16	-	3.04	0.3	-

Table 8-6 Gulf-specific characterisation factors from the ReCiPe2016 database.

Particulate Matter Formation Potential (PMFP, Kg Primary PM2.50eq/kg			
Emitted Substance			
PM2.5	NH_3	NOx	SO_2
1.22	3.24×10^{-1}	8.52×10^{-2}	3.59×10^{-1}

Table 8-7 Global warming potential characterisation factors [40], (L.N.: 5183000780256).

Global Warming	Class / Formula	GWP20	GWP100	GWP1000
Name		$kgCO_2eq/kg$ Individualist	$kgCO_2eq/kg$ Hierarchist	$kgCO_2eq/kg$ Egalitarian
Carbon Dioxide	CO_2	1	1	1
Methane	CH_4	84	34	4.8
Fossil Methane	CH_4	85	36	4.9
Nitrous Oxide	N_2O	264	298	78.8

8.4.3 LCIA of this study

LCIA classifies material and energy flows based on the impact they could cause on the environment. To calculate each impact category, a reference substance is used [42]. For example, considering the climate change impact category, the environmental impact indicator chosen is infrared radiative forcing, causing an increase in temperature globally, which is translated to a CO_2 value, used as the reference substance to indicate global warming potential. The full list of indicators for the corresponding impact categories and associated reference substances is provided from Goedkoop et al. [320].

8.5 Results

Corresponding to the life cycle inventory, a total of five environmental impact categories were recorded, as described in the methodology. For the baseline case, the environmental impact is presented in Figure 8-4. As can be seen in Figure 8-4, clearly the environmental impact of climate change as a result of CO_2 emission is magnitudes higher than the other four categories. The results show that marine ecotoxicity can be considered negligible when compared to the other categories. Figure 8-4, 5, 6 present results for the environmental impact categories with the three largest magnitudes. Clearly, a significant reduction in all these three categories is observed in Scenarios 2 and 3 for the SRF gasification case. Terrestrial acidification however showed no change in all four scenarios.

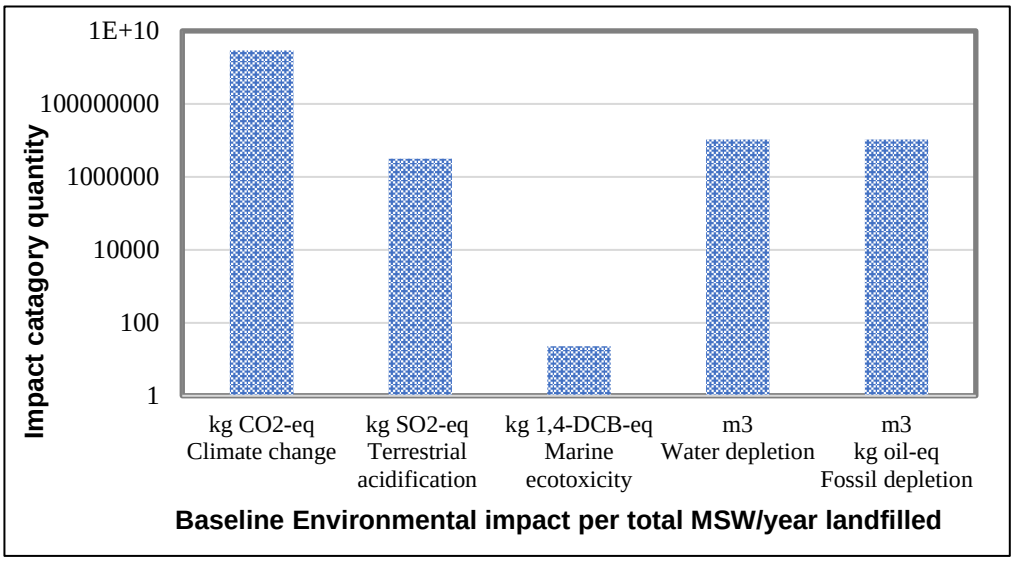

Figure 8-4 Five environmental impact categories for which non-zero values were recorded as a result of the LCA

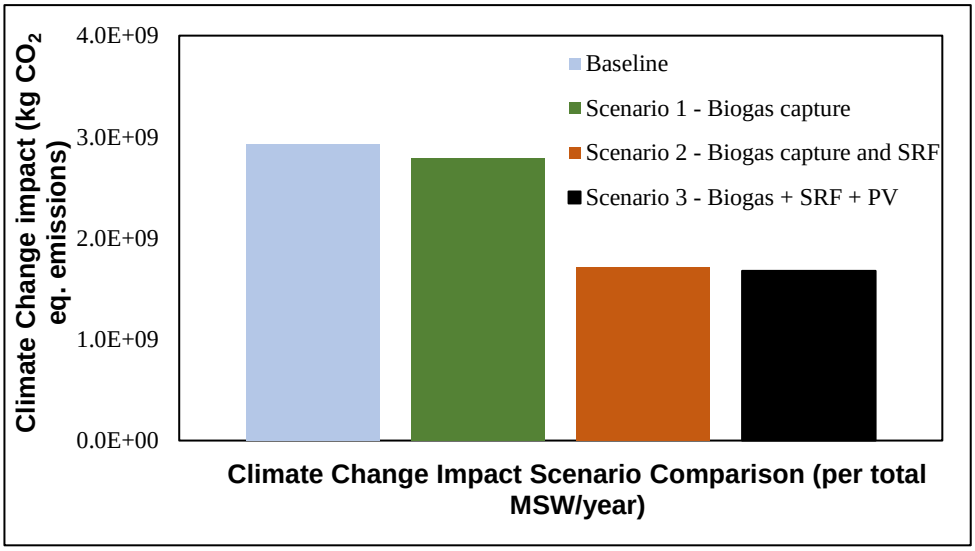

Figure 8-5 Comparison of climate change impact category (global warming potential) of all the scenarios considered in this study

Based on the previous work on solid waste processing in Qatar, Al-Maaded et al. [40] estimated the climate change impact to be 8 kg of CO_2 emissions per 10 kg of plastic waste processed, while the results in this study translate to 5 kg of CO_2 emissions per 10 kg of MSW processed, the baseline of this study uses general dry MSW while Al-Maaded et al. [40] only considered plastic waste. In addition, in the current study the updated Recipe2016 and MSW landfill data were used. These two reasons may justify the lower climate change impact as compared to Al-Maaded et al. [40] for the baseline.

When compared to the baseline, Scenarios 1, 2 and 3 result in 4.8%, 41.3% and 42.7% reductions. It is clearly shown that the greatest impact on reduction is due to the introduction of SRF gasification

whereas biogas capture and PV have comparatively minor effects. It can be established that scenarios 2 and 3 have the same magnitude of impact on climate change. That is, the level of CO_2 emission is almost equally the same.

Figure 8-6 exhibits results very similar to Figure 8-5 because the water depletion is directly linked to the electricity generation. This is because the electricity generated in gas power plants consumes a large amount of water, therefore a reduction in electricity use from fossil fuels results in indirect reduction of water depletion. Similar to the results for fossil depletion, alternatives to the baseline result in large magnitudes of reduction in this category. These are about 50 times, 100 times and 100 times impact reduction with respect to the baseline for Scenarios 1, 2 and 3, respectively.

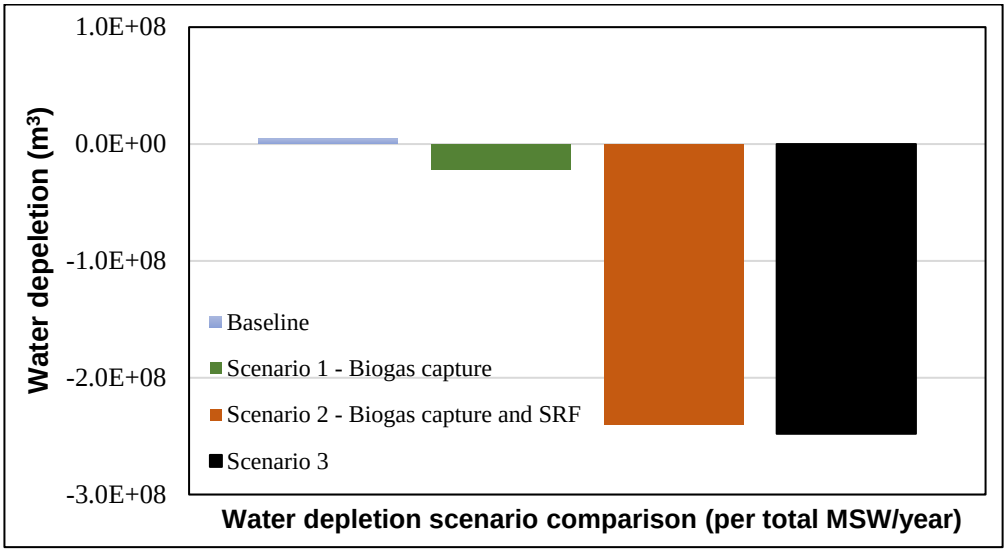

Figure 8-6 A Comparison of water depletion of all the scenarios considered in this study

Comparing the baseline Scenario with Scenarios 1 to 3, the results show about 6 times, 1.0×10^{11} times, and 1.0×10^{11} times reduction in fossil fuel depletion respectively. Again, the main reason for the significant impacts in scenarios 2 and 3 are due to the introduction of SRF gasification to produce electricity. In addition, using solar PV technology with SRF gasification produced clean energy with similar CO_2 emissions to scenario 2. One of the key elements of the arid Qatari climate is the impact of the high temperature and direct irradiation on solar panels [29]. However, some major PV challenges in Qatar reported in the literature to be considered include limited land, cost, lack of regulations, dust accumulation, high humidity and temperature [324- 325]. The use of biomass gasification with solar energy eliminates the need for a lot of capital-intensive equipment in the traditional biomass gasification approach, and the combination of the two will lead to an increase in the syngas products [28]. The large values of fossil depletion reduction arise in Scenarios 2 and 3 because the fossil fuel (natural gas) was used to generate electricity in the baseline Scenario.

8.6 Discussion

In this section, the results presented previously are discussed within the background of the literature review and the improvements achieved through the measures incorporated in the defined scenarios. As MSW treatment to produce SRF involves a variety of mass flows together with the use of electricity and generation at different steps along the supply chain, LCA is perhaps the best suited tool to assess the suitability of this process. However, a review of the literature concluded that there had been relatively few studies that have analysed waste treatment in Qatar using LCA. Al-Maaded et al. [40] used the life cycle approach to assess solid waste management and plastic recycling compared to landfilling. The authors concluded that recycling plastic reduces the global warming potential and soil toxicity from landfilling. Ayoub et al. [33] investigated the solid waste management practices and implementation of optimisation modules, but no LCA methodology was used. The authors herein conclude that utilising solid waste as a material to produce energy may reduce landfilling by 53% of total waste disposed via this method. Other LCA literature investigated the Qatari mass and energy flow system, namely transport, energy use in the residential sector and the natural gas supply chain. Therefore, the main contribution of this chapter is that this is the first LCA of SRF gasification within the context of Qatar. Additionally, the impact of using solar energy for the MSW treatment and SRF gasification process on the environment has also been quantified, where the results show that it makes a valuable difference to the reduction in environmental impact when compared to the baseline.

A total of five environmental impact categories were assessed in this LCA, namely climate change, terrestrial acidification, fossil fuel depletion, water depletion and marine ecotoxicity. Previous studies on this topic in Qatar only included climate change and terrestrial acidification. Therefore, among the five environmental impacts analysed, climate change was the largest environmental impact as shown in Figure 8-4. This was expected as natural gas is the main energy supply to Qatar. However, fossil depletion, water depletion and terrestrial acidification followed climate change in their magnitude in decreasing order.

Only the main four environmental impact categories were analysed and compared for the different scenarios. The baseline scenario represents the current MSW practice in Qatar which is simply landfilling only with no further treatment. Scenario 1 improves upon this analysis by including a 50% capture of the biogas released from the organic matter in the landfill. This measure improves climate change impact by 4.8% as presented in Figure 8-5. In addition, Scenario 2, which improves upon the 50% biogas capture by including SRF gasification, significantly reduces climate change impact. A reduction of 41.3% for Scenario 2 can be seen in a comparison with the baseline as shown in Figure 8-5. Finally, Scenario 3 considers the use of solar energy in MSW treatment and gasification to produce electricity; however, the additional impact on climate change is not deemed significant, calculated to be only a 4% improvement over Scenario 2. In summary, for the climate change category, the most significant reduction possible is for SRF gasification and production of electricity

using syngas to offset the local electricity requirements. Essentially this measure of MSW treatment and gasification-based electricity would not only reduce dependence on landfill but also reduce carbon emissions higher up in the supply chain by producing less electricity from natural gas.

Considering the analysis of fossil depletion in Figure 8-7, recovering 50% of biogas has a small improvement over the baseline. However, the gasification scenario drastically improves this environmental impact category. In the baseline scenario, fossil depletion accounted for 1.06×10^7 kg oil equivalent for the total MSW processed per year. This value reduced to -2.87×10^{18} kg oil equivalent emissions, resulting from offsetting the use of natural gas to produce electricity in Qatar. Similar to the analysis for climate change, the introduction of solar energy to the gasification process only resulted in a 3.5% further improvement over the gasification in Scenario 2.

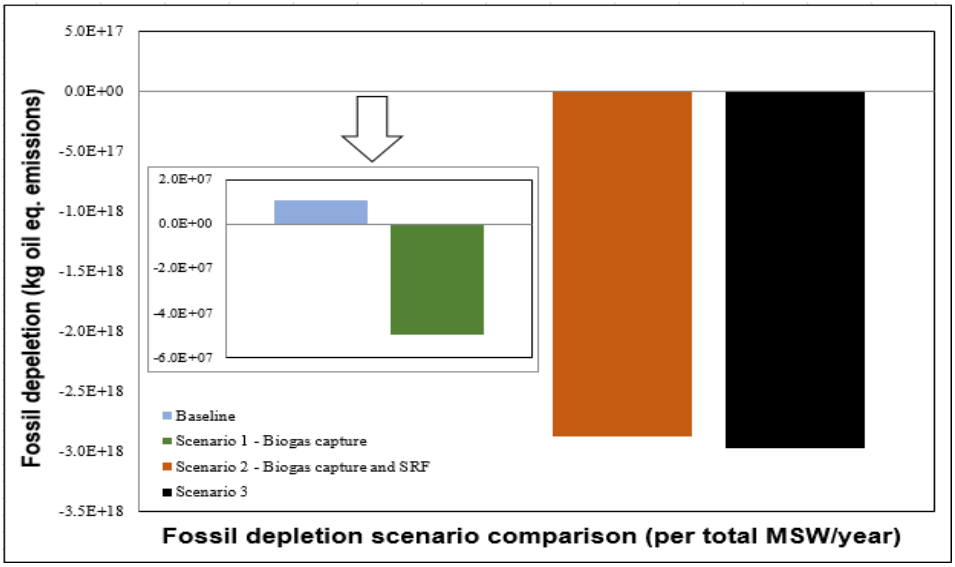

Figure 8-7 A comparison of fossil depletion of all four scenarios considered in this study

A comparison of fossil depletion of all four scenarios considered in this study. The water depletion results present a similar situation where the baseline is calculated to result in 4.7×10^6 m^3 of water depletion, as shown in Figure 8-6. This results in negative values for the improved three scenarios. As with the previous findings, the use of 50% biogas captured results in a small reduction of this environmental impact, while Scenario 2, which is the gasification process without solar energy, results in negative emissions of water depletion as a significant reduction. The use of solar energy in Scenario 3 further adds a 3.3% improvement over Scenario 2.

Terrestrial acidification however remained unchanged for all four scenarios. It must be kept in mind that the data used in this analysis incorporated average data for SRF gasification from literature. Additionally, only those country-specific characterisation factors that were available in the ReCipe2016 database were used, while for the remaining, characterisation factors for the Gulf region were used, as listed in Table 8-6.

It can be concluded that the LCA shows that the environmental improvements found in Scenarios 1–3 represent measurable improvements over the baseline However, some assumptions were made in the present study, namely, the neglection of emissions from transportation of solid wastes which may have a considerable impact on the environment. The most significant improvement was observed in Scenario 2 and 3 because this considered the produced electricity from SRF gasification. When the four categories in this LCA were compared, the largest reduction was obtained from climate change, followed by fossil depletion, water depletion and marine ecotoxicity. In view of the Qatar national vision 2030 where environmental impact and water use are key resources that need to be used more judiciously, the use of SRF in gasification technology will be an appropriate pathway.

8.7 Summary

In this chapter, the first LCA of SRF air gasification to produce electricity in Qatar has been conducted using ReCipe2016 model. LCA is a methodology that considers the various inputs and outputs along the supply chain or the production process to account for their environmental impact. A detailed general background of LCA and how it is implemented was provided. Additionally, a review of LCA literature was conducted with the aim of summarising the state-of-the-art in LCA of waste situation and gasification in Qatar. Qatar-specific characterisation factors (CF) were used from the ReCipe2016 database. The life cycle inventory was developed using ReCipe2016 resource together with information from literature and Qatari governmental reports on MSW classification. The LCA was performed considering four scenarios namely baseline, Biogas capture from landfill, Biogas capture and SRF gasification and Biogas capture and SRF gasification with solar technology. The MSW was evaluated using data from literature and Qatari governmental reports based on the 1 tonne/hr treatment process.

The LCA has been performed considering only four major environmental impact categories in Qatar. Four scenarios of operation have been adopted to perform the LCA, namely, the current practice in Qatar (baseline), capture of 50% biogas (Scenario 1), biogas capture by including SRF gasification (Scenario 2) and using solar energy in the gasification in addition to Scenario 2 settings (Scenario 3). Among the main four environmental impacts analysed, climate change was the largest environmental impact. This was expected as natural gas is the main supply to energy sector and economy in Qatar, which ultimately contributes to carbon emissions. Thus, climate change in this LCA is followed by fossil fuel depletion, water depletion and terrestrial acidification in their magnitude in decreasing order.

At the baseline stage, the landfill gas is a mix of CO_2, CH_4 and other gases created by the biochemical processes within a landfill as they cause decomposition of organic wastes such as food and paper waste. In scenario 2, adding the production of SRF to generate electricity via air gasification greatly reduces the emission of CO_2. In the case of scenario 3, it is assumed that electricity generated from

the solar PV with gasification produces similar CO_2 emissions from the thermal treatment of the SRF process in scenario 2.

The results indicated that Scenario 2 causes a large reduction in climate change at a lower cost compared to the other scenarios. Scenario 3, on the other hand, has the largest reduction in climate change. The results obtained in the present study have been compared to the study of Al-Maaded et al. [40] to confirm the validation. The current findings showed that on a 10 kg MSW processing basis, 5 kg CO_2 equivalent emissions were produced for the landfilling scenario. Given these outcomes, it can be concluded that the incorporation of SRF gasification can significantly reduce the MSW landfills and contribute to the Qatar national vision 2030. In addition, it examined the environmental impact of using SRF instead of natural gas to generate renewable electricity.

Chapter 9: Conclusions and Recommendations for Future Work

9.1 Conclusions

In this work, the thermochemical conversion behaviour of Subcoal™ was investigated using bubbling fluidised bed gasification reactor (BFBGR) and thermogravimetric analysis (TGA). In addition, solid waste management practices and LCA of SRF gasification in Qatar were studied. Since there is a global increase in the municipal solid waste (MSW,) its challenges have encouraged the development of standby strategies to convert waste to environmentally friendly energy. Gasification technology, considered the most sustainable and efficient technology, converts biomass or MSW to a gas mixture consisting mainly of CO, CO_2, CH_4, H_2, O_2 and N_2. Gasification with air is the most widely used technology due to the low cost of O_2 production and usage in multiple reactors.

This work aimed to carry out a Life-Cycle Assessment (LCA) of SRF gasification in order to evaluate the main process and environmental impact, which will contribute to Qatar's national vision of 2030. The LCA was performed using the ReCipe2016 database and Qatari governmental reports considering four scenarios namely the current situation (baseline), biogas capture from landfill, biogas capture from SRF gasification, and biogas capture from SRF gasification with solar technology. The results also indicated that biogas capture from SRF gasification leads to the largest reduction in GHG emissions at the lowest cost compared to the other scenarios. These findings assure the suitability of MSW gasification as alternative environmentally friendly technology for energy production as well as reducing the impacts of MSW landfill in Qatar.

It was useful to investigate the composition and characteristics of Subcoal™ as a solid fuel composed of non-recyclable paper and plastic wastes. The tests of Subcoal™ include proximate and ultimate analysis, XRF, XRD, particle size distribution, and other thermo-physical properties. The characterisation experiments proved that Subcoal™ is a highly acceptable solid fuel for thermal conversion processes, especially gasification. The content of moisture and volatile matter is in a suitable range for gasification technology. The particle size distribution analysis and density measurement showed that Subcoal™ particles lie in Group B and tend to undergo smooth fluidisation according to Geldart's classification. The Subcoal™ ash contains crystalline minerals and metal oxides which can catalyse decomposition reactions.

In order to evaluate the impact of catalyst loading and heating rate on the kinetics of thermal degradation of Subcoal™ PAF, TGA was used to investigate the pyrolysis, CO_2 gasification and combustion process. Generally, the TGA findings showed three decomposition stages: moisture removal, devolatilisation, and lignin decomposition. The mean degradation temperature and time

decrease with catalyst loading increases. The data of temperature, time and conversion obtained from TGA have been analysed using model-free and model-fitting methods to estimate kinetics parameters. The activation energies (E_a) and pre-exponential factors A of the pyrolysis, gasification and combustion of Subcoal™PAF were estimated in the presence and absence of catalysts. The TGA kinetics data of Subcoal™ thermal degradation, especially CO_2 gasification, would be remarkably useful for Subcoal™ reactor design and optimisation. Also, it would be essential for modelling and simulation studies for advanced Subcoal™-to-energy processes.

The gasification behaviour of Subcoal™ in laboratory-scale BFBGR has been examined for different equivalence ratios (ER), bed temperature, catalyst loading, Subcoal™ pellet shredding grades, and pellet particle size. The findings show that the optimum air gasification temperature and ER are 750 °C and 0.15, respectively, in presence of dolomite at the loading of 15 wt.%. Moreover, the small pellet sizes of Subcoal™ (6.3-10 mm) are more favourable in gasification than the large ones (14-27 mm). The study findings also provided an essential understanding of the quality of producer gas as well as the efficiency of Subcoal™ air gasification for different conditions. The data obtained are important for the industry to compare Subcoal™ to other biomass fuels when it comes to industrial gasification.

As a part of Qatar national vision 2030 one of the aims is to have the lowest possible CO_2 footprint, and, instead of MSW incineration or landfill, the non-recyclable paper and plastic waste can be utilised as a substitute fuel in waste-to-energy plant for environmentally friendly power production. This study also will contribute significantly to Qatar's national vision of 2030 through the sustainable use of natural resources in biomass gasification. It is a good substitute for fossil fuels that will help generate clean energy. Therefore, the present work makes a valuable contribution to global research of biomass gasification and clean energy technologies. In addition, Subcoal™ can be used to replace fossil fuels in cement and lime plants, steel blast furnaces, and power generation facilities. The N+P won significant contracts to supply Subcoal™ to the Uskmouth coal-fired power station in south Wales and Teesside plant in the United Kingdom because of its high conversion efficiency to renewable energy. Therefore, the global energy industry, specifically in Qatar such as QatarEnergy, can benefit from this research findings and reduce the dependency on natural gas or crude oil. Moreover, establishing facilities for MSW gasification mitigates the environmental impacts of landfill with non-recyclable plastic and paper waste.

9.1.1 Feedstock characterisation

The XRF analysis shown that Fe, Ti, Al, Ca, S, and Cl have recorded the highest content (PPM) among the mineral and soil elements. The XRD analysis finding of silica sand showed more crystalline than ash and Subcoal™ powder. Moreover, the particle size distribution has been obtained and discussed for silica sand bed (500-600 μm) and Subcoal™ powder< 3 mm using a Malvern Mastersizer 3000. The volume mean diameter for silica sand and Subcoal™ powder found as 658

μm and 890 μm, respectively. Subcoal™ powder have a larger volume than silica sand, owing to its large mixture amount of plastic paper waste.

9.1.2 LCA

First LCA of SRF gasification to produce renewable energy in Qatar has been performed considering five major environmental impact categories, namely climate change, terrestrial acidification, marine ecotoxicity, water depletion, and fossil depletion. Qatar-specific CFs were used from the ReCipe2016 database. Four scenarios of operation have been evaluated namely MSW landfills (baseline), biogas capture 50%, biogas capture with SRF gasification and SRF gasification with PV system. The LCA findings indicated that Scenario 2 caused a large reduction in climate change at a lower cost compared to the other scenarios. Scenario 3 had the largest reduction in climate change. The study shows that electricity can be generated using syngas produced from SRF gasification to offset the local power requirements. Given these outcomes, it can be concluded that the incorporation of SRF gasification can significantly reduce the MSW landfills and contribute to the Qatar national vision 2030. The results obtained in the present study have been compared to the study of Al-Maaded et al. [15]. The current findings showed that on a 10 kg MSW processing basis, 5 kg CO_2 equivalent emissions (or around 3M tonne CO_2 equivalent emissions per year) were produced for the landfilling scenario. The main assumptions made in this study include neglecting the transport emissions from the city to the landfill site in all scenarios due to no relevant data available in the literature for Qatar. Also, only paper and plastic were considered as the constituents of MSW.

9.1.3 TGA

Thermal and kinetics analysis of Subcoal™ PAF in the pyrolysis, CO_2 gasification, combustion in the presence and absence of catalyst have been determined using non-isothermal TGA. The TGA curve showed three degradation steps: dehydration (stage I), devolatilisation (stage II) and char/ash formation (stage III). The sample mass loss was measured as a function of time and temperature at various heating rates. The increase of heating rate shifts the TGA and DTG curve of fractional extent conversion to a high-temperature zone for all thermal degradation processes. Four decomposition stages and DTG peaks were obtained during degradation process may be attributed to Subcoal™ heterogeneity. The degradation of Subcoal™ in CO_2 atmosphere tends to be a complex mechanism, as shown by the DTG graphs, while combustion results obtained excellent E_a and A values. In addition, the E_a of Subcoal™ PAF obtained in this work for pyrolysis, CO_2 gasification, and combustion are lower than E_a of SRF/RDF obtained in the literature. This result proves that Subcoal™ PAF provides a faster chemical reaction time than SRF/RDF and other biomass. The influences of different loading of dolomite and olivine on the CO_2 gasification, pyrolysis, and combustion of Subcoal™ have been evaluated. The finding shows that as the catalysts loading increased the E_a decreased. Also, dolomite showed better catalytic cracking performance than olivine with low E_a value on pyrolysis, CO_2 gasification and combustion. These findings have been

compared with literature and found that Subcoal™ provided lower E_a values than other biomass, RDF or SRF.

9.1.4 BFBGR

The isothermal air gasification of Subcoal™ pellet (pellet A) and pulverised subcoal™ pellet (pellet B) have been investigated using BFBGR. The influences of ER, bed temperature, particle size and catalysts on the producer gas have been assessed. The outcomes show that at ER=0.15 the syngas composition, HHV and CGE reached to highest values. Also, the content of dry gas yield, HHV, CGE and CCE increase with temperature increase. However, char yield reduces as the temperature increased. Furthermore, as pellet sizes decreased from 27-14 to 10-6.3 mm, the gas composition increased, particularly the H_2 and CO contents. In brief, it has been found the optimum ER, bed temperature, and catalyst for gasification process in FBGR are 0.15, 750 ^{0}C and dolomite (15 wt.%,) respectively. Pellet B showed an excellent performance in terms of reaction time over the pellet A. At 750 °C, the gasification times for pellet A and pellet B are 10 and 7.9 minutes, respectively. However, no significant change was observed in the properties and composition of the producer gas from the gasification of pellet A and pellet B.

9.2 Recommendations for future work

The results obtained in the present work have led to a set of recommendations and suggestions which can be applied in future as follows:

- The effect of different particle sizes of Pulverised Subcoal™ Pellet gasification on gas composition and kinetic parameters should be further investigated in FBGR. It is anticipated that the smaller particle size of biomass the more rapid gasification reaction, hence higher syngas and lower char and tar formation.
- In the current study of gasification, air was used as a gasifying agent. However, other mediums have been reported in the literature such as steam, CO_2, O_2 or their mixture. Steam should be trialed as gasifying agent for high H_2 content of producer gas. Nevertheless, additional energy and facilities are required to generate steam as well as the increasing formation of tar. The performance and kinetics of gasification with other gasifying agents rather than air also can be investigated.
- Examine the effect of increasing the continuous feeding rate by 80 g and the time by at least 40 minutes to determine the maximum equilibrium bed temperature while avoiding external heat.
- The effectiveness of different synthetic catalysts includes char, aluminosilicate minerals, alkali metals, activated alumina, and a transition metal on the kinetic parameters and air gasification of Subcoal™ can be evaluated using the same conditions in the TGA and FBGR. The activated alumina and aluminosilicate minerals are good candidates that showed an

excellent performance with other biomass gasification in the literature. Also, a mixture of two catalysts can be tested.

- Gas chromatography (GC) is one of the widely used types of chromatography in analytical chemistry. This technique can separate a particular gas from a producer gas and measure its concentration. Therefore, the GC should be connected to TGA to analyse the gas composition and gasification performance. This procedure may require additional time and cost which is higher than the current situation. The combination of TGA and GC is well-known in the industry as Thermogravimetric Gas Chromatography (TG-GC) which is a powerful tool for determining very low levels of gases in complex mixtures. The GC is frequently accompanied by mass spectrometry (MS) for evaluating the gas identity. The combination (TG-GC/MS) provides a real-time analysis of the degradation products.
- Different biomass or waste types in Qatar should be investigated to use as feedstock for gasification technology and to support Qatar national vision 2030. In addition, decentralisation biomass facilities should be investigated to identify the effectiveness of operational cost and biomass challenges in Qatar.
- The LCA of SRF gasification to generate electricity in Qatar perspective should be further improved by using GaBi software. GaBi Software is a global tool for LCA modelling and emissions evaluation. It is able to evaluate the environmental optimisation potentials of the chemical production process at an early stage. Also, it can determine the individual life cycle stage that causes the highest environmental impact. Therefore, the most efficient measures can be identified to reduce that impact. GaBi software, on the other hand, is not available at Cardiff University, and license fees are required.
- Kinetic modelling and simulation of Subcoal™ gasification are very beneficial, considering fluid dynamics, mass and heat transfer, particle movement and chemical reaction. Also, biomass simulation of a large-scale gasification process is challenging in terms of the complexity of the reactions. Therefore, different tools should be used for performing a simulation such as UniSim and Aspen Hysys. The simulations results should be validated with the experimental findings obtained in the present study.

References

[1] I. Tiseo, “Generation of municipal solid waste worldwide in 2017, by select country (in million metric tons)*. Statista,” 2020. [Online]. Available: https://www.statista.com/statistics/916749/global-generation-of-municipal-solid-waste-by-country/. [Accessed: 28-Mar-2022].

[2] Clarke S.F and Almannai S., “Sustainable waste management in Qatar.In: Sillitoe P, ed. Sustainable Development: An Appraisal from the Gulf Region. 1st Edn. New York: United State of America.,” *books.google.com*, 2014.

[3] B. Global, “BP Statistical Review of World Energy 2019: an unsustainable path | News and insights | Home,” 2019. [Online]. Available: https://www.bp.com/en/global/corporate/news-and-insights/press-releases/bp-statistical-review-of-world-energy-2019.html. [Accessed: 06-Feb-2020].

[4] Ann C., “BESTS,” *University of Florida*, 2019. [Online]. Available: https://biogas.ifas.ufl.edu/BESTS/. [Accessed: 07-Feb-2020].

[5] F. G. van den Aarsen, A. A. C. M. Beenackers, and W. P. M. van Swaaij, “Wood Pyrolysis and Carbon Dioxide Char Gasification Kinetics in a Fluidized Bed,” *Fundam. Thermochem. Biomass Convers.*, pp. 691–715, 1985.

[6] S. Shoji, J. Delgado, A. Mosier, and Y. Miura, “Use of controlled release fertilizers and nitrification inhibitors to increase nitrogen use efficiency and to conserve air and water quality,” *Commun. Soil Sci. Plant Anal.*, vol. 32, no. 7–8, pp. 1051–1070, 2001.

[7] ReEnergy Holdings, “Biomass,” 2011. [Online]. Available: https://www.reenergyholdings.com/renewable-energy/biomass-faqs/. [Accessed: 13-Feb-2020].

[8] A. M. Salama, F. Wiedmann, A. Thierstein, S. Conventz, and W. Al Ghatam, “KNOWLEDGE ECONOMY AS AN INITIATOR OF SUSTAINABLE URBANISM IN EMERGING METROPOLISES: THE CASE OF DOHA, QATAR,” *Int. J. Archit. Res.*, 2016.

[9] World Energy Demand, “World Energy Demand, Including Oil and Gas, Rising to 2050, EIA Says - Natural Gas Intelligence,” 2022. [Online]. Available: https://www.naturalgasintel.com/world-energy-demand-including-oil-and-gas-rising-to-2050-eia-says/. [Accessed: 06-Jul-2022].

[10] E. R. E. C. (EREC), *Renewable Energy in Europe: Markets, Trends and Technologies*. 2010.

[11] IEA, “Outlook for biogas and biomethane: Prospects for organic growth – Analysis -,” *IEA*, 2020. [Online]. Available: https://www.iea.org/reports/outlook-for-biogas-and-biomethane-prospects-for-organic-growth. [Accessed: 28-Sep-2021].

[12] Central Intelligence Agency, “The World Fact book Qatar.,” 2016. [Online]. Available: https://www.cia.gov/librarY/publications/the-world-factbook/geos/qa.html. [Accessed: 06-Feb-2020].

[13] Ministry of Development Planning and Statistics, “2016–2018,” no. 10, 2015.

[14] QGEWC, “Qatar General Electricity & water Corporation,” 2009. [Online]. Available: https://www.km.com.qa/MediaCenter/pages/NewsDetails.aspx?ItemID=224. [Accessed: 13-Feb-2020].

[15] W. J. Gremm, J., Barth, J., Fietkiewicz, K. J., Stock, “Transitioning Towards a Knowledge Society. Qatar as a Case Study,” 2017.

[16] GSDP, “Qatar National Development Strategy 2011~2016,” *Qatar Gen. Secr. Dev. Plan.*, p. 288, 2011.

[17] Z. Said, “Science Education Reform in Qatar: Progress and Challenges,” *Eurasia J. Math.*, vol. 12, no. 8, pp. 2253–2265, 2016.

[18] The Millennium Report, “‘Forget Terrorism’: The Real Reason Behind The Qatar Crisis Is Natural Gas,” 2017. [Online]. Available: http://themillenniumreport.com/2017/06/forget-terrorism-the-real-reason-behind-the-qatar-crisis-is-natural-gas/. [Accessed: 13-Feb-2020].

[19] N. R. Rucevska I, Nellemann C, Isarin N, Yang W, Liu N, Sandnaes S, Olley K, McCann H, Devia L, Bisschop L, Soesilo D, Schoolmeester T, Henriksen R, *WASTE CRIME-WASTE RISKS GAPS IN MEETING THE GLOBAL WASTE CHALLENGE A RAPID RESPONSE ASSESSMENT*. 2015.

[20] D. M. Mittal, “Advancing sustainable consumption. Qatar National Vision 2030,” *Sustain. Gulf*, pp. 147–166, 2018.

[21] Qatar National Research Fund, “Qatar National Research Fund,” 2006. [Online]. Available: https://www.qnrf.org/en-us/. [Accessed: 13-Feb-2020].

[22] A. Thomas, “85% of Qatar’s solar energy is by Qatar Foundation - Products And Services - Construction Week Online,” 2014. [Online]. Available: https://www.constructionweekonline.com/article-28847-85-of-qatars-solar-energy-is-by-qatar-foundation. [Accessed: 13-Feb-2020].

[23] M. R. Nouni, S. C. Mullick, and T. C. Kandpal, “Photovoltaic projects for decentralized power supply in India: A financial evaluation,” *Energy Policy*, vol. 34, no. 18, pp. 3727–3738, 2006.

[24] D. Ghosh, A. Sagar, and V. V. N. Kishore, “Scaling Up Biomass Gasifier Use Applications, Barriers and Interventions,” 2004.

[25] V. Pozzobon, “Biomass gasification under high solar heat flux,” 2015.

[26] M. Bashir, “A novel approach for integrating concentrated solar energy with biomass thermochemical conversion processes,” (Doctoral dissertation, Aston University)., 2017.

[27] University of Minessota, “Combine solar thermal energy with biomass gasification for natural gas substitute -- ScienceDaily,” 2015. [Online]. Available: https://www.sciencedaily.com/releases/2015/02/150209130736.htm. [Accessed: 13-Feb-2020].

[28] A. H. Demirbas and I. Demirbas, “Importance of rural bioenergy for developing countries,” *Energy Convers. Manag.*, vol. 48, no. 8, pp. 2386–2398, 2007.

[29] S. . Touati, F., Massoud, A., Hamad, J.A. and Saeed, “Effects of environmental and climatic conditions on PV efficiency in Qatar,” *Int. Conf. Renew. Energies Power Qual. (ICREPQ’13). pp. 262-267.*, pp. 262–267, 2013.

[30] F. C. Luz *et al.*, “Techno-economic analysis of municipal solid waste gasification for electricity generation in Brazil,” *Energy Convers. Manag.*, vol. 103, pp. 321–337, Oct. 2015.

[31] C. Higman and M. van der Burgt, *Gasification*. Elsevier Inc., 2003.

[32] Ministry of Development Planning and Statistics, “Sustainable Development Goals 2030,” *Qatar Volunt. Natl. Rev. 2017. High Lev. Polit. Forum*, 2017.

[33] N. Ayoub, F. Musharavati, and H. Gabbar, “A Future Prospect for Domestic Waste Management in Qatar,” in *n International Conference on Earth, Environment and Life Sciences. Dubai, UAE* , 2014, pp. 96–100.

[34] S. Zafar, “Waste Management Outlook for Qatar. Echoing Sustainability in MENA.,” 2021. [Online]. Available: https://www.ecomena.org/waste-qatar/. [Accessed: 19-Feb-2020].

[35] S. Suresh, “Waste Management Outlook for Qatar | EcoMENA,” 2018. [Online]. Available: https://www.ecomena.org/waste-qatar/. [Accessed: 13-Feb-2020].

[36] J. M. Reid, K. E.-G. Hassan, and M. bin S. Al-Kuwari, “Improving the management of construction waste in Qatar,” *Proc. Inst. Civ. Eng. - Waste Resour. Manag.*, vol. 169, no. 1, pp. 21–29, Feb. 2016.

[37] The Peninsula Qatar, “Ministry launches project to recycle construction waste.,” Doha, 2018.

[38] D. B. Chandrappa, R. and Das, “Solid waste management: Principles and practice. Springer Science and Business Media. Loughborough: United Kingdom.,” 2012. [Online]. Available: https://www.google.com/search?rlz=1C1GCEB_enGB874GB874&sxsrf=ACYBGNTz-12abM42yISp0p1QXMLJCe-jNQ%3A1581008267452&ei=i0U8XuabG86agQblhqWACA&q=Chandrappa%2C+R.+and+Das%2C+D.B.%2C+%282012%29.+Solid+waste+management%3A+Principles+and+practice.+Springer+Science. [Accessed: 06-Feb-2020].

[39] P. K. Barnala, “Optimization of operating parameters of a material recovery facility using lean six sigma techniques,” Doctoral dissertation, University of Toledo, 2011.

[40] M. Al-Maaded, N. K. Madi, R. Kahraman, A. Hodzic, and N. G. Ozerkan, “An Overview of Solid Waste Management and Plastic Recycling in Qatar,” *J. Polym. Environ.*, vol. 20, no. 1, pp. 186–194, 2012.

[41] M. McHenry, “Research Institute for Sustainable Energy,” 2015. [Online]. Available: http://www.see.murdoch.edu.au/resources/info/Tech/waste/. [Accessed: 12-Feb-2020].

[42] A. Násner *et al.*, “Refuse Derived Fuel (RDF) production and gasification in a pilot plant integrated with an Otto cycle ICE through Aspen plus™ modelling: Thermodynamic and economic viability.,” *Waste Manag.*, vol. 69, pp. 187–201, 2017.

[43] V. S. Rotter, A. Lehmann, T. Marzi, E. Möhle, D. Schingnitz, and G. Hoffmann, “New techniques for the characterization of refuse-derived fuels and solid recovered fuels,” 2011.

[44] S. Suresh and S. Sundaramoorthy, *Green Chemical Engineering: An introduction to catalysis, kinetics, and chemical processes*. 2014.

[45] J. García-Serna, L. Pérez-Barrigón, and M. J. Cocero, “New trends for design towards sustainability in chemical engineering: Green engineering,” *Chem. Eng. J.*, vol. 133, pp. 7–30, 2007.

[46] J. H. Clark and F. E. I. Deswarte, “The Biorefinery Concept-An Integrated Approach,” 2008.

[47] R. C. Rivas-Cantu, K. D. Jones, and P. L. Mills, “A citrus waste-based biorefinery as a source of renewable energy: Technical advances and analysis of engineering challenges,” *Waste Manag. Res.*, vol. 31, no. 4, pp. 413–420, Apr. 2013.

[48] S. Goyal, “Biorefinery Prospects in India,” *BioEnergy Consult*, 2020. [Online]. Available: https://www.bioenergyconsult.com/biorefinery-india/. [Accessed: 24-Apr-2021].

[49] S. Sharma, R. Meena, A. Sharma, P. Kumar Goyal, and A. Prof, “Biomass Conversion Technologies for Renewable Energy and Fuels: A Review Note,” *IOSR J. Mech. Civ. Eng. (IOSR-JMCE*, vol. 11, no. 2, pp. 28–35, 2014.

[50] P. Hockenos, “The role of biofuel and hydrogen in Germany’s transport Energiewende | Clean Energy Wire,” 2016. [Online]. Available: https://www.cleanenergywire.org/factsheets/role-biofuel-and-hydrogen-germanys-transport-energiewende. [Accessed: 07-Feb-2020].

[51] R. Ulber and D. Sell, *White biotechnology*. 2007.

[52] S. Y. Lee *et al.*, “Waste to bioenergy: a review on the recent conversion technologies,” *BMC Energy*, vol. 1, no. 1, Dec. 2019.

[53] Fekete B.M, “Biomass, in Climate Vulnerability,” *Academic Press: Oxford*, 2013. [Online]. Available: https://www.google.com/search?q=Fekete+Biomass%2C+in+Climate+Vulnerability&tbm=bks&ei=--7MYvujKKW39u8PnbOXuAk&ved=0ahUKEwi7jd7MuPL4AhWlm_0HHZ3ZBZcQ4dUDCAk&uact=5&oq=Fekete+Biomass%2C+in+Climate+Vulnerability&gs_lcp=Cg1nd3Mtd2I6LWJvb2tzEANQwhBYwhBg9xRoAHAAeACAAfQBiAHFA5IBAzItMpgBAKABAqABAcABAQ&sclient=gws-wiz-books. [Accessed: 12-Jul-2022].

[54] R. Lee and J. Lavoie, “From first-to third-generation biofuels: Challenges of producing a commodity from a biomass of increasing complexity,” *Anim. Front.*, vol. 3, no. 2, pp. 6–11, 2013.

[55] P. . Alkemade, “WELKE BIJDRAGEN KUNNEN INNOVATION INTERMEDIARIES,” Erasmus University, 2018.

[56] N+P Group, “Subcoal® - N+P Recycling,” 2021. [Online]. Available: https://www.np-recycling.nl/en/alternative-fuels/subcoal.html. [Accessed: 24-Apr-2021].

[57] J. Zhang and X. Zhang, “The thermochemical conversion of biomass into biofuels,” *Biomass, Biopolym. Mater. Bioenergy*, pp. 327–368, 2019.

[58] J. R. Ansa, “GASIFICATION OF BIOMASS AND SOLID RECOVERED FUELS (SRFS) FOR THE SYNTHESIS OF LIQUID FUELS,” Rovira i Virgili, 2017.

[59] A. Moilanen and H. J. Mühlen, “Characterization of gasification reactivity peat char in pressurized conditions,” *Fuel*, vol. 75, no. 11, pp. 1279–1285, 1996.

[60] A. Beenackers and A. Bridgwater, “Gasification and pyrolysis of biomass in Europe,” *Elsevier Appl. Sci. Publ. …*, 1989.

[61] D. A. Agar, M. Kwapinska, and J. J. Leahy, “Pyrolysis of wastewater sludge and composted organic fines from municipal solid waste: laboratory reactor characterisation and product distribution,” *Environ. Sci. Pollut. Res.*, vol. 25, no. 36, pp. 35874–35882, Dec. 2018.

[62] S. A. Halim, “Biomass Pyrolysis Using Microwave Technology,” (Doctoral Dissertation, University of Sheffield), 2016.

[63] S. Besler, O. M. Kockar, A. E. Putun, E. Ekinci, and E. Putun, “Pyrolysis of Euphorbia Rigida from Central Anatolia,” in *Advances in Thermochemical Biomass Conversion*, Springer Netherlands, 1993, pp. 1103–1109.

[64] Y. Chhiti and M. Kemiha, “Thermal Conversion of Biomass, Pyrolysis and Gasification. International Journal of Engineering and Science (IJES), 2(3), pp.75-85.,” 2013.

[65] L. Li, J. Rowbotham, C. Greenwell, and P. Dyer, “An introduction to pyrolysis and catalytic pyrolysis: versatile techniques for biomass conversion.,” 2013.

[66] H. I. Graham, R.G., Bergougnou, M.A., Mok, L.K.S. and De Lasa, “Fast pyrolysis (ultrapyrolysis) of biomass using solid heat carriers. In Fundamentals of Thermochemical Biomass Conversion.,” *Springer*, pp. 397–410, 1985.

[67] T. Koido, K. and Iwasaki, “Biomass Gasification: A Review of Its Technology, Gas Cleaning Applications, and Total System Life Cycle Analysis,” *books.google.com*, 2017.

[68] A. Bridgwater, A. Beenackers, K. Sipila, and Y. Zhenhong, *An assessment of the possibilities for transfer of European biomass gasification technology to China*, vol. 1. 1999.

[69] M. L. Valderrama Rios, A. M. González, E. E. S. Lora, and O. A. Almazán del Olmo, “Reduction of tar generated during biomass gasification: A review,” *Biomass and Bioenergy*, vol. 108, no. December 2017, pp. 345–370, 2018.

[70] A. Latif, “A Study of the Design of Fluidized Bed Reactors for Biomass Gasification,” no. November, p. 215, 1999.

[71] J. Donald, “Catalytic decomposition of ammonia and tar for hot gas cleanup in biomass gasification using activated carbon supported catalysts and natural limonite ores,” 2009.

[72] H. Yang and H. Chen, “Biomass gasification for synthetic liquid fuel production,” *Gasif. Synth. Fuel Prod. (pp. 241-275). Woodhead Publ.*, 2015.

[73] A. Giaconia, “Thermochemical production of hydrogen,” *n Adv. Hydrog. Prod. Storage Distrib. Woodhead Publ.*, pp. 263–280, 2014.

[74] L. Rosendahl, *Biomass combustion science, technology and engineering*. 2013.

[75] A. Molino, S. Chianese, and D. Musmarra, “Biomass gasification technology: The state of the art overview,” *J. Energy Chem.*, vol. 25, no. 1, pp. 10–25, 2016.

[76] L. Devi, K. J. Ptasinski, and F. J. J. G. Janssen, “A review of the primary measures for tar elimination in biomass gasification processes,” *Biomass and Bioenergy*, vol. 24, no. 2, pp. 125–140, 2003.

[77] L. Zhang, C. Xu, and P. Champagne, “Overview of recent advances in thermo-chemical conversion of biomass,” *Energy Convers. Manag.*, vol. 51, no. 5, pp. 969–982, 2010.

[78] M. P. Aznar, J. Corella, J. Delgado, and J. Lahoz, “Improved Steam Gasification of Lignocellulosic Residues in a Fluidized Bed with Commercial Steam Reforming Catalysts,” *Ind. Eng. Chem. Res.*, vol. 32, no. 1, pp. 1–10, 1993.

[79] S. RapagnÂ, N. Jand, A. Kiennemann, and P. Foscolo, “Steam-Gasification of Biomass in a Fluidized-Bed of Olivine Particles Combustion of biomass and solid refused fuels View project dry reforming of methane View project Steam-gasiÿcation of biomass in a auidised-bed of olivine particles,” *Biomass and Bioenergy*, vol. 19, no. 3, pp. 187–197, 2000.

[80] P. Simell, E. Kurkela, P. Ståhlberg, and J. Hepola, “Catalytic hot gas cleaning of gasification gas,” *Catal. Today*, vol. 27, no. 2, pp. 55–62, 1996.

[81] A. Soomro, S. Chen, S. Ma, and W. Xiang, “Catalytic activities of nickel, dolomite, and olivine for tar removal and H 2-enriched gas production in biomass gasification process,” *Energy Environ.*, vol. 29, no. 6, pp. 839–867, Sep. 2018.

[82] G. Chen, Q. Yu, K. Sjöström, and E. Björnbom, “Pyrolysis/Gasification of Biomass in Presence of Dolomite in a Pressurized Fluidized Bed,” in *Advances in Thermochemical Biomass Conversion*, Springer Netherlands, 1993, pp. 1197–1204.

[83] P. Basu, “Biomass Gasification, Pyrolysis, and Torrefaction Practical Design and Theory Second Edition,” *Acad. Press*, 2018.

[84] W. . Seo, Y.C., Alam, M.T. and Yang, *Gasification of municipal solid waste*. 2018.

[85] M. Mayerhofer, P. Mitsakis, X. Meng, and W. de Jong, “Influence of pressure, temperature and steam on tar and gas in allothermal fluidized bed gasification,” *Fuel*, vol. 99, pp. 204–209, 2012.

[86] D. Murzin, *Chemical reaction technology*. 2015.

[87] R. Chhabra and V. Shankar, *Coulson and Richardson’s Chemical Engineering: Volume 1B: Heat and Mass Transfer: Fundamentals and Applications*. Butterworth-Heinemann., 2017.

[88] Energy Technology Support Unit (ETSU), *Studies on the thermal processing of biomass and waste materials*. Harwell, United Kingdom, 1997.

[89] Serio M.A. Soloman P.R. Bassilakis R., "The effects of minerals and pyrolysis conditions on char gasification rates," vol. 34, no. 1, pp. 9–21, 1989.

[90] E. Kurkela, *Formation and removal of biomass-derived contaminants in fluidized-bed gasification processes*. Technical Research Centre of Finland, 1996.

[91] J. Najser, P. Buryan, S. Skoblia, J. Frantik, J. Kielar, and V. Peer, "Problems related to gasification of biomass—properties of solid pollutants in raw gas," *Energies*, vol. 12, no. 6, pp. 1–14, 2019.

[92] P. Yrjas, K. Iisa, and M. Hupa, "Limestone and dolomite as sulfur absorbents under pressurized gasification conditions," *Fuel*, vol. 75, no. 1, pp. 89–95, 1996.

[93] D. C. Elliott *et al.*, "Chemical Processing in High-Pressure Aqueous Environments. 7. Process Development for Catalytic Gasification of Wet Biomass Feedstocks," *Ind. Eng. Chem. Res.*, vol. 43, no. 9, pp. 1999–2004, Apr. 2004.

[94] I. S. Pieta, W. S. Epling, A. Kazmierczuk, P. Lisowski, R. Nowakowski, and E. M. Serwicka, "Waste into fuel—catalyst and process development for MSW valorisation," *Catalysts*, vol. 8, no. 3, pp. 1–16, 2018.

[95] Definition of catalyst, "Chemistry Dictionary," 2017. [Online]. Available: https://www.chemicool.com/definition/catalyst.html. [Accessed: 04-Nov-2019].

[96] Y. Chen, Z., Wang, M., Jiang, E., Wang, D., Zhang, K., Ren, Y. and Jiang, "Pyrolysis of torrefied biomass," *Elsevier*, vol. 36, no. 12, pp. 1287–1298, 2018.

[97] T. Astrup and B. Bilitewski, "Pyrolysis and Gasification," in *Solid Waste Technology & Management*, Chichester, UK: John Wiley & Sons, Ltd, 2010, pp. 502–512.

[98] Z. Jun, W. Shuzhong, W. Zhiqiang, M. Haiyu, and C. Lin, "Hydrogen-rich syngas produced from the co-pyrolysis of municipal solid waste and wheat straw," *Int. J. Hydrogen Energy*, vol. 42, no. 31, pp. 19701–19708, 2017.

[99] Y. Okumura, "GASIFICATION MECHANISM OF WOODY BIOMASS-DERIVED CHAR WITH SUPPORTED Fe CATALYSTS," in *International Heat Transfer Conference*, 2018, vol. 16, pp. 7782–7789.

[100] E. C. Efika, "HYDROGEN RICH SYNGAS FROM THE PYROLYSIS AND GASIFICATION OF SOLID WASTE AND BIOMASS," 2013.

[101] G. Ertl, H. Knözinger, and J. Weitkamp, "Handbook of heterogeneous catalysis," 1997.

[102] J. Corella, J. M. Toledo, and R. Padilla, "Olivine or dolomite as in-bed additive in biomass gasification with air in a fluidized bed: Which is better?," *Energy and Fuels*, vol. 18, no. 3, pp. 713–720, May 2004.

[103] A. Erkiaga, G. Lopez, M. Amutio, and J. Bilbao, "Steam gasification of biomass in a conical spouted bed reactor with olivine and γ-alumina as primary catalysts," *Fuel Process. Technol.*, vol. 116, pp. 292–299, 2013.

[104] D. Świerczyński, C. Courson, and L. Bedel, "Oxidation Reduction Behavior of Iron-Bearing Olivines (FexMg1-x)2SiO4 Used as Catalysts for Biomass Gasification," *Chem. Mater.*, vol. 18, no. 4, pp. 897–905, 2006.

[105] M. Virginie, C. Courson, D. Niznansky, and N. Chaoui, "Characterization and reactivity in toluene reforming of a Fe/olivine catalyst designed for gas cleanup in biomass gasification," *Appl. Catal. B Environ.*, 2010.

[106] J. Kuhn, Z. Zhao, L. Felix, and R. Slimane, “Olivine catalysts for methane-and tar-steam reforming,” *Appl. Catal. B Environ.*, vol. 81, no. 1–2, pp. 14–26, 2008.

[107] T. Nordgreen, T. Liliedahl, and K. Sjöström, “Metallic iron as a tar breakdown catalyst related to atmospheric, fluidised bed gasification of biomass,” *Fuel*, vol. 85, no. 5–6, pp. 689–694, 2006.

[108] X. Nitsch, J. M. Commandré, P. Clavel, E. Martin, J. Valette, and G. Volle, “Conversion of phenol-based tars over olivine and sand in a biomass gasification atmosphere,” *Energy and Fuels*, vol. 27, no. 9, pp. 5459–5465, Sep. 2013.

[109] J. Pecho and M. Sturzenegger, “ELUCIDATION OF THE FUNCTION OF OLIVIN IN BIOMASS GASIFICATION,” 1999.

[110] M. Latifi, P. Montréal, F. Berruti, and C. Briens, “Jiggle bed reactor for testing catalytic activity of olivine in bio-oil gasification Microwave-Assisted dry reforming of methane View project Jiggle bed reactor for testing catalytic activity of olivine in bio-oil gasification,” *Powder Technol.*, vol. 316, pp. 400–409, 2016.

[111] G. Aranda, A. Van Der Drift, B. J. Vreugdenhil, H. J. M. Visser, C. F. Vilela, and C. M. Van Der Meijden, “Comparing direct and indirect fluidized bed gasification: Effect of redox cycle on olivine activity,” in *Environmental Progress and Sustainable Energy*, 2014, vol. 33, no. 3, pp. 711–720.

[112] M. Virginie *et al.*, “Effect of Fe-olivine on the tar content during biomass gasification in a dual fluidized bed,” *Appl. Catal. B Environ.*, vol. 212, pp. 214–222, 2012.

[113] R. Lancee, A. Dugulan, P. Thüne, and H. Veringa, “Chemical looping capabilities of olivine, used as a catalyst in indirect biomass gasification,” *Appl. Catal. B Environ.*, vol. 145, pp. 216–222, 2014.

[114] J. Pecho, T. J. Schildhauer, M. Sturzenegger, S. Biollaz, and A. Wokaun, “Reactive bed materials for improved biomass gasification in a circulating fluidised bed reactor,” *Chem. Eng. Sci.*, vol. 63, no. 9, pp. 2465–2476, 2008.

[115] D. Dayton, “Review of the literature on catalytic biomass tar destruction: Milestone completion report,” 2002.

[116] Y. Richardson, J. Blin, and A. Julbe, “A short overview on purification and conditioning of syngas produced by biomass gasification: catalytic strategies, process intensification and new concepts,” *Prog. Energy Combust. Sci.*, vol. 38, no. 6, pp. 765–781, 2012.

[117] D. Sutton, B. Kelleher, and J. Ross, “Review of literature on catalysts for biomass gasification,” *Fuel Process. Technol.*, vol. 73, no. 3, pp. 155–173, 2001.

[118] Q. Yu, C. Brage, T. Nordgreen, and K. Sjöström, “Effects of Chinese dolomites on tar cracking in gasification of birch,” *Fuel*, vol. 88, no. 10, pp. 1922–1926, 2009.

[119] C. Quitete and M. Souza, “Application of Brazilian dolomites and mixed oxides as catalysts in tar removal system,” *Appl. Catal. A Gen.*, vol. 536, pp. 1–8, 2017.

[120] G. Zhang, H. Liu, J. Wang, and B. Wu, “Catalytic gasification characteristics of rice husk with calcined dolomite,” *Energy*, vol. 165, pp. 1173–1177, 2018.

[121] M. Cho, T. Mun, and J. Kim, “Air gasification of mixed plastic wastes using calcined dolomite and activated carbon in a two-stage gasifier to reduce tar. Energy,” *Elsevier*, no. 53, pp. 299–305, 2013.

[122] P. Woolcock and R. Brown, “A review of cleaning technologies for biomass-derived syngas,” *Biomass and bioenergy*, vol. 52, pp. 54–84, 2013.

[123] W. Torres, S. Pansare, and J. Goodwin, “Hot gas removal of tars, ammonia, and hydrogen sulfide from biomass gasification gas,” *Catal. Rev.*, vol. 49, no. 4, pp. 407–456, 2007.

[124] I. Zamboni, C. Courson, and A. Kiennemann, “Synthesis of Fe/CaO active sorbent for CO2 absorption and tars removal in biomass gasification,” *Catal. today*, vol. 176, no. 1, pp. 197–201, 2011.

[125] C. Zhou, C. Rosén, and K. Engvall, “Fragmentation of dolomite bed material at elevated temperature in the presence of H2O & CO2: Implications for fluidized bed gasification,” *Fuel*, vol. 260, 2020.

[126] A. Duffy, G. Walker, and S. Allen, “Investigations on the adsorption of acidic gases using activated dolomite,” *Chem. Eng. J.*, vol. 117, no. 3, pp. 239–224, 2006.

[127] M. Islam, “A review of dolomite catalyst for biomass gasification tar removal,” *Fuel*, vol. 267, 2020.

[128] M. Hervy, R. Olcese, M. Bettahar, and M. Mallet, “Evolution of dolomite composition and reactivity during biomass gasification,” *Appl. Catal. A Gen.*, 2019.

[129] V. A. Rigo, C. O. Metin, Q. P. Nguyen, and C. R. Miranda, “Hydrocarbon adsorption on carbonate mineral surfaces: A first-principles study with van der Waals interactions,” *J. Phys. Chem. C*, vol. 116, no. 46, pp. 24538–24548, 2012.

[130] J. C. Lavalley, “Infrared spectrometric studies of the surface basicity of metal oxides and zeolites using adsorbed probe molecules,” 1996.

[131] A. Herman, S. Yusup, M. Shahbaz, and D. DO Patrick, “Bottom ash characterization and its catalytic potential in biomass gasification,” *Procedia Eng.*, vol. 148, pp. 432–436, 2016.

[132] V. Belgiorno, G. De Feo, C. Della Rocca, and R. M. . Napoli, “Energy from gasification of solid wastes,” *Waste Manag.*, 2003.

[133] D. . Valkenburt, C., Walton, C.W., Thompson, B.L., Gerber, M.A., Jones, S.B. and Stevens, “Municipal solid waste (MSW) to liquid fuels synthesis, volume 1: Availability of feedstock and technology,” 2008.

[134] S. Heidenreich, M. Müller, and P. Foscolo, *Advanced biomass gasification: new concepts for efficiency increase and product flexibility*. 2016.

[135] P. Wang, J. L. Zhang, and B. Gao, “Gasification Reaction Characteristics of Ferro-Coke at Elevated Temperatures,” *High Temp. Mater. Process.*, vol. 36, no. 1, pp. 101–106, 2017.

[136] A. S. Al-Rahbi and P. T. Williams, “Hydrogen-rich syngas production and tar removal from biomass gasification using sacrificial tyre pyrolysis char,” *Appl. Energy*, vol. 190, pp. 501–509, 2017.

[137] C. Agu, C. Pfeifer, M. Eikeland, and L. Tokheim, “Measurement and characterization of biomass mean residence time in an air-blown bubbling fluidized bed gasification reactor,” *Fuel*, 2019.

[138] A. Al-Farraji, “Chemical Engineering and Reactor Design of a Fluidised Bed Gasifier .,” (Doctoral dissertation, Cardiff University)., 2017.

[139] Q. M. . Waheed, “Ultra-high temperature steam gasification of biomass,” University of Leeds, 2013.

[140] F. L. Hart and H. J. Fisher, “Introduction—General methods for proximate and mineral analysis,” in *In Modern food analysis*, Springer Berlin Heidelberg, 1971, pp. 1–27.

[141] British Standards Institution (BSI), “Determination of moisture content — Oven dry method Part 3 : Moisture in general analysis sample. (BS EN 18134-3:2015).,” 2015.

[142] B. P. Ismail, “Ash Content Determination,” 2017, pp. 117–119.

[143] British Standards Institution (BSI), “Solid biofuels. Determination of Volatile matter. (BS EN 15148:2009).,” 2009.

[144] B. . McGhee, “Fundamental Studies of the Behaviour of Biomass and Waste Materials in Gasification Systems by,” 1999.

[145] British Standards Institution (BSI), “Determination of ash content. (BS EN 18122:2015).,” no. January, 2017.

[146] A. López-Córdoba and S. Goyanes, “Food Powder Properties,” 2017.

[147] British Standards Institution (BSI), “Solid Biofuels,” *Determ. Bulk Density. (BS EN 1337-91990)*, 1990.

[148] British Standards Institution (BSI), *Solid biofuels. Determination of bulk density. (BS EN 15103:2009).* 2010.

[149] V. Thangarasu and R. Anand, “Physicochemical fuel properties and tribological behavior of aegle marmelos correa biodiesel,” *Adv. eco-fuels a Sustain. Environ.* , pp. 309–336, 2019.

[150] A. Hlaba, A. Rabiu, and A. Osibote, “Refuse Derived Fuel Pellets as a Renewable Energy Source,” *Int. Proc. Chem. Biol. Environ. Eng.*, 2017.

[151] British Standards DD CEN/TS 14918, “Solid Biofuels. Method for the Determination of Calorific Value,” 2005.

[152] M. Balas, M. Lisy, and J. Moskalik, “Temperature and pressure effect on gasification process,” *Adv. Fluid Mech. Heat Mass Transf.*, pp. 198–202, 2012.

[153] LECO, “SC-144DR Sulfur/Carbon Determinator Specification Sheet [,” 2008. [Online]. Available: http://www.usbioecuador.com/descargas/SC144DR-ht.pdf. [Accessed: 02-Jul-2020].

[154] F. C. Obi, “USE OF X-RAY FLUORESCENCE SPECTROMETRY TO DETERMINE TRACE ELEMENTS IN GRAPHITE,” 1990.

[155] J. Epp, “X-ray diffraction (XRD) techniques for materials characterization,” *Mater. Charact. using Nondestruct. Eval. methods*, pp. 81–124, 2016.

[156] C. Ward, “Analysis, origin and significance of mineral matter in coal: An updated review,” *Int. J. Coal Geol.*, vol. 165, pp. 1–27, 2016.

[157] C. Rao and Gluskoter HJ, “Occurrence and distribution of minerals in Illinois coals: Illinois State Geological Survey Circular 476,” 1973.

[158] R. Gupta, “Advanced coal characterization: A review,” in *Energy and Fuels*, 2007, vol. 21, no. 2, pp. 451–460.

[159] M. A. S. Rivera, “Operating the Siemens XRD Diffraktometer D5000,” 2006.

[160] M. Dutrow, L., and Clark, “X-ray Powder Diffraction (XRD),” 2019. [Online]. Available: https://serc.carleton.edu/research_education/geochemsheets/techniques/XRD.html. [Accessed: 10-Jan-2020].

[161] M. Rahaman, M. Khandaker, M. Khan, ZR Kufian, I. Noor, and A. Arof, “Effect of gamma irradiation on poly (vinyledene difluoride)–lithium bis (oxalato) borate electrolyte,” *pubs.rsc.org*, vol. 16, no. 24, pp. 11527–11537, 2014.

[162] I. Malvern Instruments, “Mastersizer 3000,” 2016.

[163] Pharmahub, “Laser Diffraction,” 2015. [Online]. Available:

https://pharmahub.org/app/site/collections/excipients/testmethods/Laser Diffraction.pdf. [Accessed: 09-Mar-2020].

[164] S. Arridge, P. Van Der Zee, D. Delpy, and M. Cope, "Particle sizing in the Mie scattering region: singular-value analysis," *Inverse Probl.*, vol. 5, no. 5, 1989.

[165] Malvern Instruments Ltd, *Mastersizer 3000 User Manual*. United Kingdom, 2016.

[166] ISO, "ISO 11358:1997 - Plastics - Thermogravimetry (TG) of Polymers - General Principles," 2014.

[167] M. A. Arshad, A. Maaroufi, R. Benavente, and G. Pinto, "Kinetics of the Thermal Decomposition Mechanisms of Conducting and Non-conducting epoxy/Al Composites," *J. Mater. Environ. Sci*, vol. 5, no. 5, pp. 1342–1354, 2014.

[168] U. Nobbmann, "D10, D50, D90, And Span," *Malvern panalytical*, 2019. [Online]. Available: https://www.materials-talks.com/blog/2016/08/25/d90-d50-d10-and-span-for-dls/. [Accessed: 19-Feb-2020].

[169] K. Slopiecka, P. Bartocci, and F. Fantozzi, "Thermogravimetric analysis and kinetic study of poplar wood pyrolysis," *Appl. Energy*, vol. 97, 2012.

[170] L. Febrero, E. Granada, D. Patiño, P. Eguía, and A. Regueiro, "A comparative study of fouling and bottom ash from woody biomass combustion in a fixed-bed small-scale boiler and evaluation of the analytical techniques used," *Sustainability*, vol. 7, no. 5, pp. 5819–5837, 2015.

[171] M. Ram and M. Mondal, "Biomass gasification: a step toward cleaner fuel and chemicals," *Elsevier*, pp. 253–276, 2022.

[172] C. M. Earnest, "Compositional Analysis by Thermogravimetry," 1988.

[173] A. PRIME, R. B., BAIR, H. E., VYAZOVKIN, S., GALLAGHER, P. K. and RIGA, "THERMAL ANALYSIS OF POLYMERS - Fundamentals and Applications," 2009.

[174] W. Groenewoud, *Characterisation of polymers by thermal analysis*. 2001.

[175] P. Gallagher, "Thermogravimetry and thermomagnetometry.," *Handb. Therm. Anal. calorimetry.Elsevier Sci. BV*, vol. 1, pp. 225–278, 1998.

[176] Nakamura and S, "Fundamentals of Chemical Reaction Kinetics," *Sol. to Chem. Energy Convers. Theory Appl. Cham Springer Int. Publ.*, 2016.

[177] O. Levenspiel, "Chemical reaction engineering," *Industrial and Engineering Chemistry Research*, vol. 38, no. 11. American Chemical Society, pp. 4140–4143, 1999.

[178] S. Christov, *Collision theory and statistical theory of chemical reactions*. 2012.

[179] A. Kulczycki and C. Kajdas, "A New Attempt to Better Understand Arrehnius Equation and its Activation Energy," *Tribol. Eng.*, p. 47, 2013.

[180] J. Cai *et al.*, "Processing thermogravimetric analysis data for isoconversional kinetic analysis of lignocellulosic biomass pyrolysis: Case study of corn stalk.stalk. Renewable and Sustainable Energy Reviews," 2018.

[181] T. Ozawa, "A New Method of Analyzing Thermogravimetric Data," *Bull. Chem. Soc. Jpn.*, vol. 38, no. 11, pp. 1881–1886, Nov. 1965.

[182] R. L. Blaine and H. E. Kissinger, "Thermochimica Acta Homer Kissinger and the Kissinger equation," *Thermochim. Acta*, vol. 540, pp. 1–6, 2012.

[183] W. Tang, Y. Liu, H. Zhang, and C. Wang, "New approximate formula for Arrhenius

temperature integral," *Thermochim. Acta*, vol. 408, no. 1–2, pp. 39–43, 2003.

[184] M. J. Starink, "THE DETERMINATION OF ACTIVATION ENERGY FROM LINEAR HEATING RATE EXPERIMENTS: A COMPARISON OF THE ACCURACY OF ISOCONVERSION METHODS 2003.

[185] A. . Coats and J. . Redfern, "Kinetic parameters from thermogravimetric data," *nature.com*, vol. 201, no. 4914, pp. 68–69, 1964.

[186] F. Benhacine, F. Yahiaoui, and A. . Hadj-Hamou, "Thermal stability and kinetic study of isotactic polypropylene/Algerian bentonite nanocomposites prepared via melt blending," *J. Polym.*, 2014.

[187] V. Mamleev, S. Bourbigot, M. Le Bras, and J. Lefebvre, "Three model-free methods for calculation of activation energy in TG," in *Journal of Thermal Analysis and Calorimetry*, 2004, vol. 78, no. 3, pp. 1009–1027.

[188] J. Flynn and L. Wall, "General treatment of the thermogravimetry of polymers," *J. Res. Natl. Bur. Stand. Sect. A, Phys. Chem.*, 1966.

[189] H. . Kissinger, "Variation of Pedk Temperature With Hedting Rote in Differentidl Thermal Andlysis," *ournal Res. Natl. Bur. Stand.*, vol. 57, p. 217, 1956.

[190] P. Budrugeac and E. Segal, "On the Li and Tang's isoconversional method for kinetic analysis of solid-state reactions from thermoanalytical data," *J. Mater. Sci.*, vol. 36, no. 11, pp. 2707–2710, Jun. 2001.

[191] M. Starink, "Analysis of hydrogen desorption from linear heating experiments: Accuracy of activation energy determinations," *Int. J. Hydrogen Energy*, vol. 43, pp. 6632–6641, 2018.

[192] S. Vyazovkin, A. K. Burnham, J. M. Criado, L. A. Pérez-Maqueda, C. Popescu, and N. Sbirrazzuoli, "ICTAC Kinetics Committee recommendations for performing kinetic computations on thermal analysis data," *Thermochim. Acta*, vol. 520, pp. 1–19, 2011.

[193] C. Gai, Y. Dong, Z. Lv, Z. Zhang, J. Liang, and Y. Liu, "Pyrolysis behavior and kinetic study of phenol as tar model compound in micro fluidized bed reactor," *Int. J. Hydrogen Energy*, vol. 40, no. 25, pp. 7956–7964, 2015.

[194] A. Dhaundiyal, A. . Mohammad, T. Laszlo, and J. . Salcedo-Reyes, "Thermo-kinetics of Forest Waste Using Model-Free Methods," *Univ. Sci.*, vol. 24, no. 1, pp. 1–33, 2019.

[195] A. Khawam, "Application of solid-state kinetics to desolvation reactions," 2007.

[196] A. K. Burnham and L. N. Dinh, "A comparison of isoconversional and model-fitting approaches to kinetic parameter estimation and application predictions," in *Journal of Thermal Analysis and Calorimetry*, 2007, vol. 89, no. 2, pp. 479–490.

[197] P. Basu, "Biomass Gasification, Pyrolysis, and Torrefaction Practical Design and Theory Second Edition," 2018.

[198] J. Bermudez and B. Fidalgo, "Production of bio-syngas and bio-hydrogen via gasification," *Handb. Biofuels Prod.*, pp. 431–494, 2016.

[199] I. Narváez, A. Orío, M. P. Aznar, and J. Corella, "Biomass gasification with air in an atmospheric bubbling fluidized bed. Effect of six operational variables on the quality of the produced raw gas," *Ind. Eng. Chem. Res.*, vol. 35, no. 7, pp. 2110–2120, 1996.

[200] T. Renganathan, M. Yadav, and S. Pushpavanam, "CO2 utilization for gasification of carbonaceous feedstocks: a thermodynamic analysis," *Chem. Eng. Sci.*, vol. 83, pp. 159–170, 2012.

[201] A. Ghaly, A. Ergudenler, and I. Ugwu, "Mixing patterns and residence time determination in a fluidized bed system.," *Pap. Soc. Agric. Eng.*, 1989.

[202] B. Mvelase, “Optimization of the Integrated Gasification Combined Cycle using mathematical modelling,” 2016.

[203] J. A. Ruiz, M. C. Juárez, M. P. Morales, P. Muñoz, and M. A. Mendívil, “Biomass gasification for electricity generation: Review of current technology barriers,” *Renew. Sustain. Energy Rev.*, vol. 18, pp. 174–183, 2013.

[204] L. Wilson, G. R. John, C. F. Mhilu, W. Yang, and W. Blasiak, “Coffee husks gasification using high temperature air/steam agent,” *Fuel Process. Technol.*, vol. 91, no. 10, pp. 1330–1337, 2010.

[205] P. Basu, B. Acharya, and P. Kaushal, “Design methods for fluidised bed gasifiers: Comparison of three approaches,” *J. Energy Inst.*, vol. 83, no. 1, pp. 32–40, Mar. 2010.

[206] K. Daizo and O. Levenspiel, *Fluidization engineering*. 1991.

[207] D. Kunii and O. Levenspiel, *Fluidization engineering*. 2013.

[208] R. Ganesh, S. Jaisankar, and K. N. Sheeba, “Effect of equivalence ratio on gasification of granular biomaterials in self circulating fluidised bed gasifier,” *Int. J. Environ. Sustain. Dev.*, vol. 17, no. 2/3, p. 193, 2018.

[209] P. Lv, Z. Xiong, J. Chang, C. Wu, and Y. Chen, “An experimental study on biomass air–steam gasification in a fluidized bed,” *Bioresour. Technol.*, 2004.

[210] T. Hasegawa, “Developments of Gas Turbine Combustors for Air-Blown and Oxygen-Blown IGCC,” Rijeka, 2011.

[211] A. Al-Moftah, R. Marsh, and J. Steer, “Thermal decomposition kinetic study of non-recyclable paper and plastic waste by thermogravimetric analysis,” *ChemEngineering*, vol. 5, no. 3, p. 54, 2021.

[212] A. Al-Moftah, R. Marsh, and J. Steer, “Thermogravimetric Kinetic Analysis of Non-Recyclable Waste CO2 Gasification with Catalysts Using Coats–Redfern Method,” *ChemEngineering*, vol. 6, no. 2, p. 22, 2022.

[213] J. Sánchez, M. Curt, N. Robert, and J. Fernández, “Biomass resources,” *Role Bioenergy Bioeconomy*, pp. 25–111, 2019.

[214] B. Drosg, R. Braun, G. Bochmann, and T. Al Saedi, “Analysis and characterisation of biogas feedstocks,” *biogas Handb.*, pp. 52–84, 2013.

[215] T. Kittivech and S. Fukuda, “Effect of Bed Material on Bed Agglomeration for Palm Empty Fruit Bunch (EFB) Gasification in a Bubbling Fluidised Bed System,” *Energies*, vol. 12, 2019.

[216] S. Luo, B. Xiao, X. Guo, Z. Hu, S. Liu, and M. He, “Hydrogen-rich gas from catalytic steam gasification of biomass in a fixed bed reactor: Influence of particle size on gasification performance,” *Int. J. Hydrogen Energy*, vol. 34, no. 3, pp. 1260–1264, 2009.

[217] V. Sikarwar *et al.*, “An overview of advances in biomass gasification,” *Energy Environ. Sci.*, vol. 9, no. 10, pp. 2939–2977, 2016.

[218] C. Cherian and S. Siddiqua, “Pulp and Paper Mill Fly Ash: A Review,” *Sustainability*, vol. 11, no. 16, p. 4394, 2019.

[219] S. Caillat and E. Vakkilainen, “Large-scale biomass combustion plants: An overview,” *Biomass Combust. Sci. Technol. Eng.*, pp. 189–224, 2013.

[220] M. P. González-Vázquez, R. García, M. V Gil, C. Pevida, and F. Rubiera, “Unconventional biomass fuels for steam gasification: kinetic analysis and effect of ash composition on reactivity,” *Energy*, vol. 155, pp. 426–437, 2018.

[221] N. Jing, H. Zhu, and Q. Wang, “Effect of Chemical Compositions on Ash Fusibility Characterization of a Jincheng Anthracite during Combustion and Gasification,” *Chem. Eng. Commun.*, vol. 204, no. 8, pp. 858–863, Aug. 2017.

[222] R. Marsh, *Plastic film recycling from waste sources*. Cardiff University (United Kingdom), 2005.

[223] L. Febrero, E. Granada, D. Patiño, P. Eguía, and A. Regueiro, “A Comparative Study of Fouling and Bottom Ash from Woody Biomass Combustion in a Fixed-Bed Small-Scale Boiler and Evaluation of the Analytical Techniques Used,” *Sustainability*, vol. 7, no. 5, pp. 5819–5837, 2015.

[224] C. Ward and D. French, “Determination of glass content and estimation of glass composition in fly ash using quantitative X-ray diffractometry,” *Fuel*, vol. 85, no. 16, pp. 2268–2277, 2006.

[225] A. Shoppert, D. Valeev, I. Loginova, and L. Chaikin, “Complete Extraction of Amorphous Aluminosilicate from Coal Fly Ash by Alkali Leaching under Atmospheric Pressure,” *Metals (Basel).*, vol. 10, no. 12, p. 1684, 2020.

[226] S. Kim, C. Lee, and K. Kafle, “Characterization of crystalline cellulose in biomass: Basic principles, applications, and limitations of XRD, NMR, IR, Raman, and SFG,” *Korean J. Chem. Eng.*, vol. 30, no. 12, pp. 2127–2141, Dec. 2013.

[227] X. Wang *et al.*, “Effect of CaO and biomass ash on catalytic hydrogasification behavior of coal char,” *Fuel*, vol. 249, pp. 103–111, Aug. 2019.

[228] N. Hidayat, M. Yusuf, H. Widianto, A. Taufiq, and S. Sunaryono, “Natural Silica Sand/Alumina Ceramic Composites: Promising Candidates for Fuel-Cell Sealants,” *IOP Conf. Ser. Mater. Sci. Eng.*, 2017.

[229] S. Vassilev, D. Baxter, L. Andersen, and C. Vassileva, “An overview of the composition and application of biomass ash. Part 1. Phase–mineral and chemical composition and classification,” *Fuel*, vol. 105, pp. 40–76, 2013.

[230] S. Tian, Y. Zhuo, Z. Zhan, X. Shu, and Z. Kang, “Distribution of Clay Minerals in Light Coal Fractions and the Thermal Reaction Products of These Clay Minerals during Combustion in a Drop Tube Furnace,” *Energies*, vol. 9, no. 6, p. 428, 2016.

[231] Wang, G. Skjevrak, J. Hustad, and Ø. Skreiberg, “Investigation of biomass ash sintering characteristics and the effect of additives,” *Energy fuels. ACS Publ.*, vol. 28, no. 1, pp. 208–218, 2014.

[232] V. Balasundram *et al.*, “Thermogravimetric Studies on the Catalytic Pyrolysis of Rice Husk Consequence Assessment of Vapour Cloud Explosion Involving Large Commercial Airliner Crash upon Nuclear Reactor Containment View project Reaction Pathway and Kinetic Modelling for Enriched BTX Production from Catalytic Fast Pyrolysis of Municipal Plastic Wastes over Ni-CaO/HZSM-5 View project Thermogravimetric Studies on the Catalytic Pyrolysis of Rice Husk,” in *CHEMICAL ENGINEERING TRANSACTIONS*, 2017, vol. 56, pp. 427–432.

[233] H. W. Cui *et al.*, “Using the Friedman method to study the thermal degradation kinetics of photonically cured electrically conductive adhesives,” *J. Therm. Anal. Calorim.*, vol. 119, no. 1, pp. 425–433, 2015.

[234] M. R. Kessler and S. R. White, “Cure Kinetics of Ring-Opening Metathesis Polymerization of Dicyclopentadiene *,” 2002.

[235] J. Nelson, *Determination of kinetic parameters of six ablation polymers by thermogravimetric analysis*. 1967.

[236] A. Chee, R. Lim, B. Lai, F. Chin, Z. Abbas Jawad, and L. Hii, “ScienceDirect Kinetic analysis of rice husk pyrolysis using Kissinger-Akahira-Sunose (KAS) method,” *Procedia Eng.*, vol. 148, pp. 1247–1251, 2016.

[237] M. Y. Guida, S. Lanaya, Z. Rbihi, and A. Hannioui, “Thermal degradation behaviors of sawdust wood waste: pyrolysis kinetic and mechanism,” 2019.

[238] A. Li, N. Gao, and C. Quan, “Thermogravimetric analysis and kinetic study on large particles of printed circuit board wastes Furfural clean production View project MSW Gasification View project Thermogravimetric analysis and kinetic study on large particles of printed circuit board wastes,” 2009.

[239] K. Jayaraman, I. Gokalp, E. Bonifaci, and N. Merlo, “Kinetics of steam and CO2 gasification of high ash coal–char produced under various heating rates. Fuel,” *Elsevier*, vol. 154, pp. 370–379, 2015.

[240] S. D. Gunasee, M. Carrier, J. F. Gorgens, and R. Mohee, “Pyrolysis and combustion of municipal solid wastes: Evaluation of synergistic effects using 1 TGA-MS 2,” *J. Anal. Appl. Pyrolysis*, vol. 121, pp. 50–61, 2016.

[241] R. Zan, W. Wang, R. Xu, J. Schenk, H. Zheng, and H. Wang, “Gasification Characteristics and Kinetics of Unburned Pulverized Coal in Blast Furnaces,” *mdpi.com*, 2019.

[242] G.-B. Chen, S. Chatelier, H.-T. Lin, F.-H. Wu, and T.-H. Lin, “A Study of Sewage Sludge Co-Combustion with Australian Black Coal and Shiitake Substrate,” *Energies 11*, vol. 11, no. 12, 2018.

[243] L. Devi, i, K. Ptasinski, F. Janssen, S. Van Paasen, P. Bergman, and J. Kiel, “Catalytic decomposition of biomass tars: use of dolomite and untreated olivine,” *Renew. Energy*, vol. 30, pp. 565–587, 2005.

[244] J.-S. Kim, J.-W. Kim, J.-O. Kim, and T.-Y. Mun, “AIR GASIFICATION OF MIXED PLASTIC WASTES USING A TWO-STAGE GASIFIER FOR THE PRODUCTION OF A PRODUCER GAS WITH LOW TAR AND A HIGH CALORIC VALUE,” 2011.

[245] E. Quiroga, J. Moltó, J. A. Conesa, M. F. Valero, and M. Cobo, “Kinetics of the Catalytic Thermal Degradation of Sugarcane Residual Biomass Over Rh-Pt/CeO 2-SiO 2 for Syngas Production,” *Catalysts*, vol. 10, no. 5, pp. 508-undefined, 2020.

[246] M. Nasir Uddin, W. M. Daud, and H. F. Abbas, “Potential hydrogen and non-condensable gases production from biomass pyrolysis: Insights into the process variables,” *Renew. Sustain. Energy Rev.*, vol. 27, pp. 204–224, 2013.

[247] X. Gu, X. Zhou, M. Wu, X. Wang, Y. Chen, and K. Cheng, “KINETIC STUDY OF PINE SAWDUST PYROLYSIS VIA TG/DTG ANALYSIS,” 2017.

[248] T. Wanjun, L. Yuwen, Y. Xi, and W. Cunxin, “Kinetic Studies of the Calcination of Ammonium Metavanadate by Thermal Methods,” *Ind. Eng. Chem. Res.*, vol. 43, no. 9, pp. 2054–2059, Apr. 2004.

[249] J. Nisar *et al.*, “Comparative Study of Kinetics of the Thermal Decomposition of Polypropylene Using Different Methods,” *Adv. Polym. Technol.*, vol. 37, no. 4, pp. 1168–1175, Jun. 2018.

[250] Varma, Anil Kumar, and Prasenjit Mondal, “Physicochemical characterization and kinetic study of pine needle for pyrolysis process,” *J. Therm. Anal. Calorim.*, vol. 124, no. 1, pp. 487–497, Apr. 2016.

[251] A. Jess and A.-K. Andresen, “Influence of mass transfer on thermogravimetric analysis of combustion and gasification reactivity of coke,” 2009.

[252] R. Lancee, “Characterization and reactivity of olivine and model catalysts for biomass gasification,” 2014.

[253] S. Gerassimidou, C. A. Velis, P. T. Williams, and D. Komilis, “Characterisation and composition identification of waste-derived fuels obtained from municipal solid waste using thermogravimetry: A review,” *Waste Manag. Res.*, vol. 2020, no. 9, pp. 942–965, Sep. 2020.

[254] B. Tiţa, A. Fuliaş, G. Bandur, G. Rusu, and D. Tiţa, “Thermal stability of ibuprofen. Kinetic study under non-isothermal conditions,” *Rev Roum Chim*, vol. 55, 2010.

[255] M. J. Starink, “The determination of activation energy from linear heating rate experiments: a comparison of the accuracy of isoconversion methods,” 2003.

[256] M. Stanko and M. Stommel, “Kinetic Prediction of Fast Curing Polyurethane Resins by Model-Free Isoconversional Methods,” *Polymers (Basel).*, vol. 10, 2018.

[257] Y. Han, “THEORETICAL STUDY OF THERMAL ANALYSIS KINETICS,” 2014.

[258] S. Singh, C. Wu, and P. Williams, “Pyrolysis of waste materials using TGA-MS and TGA-FTIR as complementary characterisation techniques,” *J. Anal. Appl. Pyrolysis*, vol. 94, pp. 99–107, 2012.

[259] X. Gou, X. Zhao, S. Singh, and D. D Qiao, “Tri-pyrolysis: A thermo-kinetic characterisation of polyethylene, cornstalk, and anthracite coal using TGA-FTIR analysis,” *Fuel*, pp. 393–402, 2019.

[260] S. Chen, A. Meng, Y. Long, H. Zhou, and Q. Li, “TGA pyrolysis and gasification of combustible municipal solid waste,” *J. energy Inst.*, 2015.

[261] M. Azam, S. Setoodeh Jahromy, W. Raza, C. Jordan, M. Harasek, and F. Winter, “Comparison of the combustion characteristics and kinetic study of coal, municipal solid waste, and refuse-derived fuel: Model-fitting methods,” *Wiley Online Libr.*, vol. 7, no. 6, pp. 2646–2657, Dec. 2019.

[262] T. Szűcs, P. Szentannai, I. M. Szilágyi, and L. P. Bakos, “Comparing different reaction models for combustion kinetics of solid recovered fuel,” *J. Therm. Anal. Calorim.*, vol. 139, no. 1, pp. 555–565, Jan. 2020.

[263] N. Miskolczi and F. Buyong, “Thermogravimetric analysis and pyrolysis kinetic study of Malaysian refuse derived fuels Production of methane gas from biomass by using anaerobic digestion View project FACE Project UKM View project,” *Taylor Fr.*, vol. 83, no. 3, pp. 125–132, Sep. 2010.

[264] A. Marcilla, M. Beltran, and J. Conesa, “Catalyst addition in polyethylene pyrolysis: Thermogravimetric study,” *J. Anal. Appl. Pyrolysis*, 2001.

[265] A. Aboulkas and K. El Harfi, “STUDY OF THE KINETICS AND MECHANISMS OF THERMAL DECOMPOSITION OF MOROCCAN TARFAYA OIL SHALE AND ITS KEROGEN,” *Oil Shale*, vol. 25, no. 4, pp. 426–443, 2008.

[266] J. Fjellerup, J. Ahrenfeldt, U. Henriksen, and B. Gobel, “Formation, decomposition and cracking of biomass tars in gasification,” 2005.

[267] M. S. Alwani, H. A. Khalil, O. Sulaiman, M. N. Islam, and R. Dungani, “An approach to using agricultural waste fibres in biocomposites application: Thermogravimetric analysis and activation energy study,” 2014.

[268] W. Yang, A. Ponzio, C. Lucas, and W. Blasiak, “Performance analysis of a fixed-bed biomass gasifier using high-temperature air,” *Fuel Process. Technol. Elsevier*, vol. 87, pp. 235–245, 2006.

[269] R. Ebrahimi-Kahrizsangi and M. H. Abbasi, “Evaluation of reliability of Coats-Redfern method for kinetic analysis of non-isothermal TGA,” *Trans. Nonferrous Met. Soc. China*, pp. 217–221, 2008.

[270] G. Vasconcelos, R. Mazur, B. Ribeiro, E. Otelho, and M. Costa, “Evaluation of decomposition kinetics of poly (ether-ether-ketone) by thermogravimetric analysis,” *Mater. Res.*, vol. 17, pp. 227–235, 2014.

[271] F. Wong, C. Lin, K. Chen, Y. Shen, and J.-J. Huang, “Improvement of the thermal latency for epoxy-phenolic resins by novel amphiphatic imidazole catalysts,” *Macromol. Res.*, vol. 18, pp. 324–330, 2010.

[272] Z. Liu, Z. Jiang, B. Fei, and X. ’ E. Liu, “Thermal decomposition of Chinese fir,” 2013.

[273] N. Abdoulmoumine, A. Kulkarni, and S. Adhikari, “Effects of temperature and equivalence ratio on pine syngas primary gases and contaminants in a bench-scale fluidized bed gasifier,” *Ind. Eng. Chem. Res.*, vol. 53, no. 14, pp. 5767–5777, Apr. 2014.

[274] W. Azlina *et al.*, “Air Gasification of Malaysia Agricultural Waste in a Fluidized Bed Gasifier: Hydrogen Production Performance A systems approach to synergistic utilisation of secondary organic streams (SYNERGORS) View project METSOXCAT View project Air Gasification of Malaysia Agricultural Waste in a Fluidized Bed Gasifier: Hydrogen Production Performance,” *books.google.com*, vol. 2, pp. 258–268, 2014.

[275] H. Ghassemi and R. Shahsavan-Markadeh, “Effects of various operational parameters on biomass gasification process; a modified equilibrium model,” *Energy Convers. Manag.*, vol. 79, pp. 18–24, 2014.

[276] D. Upadhyay, A. Sakhiya, K. Panchal, and A. Patel, “Effect of equivalence ratio on the performance of the downdraft gasifier–An experimental and modelling approach,” *Energy*, vol. 168, pp. 833–846, 2019.

[277] T. Khosasaeng and R. Suntivarakorn, “Effect of equivalence ratio on an efficiency of single throat downdraft gasifier using RDF from municipal solid waste,” *Energy Procedia*, vol. 138, pp. 784–788, 2017.

[278] V. Dillibabu and E. Natarajan, “Effect of temperature and equivalence ratio on gasification of biomass,” *J. Chem. Pharm. Sci.*, vol. 4, pp. 92–94, 2014.

[279] M. Vaezi, M. Passandideh-Fard, M. Moghiman, and M. Charmchi, “Gasification of heavy fuel oils: A thermochemical equilibrium approach,” *Fuel*, vol. 90, no. 2, 2011.

[280] N. Abdoulmoumine, A. Kulkarni, and S. Adhikari, “Effects of temperature and equivalence ratio on mass balance and energy analysis in loblolly pine oxygen gasification,” *Energy Sci. Eng.*, vol. 4, no. 4, pp. 256–268, Jul. 2016.

[281] S. Aljbour and K. Kawamoto, “Bench-scale gasification of cedar wood–Part I: Effect of operational conditions on product gas characteristics,” *Elsevier*, vol. 90, no. 4, pp. 1495–1500, 2013.

[282] A. James, S. Helle, and R. Thring, “Investigation of air and air-steam gasification of high carbon wood ash in a fluidized bed reactor,” *Energy Environ. Res.*, vol. 4, no. 1, pp. 1–22, 2014.

[283] H. Zhang, X. Guo, and Z. Zhu, “Effect of temperature on gasification performance and sodium transformation of Zhundong coal,” *Fuel*, vol. 189, pp. 301–311, 2017.

[284] J. Fuchs, J. C. Schmid, & S. Müller, & A. M. Mauerhofer, & F. Benedikt, and & H. Hofbauer, “The impact of gasification temperature on the process characteristics of sorption enhanced reforming of biomass,” *Biomass Convers. Biorefinery*, pp. 1–12, 2019.

[285] P. Lahijani and Z. Zainal, “Gasification of palm empty fruit bunch in a bubbling fluidized bed: a performance and agglomeration study,” *Bioresour. Technol.*, vol. 10, no. 2, pp. 2068–2076, 2011.

[286] Y. Furusawa, H. Taguchi, S. Ismail, and S. Thangavel, “Estimation of cold gas efficiency and reactor size of low-temperature gasifier for advanced-integrated coal gasification combined cycle systems,” *Fuel Process. Technol.*, vol. 193, pp. 304–316, 2019.

[287] J. Fermoso *et al.*, “High-pressure co-gasification of coal with biomass and petroleum coke,” *Fuel Process. Technol.*, vol. 90, no. 7–8, pp. 926–932, 2009.

[288] M. Islam, “A review of dolomite catalyst for biomass gasification tar removal,” *Fuel*, 2020.

[289] A. in Biomass *et al.*, “Steam-Gasification of Biomass in a Fluidized-Bed of Olivine Particles Combustion of biomass and solid refused fuels View project dry reforming of methane View project Steam-gasiÿcation of biomass in a auidised-bed of olivine particles,” *Biomass and Bioenergy*, vol. 19, pp. 187–197, 2000.

[290] J. De Andres, A. Narros, M. R.- Fuel, and undefined 2011, “Behaviour of dolomite, olivine and alumina as primary catalysts in air–steam gasification of sewage sludge,” *Elsevier*.

[291] J. Corella, J. M. Toledo, and R. Padilla, “Olivine or dolomite as in-bed additive in biomass gasification with air in a fluidized bed: Which is better?,” *Energy and Fuels*, vol. 18, no. 3, pp. 713–720, May 2004.

[292] G. Hu, S. Xu, S. Li, C. Xiao, and S. Liu, “Steam gasification of apricot stones with olivine and dolomite as downstream catalysts,” *Fuel Process. Technol.*, vol. 87, no. 5, pp. 375–382, 2006.

[293] X. Ma, X. Zhao, J. Gu, and J. Shi, “Co-gasification of coal and biomass blends using dolomite and olivine as catalysts,” *Renew. Energy*, vol. 132, pp. 509–514, 2019.

[294] L. Devi, K. Ptasinski, F. Janssen, and S. van Paasen, “Catalytic decomposition of biomass tars: use of dolomite and untreated olivine,” *Renew. energy*, vol. 30, no. 4, pp. 565–587, 2005.

[295] W. Torres, S. S. Pansare, and J. G. Goodwin, “Hot gas removal of tars, ammonia, and hydrogen sulfide from biomass gasification gas,” *Catalysis Reviews - Science and Engineering*, vol. 49, no. 4. pp. 407–456, Oct-2007.

[296] H. Wang, B. Dlugogorski, and E. Kennedy, “Coal oxidation at low temperatures: oxygen consumption, oxidation products, reaction mechanism and kinetic modelling,” *Prog. energy Combust. Sci.*, 2003.

[297] F. Akgün and A. Arisoy, “Effect of particle size on the spontaneous heating of a coal stockpile,” *Combust. Flame*, vol. 99, no. 1, pp. 137–146, 1994.

[298] Wang, L. Wu, X. Hu, L. Zhang, T. Li, and C.-Z. Li, “Effects of particle size and gasification atmosphere on the changes in char structure during the gasification of mallee biomass,” *Energy & Fuels*, vol. 32, no. 7, pp. 7678–7684, 2018.

[299] M. Mohammed, A. Salmiaton, and W. Azlina, “Air gasification of empty fruit bunch for hydrogen-rich gas production in a fluidized-bed reactor,” *Energy Convers. Manag.*, 2011.

[300] A. Al-Moftah, R. Marsh, and J. Steer, “Life cycle assessment of solid recovered fuel gasification in the state of Qatar,” *ChemEngineering*, vol. 5, no. 4, 2021.

[301] IEA, “Qatar Energy Balance. Sankey Diagram,” 2020. [Online]. Available: https://www.iea.org/sankey/#?c=Qatar&s=Balance. [Accessed: 20-Oct-2020].

[302] V. Pérez, R. Lebrero, and R. Muñoz, “Comparative evaluation of biogas valorization into electricity/heat and poly (hydroxyalkanoates) in waste treatment plants: Assessing the influence of local commodity,” *ACS Sustain. Chem. Eng. ACS Publ.*, vol. 8, no. 20, pp. 7701–

7709, May 2020.

[303] KAHRAMAA, “Sustainability Report 2016,” Springer Verlag, 2016.

[304] Government Communications Office, “Qatar National Vision 2030,” *fourth pillar - Environ. Dev.* , pp. 209–230, Dec. 2020.

[305] Planning and Statistics Authority, “Environmental statistics in State of Qatar,” *Statistics in the 21st Century*, 2020. [Online]. Available: https://www.psa.gov.qa/en/Pages/default.aspx. [Accessed: 21-Oct-2020].

[306] E. Savuto, A. Di Carlo, K. Gallucci, A. Di Giuliano, and S. Rapagnà, “Steam gasification of lignite and solid recovered fuel (SRF) in a bench scale fluidized bed gasifier,” *Waste Manag.*, vol. 114, pp. 341–350, 2020.

[307] M. Finkbeiner, A. Inaba, R. Tan, K. Christiansen, and H. Klüppel, “The New International Standards for Life Cycle Assessment: ISO 14040 and ISO 14044,” *Int. J. life cycle Assess.*, vol. 11, no. 2, pp. 80–85, Mar. 2006.

[308] I. Herrmann and A. Moltesen, “Does it matter which Life Cycle Assessment (LCA) tool you choose?–a comparative assessment of SimaPro and GaBi,” *J. Clean. Prod.*, vol. 86, pp. 163–169, 2015.

[309] I. Dincer and M. Rosen, *Exergy: energy, environment and sustainable development*. 2012.

[310] S. H. Khattak, R. Greenough, I. Korolija, and N. Brown, “An exergy based approach to resource accounting for factories,” *J. Clean. Prod.*, vol. 121, pp. 99–108, May 2016.

[311] L. Xiao, R. Wang, P. Chiang, S. Pan, and Q. Guo, “Comparative life cycle assessment (LCA) of accelerated carbonation processes using steelmaking slag for CO2 fixation,” *Aerosol Air Qual. Res.*, vol. 14, no. 3, pp. 892–904, 2013.

[312] L. Jacquemin, P.-Y. Pontalier, and C. Sablayrolles, “Life cycle assessment (LCA) applied to the process industry: a review,” *Int. J. Life Cycle Assess.*, vol. 17, no. 8, pp. 1028–1041, Sep. 2012.

[313] K. Roberts, B. Gloy, S. Joseph, and N. Scott, “Life Cycle Assessment of Biochar Systems: Estimating the Energetic, Economic, and Climate Change Potential,” *Environ. Sci. Technol. ACS Publ.*, vol. 44, no. 2, pp. 827–833, Jan. 2010.

[314] J. Sundqvist *et al.*, “Life cycle assessment and solid waste: stage 2: annual report,” *agris.fao.org*, 1997.

[315] F. Cherubini, S. Bargigli, and U. Ulgiati, “Life cycle assessment (LCA) of waste management strategies: Landfilling, sorting plant and incineration,” *Energy*, vol. 34, no. 12, pp. 2116–2123, 2009.

[316] H. T. H. Nguyen and B. Min, “Leachate treatment and electricity generation using an algae-cathode microbial fuel cell with continuous flow through the chambers in series,” *Sci. Total Environ.*, vol. 723, p. 138054, Jun. 2020.

[317] I. Andric and S. Al-Ghamdi, “Climate change implications for environmental performance of residential building energy use: The case of Qatar,” Energy Reports, 2020.

[318] Qatar Second National Development Strategy 2018~2022, “Part VI: Chapter I: Sustainable Development to Preserve the Environment.,” 2018.

[319] M. Huijbregts *et al.*, “ReCiPe 2016 A harmonized life cycle impact assessment method at midpoint and endpoint level Report I,” *Int. J. Life Cycle Assess.*, vol. 22, no. 2, pp. 138–147, 2017.

[320] M. Goedkoop, R. Heijungs, M. Huijbregts, A. De Schryver, J. Struijs, and R. Van Zelm, “Recipe 2008,” *A life cycle impact Assess. method which comprises Harmon. Categ. Indic. midpoint*

endpoint Lev., vol. 1, pp. 1–126, 2009.

[321] C. Anand and B. Amor, “Recent developments, future challenges and new research directions in LCA of buildings: A critical review,” *Renew. Sustain. energy Rev.*, vol. 67, pp. 408–416, 2017.

[322] M. A. Abduli, A. Naghib, M. Yonesi, and A. Akbari, “Life cycle assessment (LCA) of solid waste management strategies in Tehran: landfill and composting plus landfill,” *Environ. Monit. Assess.*, vol. 178, no. 1–4, pp. 487–498, Jul. 2011.

[323] A. Korre, Z. Nie, and S. Durucan, “ Life Cycle Assessment of the natural gas supply chain and power generation options with CO 2 capture and storage: Assessment of Qatar natural gas production, LNG transport and power generation in the UK ,” *Sustain. Technol. Syst. Policies*, no. CCS Workshop, p. 11, May 2012.

[324] Z. Cen, P. Kubiak, C. López, and I. Belharouak, “Demonstration study of hybrid solar power generation/storage micro-grid system under Qatar climate conditions,” *Sol. Energy Mater. Sol. Cells*, vol. 180, pp. 280–288, 2018.

[325] L. Martín-Pomares, D. Martínez, J. Polo, D. Perez-Astudillo, D. Bachour, and A. Sanfilippo, “Analysis of the long-term solar potential for electricity generation in Qatar,” *Renew. Sustain. Energy Rev.*, vol. 73, pp. 1231–1246, 2017.

[326] L. Nunes, J. Matias, and J. Catalao, *Torrefaction of Biomass for Energy Applications: From Fundamentals to Industrial Scale*. 2017.

[327] A. E1641-16, “Standard test method for decomposition kinetics by thermogravimetry using the Ozawa/Flynn/Wall method,” 2016.

Appendix A: Kinetic Theory and Feedstock

1. Health and safety precautions

The high temperature conditions make the gasifier prone to operational risk, therefore, health and safety precautions were taken into consideration. Also, the biodegradable materials in the gasifier are flammable and combustible which puts more hazards in the process [326]. Therefore, protocols of storage and transportation of chemicals and pellets were followed in the laboratory. Also, personal protective equipment (PPE) was worn to avoid any contact with chemicals and setup. In addition, coronavirus (COVID-19) protocols and precautions such as social distancing and wearing masks were considered.

The high temperature of the reactor and producer gas may lead to serious injury. For example, the product gas may cause irritation to eyes, skin, respiratory tract, or even death due to toxicity of some gases such as CO, CO_2 and CH_4. Also, some products which have a carcinogenic impact, such as tar should be carefully handled. Other safety considerations included excessive noise, poor ventilation, slip hazards, falling objects, chemical spills, and dangers posed by electricity. Therefore, laboratory safety induction and risk assessment were considered before starting any activity or experiments. Toxic gas detectors coupled with alarms were used to identify levels of harmful gases in the laboratory before exceeding safe concentrations. Fire and explosion hazards are among the most frequent accidents in industrial and research laboratories and facilities due to using combustible fuel and furnaces. In this case, packing the Subcoal™ was performed based on the storage protocols of flammable substances, in a glass container in a designated cupboard. An extraction fan was operated to ventilate the toxic gaseous from the laboratory.

Table A-1 Numerical integration constant (a) for Eq. 4.17 [327].

E/RT	a	b
8	5.3699	0.5398
9	5.8980	0.5281
10	6.4167	0.5187
11	6.928	0.511
12	7.433	0.505
13	7.933	0.500
14	8.427	0.494
15	8.918	0.491
16	9.406	0.488
17	9.890	0.484
18	10.372	0.482
19	10.851	0.479
20	11.3277	0.4770
21	11.803	0.475
22	12.276	0.473
23	12.747	0.471
24	13.217	0.470
25	13.686	0.469
26	14.153	0.467
27	14.619	0.466
28	15.084	0.465
29	15.547	0.463
30	16.0104	0.4629
31	16.472	0.462
32	16.933	0.461
33	17.394	0.461
34	17.853	0.459
35	18.312	0.459
36	18.770	0.458
37	19.228	0.458
38	19.684	0.456
39	20.141	0.456
40	20.5967	0.4558
41	21.052	0.455
42	21.507	0.455
43	21.961	0.454
44	22.415	0.454
45	22.868	0.453
46	23.321	0.453
47	23.774	0.453
48	24.226	0.452
49	24.678	0.452
50	25.1295	0.4515
51	25.5806	0.4511
52	26.0314	0.4508
53	26.4820	0.4506
54	26.9323	0.4503
55	27.3823	0.4500
56	27.8319	0.4498
57	28.2814	0.4495
58	28.7305	0.4491
59	29.1794	0.4489
60	29.6281	0.4487

Table A-2 Subcoal™ powder sample data obtained from XRD analysis.

Pos.[°2Th.]	Height [cts]	FWHMLeft[°2Th.]	d-spacing [Å]	Rel. Int. [%]
21.77	72.20	0.55	4.08	100.00
26.98	30.19	0.47	3.31	41.82
29.94	55.12	0.31	2.98	76.35
38.77	12.47	0.79	2.32	17.28
65.05	7.34	0.94	1.43	10.16

Table A-3 Subcoal™ ash data obtained from XRD analysis.

Pos.[°2Th.]	Height [cts]	FWHMLeft[°2Th.]	d-spacing [Å]	Rel. Int. [%]
25.94	20.36	0.24	3.43	16.85
26.67	64.97	0.24	3.34	53.76
27.35	24.45	0.24	3.26	20.23
29.72	29.61	0.20	3.07	24.50
31.19	87.50	0.19	2.87	72.39
32.07	105.07	0.31	2.79	86.93
33.25	120.87	0.31	2.69	100.00
36.62	42.26	0.24	2.45	34.96
38.50	88.13	0.47	2.34	72.92
39.49	16.93	0.24	2.28	14.00
41.17	40.50	0.31	2.19	33.51
42.87	10.20	0.47	2.11	8.44
44.74	22.41	0.24	2.03	18.54
46.06	22.30	0.39	1.97	18.45
47.46	17.16	0.39	1.92	14.20
49.20	16.22	0.47	1.85	13.42
55.05	15.86	0.31	1.67	13.12
57.29	29.19	0.31	1.61	24.15
60.03	13.80	0.47	1.54	11.42
63.78	7.74	0.47	1.46	6.40
65.09	13.68	0.24	1.43	11.32
68.18	8.36	0.31	1.38	6.92
78.25	15.74	0.39	1.22	13.02

Table A-4 Silica sand data obtained from XRD analysis.

Pos.[°2Th.]	Height [cts]	FWHMLeft[°2Th.]	d-spacing [Å]	Rel. Int. [%]
20.95	246.13	0.24	4.24	23.46
26.78	588.31	0.24	3.33	56.08
36.67	97.48	0.24	2.45	9.29
39.67	16.56	0.31	2.27	1.58
40.41	15.39	0.39	2.23	1.47
42.57	21.09	0.24	2.12	2.01
45.98	49.27	0.24	1.97	4.70
50.25	1049.00	0.19	1.82	100.00
55.10	118.58	0.24	1.67	11.30
57.61	5.59	0.47	1.60	0.53
60.03	284.16	0.24	1.54	27.09
67.97	221.20	0.24	1.38	21.09
75.72	11.65	0.39	1.26	1.11
81.52	6.95	0.47	1.18	0.66
83.99	34.50	0.39	1.15	3.29
87.47	6.78	0.47	1.11	0.65

Appendix B: TGA Conversion Repeatability

The experiments were repeated three times to verify the results obtained and eliminate potential experimental errors. The results achieved from three TGA runs showed a high degree of agreement. The repeats for the heating rate experiments are shown in this section. The results include the kinetics curves and TGA tables.

Table B-1 Thermal pyrolysis parameters without catalyst at different heating rates.

β	Run1		Run2		Run3	
	T_m	DTG_{Tm}	T_m	DTG_{Tm}	T_m	DTG_{Tm}
°C/min	°C	wt%/min	°C	wt%/min	°C	wt%/min
5	468.8	-0.0079	478.7	-0.0112	463.6	-0.0091
10	476.7	-0.0107	480.2	-0.0235	482.6	-0.0220
15	482.3	-0.0129	485.4	-0.0261	485.8	-0.0225
20	487.9	-0.0318	487.2	-0.0392	487.1	-0.0244
β	Mean		St. Deviation			
	T_m	DTG_{Tm}	T_m	DTG_{Tm}		
°C/min	°C	wt%/min	°C	wt%/min		
5	471.1	-0.0094	7.0	0.0014		
10	481.4	-0.0187	6.7	0.0057		
15	485.6	-0.0205	4.7	0.0056		
20	487.1	-0.0318	1.1	0.0060		

Table B-2 Thermal CO_2 gasification parameters without catalyst at different heating rates.

β	Run1		Run2		Run3	
	T_m	DTG_{Tm}	T_m	DTG_{Tm}	T_m	DTG_{Tm}
°C/min	°C	wt%/min	°C	wt%/min	°C	wt%/min
5	464.1	-0.0079	460.9	-0.0099	473.1	-0.0112
10	467.2	-0.0107	474.7	-0.0176	480.8	-0.0297
15	475.6	-0.0129	481.2	-0.0258	488.0	-0.0301
20	489.4	-0.0318	486.6	-0.0354	488.0	-0.0301
β	Mean		St. Deviation			
	T_m	DTG_{Tm}	T_m	DTG_{Tm}		
°C/min	°C	wt%/min	°C	wt%/min		
5	466.1	-0.0097	5.2	0.0014		
10	474.2	-0.0193	5.5	0.0079		
15	481.6	-0.0229	5.1	0.0073		
20	488.0	-0.0324	1.1	0.0022		

Table B-3 Thermal combustion parameters without catalyst at different heating rates.

β °C/min	Run1		Run2		Run3	
	T_m	DTG_{Tm}	T_m	DTG_{Tm}	T_m	DTG_{Tm}
	°C	wt%/min	°C	wt%/min	°C	wt%/min
5	313.4	-0.0080	314.5	-0.0077	322.8	-0.0059
10	320.3	-0.0141	331.2	-0.0176	332.5	-0.0117
15	333.2	-0.0272	338.0	-0.0268	336.6	-0.0212
20	338.1	-0.0352	344.4	-0.0347	338.3	-0.0271
β °C/min	Mean		St. Deviation			
	T_m	DTG_{Tm}	T_m	DTG_{Tm}		
	°C	wt%/min	°C	wt%/min		
5	316.9	-0.0072	4.2	0.0009		
10	328.2	-0.0145	5.5	0.0024		
15	335.9	-0.0251	2.0	0.0028		
20	340.3	-0.0323	2.9	0.0037		

Appendix C: Model Free Kinetic Repeatability

OFW Method

(a)

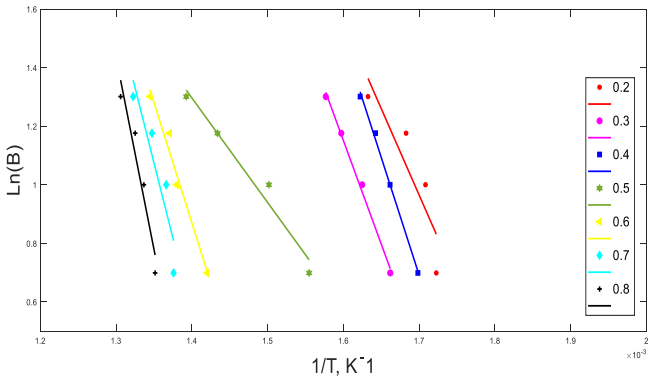

(b)

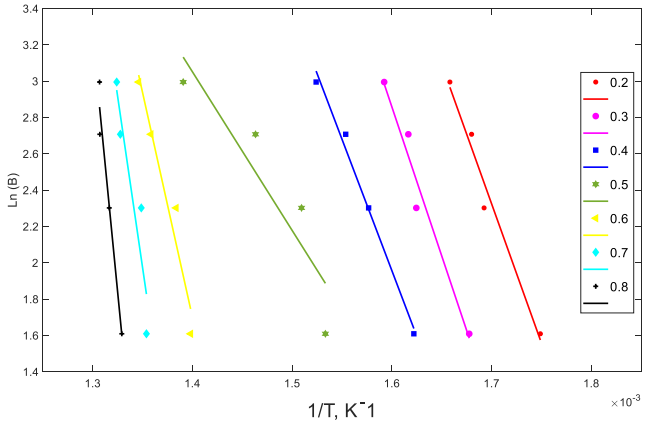

Figure C-1 OFW plots of pyrolysis for various values of degrees of conversion run 1 (a) and 2 (b) at different heating rates

Table C-1 Kinetic parameters of pyrolysis obtained by OFW at different heating rates.

Run 1				Run 2		
X	E_a(kJ/mol)	R^2	A(min^{-1})	E_a(kJ/mol)	R^2	A(min^{-1})
0.2	118.9	0.802	2.7E+09	134.2	0.975	7.6E+10
0.3	142.5	0.995	1.6E+11	143.6	0.964	3.6E+10
0.4	161.9	0.996	2.7E+13	126.5	0.990	2.1E+10
0.5	71.9	0.966	6.9E+04	76.4	0.832	1.0E+10
0.6	165.4	0.970	2.7E+11	216.3	0.945	7.3E+08
0.7	207.2	0.857	2.4E+14	329.6	0.872	3.7E+08
0.8	264.2	0.931	2.4E+18	491.6	0.966	2.2E+08
Average	161.7	0.931	3.4E+17	216.9	0.935	2.1E+10

Run 3			
X	E_a(kJ/mol)	R^2	A(min^{-1})
0.2	241.4	0.917	4.5E+20
0.3	232.1	0.996	1.0E+20
0.4	201.6	0.985	4.2E+19
0.5	116.6	0.979	2.6E+18
0.6	215.7	0.841	1.8E+17
0.7	265.8	0.977	5.9E+16
0.8	203.4	0.996	3.9E+16
Average	210.9	0.956	8.6E+19

(a)

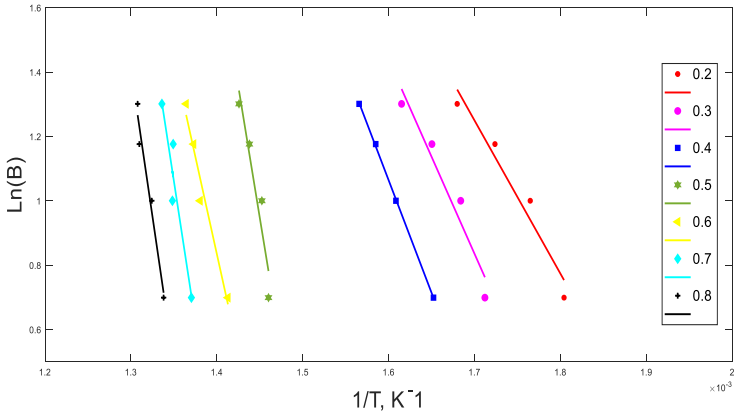

(b)

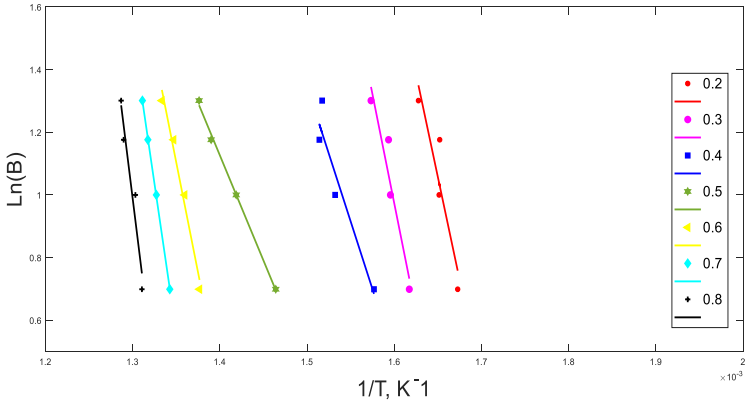

Figure C-2 The OFW plots of CO_2 gasification for various values of degrees of conversion run 1 (a) and 2 (b) at different heating rates

Table C-2 Kinetic parameters of CO_2 gasification obtained by OFW at different heating rates.

Run 1				Run 2		
X	E_a(kJ/mol)	R^2	A(min^{-1})	E_a(kJ/mol)	R^2	A(min^{-1})
0.2	95.9	0.951	4.5E+07	139.2	0.988	1.5E+11
0.3	121.6	0.939	5.3E+09	216.5	0.977	6.4E+10
0.4	140.9	1	1.4E+11	140.4	0.959	5.1E+10
0.5	328.9	0.912	6.7E+24	139.6	0.934	4.1E+09
0.6	243.4	0.967	2.2E+17	241.4	0.968	1.4E+09
0.7	351.8	0.910	1.1E+25	259.5	0.967	1.1E+09
0.8	367.7	0.973	5.3E+25	264.6	0.981	9.5E+08
Average	235.7	0.950	1.0E+25	200.2	0.968	3.9E+10

Run 3			
X	E_a(kJ/mol)	R^2	A(min^{-1})
0.2	264.7	0.858	2.1E+22
0.3	280.7	0.918	4.6E+21
0.4	173.9	0.912	1.5E+21
0.5	135.2	0.997	4.4E+19
0.6	283.1	0.980	3.2E+18
0.7	384.4	1.000	1.1E+18
0.8	453.7	0.943	5.2E+17
Average	282.2	0.944	3.8E+21

(a)

(b)

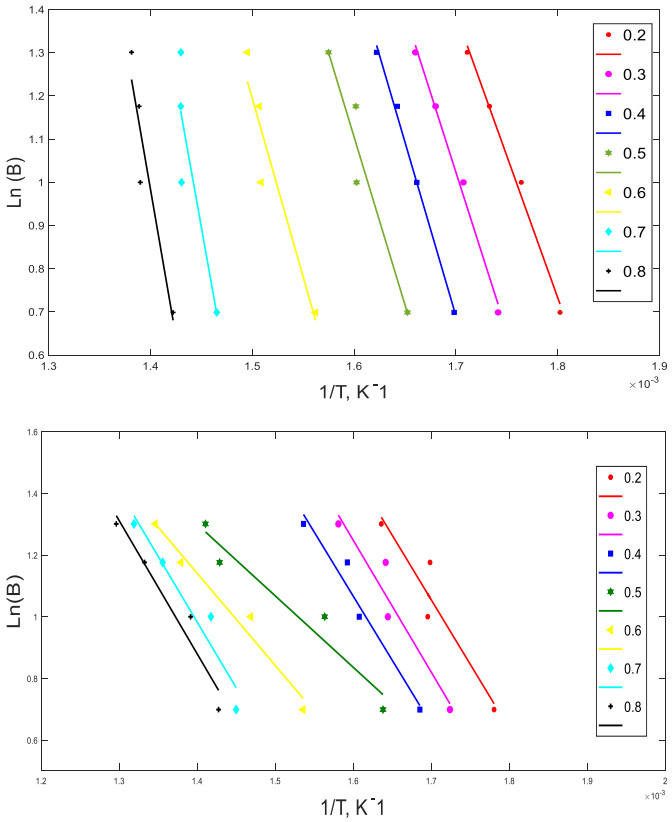

Figure C-3 The OFW plots of combustion for various values of degrees of conversion for run1 (a) and 2 (b) at different heating rates

Table C-3 Kinetic parameters of combustion obtained by OFW at different heating rates.

Run 1				Run 2		
X	E_a(kJ/mol)	R^2	A(min^{-1})	E_a(kJ/mol)	R^2	A(min^{-1})
0.2	57.4	0.992	1.5E+04	76.7	0.924	5.6E+05
0.3	64.5	0.992	1.4E+04	72.0	0.701	2.1E+05
0.4	70.3	0.996	1.4E+04	64.5	0.619	4.1E+04
0.5	68.0	0.929	1.4E+04	24.1	0.264	4.8E+00
0.6	72.3	0.896	8.7E+03	18.9	0.113	1.4E+00
0.7	115.7	0.789	4.1E+03	25.2	0.096	6.3E+00
0.8	119.5	0.901	3.8E+03	44.3	0.252	5.0E+02
Average	81.1	0.928	1.0E+04	46.5	0.424	1.2E+05

Run 3			
X	E_a(kJ/mol)	R^2	A(min^{-1})
0.2	84.6	0.993	2.7E+06
0.3	86.8	0.993	2.2E+06
0.4	80.0	0.957	2.2E+06
0.5	52.8	0.981	2.0E+06
0.6	54.2	0.951	1.0E+06
0.7	81.1	0.934	4.6E+05
0.8	97.7	0.991	3.5E+05
Average	76.7	0.971	1.6E+06

KAS method

(a)

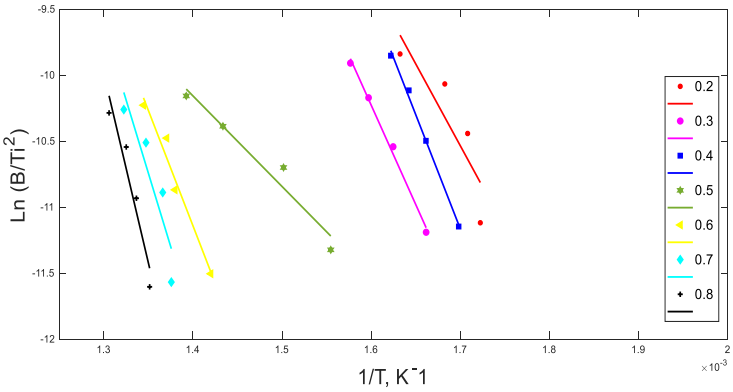

(b)

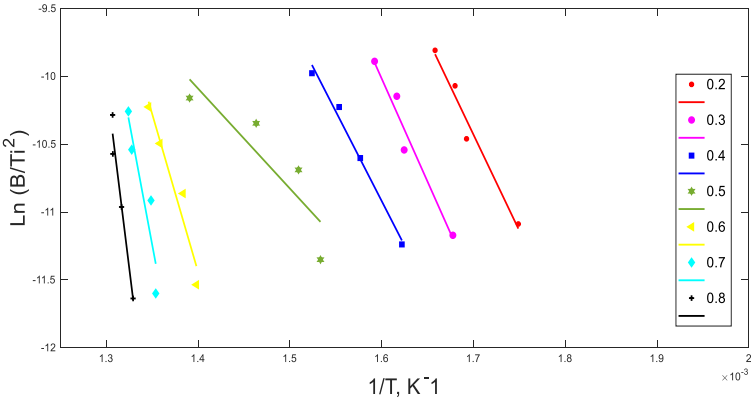

Figure C-4 The KAS plots of pyrolysis for various values of degrees of conversion run 1 (a) and 2 (b) at different heating rates

Table C-4 Kinetic parameters of pyrolysis obtained by KAS at different heating rates.

Run 1				Run 2		
X	E_a(kJ/mol)	R^2	A(min^{-1})	E_a(kJ/mol)	R^2	A(min^{-1})
0.2	103.2	0.771	1.8E+08	117.9	0.971	1.7E+07
0.3	125.3	0.994	1.9E+10	126.4	0.959	6.9E+07
0.4	143.9	0.996	9.8E+11	109.8	0.988	4.3E+06
0.5	57.1	0.951	9.4E+03	61.3	0.777	1.1E+03
0.6	145.3	0.965	1.3E+12	193.7	0.938	4.7E+12
0.7	184.8	0.840	4.9E+15	301.2	0.862	1.9E+20
0.8	238.8	0.924	3.7E+20	455.1	0.964	1.2E+31
Average	142.6	0.920	5.3E+19	195.1	0.923	1.8E+30
Run 3						
X	E_a(kJ/mol)	R^2	A(min^{-1})			
0.2	219.7	0.909	3.8E+14			
0.3	210.6	0.995	8.4E+13			
0.4	181.3	0.983	6.8E+11			
0.5	99.5	0.973	8.0E+05			
0.6	193.2	0.824	4.8E+12			
0.7	240.5	0.974	1.2E+16			
0.8	180.9	0.996	6.3E+11			
Average	189.4	0.951	1.7E+15			

(a)

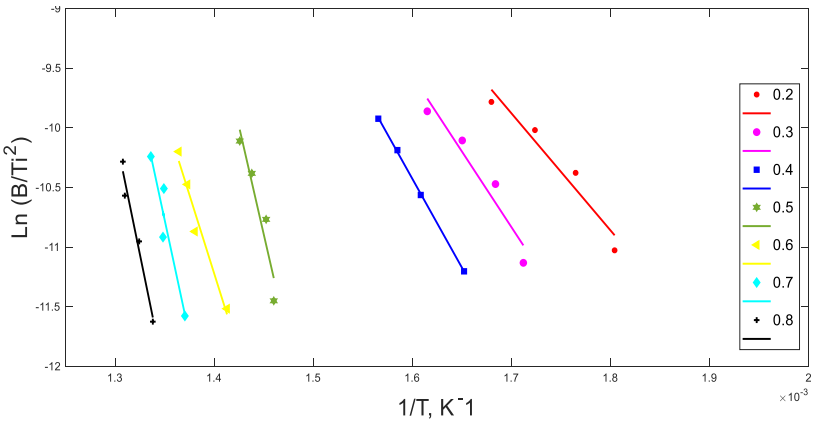

(b)

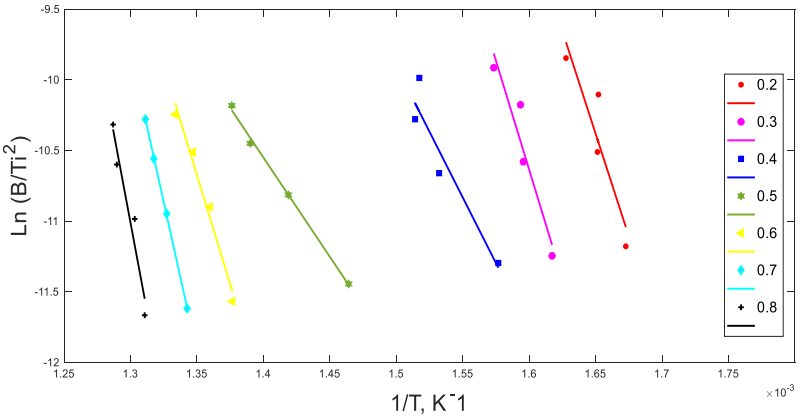

Figure C-5 The KAS plots of CO_2 gasification for various values of degrees of conversion run 1 (a) and 3 (b) at different heating rates

Table C-5 Kinetic parameters of CO_2 gasification obtained by KAS at different heating rates.

Run 1				Run 2		
X	E_a(kJ/mol)	R^2	A(min^{-1})	E_a(kJ/mol)	R^2	A(min^{-1})
0.2	81.6	0.939	1.9E+06	122.5	0.986	4.8E+07
0.3	105.5	0.927	3.0E+08	195.8	0.974	1.1E+13
0.4	123.8	1	1.4E+10	122.9	0.952	5.2E+07
0.5	301.3	0.905	1.5E+26	121.2	0.922	3.8E+07
0.6	219.6	0.963	6.8E+18	217.5	0.964	3.9E+14
0.7	322.4	0.903	1.2E+28	234.5	0.963	6.6E+15
0.8	337.2	0.971	2.6E+29	239.2	0.979	1.4E+16
Average	213.1	0.944	3.9E+28	179.1	0.963	3.1E+15
Run 3						
X	E_a(kJ/mol)	R^2	A(min^{-1})			
0.2	241.7	0.850	1.4E+16			
0.3	256.6	0.912	1.5E+17			
0.4	154.7	0.900	8.3E+09			
0.5	116.9	0.997	1.5E+07			
0.6	257.0	0.978	1.7E+17			
0.7	353.2	1.000	1.1E+24			
0.8	418.8	0.940	4.7E+28			
Average	256.9	0.939	6.8E+27			

(a)

(b)

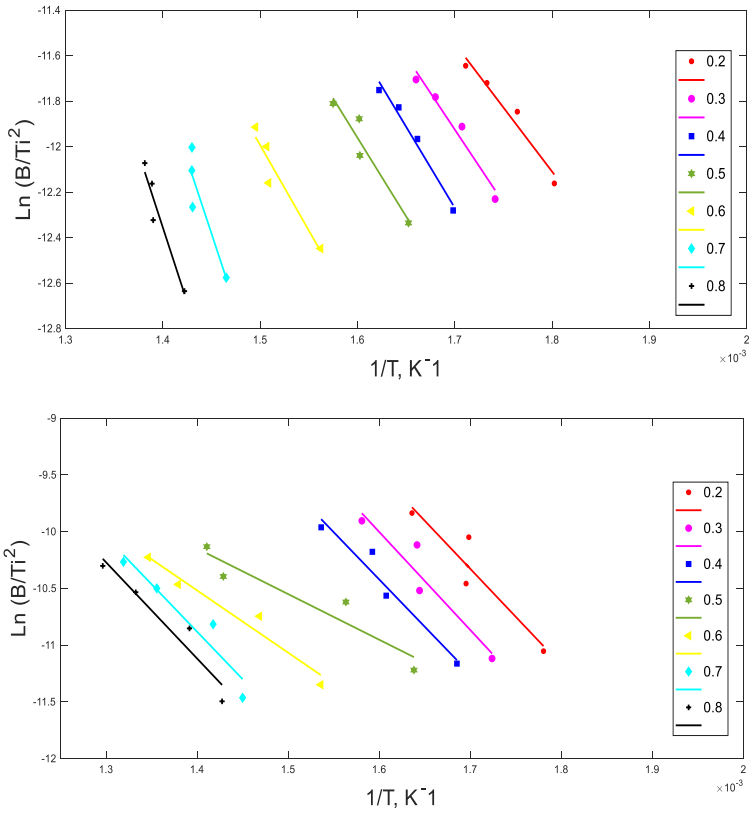

Figure C-6 The KAS plots of combustion for various values of degrees of conversion run 1 (a) and 2 (b) at different heating rates

Table C-6 Kinetic parameters of combustion obtained by KAS at different heating rates.

Run 1				Run 2		
X	E_a(kJ/mol)	R^2	A(min^{-1})	E_a(kJ/mol)	R^2	A(min^{-1})
0.2	46.9	0.957	9.9E+02	70.4	0.880	1.5E+05
0.3	53.6	0.958	4.3E+03	71.9	0.902	2.0E+05
0.4	59.3	0.977	1.5E+04	69.3	0.946	1.2E+05
0.5	57.6	0.918	1.1E+04	33.4	0.895	4.3E+01
0.6	62.5	0.914	3.0E+04	45.7	0.953	6.7E+02
0.7	107.9	0.856	4.9E+08	69.6	0.906	1.2E+05
0.8	109.3	0.927	6.8E+08	70.5	0.922	1.5E+05
Average	71.0	0.925	1.7E+08	61.6	0.915	1.1E+05

Run 3			
X	E_a(kJ/mol)	R^2	A(min^{-1})
0.2	70.8	0.991	1.1E+05
0.3	72.5	0.991	1.5E+05
0.4	65.8	0.943	3.7E+04
0.5	39.3	0.967	1.2E+02
0.6	40.1	0.919	1.4E+02
0.7	65.2	0.909	3.2E+04
0.8	80.6	0.988	8.4E+05
Average	62.1	0.958	1.7E+05

ST Method

(a)

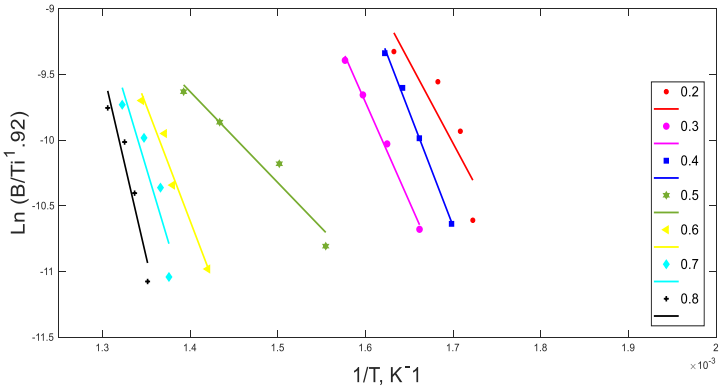

(b)

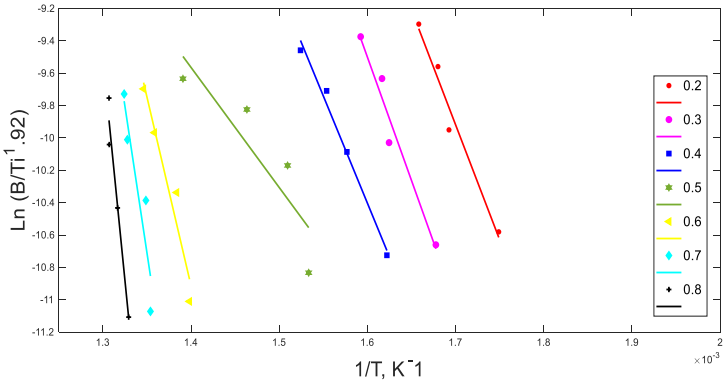

Figure C-7 The ST plots of pyrolysis for various values of degrees of conversion run 1 (a) and 2 (b) at different heating rates

Table C-7 Kinetic parameters of pyrolysis obtained by ST at different heating rates.

Run 1				Run 2		
X	E_a(kJ/mol)	R^2	A(min^{-1})	E_a(kJ/mol)	R^2	A(min^{-1})
0.2	103.6	0.772	2.0E+08	118.3	0.971	1.8E+07
0.3	125.7	0.994	2.1E+10	126.8	0.959	7.5E+07
0.4	144.4	0.996	1.1E+12	110.2	0.988	4.6E+06
0.5	57.6	0.952	1.0E+04	61.7	0.780	1.2E+03
0.6	145.8	0.966	1.4E+12	194.2	0.939	5.0E+12
0.7	185.2	0.841	5.4E+15	301.7	0.863	2.1E+20
0.8	239.3	0.924	4.1E+20	455.6	0.964	1.3E+31
Average	143.1	0.921	5.8E+19	195.5	0.923	1.9E+30
Run 3						
X	E_a(kJ/mol)	R^2	A(min^{-1})			
0.2	220.1	0.910	4.0E+14			
0.3	210.9	0.995	9.0E+13			
0.4	181.7	0.983	7.3E+11			
0.5	99.9	0.974	8.7E+05			
0.6	193.7	0.825	5.2E+12			
0.7	241.0	0.974	1.3E+16			
0.8	181.4	0.996	6.9E+11			
Average	189.8	0.951	1.9E+15			

(a)

(b)

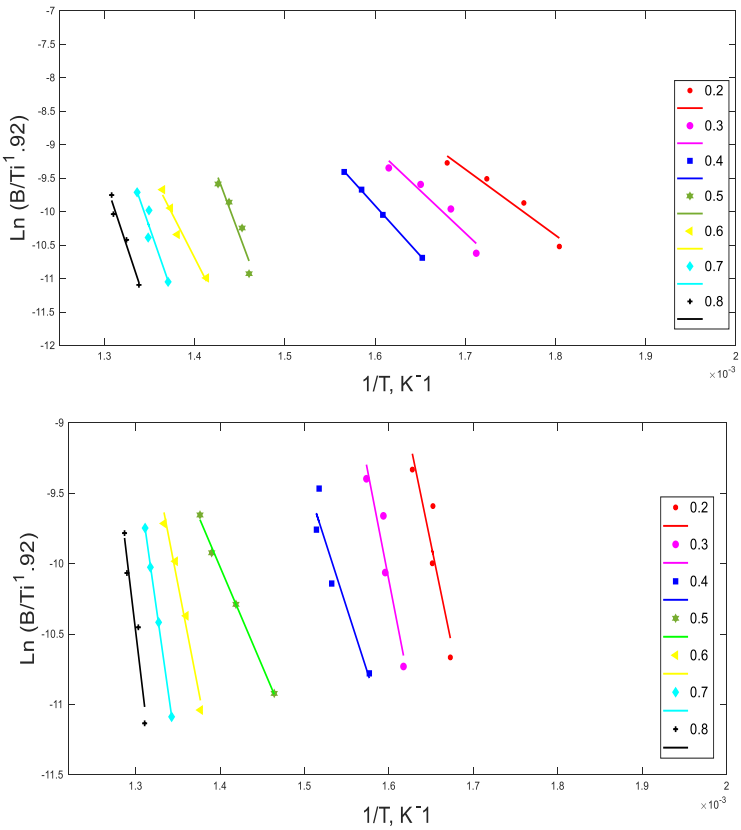

Figure C-8 The ST plots of CO_2 gasification for various values of degrees of conversion run 1 (a) and 2 (b) at different heating rates

Table C-8 Kinetic parameters of CO_2 gasification obtained by ST at different heating rates.

Run 1				Run 2		
X	E_a(kJ/mol)	R^2	A(min^{-1})	E_a(kJ/mol)	R^2	A(min^{-1})
0.2	82.0	0.939	2.0E+06	122.9	0.986	5.2E+07
0.3	105.9	0.928	3.3E+08	196.2	0.974	1.1E+13
0.4	124.2	1.000	1.5E+10	123.3	0.952	5.6E+07
0.5	301.8	0.906	1.7E+26	121.6	0.922	4.2E+07
0.6	220.1	0.964	7.6E+18	217.9	0.964	4.3E+14
0.7	322.9	0.904	1.3E+28	234.9	0.963	7.2E+15
0.8	337.7	0.971	2.9E+29	239.7	0.979	1.6E+16
Average	213.5	0.944	4.3E+28	179.5	0.963	3.3E+15

Run 3			
X	E_a(kJ/mol)	R^2	A(min^{-1})
0.2	242.1	0.850	1.5E+16
0.3	257.0	0.912	1.7E+17
0.4	155.1	0.901	8.9E+09
0.5	117.4	0.997	1.6E+07
0.6	257.5	0.978	1.9E+17
0.7	353.7	1.000	1.2E+24
0.8	419.3	0.940	5.1E+28
Average	257.4	0.939	7.4E+27

(a)

(b)

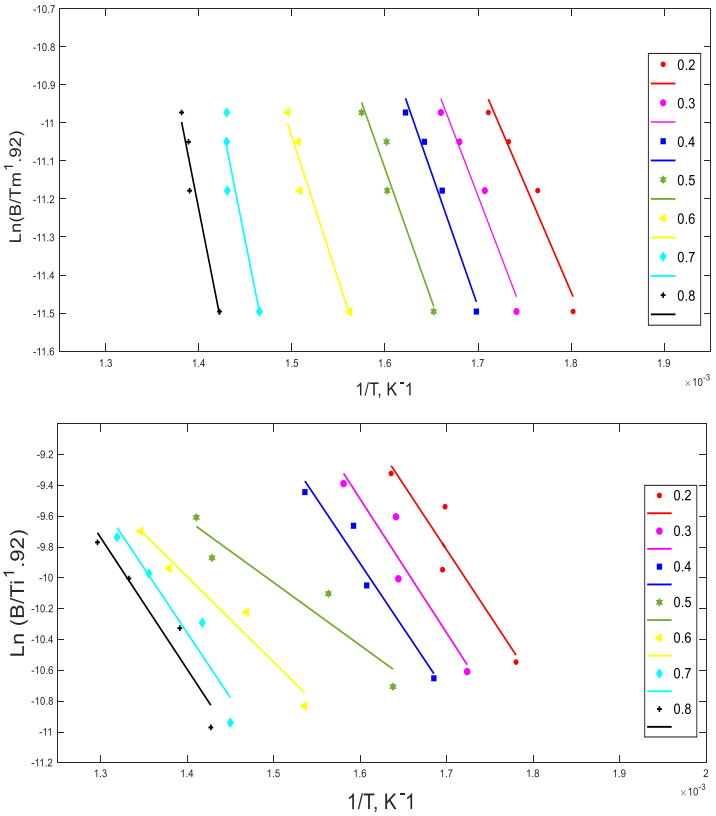

Figure C-9 ST plot of combustion for various values of degrees of conversion for run 1 (a) and 2 (b) at different heating rates

Table C-9 Kinetic parameters of combustion obtained by ST at different heating rates.

Run 1				Run 2		
X	E_a(kJ/mol)	R^2	A(min^{-1})	E_a(kJ/mol)	R^2	A(min^{-1})
0.2	47.3	0.958	1.1E+03	70.8	0.881	1.6E+05
0.3	53.9	0.959	4.7E+03	72.3	0.903	2.2E+05
0.4	59.7	0.977	1.7E+04	69.7	0.947	1.3E+05
0.5	58.0	0.919	1.1E+04	33.9	0.897	4.8E+01
0.6	62.9	0.915	3.3E+04	46.1	0.954	7.5E+02
0.7	108.4	0.827	5.5E+08	70.1	0.907	1.4E+05
0.8	109.8	0.927	7.5E+08	71.0	0.923	1.7E+05
Average	71.4	0.926	1.9E+08	61.9	0.916	1.2E+05
Run 3						
X	E_a(kJ/mol)	R^2	A(min^{-1})			
0.2	71.2	0.992	1.1E+05			
0.3	72.9	0.991	1.7E+05			
0.4	66.3	0.943	4.0E+04			
0.5	39.7	0.968	1.3E+02			
0.6	40.6	0.921	1.6E+02			
0.7	65.6	0.910	3.5E+04			
0.8	81.2	0.988	9.4E+05			
Average	62.5	0.959	1.8E+05			

TA Method

(a)

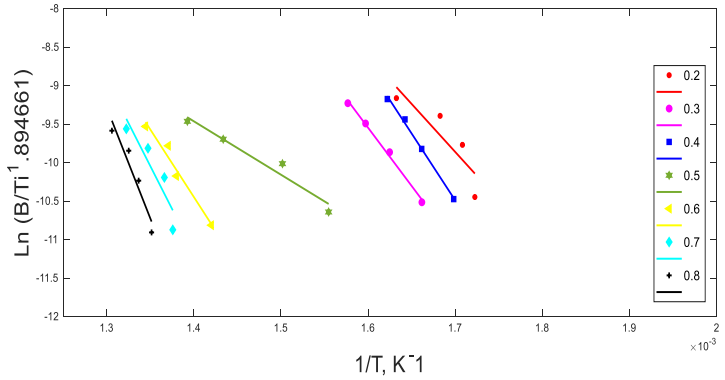

(b)

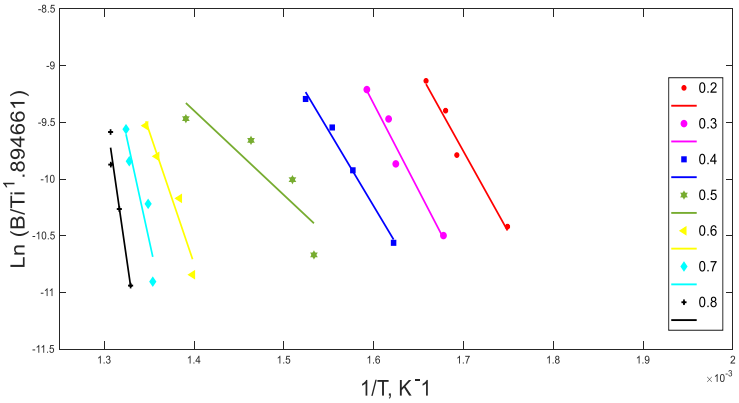

Figure C-10 TA plots of pyrolysis for various values of degrees of conversion run 1 (a) and 2 (b) at different heating rates

Table C-10 Kinetic parameters of pyrolysis obtained by TA at different heating rates.

Run 1				Run 2		
X	E_a(kJ/mol)	R^2	A(min^{-1})	E_a(kJ/mol)	R^2	A(min^{-1})
0.2	102.7	0.871	1.6E+08	118.4	0.972	1.8E+07
0.3	116.5	0.881	3.0E+09	126.9	0.959	7.6E+07
0.4	126.6	0.909	2.6E+10	110.4	0.988	4.7E+06
0.5	121.9	0.948	9.6E+09	61.9	0.781	1.2E+03
0.6	135.5	0.849	1.7E+11	194.3	0.939	5.2E+12
0.7	212.6	0.691	1.6E+18	301.8	0.863	2.1E+20
0.8	230.4	0.855	6.5E+19	455.7	0.964	1.4E+31
Average	149.5	0.858	9.5E+18	195.6	0.923	1.9E+30
Run 3						
X	E_a(kJ/mol)	R^2	A(min^{-1})			
0.2	220.2	0.910	4.1E+14			
0.3	211.1	0.995	9.2E+13			
0.4	181.9	0.983	7.4E+11			
0.5	100.1	0.974	8.9E+05			
0.6	193.8	0.825	5.4E+12			
0.7	241.2	0.974	1.3E+16			
0.8	181.5	0.996	7.1E+11			
Average	189.9	0.951	1.9E+15			

(a)

(b)

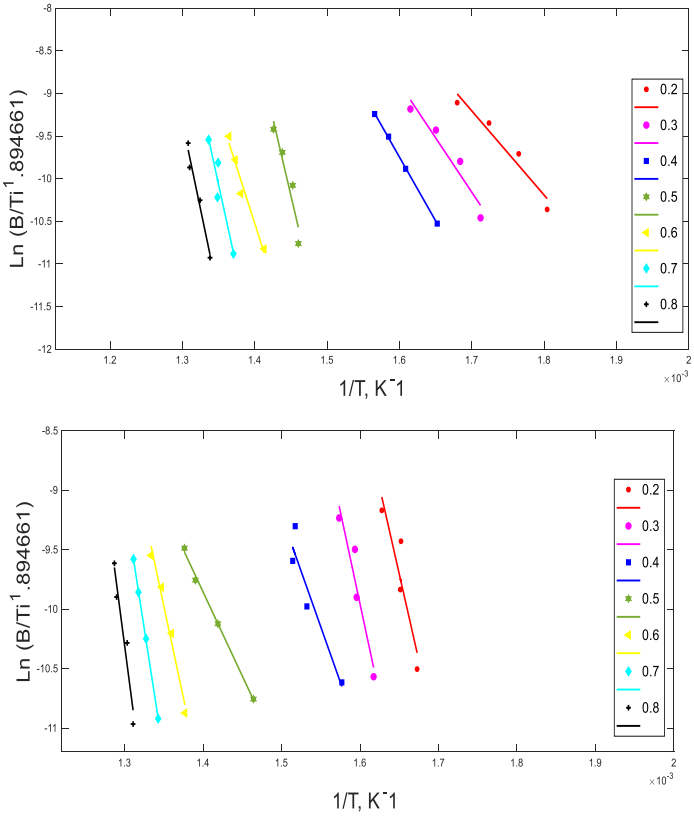

Figure C-11 TA plots of CO_2 gasification for various values of degrees of conversion run 1 (a) and 2 (b) at different heating rates

Table C-11 Kinetic parameters of CO_2 gasification obtained by TA at different heating rates.

Run 1				Run 2		
X	E_a(kJ/mol)	R^2	A(min^{-1})	E_a(kJ/mol)	R^2	A(min^{-1})
0.2	103.7	0.773	2.1E+08	123.0	0.986	5.3E+07
0.3	125.8	0.994	2.2E+10	196.3	0.974	1.2E+13
0.4	144.5	0.996	1.1E+12	123.5	0.952	5.7E+07
0.5	57.7	0.952	1.1E+04	121.8	0.922	4.3E+07
0.6	145.9	0.966	1.5E+12	218.1	0.964	4.4E+14
0.7	185.4	0.841	5.6E+15	235.1	0.963	7.4E+15
0.8	239.5	0.924	4.2E+20	239.8	0.979	1.6E+16
Average	143.2	0.921	6.0E+19	179.7	0.963	3.4E+15

Run 3			
X	E_a(kJ/mol)	R^2	A(min^{-1})
0.2	242.3	0.849	1.5E+16
0.3	257.1	0.912	1.7E+17
0.4	155.3	0.901	9.1E+09
0.5	117.5	0.997	1.7E+07
0.6	257.7	0.978	1.9E+17
0.7	353.8	1.000	1.2E+24
0.8	419.5	0.940	5.3E+28
Average	257.6	0.940	7.5E+27

(a)

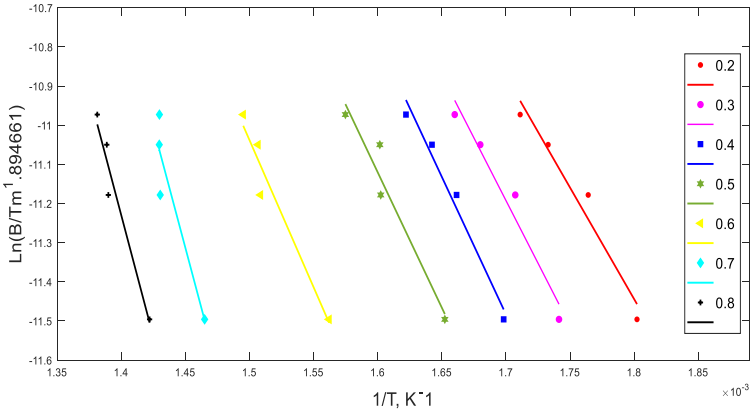

(b)

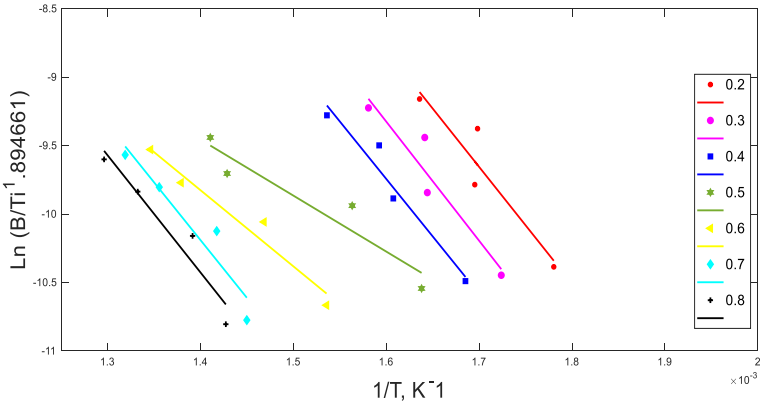

Figure C-12 TA plots of combustion for various values of degrees of conversion run 1 (a) and 2 (b) at different heating rates

Table C-12 Kinetic parameters of combustion obtained by TA at different heating rates.

Run 1				Run 2		
X	E_a(kJ/mol)	R^2	A(min^{-1})	E_a(kJ/mol)	R^2	A(min^{-1})
0.2	47.4	0.958	1.1E+03	70.9	0.881	1.6E+05
0.3	54.1	0.959	4.8E+03	72.4	0.903	2.2E+05
0.4	59.9	0.977	1.7E+04	69.9	0.947	1.3E+05
0.5	58.2	0.919	1.2E+04	34.0	0.898	4.9E+01
0.6	63.1	0.916	3.4E+04	46.3	0.954	7.7E+02
0.7	108.5	0.827	5.7E+08	70.2	0.907	1.4E+05
0.8	109.9	0.927	7.7E+08	71.2	0.924	1.7E+05
Average	71.6	0.926	1.9E+08	62.1	0.916	1.2E+05

Run 3			
X	E_a(kJ/mol)	R^2	A(min^{-1})
0.2	71.3	0.992	1.2E+05
0.3	73.1	0.991	1.7E+05
0.4	66.4	0.944	4.1E+04
0.5	39.9	0.968	1.4E+02
0.6	40.7	0.922	1.6E+02
0.7	65.8	0.910	3.6E+04
0.8	81.3	0.988	9.7E+05
Average	62.6	0.959	1.9E+05

Appendix D: CR Method Kinetic Parameters

Effect of dolomite on kinetic parameters

Table D-1 Kinetic parameters obtained by CR for pyrolysis of Subcoal™ PAF at different dolomite loadings.

0 wt.%				5 wt.%		
Model	E_a(kJ/mol)	A(min^{-1})	R^2	E_a(kJ/mol)	A(min^{-1})	R^2
G1	68.9	1.3E+04	0.896	48.2	3.1E+02	0.834
G2	76.3	5.7E+04	0.918	53.9	1.5E+05	0.860
G6	98.9	6.9E+06	0.955	66.9	7.9E+03	0.898
G7	43.2	2.9E+02	0.943	28.1	7.4E+00	0.855
G8	43.2	1.9E+02	0.943	28.1	4.9E+00	0.855
G9	43.2	1.4E+02	0.943	28.1	3.7E+00	0.855
G10	134.9	1.9E+09	0.833	123.0	2.6E+06	0.992
G14	98.1	2.9E+07	0.992	53.3	5.4E+03	0.914
G15	67.2	8.1E+04	0.980	39.7	2.4E+02	0.902
G16	44.2	5.7E+02	0.943	28.1	1.5E+01	0.855
10 wt.%				15 wt.%		
Model	E_a(kJ/mol)	A(min^{-1})	R^2	E_a(kJ/mol)	A(min^{-1})	R^2
G1	45.0	1.8E+02	0.865	36.4	6.2E+01	0.895
G2	51.2	3.0E+02	0.885	40.8	8.9E+01	0.909
G6	62.9	3.1E+03	0.911	48.5	6.1E+02	0.922
G7	26.1	4.4E+00	0.872	21.9	1.8E+00	0.881
G8	26.1	2.9E+00	0.872	21.9	1.2E+00	0.881
G9	26.1	2.2E+00	0.872	21.9	9.0E-01	0.881
G10	99.8	2.9E+10	0.999	88.7	2.5E+20	0.952
G14	48.5	1.8E+03	0.901	34.0	3.3E+02	0.880
G15	36.5	1.1E+02	0.900	26.3	3.1E+01	0.976
G16	26.1	8.7E+00	0.872	21.9	3.6E+00	0.932
20 wt.%						
Model	E_a(kJ/mol)	A(min^{-1})	R^2			
G1	39.9	6.7E+01	0.893			
G2	45.9	1.4E+02	0.926			
G6	60.6	2.9E+02	0.973			
G7	24.8	4.0E+00	0.909			
G8	24.9	9.0E+03	0.909			
G9	24.9	8.1E+00	0.921			
G10	92.5	3.0E+06	0.912			
G14	42.6	6.5E+02	0.930			
G15	30.3	6.1E+01	0.932			
G16	24.9	8.4E+00	0.909			

Table D-2 Kinetic parameters obtained by CR for CO_2 gasification of Subcoal™ PAF at different dolomite loadings.

0 wt.%				5 wt.%		
Model	E_a(kJ/mol)	A(min^{-1})	R^2	E_a(kJ/mol)	A (min^{-1})	R^2
G1	83.9	1.3E+04	0.896	46.9	2.9E+02	0.883
G2	93.3	5.7E+04	0.918	52.2	5.2E+02	0.891
G6	112.9	6.9E+06	0.955	63.9	5.5E+03	0.911
G7	59.2	2.9E+02	0.943	26.9	6.4E+00	0.883
G8	56.2	1.9E+02	0.943	26.9	4.3E+00	0.882
G9	43.3	1.4E+02	0.943	27.9	3.2E+00	0.881
G14	103.9	2.9E+07	0.992	50.1	3.4E+03	0.941
G15	74.2	8.1E+04	0.980	37.6	1.8E+02	0.923
G16	62.2	5.7E+02	0.943	26.9	1.3E+01	0.881
10 wt.%				15 wt.%		
Model	E_a(kJ/mol)	A(min^{-1})	R^2	E_a(kJ/mol)	A(min^{-1})	R^2
G1	43.4	1.1E+02	0.862	41.7	7.2E+01	0.899
G2	48.2	1.8E+02	0.829	46.1	1.1E+02	0.858
G6	58.6	1.4E+03	0.852	55.5	6.6E+02	0.874
G7	24.2	2.98	0.798	22.6	1.98	0.888
G8	24.2	1.99	0.798	22.6	1.32	0.898
G9	25.2	1.49	0.798	23.6	9.9E-01	0.928
G11	-	-	-	15.4	2.8E-01	0.911
G12	-	-	-	13.5	1.6E-01	0.871
G13	-	-	-	13.5	1.2E-01	0.861
G14	44.8	8.9E+02	0.890	41.1	3.7E+02	0.964
G15	33.7	6.4E+01	0.855	31.2	3.5E+01	0.949
G16	24.2	5.96	0.798	22.6	3.96	0.928
20 wt.%						
Model	E_a(kJ/mol)	A(min^{-1})	R^2			
G1	43.2	1.7E+01	0.903			
G2	49.4	2.8E+01	0.910			
G6	57.6	3.3E+02	0.908			
G7	24.1	1.2E+00	0.936			
G8	24.3	8.3E+02	0.942			
G9	25.1	6.4E+01	0.924			
G14	43.5	5.8E+01	0.965			
G15	33.3	2.8E+01	0.913			
G16	24.1	6.7E+01	0.922			

Table D-3 Kinetic parameters obtained by CR for combustion of Subcoal™ PAF at different dolomite loadings.

0 wt.%				5 wt.%		
Model	E_a(kJ/mol)	A(min^{-1})	R^2	E_a(kJ/mol)	A(min^{-1})	R^2
G1	63.9	1.3E+04	0.896	46.9	2.5E+02	0.852
G2	73.3	5.7E+04	0.918	52.4	4.6E+02	0.841
G6	96.9	6.9E+06	0.955	64.4	5.0E+03	0.865
G7	43.2	2.9E+02	0.943	27.1	6.03	0.821
G8	43.2	1.9E+02	0.943	27.1	4.02	0.821
G9	43.2	1.4E+02	0.943	27.1	3.02	0.821
G10	124.9	1.9E+09	0.833	-	-	-
G14	92.1	2.9E+07	0.942	43.9	3.4E+03	0.906
G15	65.2	8.1E+04	0.980	33.1	1.7E+02	0.874
G16	43.2	5.7E+02	0.993	27.1	1.2E+01	0.821
10 wt.%				15 wt.%		
Model	E_a(kJ/mol)	A(min^{-1})	R^2	E_a(kJ/mol)	A(min^{-1})	R^2
G1	39.4	6.5E+01	0.888	31.5	2.1E+01	0.892
G2	44.9	9.6E+01	0.834	37.3	2.6E+01	0.920
G6	53.5	6.3E+02	0.855	42.2	1.2E+02	0.939
G11	-	-	-	12.7	1.3E-01	0.802
G12	-	-	-	13.7	9.3E-02	0.802
G13	-	-	-	13.7	6.9E-02	0.802
G14	39.6	4.0E+02	0.893	36.6	8.0E+01	0.999
G15	29.4	3.5E+01	0.858	23.2	1.0E+01	0.962
20 wt.%						
Model	E_a(kJ/mol)	A(min^{-1})	R^2			
G1	39.4	6.5E+01	0.888			
G2	44.9	9.6E+01	0.834			
G6	53.5	6.3E+02	0.855			
G14	39.6	4.0E+02	0.893			
G15	29.4	3.5E+01	0.858			

Effect of olivine on kinetic parameters

Table D-4 Kinetic parameters obtained by CR for pyrolysis of Subcoal™ PAF at different olivine loadings.

0 wt.%				5 wt.%		
Model	E_a(kJ/mol)	A(min^{-1})	R^2	E_a(kJ/mol)	A(min^{-1})	R^2
G1	68.9	1.3E+04	0.896	52.4	1.2E+03	0.929
G2	76.3	5.7E+04	0.918	54.4	3.0E+03	0.947
G6	98.9	6.9E+06	0.955	75.9	9.0E+04	0.967
G7	43.2	2.9E+02	0.943	32.9	2.9E+01	0.961
G8	43.2	1.9E+02	0.943	32.9	2.0E+01	0.961
G9	43.2	1.4E+02	0.943	32.9	1.5E+01	0.961
G10	134.9	1.9E+09	0.833	-	-	-
G14	98.1	2.9E+07	0.992	66.9	1.5E+05	0.995
G15	67.2	8.1E+04	0.980	48.4	2.2E+03	0.987
G16	44.2	5.7E+02	0.943	32.9	5.9E+01	0.961
10 wt.%				15 wt.%		
Model	E_a(kJ/mol)	A(min^{-1})	R^2	E_a(kJ/mol)	A(min^{-1})	R^2
G1	47.9	1.9E+02	0.861	40.5	2.1E+01	0.892
G2	52.0	3.3E+02	0.843	44.3	2.6E+01	0.880
G6	63.3	3.1E+03	0.872	54.2	1.2E+02	0.839
G7	26.0	4.62	0.824	-	-	-
G8	27.0	3.08	0.822	-	-	-
G9	27.6	2.31	0.825	-	-	-
G14	49.3	1.9E+03	0.902	40.6	8.0E+01	0.946
G15	36.4	1.2E+02	0.871	30.2	1.0E+01	0.892
G16	26.0	9.25	0.823	-	-	-
20 wt.%						
Model	E_a(kJ/mol)	A(min^{-1})	R^2			
G1	45.8	4.9E+01	0.913			
G2	49.4	9.9E+01	0.910			
G6	59.4	1.8E+02	0.969			
G14	51.3	9.5E+01	0.955			
G15	36.0	1.5E+02	0.894			

Table D-5 Kinetic parameters obtained by CR for CO_2 gasification of Subcoal^{TM} PAF at different olivine loadings.

0 wt.%				5 wt.%		
Model	E_a(kJ/mol)	A(min^{-1})	R^2	E_a(kJ/mol)	A(min^{-1})	R^2
G1	83.9	1.3E+04	0.896	54.9	2.1E+03	0.904
G2	93.3	5.7E+04	0.918	63.4	7.3E+03	0.927
G6	112.9	6.9E+06	0.955	84.3	5.4E+05	0.963
G7	59.2	2.9E+02	0.943	36.9	7.2E+01	0.950
G8	56.2	1.9E+02	0.943	38.9	4.8E+01	0.950
G9	43.3	1.4E+02	0.943	37.9	3.6E+01	0.950
G14	103.1	2.9E+07	0.992	80.9	2.6E+06	0.993
G15	74.2	8.1E+04	0.980	56.4	1.3E+04	0.984
G16	62.2	5.7E+02	0.943	36.9	1.4E+02	0.950
10 wt.%				15 wt.%		
Model	E_a(kJ/mol)	A(min^{-1})	R^2	E_a(kJ/mol)	A(min^{-1})	R^2
G1	54.8	2.0E+03	0.926	52.9	2.7E+03	0.949
G2	62.9	6.4E+03	0.945	61.4	9.3E+03	0.965
G6	83.2	4.1E+05	0.975	82.6	6.8E+05	0.976
G7	36.3	6.2E+01	0.965	35.9	8.2E+01	0.981
G8	37.3	4.1E+01	0.965	36.9	5.4E+01	0.981
G9	36.4	3.1E+01	0.965	35.9	4.1E+01	0.981
G11	23.0	1.8E+00	0.886	22.0	2.21	0.921
G12	23.9	1.2E+00	0.886	21.0	1.47	0.921
G13	21.9	9.1E-01	0.886	21.0	1.10	0.921
G14	80.1	1.5E+06	0.990	77.5	2.7E+06	0.977
G15	56.1	9.4E+03	0.989	55.6	1.4E+04	0.992
G16	36.3	1.2E+02	0.965	35.2	1.6E+02	0.981
G17	23.0	3.7E+00	0.886	22.0	4.4E+00	0.921
20 wt.%						
Model	E_a(kJ/mol)	A(min^{-1})	R^2			
G1	54.3	2.3E+01	0.899			
G2	62.1	3.4E+01	0.925			
G6	83.6	8.8E+01	0.882			
G7	38.8	3.2E+00	0.863			
G8	37.9	2.2E+01	0.942			
G9	37.2	5.5E+01	0.923			
G14	80.0	6.5E+01	0.968			
G15	57.2	2.5E+02	0.932			
G16	36.3	4.3E+01	0.891			

Table D-6 Kinetic parameters obtained by CR for combustion of Subcoal™ PAF at different olivine loadings.

0 wt.%				5 wt.%		
Model	E_a(kJ/mol)	A(min^{-1})	R^2	E_a(kJ/mol)	A(min^{-1})	R^2
G1	63.9	1.3E+04	0.896	53.1	1.0E+02	0.876
G2	73.3	5.7E+04	0.918	47.8	1.6E+02	0.894
G6	96.9	6.9E+06	0.955	58.5	1.3E+03	0.915
G7	43.2	2.9E+02	0.943	23.9	2.8E+00	0.871
G8	43.2	1.9E+02	0.943	23.9	1.8E+00	0.871
G9	43.2	1.4E+02	0.943	23.8	1.4E+00	0.871
G10	124.9	1.9E+09	0.833	-	-	-
G14	92.1	2.9E+07	0.942	62.9	7.4E+02	0.892
G15	65.2	8.1E+04	0.980	38.2	5.6E+01	0.896
G16	43.2	5.7E+02	0.993	23.9	5.5E+00	0.871
10 wt.%				15 wt.%		
Model	E_a(kJ/mol)	A(min^{-1})	R^2	E_a(kJ/mol)	A(min^{-1})	R^2
G1	41.9	4.5E+01	0.885	37.5	2.4E+01	0.890
G2	45.2	6.4E+01	0.896	41.5	3.2E+01	0.961
G6	55.8	4.2E+02	0.904	50.4	1.8E+02	0.893
G14	48.6	2.5E+02	0.848	44.4	1.1E+02	0.855
G15	31.9	2.4E+01	0.863	27.5	1.3E+01	0.898
G16	-	-	-	19.7	1.8E+00	0.847
20 wt.%						
Model	E_a(kJ/mol)	A(min^{-1})	R^2			
G1	39.9	4.4E+01	0.894			
G2	44.4	8.3E+01	0.927			
G6	53.8	2.7E+00	0.967			
G14	47.9	1.2E+02	0.931			
G15	29.3	3.9E+01	0.897			

Appendix E: FBGR Parameters

Gasification parameters

Table E-1 Operating parameters for ER experiments.

Effect of ER						
Operating Parameters	Unit	ER				
		0.15	0.2	0.25	0.3	0.35
Airflow rate	l/min	40	40	40	40	40
Reaction bed temperature T2	°C	750	750	750	750	750
Bed material (sand) particle size	μm	500-600	500-600	500-600	500-600	500-600
Pellet	/	Pellet B	Pellet B	Pellet B	Pellet B	Pellet B
Static bed height (Hs)	cm	6.225	6.225	6.225	6.225	6.225
Mass rate of biomass feeding	g/min	43.2	32.4	25.9	21.6	18.5
(MAFR) stoichiometric	/	8.33	8.33	8.33	8.33	8.33
Air superficial velocity Uo	m/s	0.89	0.89	0.89	0.89	0.89

Table E-2 Gasification parameters at different ER at 750 °C.

Experiments	**1**	**2**	**3**	**4**	**5**
Equivalence ratio	0.15	0.2	0.25	0.3	0.35
Higher heating value (MJ/Nm^3)	6.10	5.95	5.76	4.56	3.78
Producer gas yield (Nm^3/kg)	1.11	1.19	1.25	1.25	1.28
Carbon conversion efficiency (%)	37.98	44.61	47.12	49.456	52.98
Cold gas efficiency (%)	33.94	31.88	29.29	23.45	18.21
Char yield (g/min)	8.50	7.50	7.00	5.00	4.00

Table E-3 Producer gas composition (vol%) of pellet B with different ER.

ER	**CO**	**CO_2**	**CH_4**	**H_2**	**N_2**
0.15	16.24	10.42	7.24	9.14	56.96
0.2	15.23	10.65	7.78	8.04	58.3
0.25	14.62	11.64	7.19	8.22	58.33
0.3	12.31	13.98	5.42	6.65	61.64
0.35	10.42	14.19	4.54	5.12	65.73

Table E-4 Operating parameters for different temperature experiments.

Effect of the Bed Temperature						
Operating Parameters	Unit	Pellet A/B				
Bed temperature	°C	350	450	550	650	750
Airflow rate	l/min (kg/hr)	40	40	40	40	40
Equivalence ratio (ER)	/	0.15	0.15	0.15	0.15	0.15
Bed (sand) particle size	μm	500-600	500-600	500-600	500-600	500-600
Static bed height (Hs)	cm	6.225	6.225	6.225	6.225	6.225
Mass rate of biomass feeding	g/min	43	43	43	43	43
(MAFR) stoichiometric	/	8.33	8.33	8.33	8.33	8.33
Air superficial velocity Uo	m/s	0.89	0.89	0.89	0.89	0.89

Table E-5 Gasification parameters of pellet A at different temperatures.

Experiments	**1**	**2**	**3**	**4**	**5**
Temperature (°C)	350	450	550	650	750
Higher heating value (MJ/Nm^3)	1.54	2.74	5.50	6.05	6.32
Producer gas yield (m^3/kg)	0.87	0.98	1.23	1.28	1.33
Carbon conversion efficiency (%)	14.47	25.03	49.49	50.43	54.69
Cold gas efficiency (%)	5.79	11.59	29.44	33.61	36.30
Char yield (g/min)	11.00	10.00	9.50	9.00	8.50

Table E-6 Gasification parameters of pellet B at different temperatures.

Experiments	**1**	**2**	**3**	**4**	**5**
Temperature (°C)	350	450	550	650	750
Higher heating value (MJ/Nm^3)	1.55	2.89	5.60	6.11	6.35
Producer gas yield (m^3/kg)	0.87	0.99	1.25	1.29	1.33
Carbon conversion efficiency (%)	14.56	25.79	50.34	51.09	54.93
Cold gas efficiency (%)	5.83	12.37	30.31	34.06	36.55
Char yield (g/min)	11.00	10.00	9.50	9.00	8.50

Table E-7 Producer gas composition (vol%) of pellet A with different temperatures.

Temperature (°C)	**CO**	**CO_2**	**CH_4**	**H_2**	**N_2**
350	5.21	7.24	1.83	1.22	84.5
450	8.62	10.14	3.14	3.15	74.95
550	12.14	14.22	7.86	6.56	59.22
650	14.32	11.62	7.63	9.41	57.02
750	16.82	10.95	7.45	9.62	55.16

Table E-8 Producer gas composition (vol%) of pellet B with different temperatures.

Temperature (°C)	**CO**	**CO_2**	**CH_4**	**H_2**	**N_2**
350	5.36	7.18	1.81	1.22	84.43
450	8.75	10.24	3.31	3.65	74.05
550	12.28	14.21	7.95	6.96	58.6
650	14.12	11.88	7.92	9.21	56.87
750	17.14	10.75	7.4	9.68	55.03

Table E-9 Operating parameters for olivine and dolomite experiments.

Olivine/Dolomite					
Operating Parameters	unit	Pellet B			
Catalyst ratio	Wt.%	15	15	15	15
ER	0.15	0.15	0.15	0.15	0.15
Airflow rate	l/min	40	40	40	40
Reaction bed temperature (T)	°C	600	650	700	750
Bed material (sand) particle size	µm	500-600	500-600	500-600	500-600
Static bed height (Hs)	cm	6.225	6.225	6.225	6.225
Mass rate of biomass feeding	g/min	43	43	43	43
(MAFR) stoichiometric		8.33	8.33	8.33	8.33
Air superficial velocity Uo	m/s	0.89	0.89	0.89	0.89

Table E-10 Gasification parameters of pellet B without catalyst.

Experiments	**No Catalyst**			
Temperature (°C)	600	650	700	750
Higher heating value (MJ/Nm^3)	3.63	6.04	6.16	6.18
Producer gas yield (m^3/kg)	1.06	1.18	1.31	1.32
Carbon conversion efficiency (%)	40.34	43.09	50.27	52.93
Cold gas efficiency (%)	18.81	20.06	26.25	33.55

Table E-11 Gasification parameters of pellet B in the presence of olivine.

Experiments	**Olivine 15 wt.%**			
Temperature (°C)	600	650	700	750
Higher heating value (MJ/Nm^3)	4.05	6.16	6.28	6.38
Producer gas yield (m^3/kg)	1.14	1.20	1.32	1.35
Carbon conversion efficiency (%)	42.67	45.67	53.73	54.97
Cold gas efficiency (%)	20.02	23.45	28.76	34.76

Table E-12 Gasification parameters of pellet B in the presence of dolomite

Experiments	**Dolomite 15 wt.%**			
Temperature (°C)	600	650	700	750
Higher heating value (MJ/Nm^3)	4.12	6.25	6.37	6.45
Producer gas yield (m^3/kg)	1.14	1.21	1.34	1.40
Carbon conversion efficiency (%)	43.06	45.97	54.44	55.20
Cold gas efficiency (%)	20.34	24.52	29.45	36.97

Table E-13 Producer gas composition (vol%) of pellet B without catalyst at different temperatures.

Temperature (°C)	**CO**	**CO_2**	**CH_4**	**H_2**	**N_2**
600	11.36	15.72	8.15	5.25	59.52
650	14.12	11.88	7.92	9.21	56.87
700	15.32	11.68	7.2	9.53	56.27
750	17.14	10.75	7.4	9.68	55.03

Table E-14 Producer gas composition (vol%) of pellet B with olivine 15 wt.% at different temperatures.

Temperature (°C)	**CO**	**CO_2**	**CH_4**	**H_2**	**N_2**
600	11.12	15.43	5.42	3.85	64.18
650	13.14	14.29	5.12	6.41	61.04
700	16.82	13.68	4.84	8.32	56.34
750	18.62	11.55	4.54	11.21	54.08

Table E-15 Producer gas composition (vol%) of pellet B with dolomite 15 wt.% at different temperatures.

Temperature (°C)	CO	CO_2	CH_4	H_2	N_2
600	12.23	14.2	5.11	4.24	64.22
650	14.57	12.78	4.55	7.89	60.21
700	17.9	11.14	4.24	10.21	56.51
750	21.44	8.25	2.93	14.21	53.17

E-16 MATLAB code

Conversion curves

```
clc
clear
[data_a, data_b, alldata_received]=xlsread('G:\PhD writing
Cardiff\Experiments\ahmed TGA\Matlab001\Exctra Copy of Dolomite
0%.Air.20C.Run2.Kinetic.xlsx',20,'A6:AL6456');

figure(1)
X=data_a(:,1:2:8);
Y=data_a(:,2:2:8);
plot(X(:,1),Y(:,1),'g')
ylabel('Conversion X')
xlabel('Temperature, (^oC)')

hold on
plot(X(:,2),Y(:,2),'r')
plot(X(:,3),Y(:,3),'b')
plot(X(:,4),Y(:,4),'k')

hold off
legend('boxon')
legend({'5 ^oC/min','10 ^oC/min','15 ^oC/min','20
^oC/min'},'Location','southwest','FontSize',2)
```

Kinetic model free curves

```
clear
[data_a, data_b, alldata_received]=xlsread('G:\PhD writing
Cardiff\Experiments\matlab\Ln(B dadT).xlsx','A1:N6');
y1=xlsread('Ln(B dadT).xlsx','Sheet20','A3:A6');
x1=xlsread('Ln(B dadT).xlsx','Sheet20', 'B3:B6');

y2=xlsread('Ln(B dadT).xlsx','Sheet20','C3:C6');
x2=xlsread('Ln(B dadT).xlsx','Sheet20', 'D3:D6');

y3=xlsread('Ln(B dadT).xlsx','Sheet20','E3:E6');
x3=xlsread('Ln(B dadT).xlsx','Sheet20', 'F3:F6');
```

```
y4=xlsread('Ln(B dadT).xlsx','Sheet20', 'G3:G6');
x4=xlsread('Ln(B dadT).xlsx','Sheet20', 'H3:H6');

y5=xlsread('Ln(B dadT).xlsx','Sheet20', 'I3:I6');
x5=xlsread('Ln(B dadT).xlsx','Sheet20', 'J3:J6');

y6=xlsread('Ln(B dadT).xlsx','Sheet20', 'K3:K6');
x6=xlsread('Ln(B dadT).xlsx','Sheet20', 'L3:L6');

y7=xlsread('Ln(B dadT).xlsx','Sheet20', 'M3:M6');
x7=xlsread('Ln(B dadT).xlsx','Sheet20', 'N3:N6');

figure(1);
hold on
axis([0.0013,0.002,-5,-1]);
p1 = polyfit(x1, y1, 1);
v1 = polyval(p1,x1);
plot(x1,y1,'r*',x1,v1,'r-','LineWidth',2.0);

p2 = polyfit(x2, y2, 1);
v2 = polyval(p2,x2);
plot(x2,y2,'mo',x2,v2,'m-','LineWidth',2.0);

p3 = polyfit(x3, y3, 1);
v3 = polyval(p3,x3);
plot(x3,y3,'bs',x3,v3,'b-','LineWidth',2.0);

p4 = polyfit(x4, y4, 1);
v4 = polyval(p4,x4);
plot(x4,y4,'gh',x4,v4,'g-','LineWidth',2.0);

p5 = polyfit(x5, y5, 1);
v5 = polyval(p5,x5);
plot(x5,y5,'y<',x5,v5,'y-','LineWidth',2.0);

p6 = polyfit(x6, y6, 1);
v6 = polyval(p6,x6);
plot(x6,y6,'cd',x6,v6,'c-','LineWidth',2.0);


p7 = polyfit(x7, y7, 1);
v7 = polyval(p7,x7);
plot(x7,y7,'k+',x7,v7,'k-','LineWidth',2.0);

legend('0.2', '', '0.3', '', '0.4', '', '0.5', '', '0.6', '', '0.7', '',
'0.8','');
hold off

ylabel('Ln (B/Ti^1.894661)');
xlabel('1/T, K^-1');
```